Design Strategy for Highly Efficient Purely Organic Photoredox Catalysis

Yonghwan Kwon

Department of Materials Science and Engineering

Ulsan National Institute of Science and Technology

Design Strategy for Highly Efficient Purely Organic Photoredox Catalysis

A thesis/dissertation submitted to

Ulsan National Institute of Science and Technology

in partial fulfillment of the

requirements for the degree of

Doctor of Philosophy

Yonghwan Kwon

12.15.2022 of submission

Approved by

_____

Advisor

Prof. Wook Jo

Design Strategy for Highly Efficient Purely Organic Photoredox Catalysis

Yonghwan Kwon

This certifies that the thesis/dissertation of Yonghwan Kwon is approved.
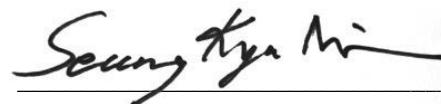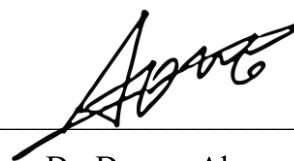
12.15.2022 of submission

Advisor: Prof. Wook Jo

Prof. Min Sang Kwon

Prof. Chaenyung Cha

Prof. Seung Kyu Min

Dr. Dowon Ahn

Abstract

Sunlight is an essential energy source that profoundly affects our lives (e.g., photosynthesis), and as light is regarded as one of the next-generation energy sources owing to its economic and environmental benefits, there have been attempted to utilize light as an energy source. To handle the sunlight in organic chemistry, in the beginning, sunlight was employed just as a heat source for distillation.[1] Today, beyond thermal energy source, photochemistry has attracted much academic interest for generation of new reactive species (i.e., photoexcited species) in organic synthesis and polymerization. Consequently, in more future-oriented perspectives, those synthetic advances have been expanding into the utilization of the visible-light or near-infrared regions over the ultraviolet light region.

In the present dissertation, the design strategies for highly efficient photoredox catalysis under visible-light irradiation was studied. In addition, designed purely organic photoredox catalysts (PCs) based on cyanoarenes, one of the classes of thermally activated delayed fluorescence (TADF) compounds, were prepared to perform highly efficient organic (i.e., reductive dehalogenation) and polymeric (i.e., pressure-sensitive adhesive, PSA) syntheses. **Chapter 1** presents an introduction to photoredox catalysis and a synopsis of the dissertation. In **Chapter 2**, the design strategies for highly efficient formation of radical anion of cyanoarene-based PCs (PC$^{\bullet-}$) were studied; under visible-light irradiation, photoexcited PCs which have long-lived triplet excited state (T_1) become one-electron-reduced species in the presence of sacrificial reducing agents. Furthermore, the photodegradation behavior of PCs, which would reduce their catalytic efficiencies, was studied using the density functional theory (DFT) calculations and detailed structural analysis of photodegraded products. Subsequently, based on the understanding of formation and degradation of PC$^{\bullet-}$, the highly efficient photoredox-mediated reductive dehalogenation combined with both ultra-low PC loading (ca. 0.005 mol%) and oxygen tolerance was realized. In **Chapter 3**, UV-blocking acrylic PSAs were successfully prepared with cyanoarene-based PCs under visible-light irradiation. In particular, PC design strategies were studied to efficiently generate the PC$^{\bullet-}$ with various donor moieties to control their electrochemical properties. Bulk polymerization of the prepolymer was mechanistically studied combined with DFT calculations. Oxygen tolerance behavior in bulk polymerization was also observed, and an oxygen tolerance mechanism was proposed. The overall conclusion of this dissertation and additional supplementary contents are presented in **Chapter 4** and the **Appendix**, respectively.

Contents

List of Figures

List of Tables

List of Abbreviations

UV	Ultraviolet light
NIR	Near-infrared light
PC	Photoredox catalyst
$h\nu$	Photoexcitation
SET	Single-electron transfer
ET	Electron transfer
PET	Photoinduced electron transfer
ΔG_{PET}	Driving force for photoinduced electron transfer
$E_{0\text{-}0}$	Photo-excited state energy
E_{red}^{0}	Ground state reduction potential
E_{ox}^{0}	Ground state oxidation potential
E_{red}^{*}	Excited state reduction potential
E_{ox}^{*}	Excited state oxidation potential
S_1	Singlet excited state
T_1	Triplet excited state
SCE	Saturated calomel electrode
CT	Charge-transfer
MLCT	Metal-to-ligand charge-transfer
SOC	Spin-orbital coupling
IC	Internal conversion
ISC	Intersystem crossing
RISC	Reverse intersystem crossing
TTA	Triplet-triplet annihilation
PTH	10-phenylphenothazine
HOMO	Highest occupied molecular orbital
LUMO	Lowest unoccupied molecular orbital
PTH	10-phenylphenothaizine
ConPET	Consecutive photoinduced electron transfer
$PC^{\bullet-}$	Radical anion of photoredox catalyst
$^{1/3}PC^{*}$	Photo-excited photoredox catalyst
TADF	Thermally activated delayed fluorescence
PF	Prompt fluorescence

DF	Delayed fluorescence
RT	Room temperature
ΔE_{ST}	Singlet-triplet energy gap
XAT	Halogen atom transfer
BPI	Benzo[*ghi*]perylene imides
Np	Naphthalene
LED	Light-emitting diode
PSA	Pressure-sensitive adhesive
TCSPC	Time-correlated single photon counting
CV	Cyclic voltammetry
DIPEA	*N,N*-diisopropylethylamine
DIPMA	*N,N*-diisopropylmethylamine
DIPA	*N,N*-diisopropylamine
TBA	Tributylamine
TEA	Triethylamine
TMB	1,3,5-trimethoxybenzene
GC	Gas chromatography
FID	Flame ionization detector
NMR	Nuclear magnetic resonance spectroscopy
TLC	Thin layer chromatography
DFT	Density functional theory
BET	Back electron transfer
TCRIP	Triplet contact radial ion pair
BA	n-Butyl acrylate
HBA	4-hydroxybutyl acrylate
DMAEA	2-dimethylaminoethyl acrylate
DMAEMA	2-dimethylaminoethyl methacrylate
DMAEAc	2-dimethylaminoethyl acetate
DMBA	*N,N*-dimethylbenzylamine
EA	Ethyl acetate
$R_3N^{\bullet+}$	Tertiary amine radical cation
COSY NMR	Correlation spectroscopy NMR
NOESY NMR	Nuclear overhauser effect spectroscopy NMR

Chapter 1. Photoredox Catalysis

1.1 Introduction to Photoredox Catalysis

Over the past decades in organic syntheses, photoredox catalysis has become a promising method for electron transfer (ET) process because of its mild conditions, high functional-group tolerance, unique operating mechanism, and feasible spatial-temporal control.[2-6] **Figure 1.1** illustrate proposed photoredox catalysis mechanism where after light absorption excited photoredox catalysts (PCs) participate in single-electron transfer (SET) events with substrates. Consequently, reactive radical intermediates are generated from various bench-stable substrates, where new $C(sp^2/sp^3)$–$C(sp^2/sp^3)$ or other chemical bonds can be formed. This photoredox catalysis contributes to successful organic transformations, including the synthesis of organic compounds[7-10] and polymerization.[11-16] Nowadays, because ultraviolet (UV) light (or high-energy visible light) can cause photodamage and afford undesired products,[4] the trends of visible light utilization have steadily increased in the synthesis of organic compounds.[2-4] Therefore, this dissertation mainly studied visible-light-driven photoredox catalysis.
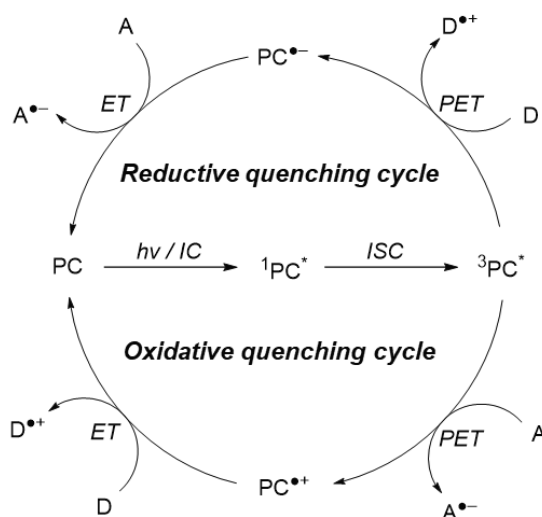
Figure 1.1. Photoredox catalysis mechanism involving reductive and oxidative quenching cycles. PC, ET, PET, D, A, IC, and ISC denote photoredox catalyst, electron transfer, photoinduced ET, electron donor, electron acceptor, internal conversion, and intersystem crossing, respectively.

Photoredox catalysis enables the realization of the electron transfer (ET) process, which is impossible between PCs in ground-state and the target substrate, conferring energy of the absorbed photon (E_{0-0}), thus, the photoinduced electron transfer (PET) process has a larger driving force (ΔG_{PET}) for PCs to be reduced (or oxidized) (**Figure 1.2**). The feasibility of the PET process between photoexcited PCs and target substrates can be evaluated by ΔG_{PET} following the Rehm–Weller equation, eqs. (1–2), and the rate constant of ET process was predicted using the Marcus theory[17] mediated by the outer-sphere ET mechanism.[18,19]

$$\Delta G_{PET} = -F\left(E_{red}^{*}(PC^{*}/PC^{\cdot-}) - E_{ox}^{0}(Sub^{\cdot+}/Sub)\right) \text{ for reductive quenching cycle,} \qquad \text{(eq. 1)}$$

$$\Delta G_{PET} = -F\left(E_{red}^{0}(Sub/Sub^{\cdot-}) - E_{ox}^{*}(PC^{\cdot+}/PC^{*})\right) \text{ for oxidative quenching cycle,} \qquad \text{(eq. 2)}$$

where F is the Faraday constant, E_{ox}^{0}/E_{red}^{0} are ground state oxidation/reduction potentials, and E_{ox}^{*}/E_{red}^{*} are excited state oxidation/reduction potentials, respectively. In this dissertation, all ground state reduction potentials of PCs ($E_{red}^{0}(PC)$) were measured in CH_3CN against the saturated calomel electrode (SCE) unless otherwise specified. Their excited state reduction potentials ($E_{red}^{*}(PC)$) were estimated using $E_{red}^{*} = E_{0-0} + E_{red}^{0}$; $E_{0-0}(S_1)$ and $E_{0-0}(T_1)$ were evaluated by the onset of PL emission and gated PL emission in the reaction solvent, respectively, at 65 K.

Figure 1.2. Thermodynamics of the ET and PET process of PC in the ground and photoexcited states with target substrates under (a) reductive and (b) oxidative quenching cycles.

1.2 Organic Photoredox Catalysis

For years, photoredox catalysis has relied mainly on transition-metal complexes such as coordinately saturated Ir(III)[20–22] and Ru(II)[23–27] polypyridyl complexes. The combination of a strongly σ-donating metalated carbon atom and a π-accepting pyridine ring can result in low-energy metal-to-ligand charge transfer (MLCT) states. Following absorption of light for MLCT states in the singlet excited state (S_1), the strong spin–orbit coupling (SOC) associated with the heavy metal atom considerably increases the rate of intersystem crossing (ISC) to the corresponding triplet excited state (T_1) ($\tau_{ISC} < 1$ ps and $\Phi_{ISC} \sim$ 100%) (**Figure 1.3**). This highly efficiently generated T_1 in an excited state mainly participates in the PET process with substrates. However, photoredox catalysis using a transition-metal complex as a PC still has limitations because the cost of the rare-earth element is not only relatively high but also easily affected by the international situation. Furthermore, a potential hazard from metal residue limits application scope, such as biomaterial and electronics.

Concerning applications in green chemistry, organic PCs have recently attracted considerable interest because they can provide solutions to the critical issues of transition-metal PCs owing to their low price, low toxicity profiles, broad structural diversity, and environmental profile.[5] In particular, the structural variety of organic compounds allows for reaching new properties and reactivity of PCs, which are inaccessible by transition-metal PCs. Based on the structural diversity, the organic PCs (e.g., acridiniums,[7,28,29] xanthenes,[30–34] and phenothiazines[35,36]) have been employed to drive different types of organic reactions[5,29,37] and polymerizations.[11,13] However, a challenge of organic PCs remains, which is the activation of substrates with highly negative reduction potentials ($E_{red}^0 < -2$ V), such as aryl halides, one of the most conventional substrates to give carbon-centered radical intermediates. Further advanced methodologies to activate aryl halides under milder conditions via organic photoredox catalysis have been developed to overcome this challenge, of which the energy of the lowest unoccupied molecular orbital (LUMO) in a PC was increased for highly reducing potentials. For example, recently, the de Alaniz and Hawker groups reported the reductive dehalogenation of aryl/alkyl halides with a high degree of oxygen tolerance using 10-phenylphenothiazine (PTH) as a PC associated with a highly negative excited state oxidation potential ($E_{ox}^* = -2.1$ V).[36] The reduction of aryl halides was quite successful even in the presence of oxygen that acts as a potent T_1 excited state quencher because the lowest excited S_1 state of PTH is primarily responsible for the catalysis. However, owing to the greater LUMO energy, the 380 nm UV light is needed to photoexcite PTH, which comes with a significant risk of photodamage and undesirable byproducts.[4] Therefore, the utilization of visible-light irradiation for challenging substrate activation has recently been attempted (see **Chapter 1.3**) to achieve energy efficiency and avoid undesired products.

a) ■ *Transition-metal complex photoredox catalysts*

S_1
(^{1}MLCT)

T_1 (^{3}MLCT) ET

ISC
τ_{ISC} = 0.1~1 ps
Φ_{ISC} = 100 %

Photoinduced ET
• Strong spin-orbit coupling
• 100% ISC QY
• Only triplet generation

Phosphorescence
τ_P = 1 µs~1000 µs

S_0

e.g.

[Ru(bpy)$_3$]Cl$_2$ *fac*-Ir(ppy)$_3$ [Ir(ppy)$_2$(dtbbpy)]PF$_6$

b) ■ *Purely organic photoredox catalysts*

S_1

T_1 ET

ISC
τ_{ISC} = 0.1~10 ns
Φ_{ISC} = 0~100 %

Fluorescence
τ_F = 1 ns~100 ns

Phosphorescence
τ_P = 1 ms~1000 s

Photoinduced ET
• Consider both singlet and triplet
• Both contribution of singlet and triplet to PET

S_0

e.g.

4Cz-IPN

Perylene diimide (PDI)

Phenothiazine (PTH)

Xanthenes (e.g. Rh6G)

Figure 1.3. Comparison between the transition-metal complex PC and purely organic PC in the PET process; S_0, S_1, and T_1 denote PC in the ground, singlet excited, and triplet excited states, respectively.

4

1.3 Consecutive Photoinduced Electron Transfer

The single visible-light photon energy is limited to ca. 3.1 eV (for 400 nm), establishing a theoretical energy threshold between the PC and the target substrate. Multiphoton excitation has been actively developed to overcome the energy threshold. In 2014, König et al. demonstrated a consecutive photoinduced electron transfer (ConPET) process (**Figure 1.4**) that generates strongly reducing photoexcited organic PCs of the perylene diimide (PDI) analog using multiphoton excitation inspired by the Z scheme of the biological photosynthesis and a reductive transformation of inactivated aryl halides based on the ConPET process.[38] Accordingly, after PCs are photoexcited and undergo reductive quenching cycle, the PC$^{\bullet-}$ which has visible-light absorption, is formed. Consequently, under continuous irradiation, the formed PC$^{\bullet-}$ are re-photoexcited generating a highly active PC species (i.e., PC$^{\bullet-*}$) with comparable reducing power to PC in a singly photoexcited state (PC*).
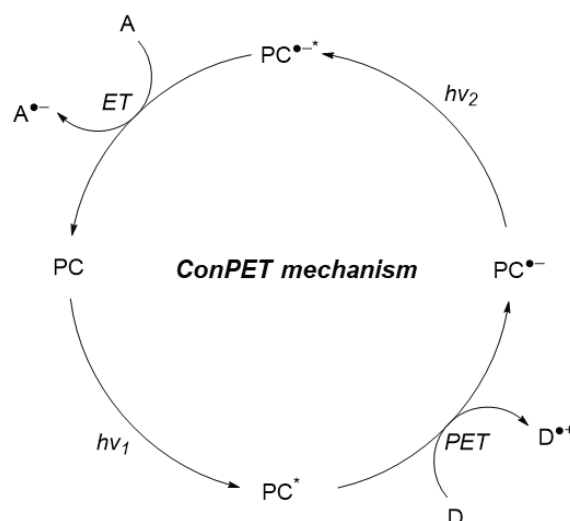
Figure 1.4. The proposed consecutive photoinduced electron transfer (ConPET) mechanism.

The ConPET mechanism can be applied to various PC classes, such as xanthenes,[31,39] cyanoarenes,[40–42] and Ir complexes,[21] involved in reductive quenching cycles.[43–45] In particular, in 2021 Nicewicz et al. discovered photoexcited acridine radical species that could be applied as a photo-oxidant and photo-reductant with a wide range of redox potential, showing a successful visible-light-driven reductive dehalogenation, detosylation, and sulfonamide cleavages that cannot be realized using conventional photoredox catalysis.[7] Meanwhile, the electrochemical approach for PC$^{\bullet-}$ formation has been studied with advantages, including a broadening accessible redox potential window and user-friendly reaction conditions because the ConPET system is mediated by PC$^{\bullet-}$.[8] However, although the ConPET process is a novel strategy for enabling reductive transformations of challenging substrates for reduction with highly negative $E_{red}^0 < -2.7$ V, it commonly requires high PC loadings (ca. 5–10 mol%) and an inert

5

atmosphere to generate sufficient amounts of PC intermediates, which increases the reaction cost under harsh conditions, such as those involving toxic additives and elevated temperature. Furthermore, the mechanistic pathway of ConPET remains unclear in this photoredox catalysis field, with both supporting[46] and opposing[47] studies based on the transient absorption spectroscopic technique.

1.4 Thermally Activated Delayed Fluorescence Compounds in Photoredox Catalysis

Recently, among purely organic PCs, thermally activated delayed fluorescence- (TADF-) based PCs have attracted considerable interest for their excellent photocatalytic performances. Because TADF-based PCs have a unique photophysical characteristic compared with conventional PCs such as transition-metal complexes or PTH, they have both S_1 and T_1 excited states (**Figure 1.5**).[48,49] After the photoexcitation of TADF-based PCs, the S_1 state is quickly generated and subsequently decayed by radiative and nonradiative pathways. The initial radiative decay exhibits a prompt fluorescence (PF) with a nanosecond-scale lifetime. Moreover, the nonradiative decay pathway of the S_1 state includes the decay back to the ground state and ISC to the triplet manifold (i.e., T_n, n = 1, 2, 3, ...) followed by internal conversion (IC) causing an electron to occupy the lowest triplet excited state (i.e., T_1 state). As phosphorescence from the T_1 excited state remains a spin-forbidden process, it is typically not seen in the T_1 excited state of these molecules at RT owing to the large singlet–triplet energy gap (ΔE_{ST}) between S_0 and T_1. Therefore, the excited state in T_1 mostly decays with the nonradiative decay. However, because the small ΔE_{ST} between the S_1 and T_1 excited states can be overcome thermally even at RT (ca. 0.2 eV), a reverse intersystem crossing (RISC) process from T_1 to S_1 is possible at RT, regenerating S_1 in the excited state with delayed fluorescence (DF) with microsecond-scale lifetime. Both S_1 and T_1 excited states coexist in a TADF-based PC, thus, they would simultaneously contribute to photoredox catalysis, and it is not easy to separate each contribution to PET of photoexcited states. To control each contribution to PET rate in organic reactions and polymerization, the relative exciton populations of the S_1 and T_1 states of TADF-based PCs are determined by their photophysical properties associated with the structural diversity such as cyanoarenes,[11,50,51] dihydrophenazines,[15,52] phenoxazines,[53,54] phenothiazines,[35] and dimethyl-dihydroacridines.[55]
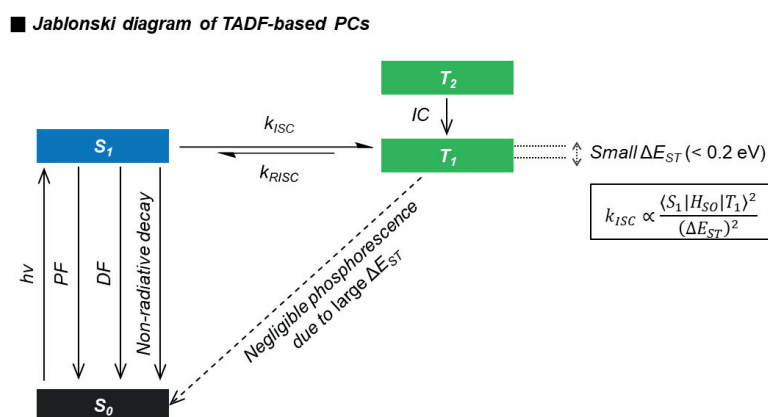
Figure 1.5. Jablonski diagram of thermally activated delayed fluorescence-based PCs.

7

1.5 Objective of the Dissertation

Maximizing the reducing (or oxidizing) power and concentration of active PC species that activate the substrate of interest using an ET process is essential to surmount the inherent limitations of traditional visible-light-driven photoredox catalysis. This can mainly be facilitated in a reductive quenching cycle where PC$^{\bullet-}$ primarily acts as an active PC species because it commonly has a far longer lifetime than the excited PC species (i.e., ^{1,3}PC*), working as an active PC intermediate in an oxidative quenching cycle.[56] Moreover, PC$^{\bullet-}$ formation by the reductive quenching cycle is a key process for an unconventional photoredox catalysis, such as the ConPET or halogen atom transfer (XAT) process reported by Leonori's group.[57] Highly effective photoredox catalysis depends heavily on the PC$^{\bullet-}$ concentration in the photostationary state and the ground-state reduction potential E_{red}^0(PC). Under visible-light irradiation, a high PC$^{\bullet-}$ concentration indicates a high collision frequency between the active PC species and substrates, which promotes the ET and/or ConPET events.

However, PC with extremely negative E_{red}^0(PC) faces difficulty in obtaining a high PC$^{\bullet-}$ concentration. Accordingly, the PC$^{\bullet-}$ formation was typically performed in PCs with less negative E_{red}^0(PC) (e.g., PDI,[38,46] acridiniums,[7,28,29] xanthenes,[30,31] and Ru(bpy)$_3^{2+}$,[23–27]). Otherwise, special reaction conditions were used for the effective formation of PC$^{\bullet-}$ (**Figure 1.6**). For example, Miyake et al. developed a new PC based on benzo-*ghi*-perylene imides (BPI) with significantly negative E_{red}^0(PC) of approximately −1.30 V to successfully perform a photoredox-mediated Birch reduction,[45]; in their work, the highly reducing PC$^{\bullet-}$ of BPI was produced through an OH$^-$-associated complex (i.e., BPI–OH$^-$) as an intermediate. The Wickens group successfully generated PC$^{\bullet-}$ with high reducing power from a naphthalene-based analog (Np) (E_{red}^0(PC) ≈ −1.3 V).[43] Electrochemistry was employed to produce Np$^{\bullet-}$ rather than a sacrificial electron donor, such as tertiary amines. However, a recent report of the Nocera group suggested that the Meisenheimer complex of Np (Np(H)$^-$), not Np$^{\bullet-}$, is an active intermediate for photoelectrocatalysis.[47] Moreover, König et al. reported the successful generation of highly reducing radical species from a cationic Ir complex (Ir(dtbby)(ppy)$_2$PF$_6$, E_{red}^0(PC) ≈ −1.51 V) *via* an assembly-promoted SET strategy.[21] Although the generation of Ir(dtbby$^{\bullet-}$)(ppy)$_2$ was not very successful in organic solvents because of the insufficient stability, the Ir(dtbby$^{\bullet-}$)(ppy)$_2$ complex was stabilized in aqueous micellar solutions through noncovalent interactions and compartmentation of the reacting species.
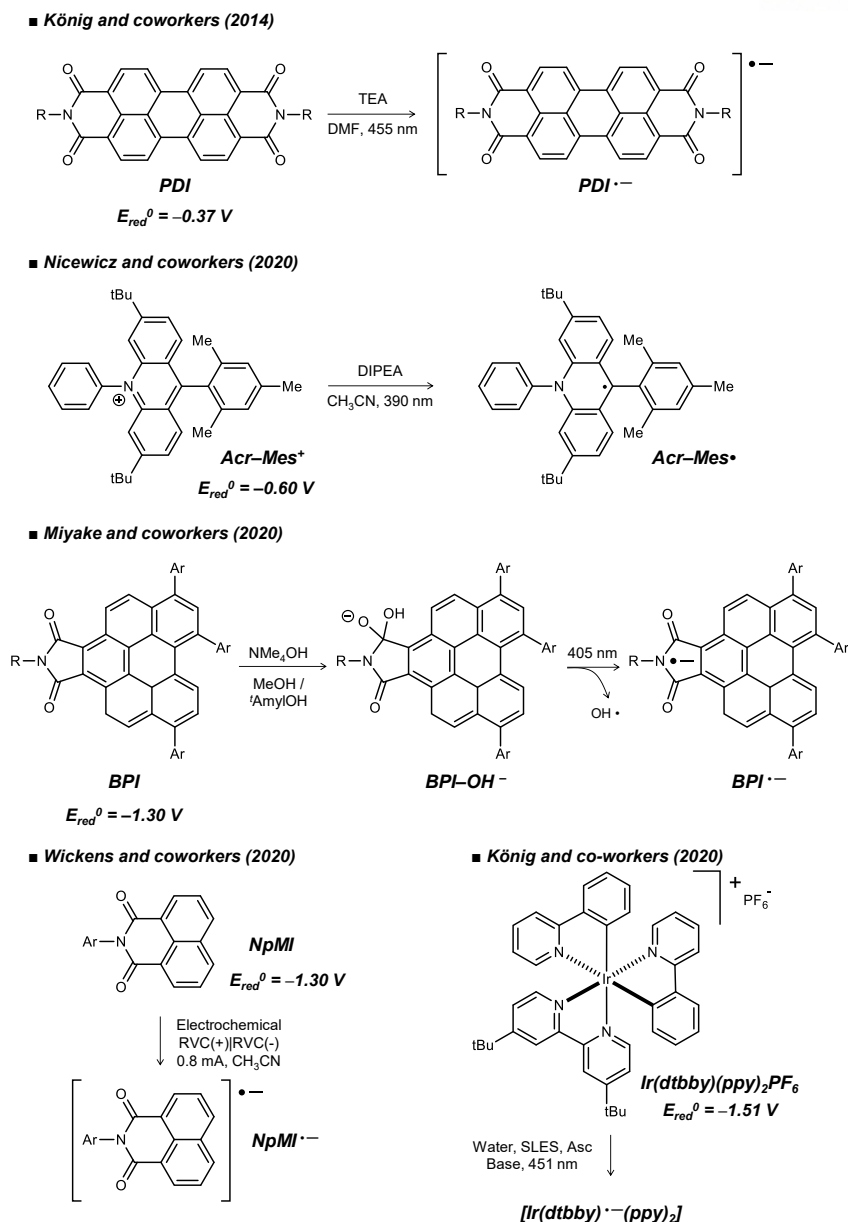
Figure 1.6. Previous studies for the PC$^{\bullet-}$ formation.

Despite the abovementioned recent advances and beyond the existing examples of organic radical anions, no general guideline exists for the discovery of PCs that efficiently generate PC$^{\bullet-}$ with a highly negative reduction potential under mild visible-light irradiation conditions. In this dissertation, the general design strategy of these PCs was studied using the purely organic TADF compound as a model PC, particularly cyanoarenes, to determine the origin of the well-formed PC$^{\bullet-}$ and its behavior in actual photoredox catalysis. Furthermore, cyanoarene-based PCs were designed and prepared based on the design principle of PCs to derive highly effective visible-light-driven photoredox catalysis in the synthesis of pressure-sensitive adhesive (PSA) with UV-blocking properties for foldable display applications combined with lower PC loadings and oxygen tolerance.

Chapter 2. Formation and Degradation of Radical Anion of Cyanoarenes

This chapter was written based on the submitted manuscript to be published.

2.1 Introduction

Cyanoarenes have become a desirable organic PC since recent studies by the groups of Zhang,[50] Zeitler,[51] Kwon,[11] and others.[49,58–60] Such PCs have demonstrated good catalytic capabilities in a range of visible-light-driven organic reactions[58–60] and polymerizations.[61–65] Owing to their higher photocatalytic activity in radical anion–mediated photoredox catalysis, 4DP-IPN and its analogs have attracted considerable attention. For example, Wickens et al. reported that strong $C(sp^2)$–N and $C(sp^2)$–O bonds were successfully activated via photocatalyzed reductive cleavage by the 4DP-IPN$^{\bullet-}$ produced electrochemically.[41] More recently, the groups of Wickens[42] and Wu[40] used 4DP-IPN analogs as PCs to perform the phosphonylation, borylation, and hydroarylation of highly inactivated aryl chlorides. Through careful characterization of the 4DP-IPN$^{\bullet-}$ (i.e., UV–Vis absorption and electron paramagnetic resonance spectra), 4DP-IPN$^{\bullet-}$ was found to be an intermediate species for the ConPET mechanism and that its high reducing power ($E_{red}^0 = -1.66$ V) is the crucial element. Nevertheless, it is very unusual for PCs with substantially negative E_{red}^0 to be reduced, as noted in **Chapter 1.5**.

Despite these significant advancements, the conditions where PC$^{\bullet-}$ of cyanoarenes forms remain unclear. Indeed, inadequate PC selection, high PC loading, and a poorly selected excitation source are examples of how lack of understanding of formation of PC$^{\bullet-}$ can result in ineffective radical anion–mediated photoredox processes. Herein, we investigated the formation and degradation of PC$^{\bullet-}$ using cyanoarenes in photoredox-mediated reactions. After screening cyanoarene-based PCs with a range of redox potentials and T_1-excited-state generation abilities, the formation of cyanoarene-based PC$^{\bullet-}$ was affected by the highly efficient generation of long-lived T_1 and the moderately positive E_{red}^*(PC). Furthermore, different photodegradation behaviors of cyanoarene-based PCs based on their electronic and steric features were observed. For a detailed investigation on the behaviors in actual photoredox catalysis, the photoredox reductive dehalogenation of aryl halides was performed as a model reaction, confirming that the dehalogenation of aryl halides and photodegradation of PCs coexist and they depend on the rate of the ET process between PC$^{\bullet-}$ and aryl halides from the *in-situ* monitoring of the dehalogenation reaction. Moreover, based on the highly efficient formation of 4DP-IPN$^{\bullet-}$, the extremely efficient dehalogenation reactions of aryl halides were demonstrated under minimal loading of PC (0.001 mol%) to aryl halides, outperforming other conventional organic PCs.

2.2 Experimental

2.2.1 Materials

Commercially available PCs (Ir and Ru complexes, Rh6G and PDI) were purchased from Aldrich, TCI, and Alfa Aesar. Other cyanoarene-based PCs were prepared according to the procedures previously reported.[11] The synthetic procedures and structural characterization of PCs are fully described in **Appendix 1**. All chemicals (i.e., aryl halides and tertiary amines) and organic solvents were purchased commercially and used without further purification.

2.2.2 General Procedure

2.2.2.1 General Procedure for PC$^{\bullet-}$ Formation

Inside the glove box, a sealable quartz cuvette was charged with PC (1.0×10^{-4} M) and N,N-diisopropylethylamine (DIPEA) (0.5 M) in 3 ml of anhydrous CH_3CN. Subsequently, the quartz cuvette was capped with a screw cap and sealed with parafilm. The reaction was performed under the illumination of two 3 W 455 or 515 nm LEDs for 1 min at RT. After illumination, UV–Vis absorption of the illuminated solutions was measured immediately. In preparation for the reaction, pre-prepared stock solutions of PCs were used to increase the reproducibility of results.

2.2.2.2 General Procedure for Photodegradation of Cyanoarene-Based PCs

Outside the glove box, a 20-ml glass vial equipped with a stirring bar was charged with PC (1.0×10^{-4} M) and DIPEA (0.5 M) in 1 ml of anhydrous CH_3CN as a solvent. Then, the vial was capped with a rubber septum or screw cap and sealed with parafilm. The reaction batches were purged with N_2 (99.999%) for 30 min outside the glove box. Subsequently, the reaction was performed for 2 h under the illumination of two 3 W 455 nm LEDs at RT. Without product isolation, the aliquots of the reaction mixture were diluted with CH_2Cl_2 and monitored by Thin-layer chromatography (TLC). In preparation for the reaction, the pre-prepared stock solutions of PCs were used for higher result reproducibility. For a scale-up reaction of photodegradation, a 20-ml glass vial equipped with a stirring bar was charged with PC (1.0×10^{-2} M) and DIPEA (1 M) in 5~6 ml of anhydrous CH_3CN as a solvent. Then, the vial was capped with a rubber septum or screw cap and sealed with parafilm. Subsequently, the reaction was performed for 2 h under the illumination of four 3 W 455 nm LEDs at RT without any degassing process. Afterward, the reaction mixture was evaporated under low-pressure and the concentrated crude products were further purified by column chromatography on silica gel.
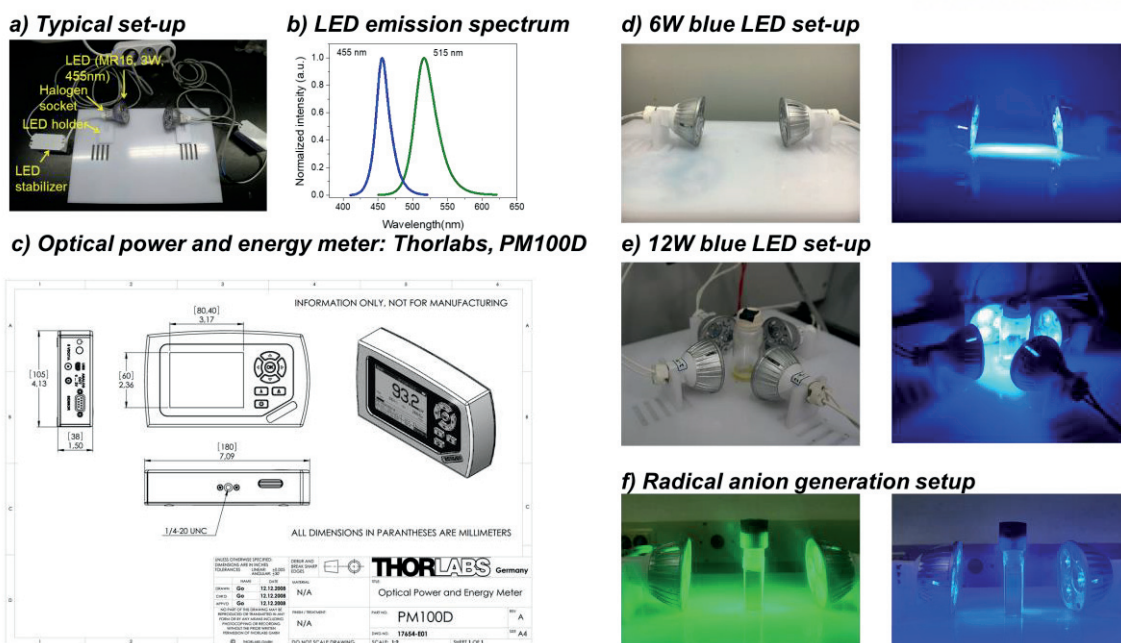
Figure 2.1. Setup and equipment to prepare photoredox reductive dehalogenation.

2.2.2.3 General Procedure for Photoredox Reductive Dehalogenation

Inside the glove box, a 20-ml glass vial equipped with a stirring bar was charged with aryl halides (0.1 mmol), DIPEA (174 μl, 1 mmol), PC (5–0.001 mol% to relative aryl halides), 1,3,5-trimethoxybenzene (TMB) (33.6 mg, 0.2 mmol) as the internal standard for gas chromatography (GC) coupled with a flame ionization detector (FID) and ^{1}H nuclear magnetic resonance (NMR) spectroscopy, and anhydrous CH_3CN (1 ml, 0.1 M of aryl halides) as the solvent. Afterward, the vial was capped with a rubber septum or screw cap and sealed with parafilm. The reaction batches were purged with Ar (99.9999%), air, or O_2 (99.995%) for 30 min outside the glove box. Subsequently, the reaction was performed for several hours under the illumination of two 3 W 455 nm LEDs at RT. Without the isolation process, the aliquots of the reaction mixture were analyzed by GC-FID or ^{1}H NMR to obtain yields of the dehalogenated products. In preparation for the reaction, the pre-prepared stock solutions of PCs were used to increase the reproducibility of results. Newly dehalogenated products were characterized by GC-FID and ^{1}H NMR spectrometer (400 MHz) with $CDCl_3$ or DMSO-d_6 as the solvent. The yields of dehalogenated products were determined by GC-FID and (5%-phenyl)-methylpolysiloxane column (Agilent HP-5) or ^{1}H NMR in the presence of TMB as the internal standard to determine conversion and yields. GC-FID was programmed with gradient temperature analysis using N_2 as the carrier gas.

2.3 Results and Discussion

2.3.1 Design Strategy

The highly negative E_{red}^0 of a PC requires a LUMO with high energy.[11,62] To ensure visible-light absorption in such a PC, the HOMO energy should scale with the LUMO energy, decreasing E_{red}^* that causes difficulties in PET between a PC and sacrificial reductant. In other words, it is challenging to target PCs that combine the following properties: i) good visible-light absorption, ii) adequate initial PET with a sacrificial reductant, and iii) highly negative reduction potential.

For high steady-state $PC^{\bullet-}$ concentration, the highly efficient generation and sufficiently slow decay of $PC^{\bullet-}$ are necessary along with the following conditions: i) efficient initial PET from a sacrificial reductant (e.g., tertiary amines) and ii) suppression of back electron transfer (BET) to oxidized sacrificial reductant. To fulfill the two conditions, we envisioned that a PC capable of the highly efficient generation of long-lived T_1 might solve this challenge. Firstly, generating abundant long-lived T_1 maximizes the PC concentration in the excited state. A high PC concentration in the excited state accelerates the PET event between T_1 of PC ($^3PC^*$) and a sacrificial electron donor (see **Chapter 2.3.2**). Moreover, such a $^3PC^*$ contributes to the BET suppression that eliminates the produced $PC^{\bullet-}$.[5] The PET event between $^3PC^*$ and the sacrificial electron donor forms a triplet contact radical ion pair (TCRIP) in which the BET reaction is usually prolonged because it requires a spin-flip process, which is further retarded in purely organic molecules owing to the absence of heavy metal atoms and rather weak SOC.[5] Furthermore, the BET process within the TCRIP, generated during the PET process, might be mainly located in the Marcus-inverted region because of its very high thermodynamic driving force, which might delay the BET for a highly reducing $PC^{\bullet-}$.[66,67]

We have recently proposed a computer-aided strategy to design highly efficient organic PCs based on a strongly twisted donor–acceptor structure,[11] which enables the strong CT property of the lowest S_1 and T_1 states, facilitating the formation of long-lived T_1 by small ΔE_{ST} and fast ISC according to El-Sayed rules.[35,48] 4DP-IPN and its derivatives were discovered and applied to successfully catalyze photoredox-mediated polymerization using this strategy.[11,12,61–64] We focused on the excellent catalytic performance of 4DP-IPN and further conceived that 4DP-IPN would be working on the oxidative and reductive quenching cycles owing to its adequate photophysical and electrochemical properties: i) highly negative E_{red}^0(PC) of −1.66 V and ii) efficient generation of a long-lived T_1 (τ_{obs} = 104 μs and Φ_{ISC} = 84%, **Figure 2.2**). Therefore, we envisioned that 4DP-IPN would be an excellent model for studying the behavior of strongly reducing $PC^{\bullet-}$. Subsequently, we synthesized nine additional cyanoarene-based PCs with different redox potentials and T_1 generation abilities to systematically investigate the factors affecting the formation of strongly reducing $PC^{\bullet-}$ at a high concentration and

observe further reactivities after the PC$^{\bullet-}$ formation of cyanoarene-based PCs in the presence of a conventional sacrificial reducing agent (i.e., tertiary amines).

Figure 2.2. Photophysical properties of 4DP-IPN. a) Reaction scheme of the 4DP-IPN$^{\bullet-}$ formation. The calculated frontier molecular orbitals topologies of 4DP-IPN and 4DP-IPN$^{\bullet-}$ are shown. Their excited state redox potentials [E_{red}^*(PC) and E_{ox}^*(PC$^{\bullet-}$)] were estimated from the Rehm–Weller equation, $E_{red}^* = E_{0-0} + E_{red}^0$ and E_{ox}^* (PC$^{\bullet-}$) $= -E_{0-0}$(PC$^{\bullet-}$) $+ E_{red}^0$(PC). E_{0-0}(PC) and E_{0-0}(PC$^{\bullet-}$) were evaluated by the onset of gated photoluminescence (PL) emission in CH$_3$CN at 65 K and the onset of UV–Vis absorption at room temperature (RT), respectively. (b) PL decay (left), steady-state PL at RT (right) of 4DP-IPN studied in the current work. (a) 4DP-IPN. (c) The Jablonski diagram of 4DP-IPN. The rate constants of all photophysical processes were evaluated from the experiments performed in the current work.

2.3.2 PET Event Between 4DP-IPN and Tertiary Amines

We first investigated the initial PET from the amine-based sacrificial donors to 4DP-IPN because they were the most used sacrificial reducing agents in photoredox catalysis, that is, DIPEA, triethylamine (TEA), and tributylamine (TBA) were used in the current study. Given the ground state oxidation potentials of the prepared amines (E_{ox}^0(DIPEA) = 0.68 V, E_{ox}^0(TBA) = 0.88 V, and E_{ox}^0(TEA) = 0.96 V))[68,69] and the excited-state reduction potential of the PC (E_{red}^*(4DP-IPN) = 0.63 V), owing to its unfavorable thermodynamics, the PET is predicted to be highly sluggish. We performed photoluminescence (PL) decay quenching studies to track the rate constant of PET using the time-correlated single photon counting (TCSPC) method. Under degassed conditions without a sacrificial electron donor, 4DP-IPN has two types of PL lifetime; the prompt and delayed components were measured as 3.3 ns and 104 μs, respectively. After the injection of tertiary amines in the 4DP-IPN solution, tertiary amines significantly shortened the delayed components with no discernible effect on the prompt components, suggesting that T_1 is primarily responsible for the PET events. The rate constant for PET (k_{PET}), measured using the Stern–Volmer relationship, is larger than the rate constant of RISC and smaller than that of ISC, further supporting our argument **(Figure 2.2(c))**. Among the tertiary amines, DIPEA exhibited the strongest quenching effect (**Figure 2.3**). k_{PET} increased with the increasing $-\Delta G_{PET}$, consistent with the Marcus "normal region" behavior.[17]
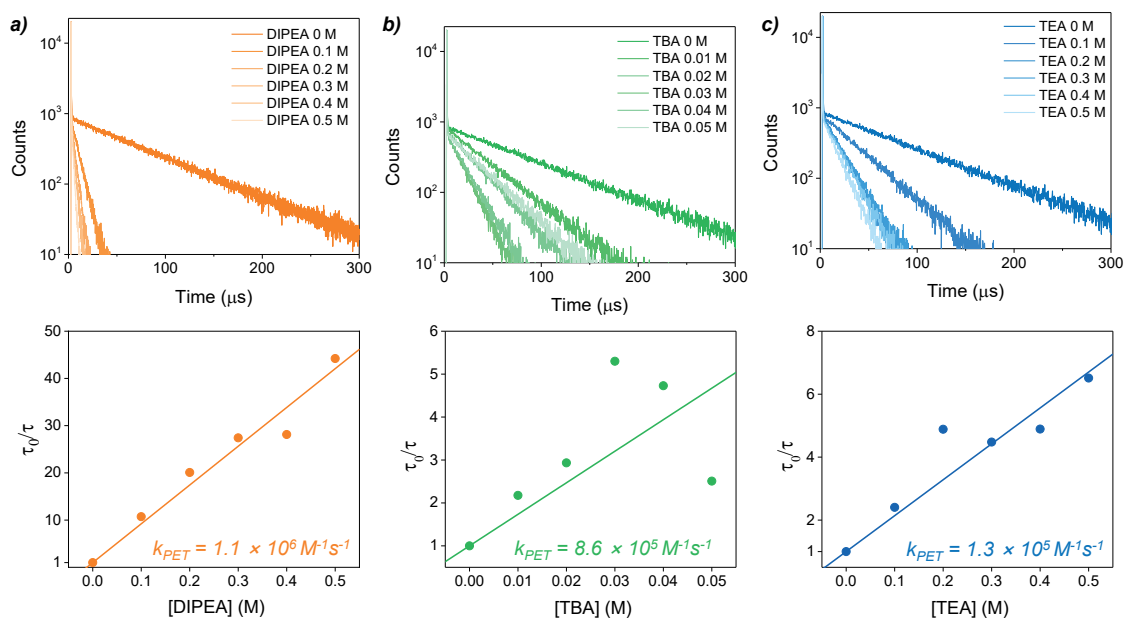
Figure 2.3. The Stern–Volmer plots of delayed fluorescence of 4DP-IPN quenched by (a) DIPEA, (b) TBA, and (c) TEA in CH$_3$CN (1.0 × 10^{-5} M) monitored at λ_{det} = 550 nm.

We employed $Ru(bpy)_3Cl_2$, a common PC for reductive quenching photocatalytic cycles, as a control experiment in PL quenching with DIPEA.[25,70] Using the same amount of DIPEA, k_{PET} for $Ru(bpy)_3Cl_2$ (9.7×10^6 $M^{-1}\cdot s^{-1}$) was higher than that for 4DP-IPN (k_{PET} (4DP-IPN) = 1.1×10^6 $M^{-1}\cdot s^{-1}$) which was in accordance with the trend in the excited state reduction potentials of the PC (E_{red}^*($Ru(bpy)_3Cl_2$) = 0.77 V).[71] Interestingly, despite the same amount of DIPEA, the PL decay quenching in 4DP-IPN changed more than in $Ru(bpy)_3Cl_2$, suggesting that, the rate of PET (v_{PET}) from DIPEA to the PC is faster in 4DP-IPN than in $Ru(bpy)_3Cl_2$ despite the less favorable thermodynamic driving force for PET in 4DP-IPN. This finding results from the fact that 4DP-IPN generates highly effective, long-lived T_1. The concentration of PCs in the excited state is another crucial element in producing $PC^{\bullet-}$ because of the molar rate of PET, v_{PET} (in $M\cdot s^{-1}$), described by

$$v_{PET} = v_{PET} [PC^*][Q], \qquad\qquad \text{(eq. 3)}$$

where $[PC^*]$ is the PC concentration in the excited state and $[Q]$ is the quencher concentration (i.e., DIPEA). We estimated the time-dependent photoexcited state concentrations of a few PCs. This model was based on the rate law to gauge the PET capabilities of 4DP-IPN and contrast them with those of other well-known PCs (**Figure 2.4**). The literature or our experiments provided the rate constants used in the kinetic simulations. In the photostationary state, the concentration of 4DP-IPN molecules in T_1 was approximately 10^2 times higher than those of $Ru(bpy)_3Cl_2$ and $Ir(ppy)_3$ and $\sim 10^5$ times higher than that of PTH, which has commonly been used as a highly reducing PC (E_{ox}^*(PTH) = -2.10 V).[36] Despite its adverse thermodynamics, this does imply that 4DP-IPN is preferable for PET with sacrificial agents.
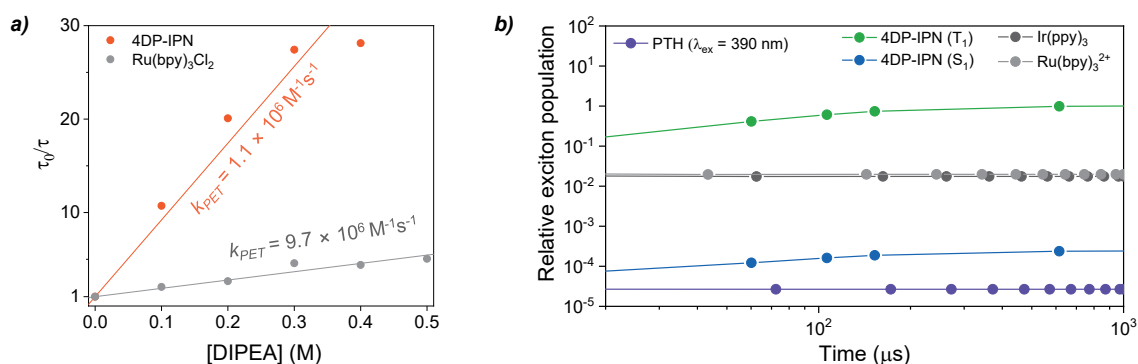
Figure 2.4. (a) The Stern–Volmer plots for the PL quenching of 4DP-IPN and $Ru(bpy)_3Cl_2$ in CH_3CN by DIPEA at RT. The Stern–Volmer plots were obtained from PL decays of PCs. (b) Kinetic simulation results based on the rate-law equations for the relative excited state population variations, referred to as the total concentration, of selected PCs (5.0×10^{-3} M) over time after turn-on continuous 455 nm irradiation. 390 nm light was assumed to be irradiated for 10-phenylphenothiazine (PTH) as it shows no absorption at 455 nm.

16
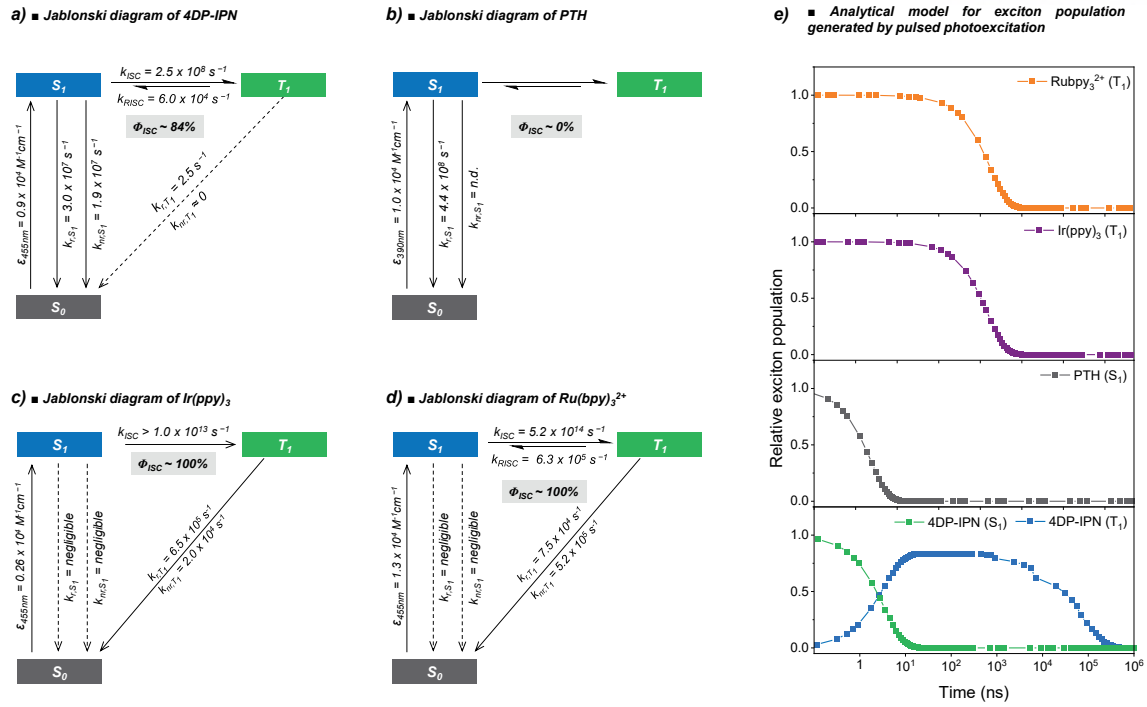
Figure 2.5. Jablonski diagrams of (a) 4DP-IPN, (b) PTH,[5] (c) Ir(ppy)$_3$,[72,73] and (d) Ru(bpy)$_3^{2+}$[74] based on photophysical rate constants obtained from the current work or referred to literature. The extinction coefficients of 4DP-IPN, Ir(ppy)$_3$, and Ru(bpy)$_3^{2+}$ were measured in CH$_3$CN in our group. (e) The exciton dynamics of selected PCs generated by pulsed photoexcitation.

2.3.3 Formation of Radical Anion of Cyanoarene-Based PCs

UV–Vis absorption spectroscopy allows direct observation of the PC$^{\bullet-}$ production of 4DP-IPN. All samples were prepared inside a glovebox because the PC$^{\bullet-}$ is very sensitive to oxygen and moisture.[7,75] First, a 515-nm light-emitting diode (LED) was used to illuminate a degassed solution of 4DP-IPN for 1 min while an excessive quantity of DIPEA was present. The exogenous tertiary amines might contribute to the suppression of the BET event.[76] The 4DP-IPN solution UV–Vis absorption spectra were obtained immediately after irradiation (**Figure 2.6**). A color shift that could be seen with the naked eye was confirmed by the observed spectral changes (**Figure 2.6**, inset). While a new, broad absorption band developed at 500–750 nm, showing the 4DP-IPN$^{\bullet-}$ formation, perfect isosbestic points (at 428 and 493 nm) emerged for the reaction, indicating that the 4DP-IPN was depleted. The UV–Vis absorption spectra of the freshly generated PC$^{\bullet-}$ were monitored every 2 min in complete darkness to measure the PC stability (orange line in **Figure 2.6**). A gradual decay was observed in the dark for more than 20 min, approximately twice longer than that of Ir(dtbby)$^{\bullet-}$(ppy)$_2$PF$_6$ reported by König's group under similar conditions (green line in **Figure 2.6**).[21] Because of the absence of heavy atoms and lower SOC, the 4DP-IPN radical anion's better stability probably results from delayed BET in the TCRIP.
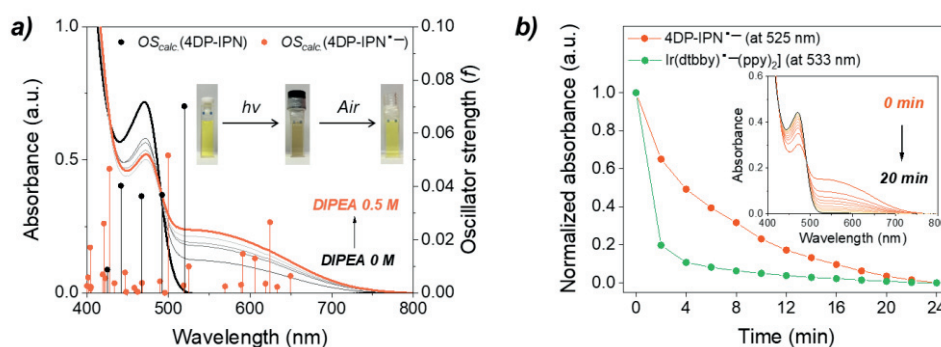
Figure 2.6. (a) UV–Vis absorption spectra of 4DP-IPN (black line) and 4DP-IPN$^{\bullet-}$ (orange line) in CH$_3$CN. UV–Vis absorption spectra were obtained from the degassed mixture solutions of 4DP-IPN (1.0×10^{-4} M) and DIPEA (0–0.5 M) in CH$_3$CN immediately after illumination by two 3 W 515 nm LEDs for 1 min at RT. TD-DFT results (oscillator strengths) are shown as stick spectra. (b) Time-dependent changes of the UV–Vis absorbance of 4DP-IPN$^{\bullet-}$ at 525 nm and Ir(dtbby)$^{\bullet-}$(ppy)$_2$PF$_6$ at 533 nm. Generally, PC$^{\bullet-}$ was generated from the degassed mixture solutions of PCs (1.0×10^{-4} M) and DIPEA (0.5 M) in CH$_3$CN under the illumination of two 3 W 515 nm LEDs for 3 min (for 4DP-IPN) or two 3 W 455 nm LEDs for 1 min (for Ir(dtbby)(ppy)$_2$PF$_6$) at RT. Changes in the UV–Vis absorption spectrum of freshly generated 4DP-IPN$^{\bullet-}$ were recorded every 2 min under dark conditions (inset).
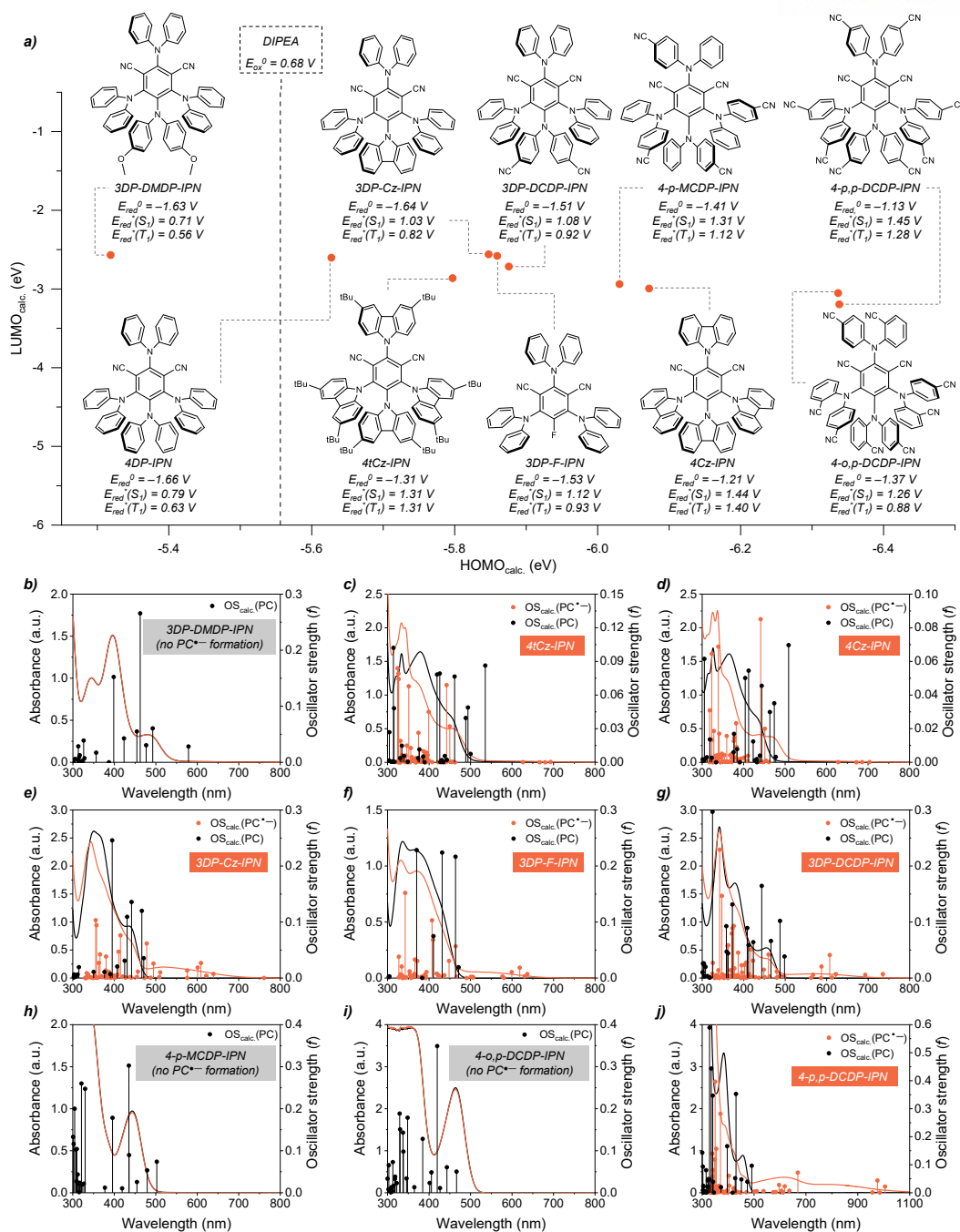
Figure 2.7. (a) Chemical structures of selected cyanoarene-based PCs and their calculated HOMO and LUMO energies. UV–Vis absorption spectra of selected PC (black line) and PC$^{\bullet-}$ (orange line). TD-DFT calculation results (oscillator strengths) are shown as stick spectra. UV–Vis absorption spectra were obtained from the degassed solutions of PCs (1.0×10^{-4} M) and DIPEA (0.5 M) in CH$_3$CN immediately after illumination of two 3 W 455 nm LEDs for 1 min at RT, (b) 3DP-DMDP-IPN, (c) 4tCz-IPN, (d) 4Cz-IPN, (e) 3DP-Cz-IPN, (f) 3DP-F-IPN, (g) 3DP-DCDP-IPN, (h) 4-p-MCDP-IPN, (i) 4-o,p-DCDP-IPN, and (j) 4-p,p-DCDP-IPN. All solutions were prepared in a glove box and fully degassed.

The PC$^{\bullet-}$ formation was studied for a group of cyanoarene-based PCs with various redox potentials and the capacity to produce T_1. Nine additional PCs were synthesized with different donor moieties (**Figure 2.7**). These outcomes demonstrate the broad applicability of our method. Additionally, to confirm the significance of T_1 for PC$^{\bullet-}$ formation, two 4DP-IPN analogs (4-p-MCDP-IPN and 4-o,p-DCDP-IPN) with better E_{red}^* (i.e., a lower HOMO) but a negligibly small concentration of T_1 were prepared (**Table 2.1** and **Figure 2.8**). This discovery may be responsible for the fast RISC resulting from the vibronic coupling.[77] Further in-depth investigations are currently underway. Interestingly, PC$^{\bullet-}$ was not noticeably generated for such PCs under our experimental conditions, clearly confirming that the long-lived T_1 generation of PC is crucial for the PC$^{\bullet-}$ formation. Nevertheless, ^{3}PC* is efficiently produced in most cyanoarenes structures. The redox potentials can be delicately controlled over a wide range by altering the donor and acceptor moieties, which allows the use of radical ions with specific redox potentials for various highly effective conventional photoredox catalysis, multiphoton excitation catalysis, and photoelectrocatalysis.[10,11,56]

Table 2.1. Photophysical properties of PCs in CH_3CN. The photophysical rate constants were derived by experimental values for τ_{PF}, τ_{DF}, and Φ_F and the TD-DFT calculated oscillator strength (f), the spectral positions for absorption, and emission followed by the procedure described in the literature[12] under the assumptions of i) $k_{nr,T}$, $k_{PH} \ll k_{RISC}$ and ii) $k_{ISC} \gg k_{RISC}$ and the estimation of $k_{r,S1}$ via the Strickler–Berg equation.[78,79]

PC	$E_{0-0}(S_1)$ (eV)[a]	$E_{0-0}(T_1)$ (eV)[b]	τ_{PF} (ns)	τ_{DF} (μs)	$\lambda_{max,abs}$ (nm)	$\lambda_{max,em}$ (nm)	$f_{S0\to S1}$[c]	Φ_F	$k_{r,S1}$ (10^7 s^{-1})	$k_{nr,S1}$ (10^7 s^{-1})	k_{ISC} (10^8 s^{-1})	$k_{r,T1}$ (s^{-1})	$k_{nr,T1}$ (10^3 s^{-1})	k_{RISC} (10^5 s^{-1})
4DP-IPN	2.45	2.29	3.30	104	469	531	0.0790	0.61	3.0	1.9	2.5	2.5	—	0.60
4tCz-IPN	2.62[d]	2.62[d]	8.26	1.29	440[d]	578[d]	0.0863	0.05	2.4	45	-[e]	—	—	2.0
4Cz-IPN	2.65	2.60	13.99	1.67	420	551	0.0697	0.18	2.1	9.5	-[e]	—	—	3.7
4-p,p-DCDP-IPN	2.58	2.41	1.79	196	458	500	0.0964	0.61	4.2	2.7	4.9	—	—	0.41
3DP-F-IPN	2.65	2.46	4.56	45.3	414	540	0.0192	0.17	0.6	3.0	1.8	—	—	1.4
3DP-Cz-IPN	2.67	2.46	4.03	140	435	521	0.0355	0.52	1.3	1.2	2.2	—	—	0.7
3DP-DMDP-IPN	2.34	2.19	1.01	2.77	480	618	0.0065	<0.01	0.16	16	8.3	—	—	23
3DP-DCDP-IPN	2.59	2.43	2.35	47.6	455	513	0.0385	0.43	1.6	2.1	3.9	—	—	2.5
4-p-MCDP-IPN	2.72	2.53	4.96	0.32	434	522	0.0738	0.40	2.7	4.0	1.3	—	—	93
4-o,p-DCDP-IPN	2.63	2.25	3.81	0.33	464	526	0.0503	0.34	1.9	3.7	2.1	—	—	140

[a,b]E_{0-0} were extracted from the [a]onset of PL in CH_3CN at RT and the [b]onset of the gated PL in CH_3CN at 65 K, respectively. The onsets were obtained from the tangential method: the tangent intersection, set at the high energy slope of the spectrum, with the x-axis.[80] [c]Oscillator strengths were obtained from the TD-DFT calculation. [d]The photophysical properties were referred to the literature measured in DMF.[11] [e]Because of i) the approximation conditions, ii) the error in the experimental and theoretical (Strickler–Berg equation) determination of k_{ISC}, or both, the rate constants were evaluated as negative values.

■ *PL decays* ■ *Steady-state PL emission spectra* ■ *Cyclic voltammetry for reduction cycle*

a)

4DP-IPN

τ_{PF} = 3.3 ns

τ_{DF} = 104 μs

$E_{1/2,red}°$ = −1.66 V

b)

4tCz-IPN

τ_{PF} = 8.26 ns

τ_{DF} = 1.29 μs

$E_{1/2,red}°$ = −1.31 V

c)

4Cz-IPN

τ_{PF} = 13.99 ns

τ_{DF} = 1.67 μs

$E_{1/2,red}°$ = −1.21 V

d)

4-p,p-DCDP-IPN

τ_{PF} = 1.79 ns

τ_{DF} = 196 μs

$E_{1/2,red}°$ = −1.13 V

O_2

e)

3DP-F-IPN

τ_{PF} = 4.56 ns

τ_{DF} = 45.3 μs

$E_{1/2,red}°$ = −1.53 V

f)

3DP-Cz-IPN

τ_{PF} = 4.03 ns

τ_{DF} = 140 μs

$E_{1/2,red}°$ = −1.64 V

O_2

22
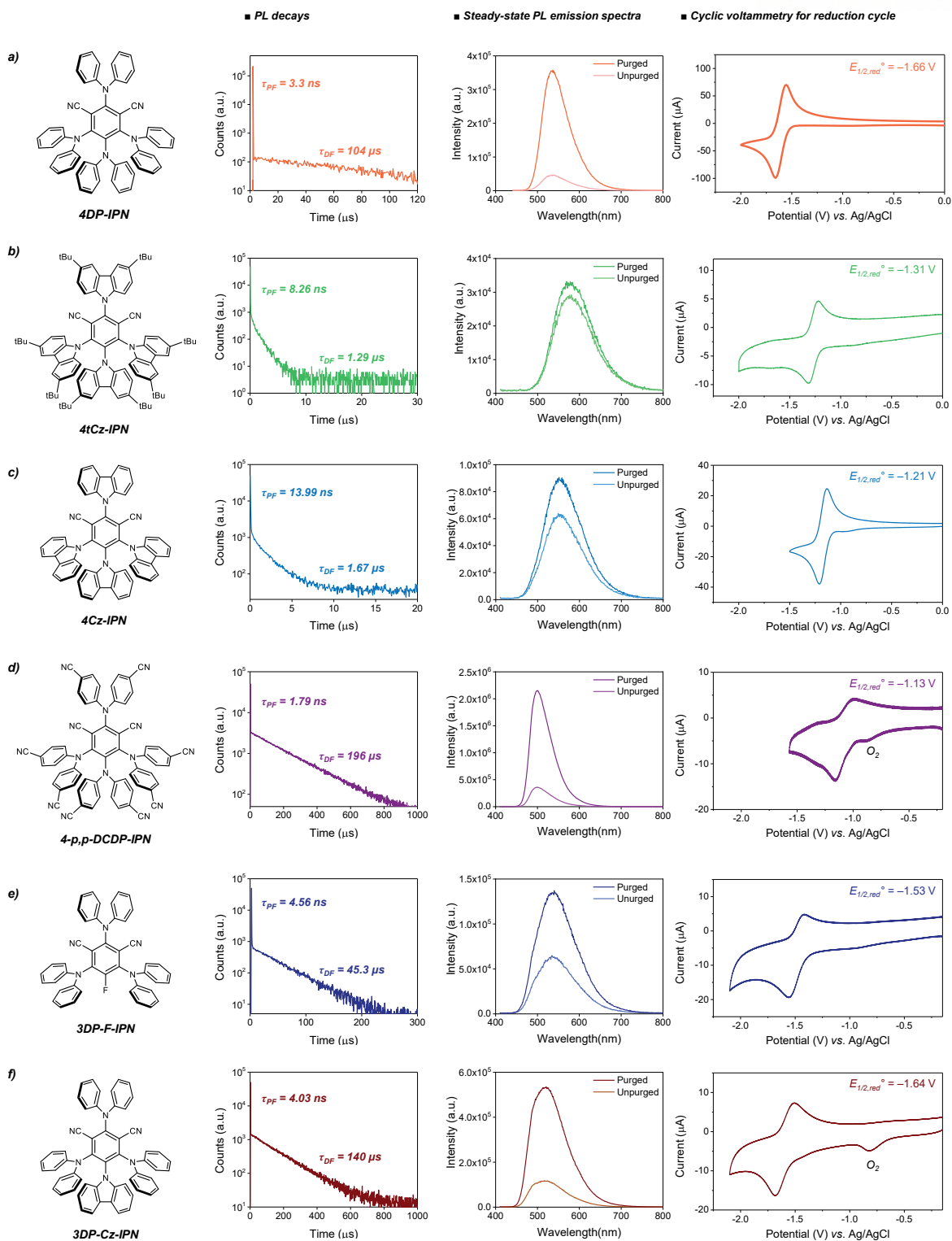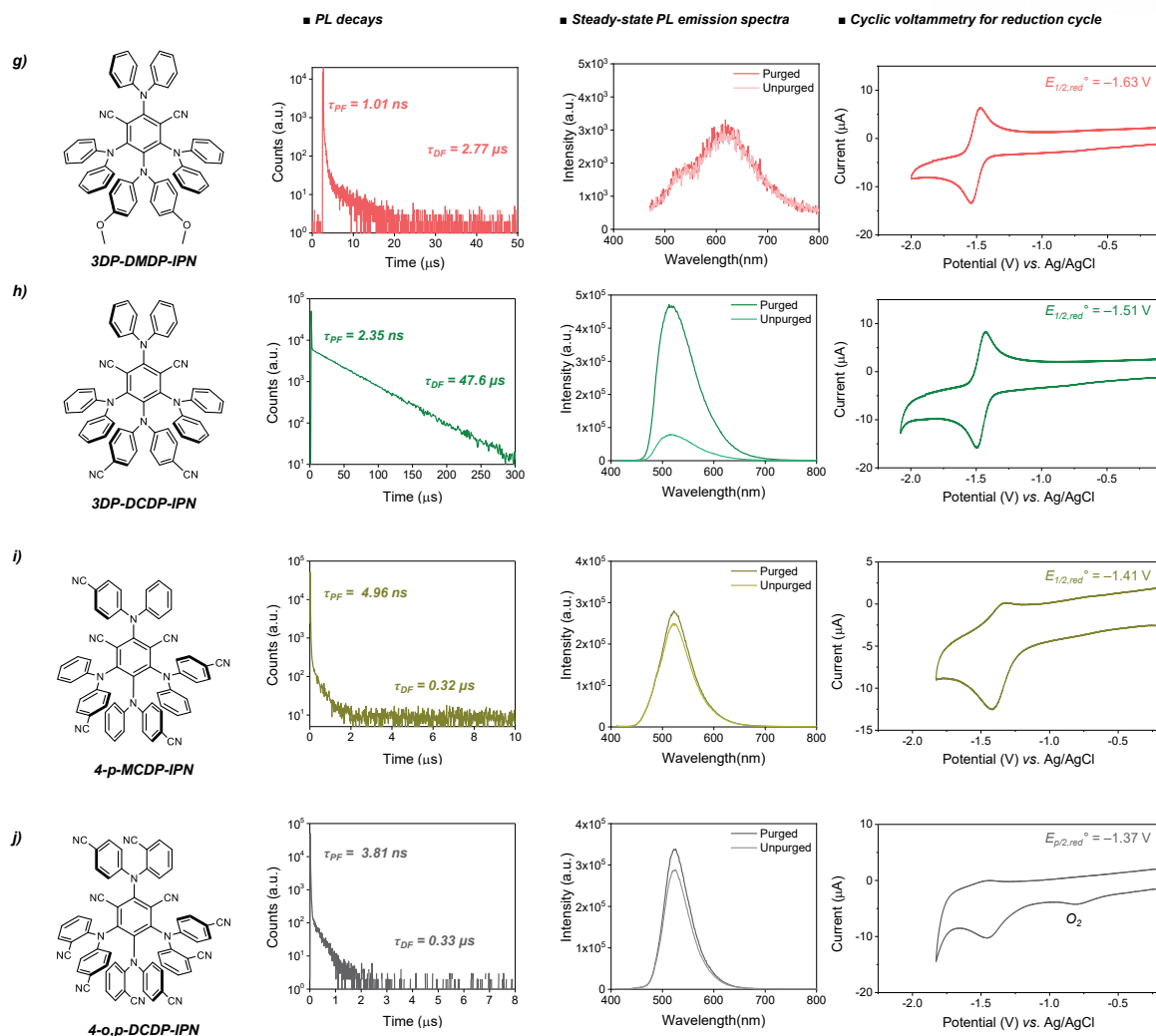
Figure 2.8. Chemical structures, PL decay (left), steady-state PL at RT (center), and cyclic voltammetry (CV) spectra of the reduction cycle (right) of PCs studied in the current work. (a) 4DP-IPN, (b) 4tCz-IPN, (c) 4Cz-PN, (d) 4-p,p-DCDP-IPN, (e) 3DP-F-IPN, (f) 3DP-Cz-IPN, (g) 3DP-DMDP-IPN, (h) 3DP-DCDP-IPN, (i) 4-p-MCDP-IPN, and (j) 4-o,p-DCDP-IPN. Generally, PL decay and steady-state PL at RT spectra were obtained from the degassed solutions of PCs (1.0×10^{-5} M, except for 3DP-DMDP-IPN as 1.0×10^{-4} M owing to low PL intensity) in CH_3CN at RT. CV spectra of the reduction cycle of PC (2.0×10^{-4} M) (except for 4-o,p-DCDP-IPN as 1.0×10^{-3} M) were obtained in CH_3CN at RT after the degassing process by purging with Ar for 15 min.

23
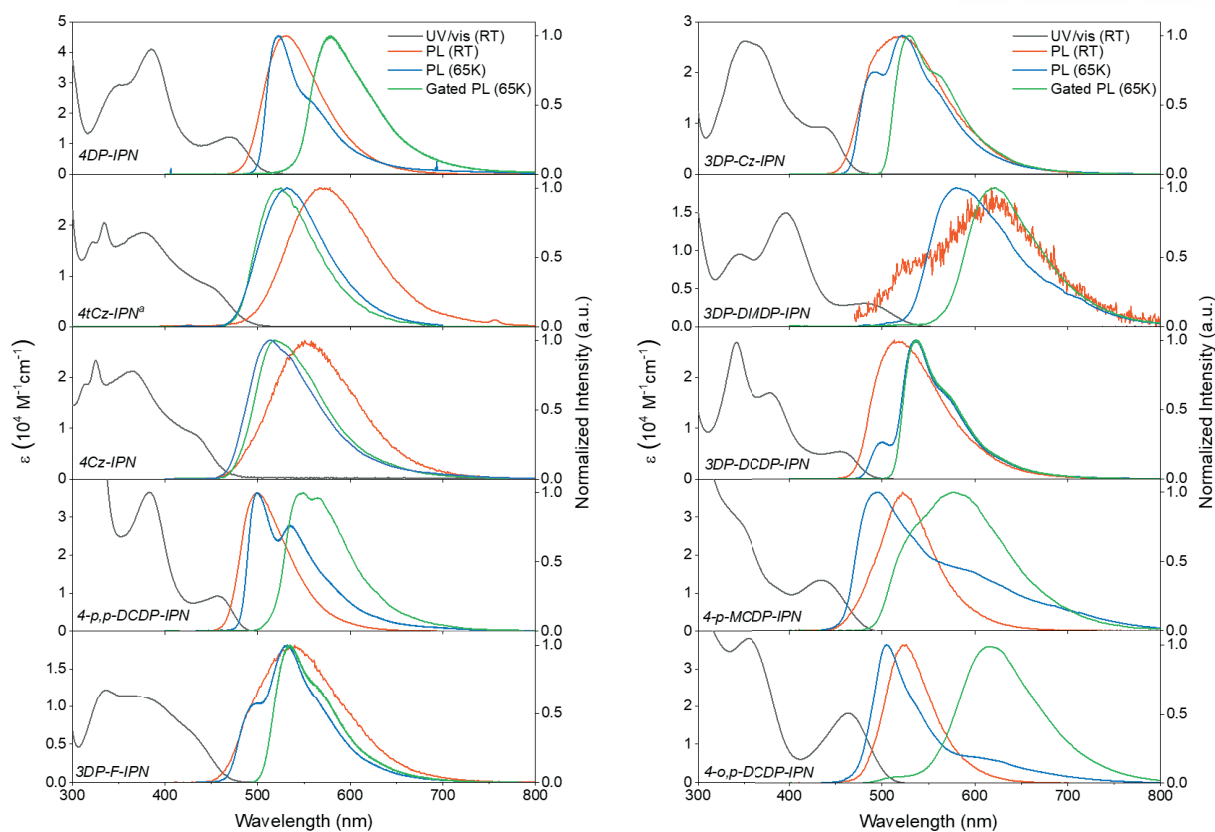
Figure 2.9. UV–Vis absorption and PL emission spectra of PCs studied in current work. UV–Vis absorption spectra of PC $(1.0 \times 10^{-5}\,\mathrm{M})$ in CH_3CN solution were measured at RT. Steady-state photoluminescence (PL) spectra of PCs $(1.0 \times 10^{-5}\,\mathrm{M})$ in CH_3CN at RT and 65 K. [a]UV–Vis absorption and PL emission spectra of 4tCz-IPN were referred to in the literature.[11]

2.3.4 Photodegradation of Cyanoarene-Based PCs

The PC• formation was sensitive to the irradiation's wavelength and intensity. When exposed to a 455 nm LED for 1 min, spectral changes comparable to those in the solutions of 4DP-IPN and DIPEA under 515 nm irradiation were seen. However, the spectrum did not entirely recover even after exposure to air, indicating that the PC is probably damaged by the 455 nm irradiation (**Figure 2.10**). 4DP-IPN underwent photodegradation after continuous exposure to 455 nm LED light for 5 min. These discoveries imply that the PC$^{\bullet-}$ formation can be efficiently conducted under 455 nm LED irradiation, although followed by molecular degradation or undesired chemical reactions.[81]
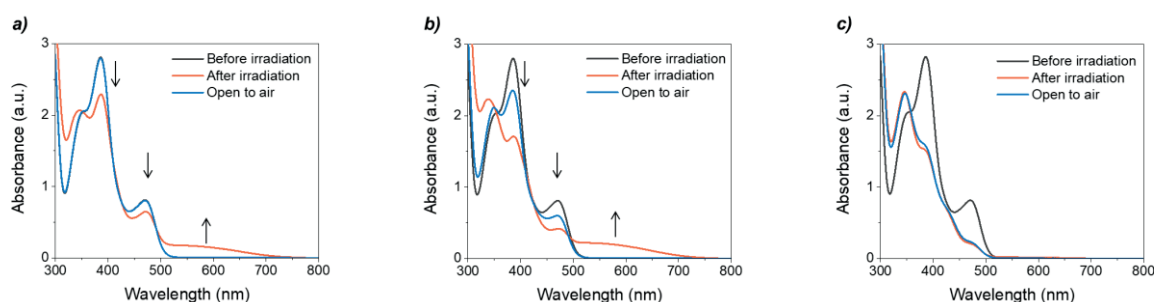
Figure 2.10. UV–Vis absorption of 4DP-IPN/4DP-IPN$^{\bullet-}$. The generation of 4DP-IPN$^{\bullet-}$ was performed with 4DP-IPN (1.0×10^{-4} M) and DIPEA (0.5 M) in CH$_3$CN under the illumination of (a) two 3 W 515 nm LEDs for 1 min, (b) two 3 W 455 nm LEDs for 1 min, and (c) two 3 W 455 nm LEDs for 5 min at RT.

We carefully monitored the degradation of 4DP-IPN with TLC in the presence of the sacrificial reductant (i.e., DIPEA) alone under the LED irradiation of 455 nm and 515 nm. The degradation under 455 nm illumination was significantly faster than that under 515 nm illumination, which may have been caused by different absorption efficiencies ($\varepsilon = 9.0 \times 10^3$ M$^{-1}\cdot$cm^{-1} (at 455 nm) and $\varepsilon = 4.5 \times 10^2$ M$^{-1}\cdot$cm^{-1} (at 515 nm)). As illustrated in **Figure 2.11**, two green luminous compounds were observed when 4DP-IPN was photodegraded. We effectively isolated the photodegraded adducts after scaling up the procedure. One of the two CN groups of 4DP-IPN was replaced with a methyl group or a hydrogen atom, producing 4DP-Me-BN (the major product) and 4DP-H-BN (the minor product), respectively, according to the extensive structural analysis conducted using 1D/2D NMR studies and mass spectroscopy (**Figures 2.11–2.13**).
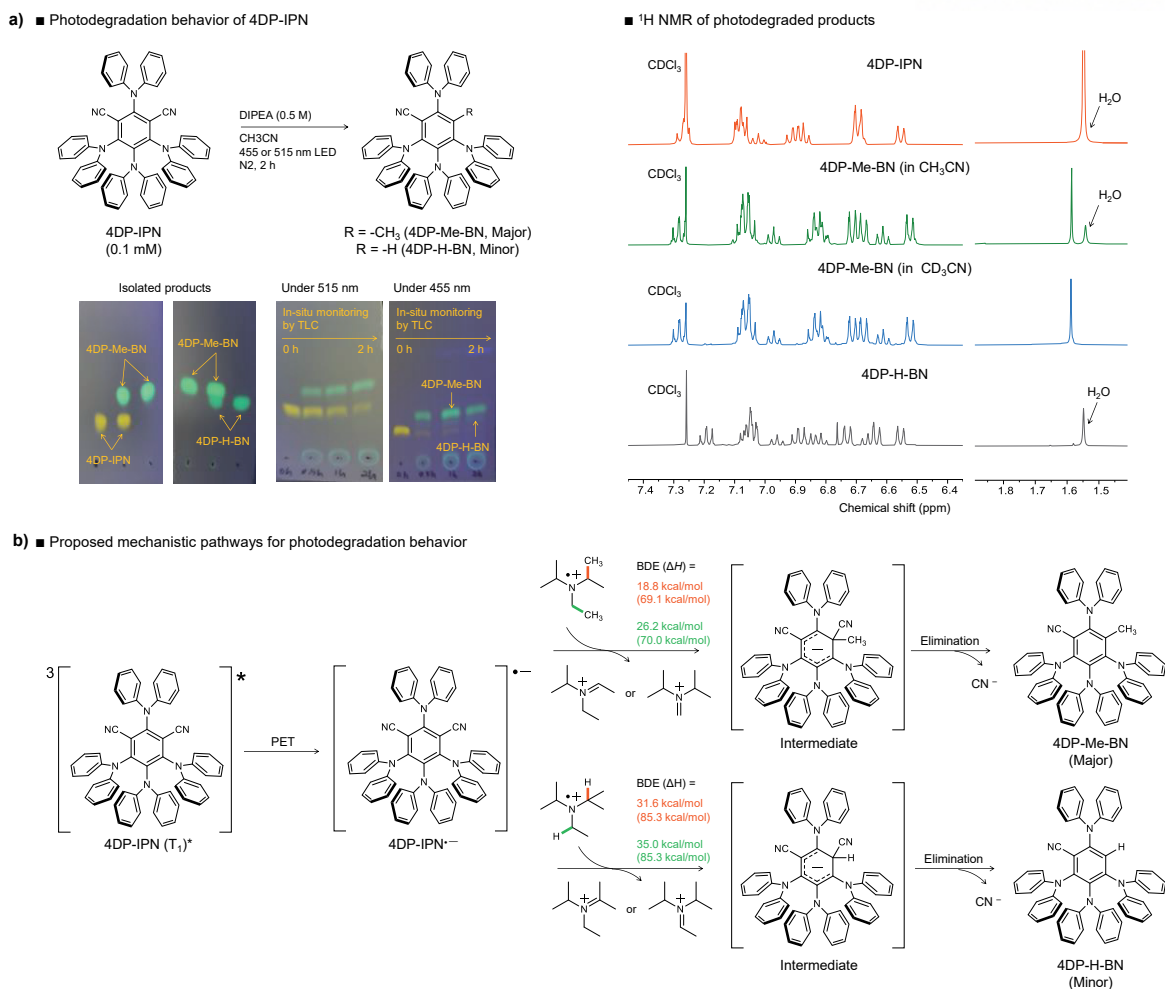
Figure 2.11. (a) Photodegradation behavior of 4DP-IPN in the presence of DIPEA. Reactions were performed with 4DP-IPN (1.0×10^{-4} M) and DIPEA (0.5 M) in CH_3CN under the illumination of two 3 W 515 nm LEDs or two 3 W 455 nm LEDs at RT. PC degradations were monitored *in situ* by thin-layer chromatography with eluent conditions of CH_2Cl_2:hexanes, 7:3 v/v). The photodegraded products were isolated by column chromatography, and ^{1}H NMR spectra confirmed that a methyl (as well as hydrogen) substitution reaction occurred at the CN position of 4DP-IPN to yield 4DP-Me-BN (as well as 4DP-H-BN). (b) Proposed mechanistic pathway for the photodegradation behavior of 4DP-IPN in the presence of DIPEA and DFT calculations for the bond dissociation energies (ΔH) in DIPEA$^{\bullet+}$. The values between parentheses correspond to the calculated bond dissociation energies in DIPEA.
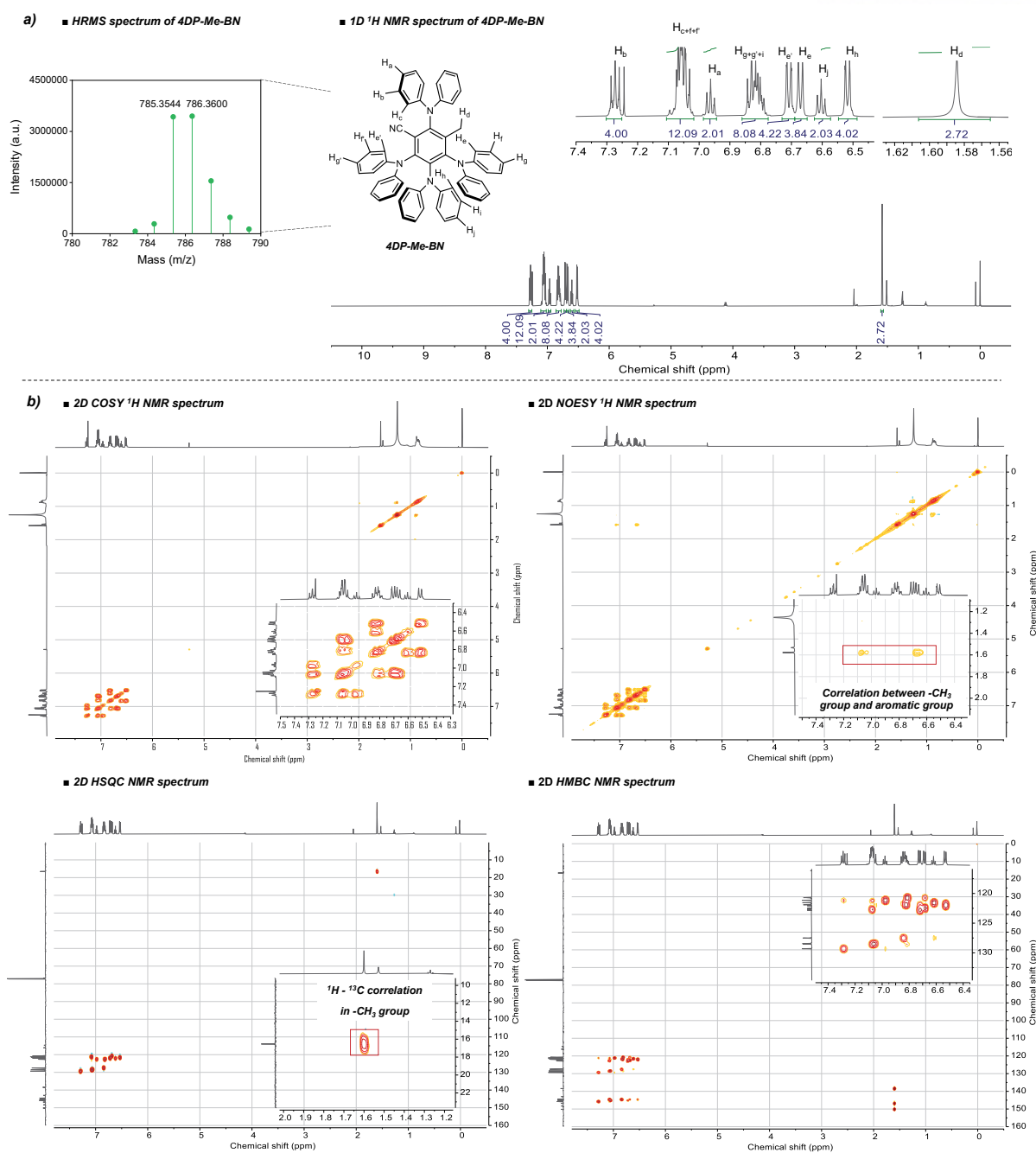
Figure 2.12. Structural characterization of 4DP-Me-BN. Structural analysis of 4DP-Me-BN with (a) 1D ^{1}H NMR analyses combined with HRMS, MS (GC-FAB-HRMS): calculated for $C_{56}H_{44}N_5$ [M+H]$^+$: 786.3597; found as 786.3600, and (b) intense 2D NMR analyses, including COSY, NOESY, HSQC, and HMBC NMR. ^{1}H NMR (600 MHz, CDCl$_3$) δ 7.30–7.25 (t, 4H), 7.11–7.02 (m, 12H), 6.96 (t, 2H), 6.86–6.78 (m, 8H), 6.73–6.69 (d, 4H), 6.69–6.65 (d, 4H), 6.60 (t, 2H), 6.55–6.49 (d, 4H), 1.58 (s, 3H). ^{13}C NMR (151 MHz, CDCl$_3$) δ 150.15, 148.35, 146.81, 145.76, 145.15, 144.58, 144.56, 142.97, 138.44, 129.31, 128.53, 128.44, 127.50, 122.83, 122.65, 122.46, 122.07, 121.90, 121.55, 121.14, 120.70, 116.15, 114.68, 16.54.
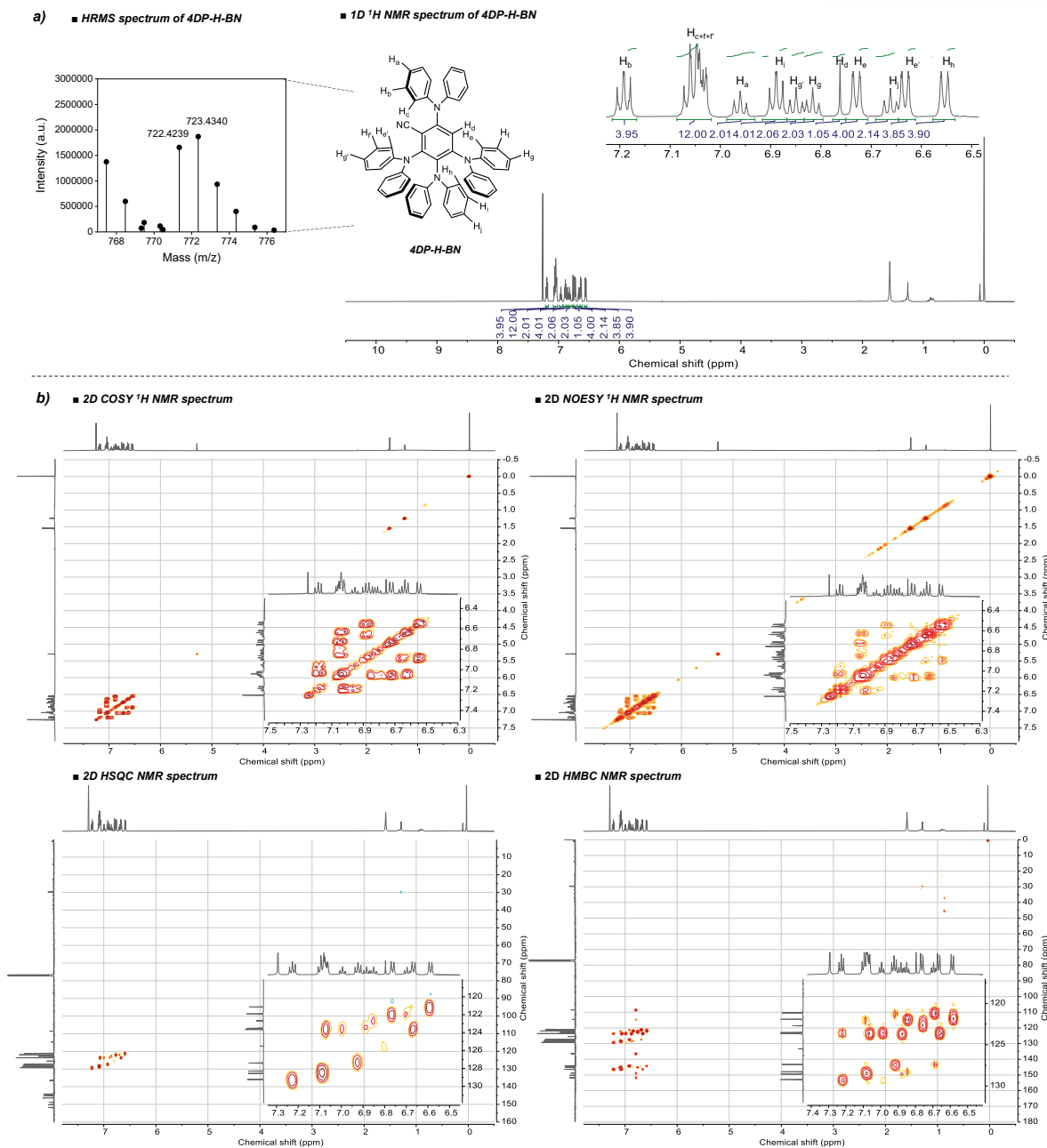
Figure 2.13. Structural characterization of 4DP-H-BN. Structural analysis of 4DP-H-BN with (a) 1D ^{1}H NMR analyses combined with HRMS, MS (GC-FAB-HRMS): calculated for $C_{55}H_{42}N_5$ [M+H]$^+$: 772.3440; found as 772.3444, and (b) intense 2D NMR analyses, including COSY, NOESY, HSQC, and HMBC NMR. ^{1}H NMR (600 MHz, CDCl$_3$) δ 7.22–7.17 (t, 4H), 7.09–7.02 (m, 12H), 6.96 (t, 2H), 6.92–6.87 (t, 4H), 6.87–6.83 (t, 2H), 6.83–6.80 (t, 2H), 6.76 (s, 1H), 6.75–6.71 (d, 4H), 6.69–6.65 (t, 2H), 6.65–6.61 (m, 4H), 6.58–6.53 (t, 4H). ^{13}C NMR (151 MHz, CDCl$_3$) δ 151.76, 150.19, 148.79, 146.38, 146.37, 145.05, 144.21, 136.47, 129.23, 128.56, 128.30, 127.41, 125.51, 123.66, 123.53, 123.51, 122.70, 121.92, 121.15, 114.66, 108.55.

Control experiments were performed along with DFT calculations to explore the mechanistic pathway of the 4DP-IPN degradation under the specified conditions. Interestingly, TLC did not detect any degradation in the absence of DIPEA (**Figure 2.14(a)**), indicating that DIPEA is specifically involved in the 4DP-IPN photodegradation. Therefore, we postulated that in the presence of DIPEA, the long-lived 4DP-IPN$^{\bullet-}$ initially formed, followed by the methyl and hydrogen substitution process of PC$^{\bullet-}$. In this case, the methyl and hydrogen were produced by the one-electron oxidized adduct of DIPEA (DIPEA$^{\bullet+}$). Generally, the C-C (as well as C-H) bonds in the β-position of DIPEA•+ are much weaker than those of neutral DIPEA. Hence, β-scission occurs normally to generate the radical species,[62,82–85] which was well reproduced by our DFT calculations (**Figure 2.11(b)**). Furthermore, excluding the hypothesis that the hydrogen and methyl came from the solvent (CH$_3$CN) would be possible. The CD$_3$ substitution process was not seen in deuterated acetonitrile (CD$_3$CN) but in the CH$_3$ substitution reaction (**Figure 2.11(a)**).
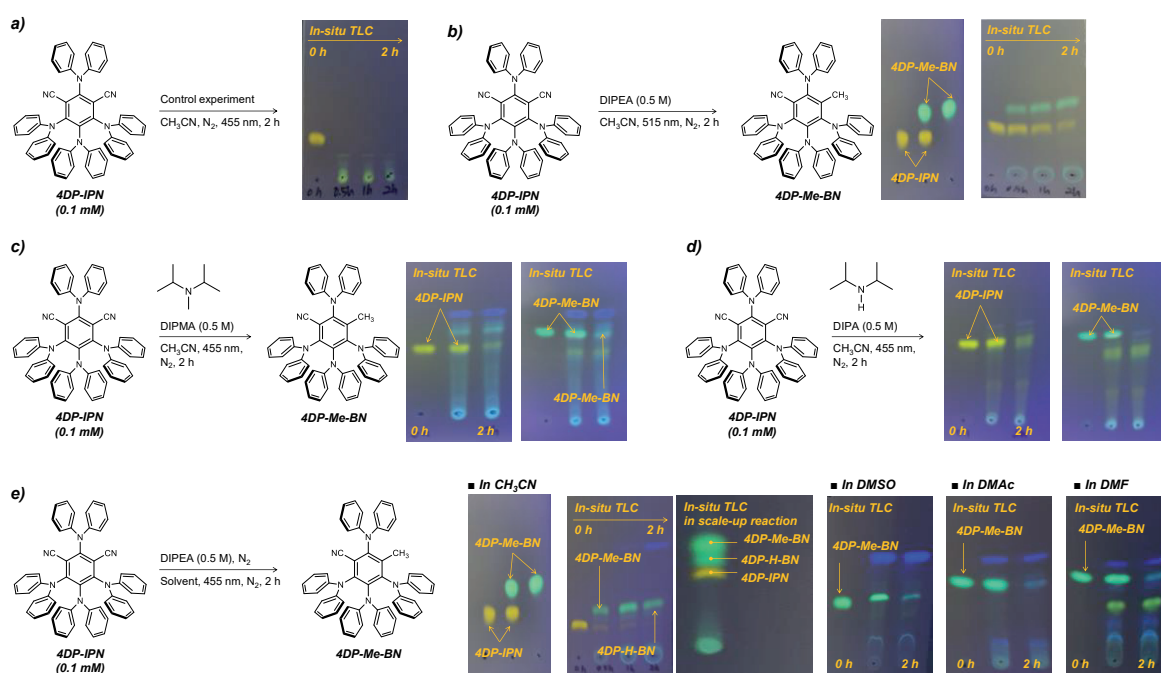
Figure 2.14. Estimation of the photodegradation behavior of 4DP-IPN. The reaction conditions were the same as described above for the general procedure. Reactions were monitored by TLC (EA:hexanes, 1:4 v/v). (a) The photodegradation behavior of 4DP-IPN was monitored without DIPEA as a control experiment. (b) In the presence of DIPEA, the photodegradation experiments were performed under the illumination of two 3 W 515 nm LEDs. (c,d) The photodegradation experiments were performed under the illumination of two 3 W 455 nm LEDs in the presence of (c) *N,N*-diisopropylmethylamine (DIPMA) and (d) *N,N*-diisopropylamine) as a reducing agent instead of DIPEA. (e) The photodegradation experiments were performed under the illumination of two 3 W 515 nm LEDs in various organic solvents at RT.

We examined other cyanoarene-based PCs photodegradation in more detail. As shown in **Figure 2.16**, highly intriguing patterns developed depending on the electrical characteristics (i.e., the ability to form PC$^{\bullet-}$) and structural features (i.e., steric environments nearby the CN group) of PCs. As in 4DP-IPN, CH$_3$ substitution at one of the two CN groups was observed for 3DP-Cz-IPN and 3DP-DCDP-IPN, both of which have similar electronic and structural properties to 4DP-IPN (**Figure 2.16(a)**). However, C$_2$H$_5$ substitution happened with only a small amount of CH$_3$ substitution in 4Cz-IPN and 4tCz-IPN, indicating that the steric environment close to the CN group is vital for the substitution reaction **(Figure 2.16(b))**. The ethyl group was probably provided by the C−N bond cleavage of DIPEA$^{\bullet+}$ assisted by a 1,2-methyl shift. The use of diisopropylmethylamine (DIPMA) instead of DIPEA generated a CH$_3$-substituted adduct as a major product, which supports our hypothesis. **Figure 2.16(c)** shows the results of photodegradation experiments for PCs in which PC$^{\bullet-}$ was not properly formed. No photodegradation was shown for 3DP-DMDP-IPN or 4-o,p-DCDP-IPN, whereas complex degradation mixtures were formed in 4-p-MCDP-IPN. These findings indicate there is no well-defined degradation pathway through the PC$^{\bullet-}$ intermediate in these PCs and that their inherent photostability controls their reaction to light. Finally, we examined the photodegradation behavior of 3DP-F-IPN and 4-p,p-DCDP-IPN, which effectively generated PC$^{\bullet-}$ and contained additional labile groups, such as C−F bonds or other types of C−CN bonds. Complex reaction mixtures formed for both PCs, probably owing to the degradation of these labile groups (**Figure 2.16(d)**).
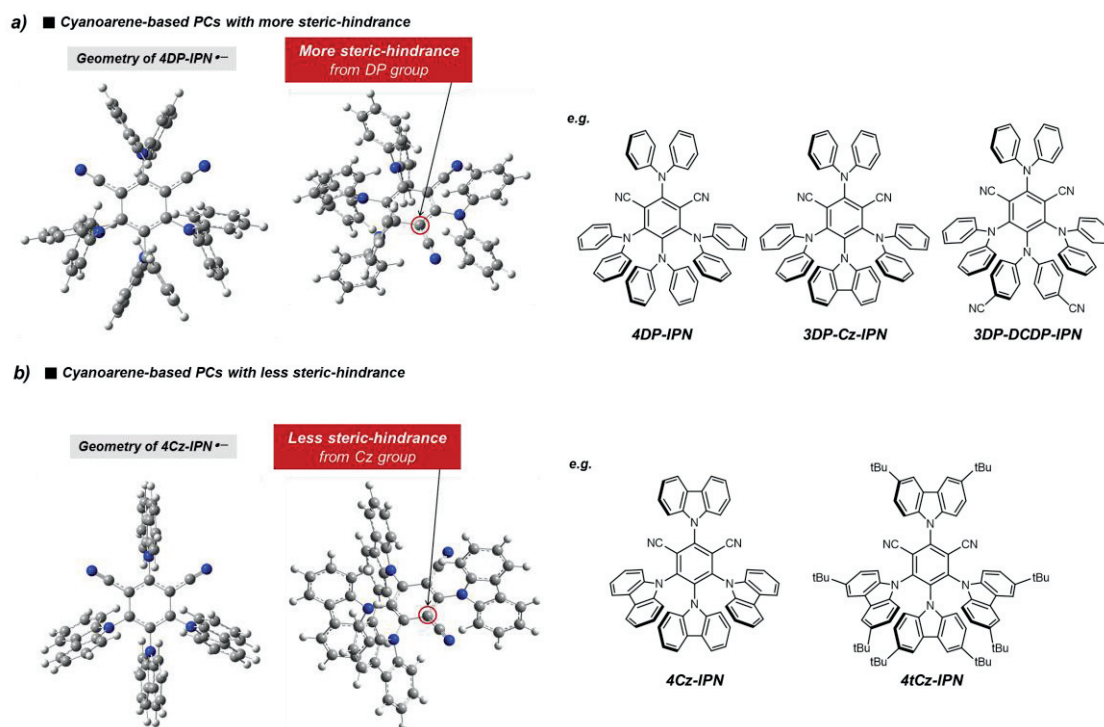
Figure 2.15. Chemical structures of cyanoarene-based PCs with (a) more steric hindrance and (b) less steric hindrance in the CN position.
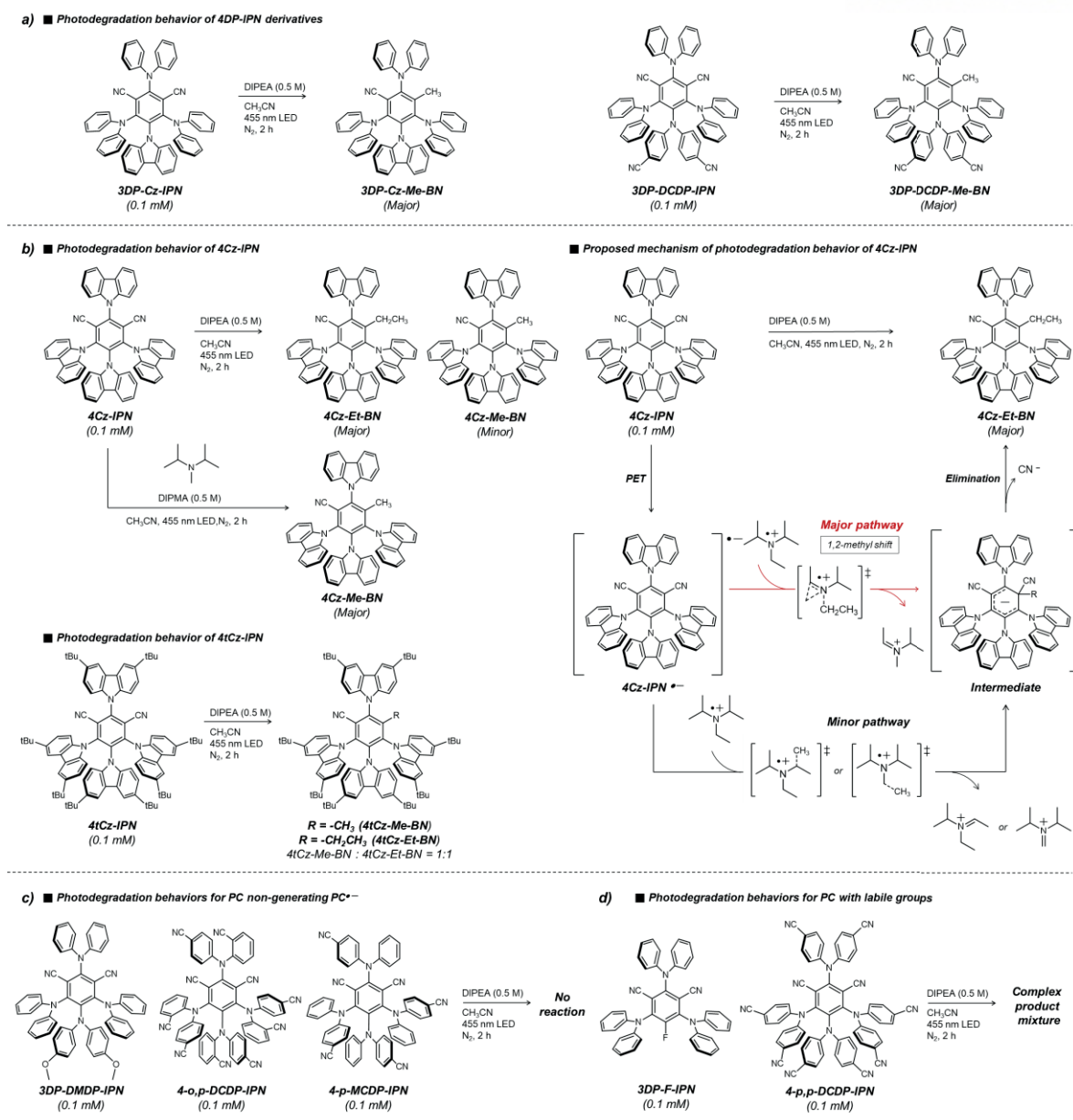
Figure 2.16. (a) Photodegradation behavior of various cyanoarene-based PCs. For the characterization of the isolated products, see **Figure 2.17–2.22**. (a) Photodegradation behavior of 3DP-Cz-IPN and 3DP-DCDP-IPN. (b) Photodegradation behavior of 4Cz-IPN and 4tCz-IPN and the proposed photodegradation mechanism with DIPEA and DIPMA as reducing agents. (c) Photodegradation behavior of PCs' nongenerating PC•⁻. (d) Photodegradation behavior of PCs with labile groups.
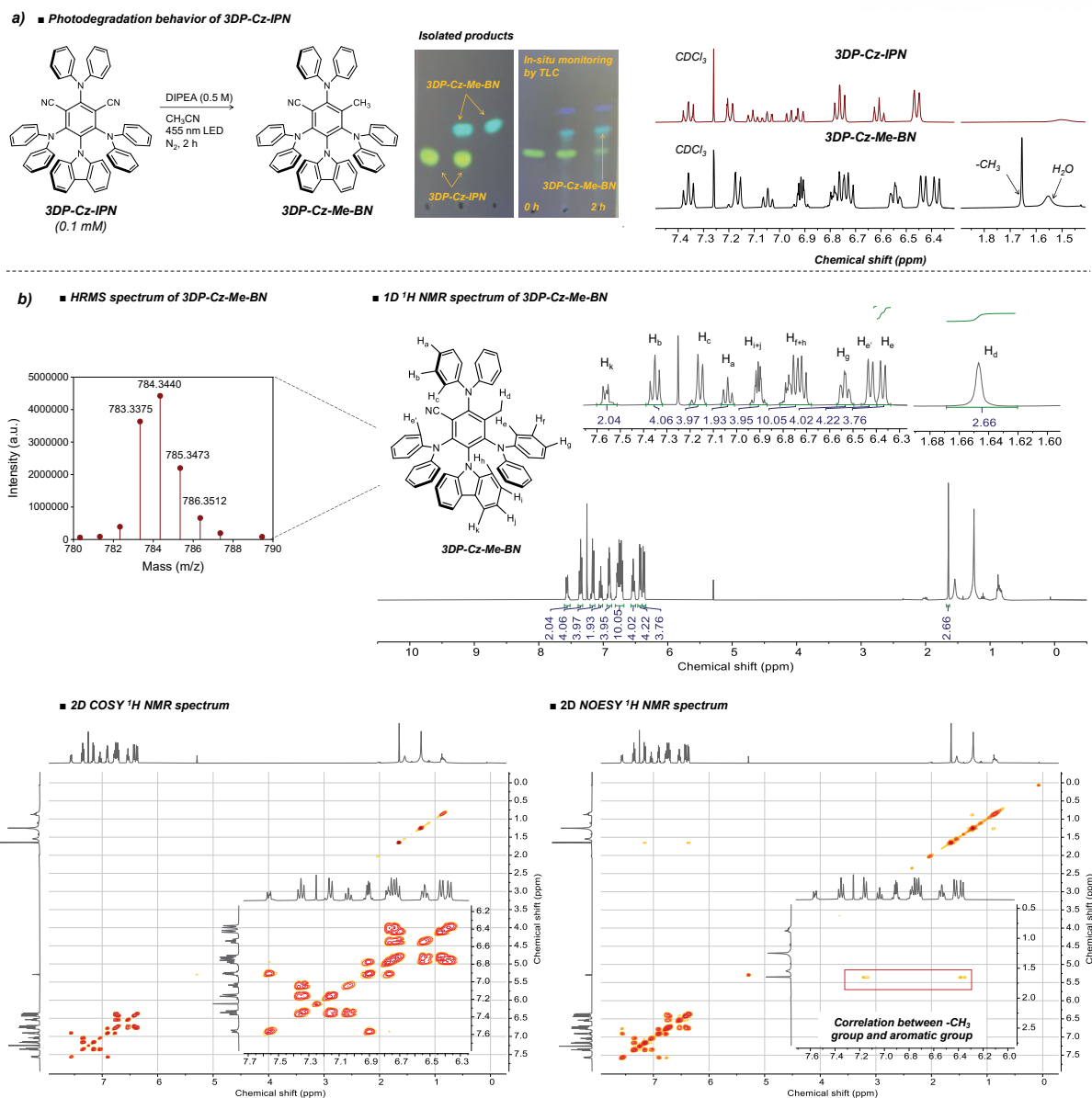
Figure 2.17. (a) Photodegradation behavior of 3DP-Cz-IPN. Reactions were performed with PC (1.0×10^{-4} M) and DIPEA (0.5 M) in CH_3CN under the illumination of two 3 W 455 nm LEDs for 2 h at RT. PC degradations were monitored *in situ* by TLC (EA:hexanes, 1:2 v/v). The left and right spots were collected before and after irradiation, and the middle spot was a co-spot. The photodegraded products were successfully isolated by column chromatography that gives ^{1}H NMR spectra, confirming that a methyl substitution reaction occurred at the CN position. (b) Structural analysis of 3DP-Cz-Me-BN with 2D ^{1}H NMR analyses combined with HRMS, MS (GC-FAB-HRMS): calculated for $C_{56}H_{42}N_5$ [M+H]$^+$: 784.3440; found as 784.3440. ^{1}H NMR (400 MHz, CDCl$_3$) δ 7.60–7.51 (m, 2H), 7.35 (t, 4H), 7.16 (d, 4H), 7.04 (t, 2H), 6.94–6.87 (m, 4H), 6.81–6.68 (m, 10H), 6.53 (td, 4H), 6.43 (d, 4H), 6.37 (d, 4H), 1.65 (s, 3H).
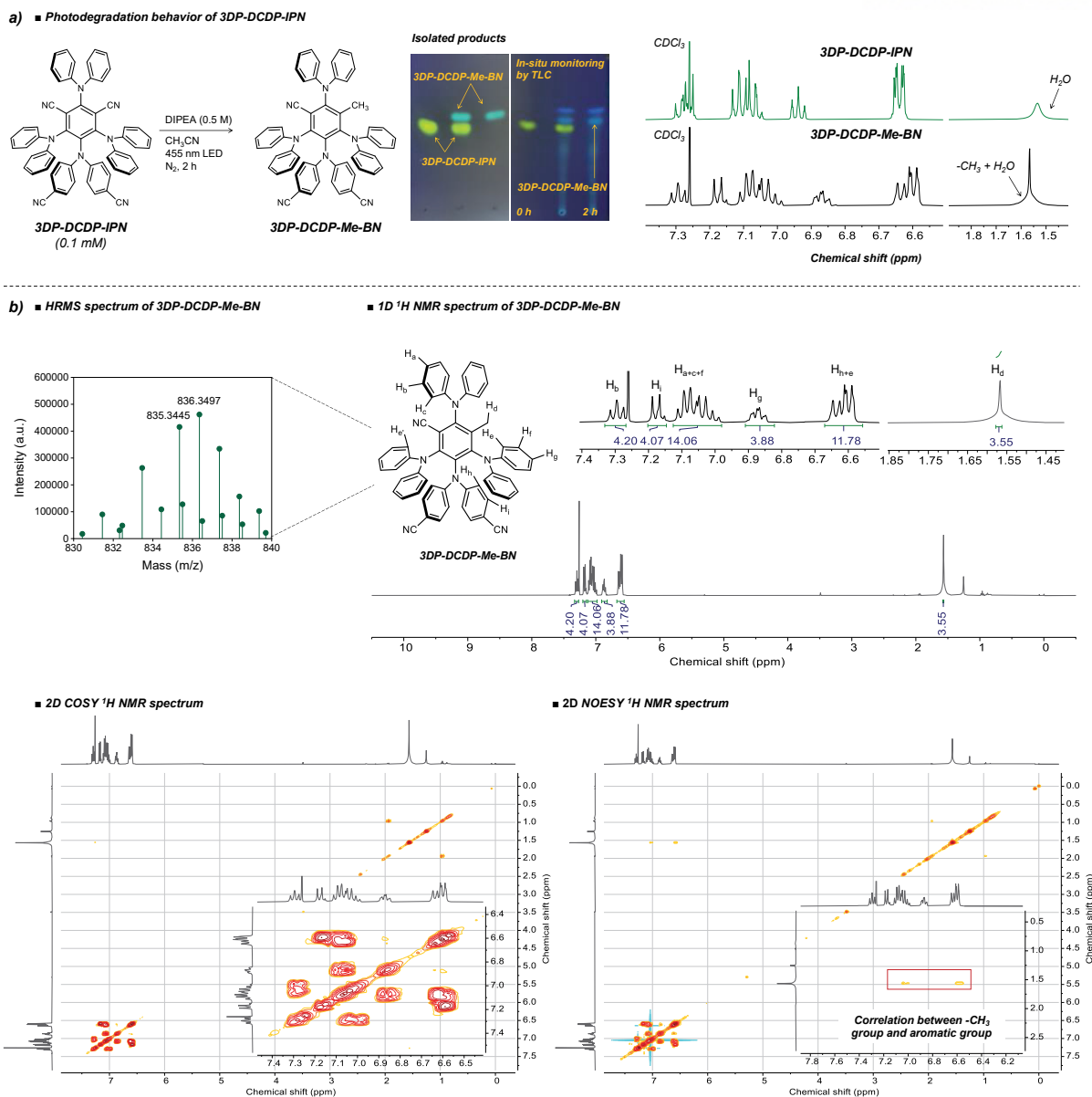
Figure 2.18. (a) Photodegradation behavior of 3DP-DCDP-IPN. Reactions were performed with PC (1.0×10^{-4} M) and DIPEA (0.5 M) in CH_3CN under the illumination of two 3 W 455 nm LEDs for 2 h at RT. PC degradations were monitored *in situ* by TLC (EA:hexanes, 1:1 v/v). The left and right spots were collected before and after irradiation, and the middle spot was a co-spot. The photodegraded products were successfully isolated by column chromatography that gives ^{1}H NMR spectra, confirming that a methyl substitution reaction occurred at the CN position. (b) Structural analysis of 3DP-DCDP-Me-BN with 2D ^{1}H NMR analyses combined with HRMS, MS (GC-FAB-HRMS): calculated for $C_{58}H_{42}N_7$ [M+H][+]: 836.3502; found as 836.3497. ^{1}H NMR (400 MHz, $CDCl_3$) δ 7.29 (t, 4H), 7.17 (d, 4H), 7.13–6.98 (m, 14H), 6.87 (td, 4H), 6.67–6.56 (m, 12H), 1.58 (s, 3H).

Figure 2.19. Photodegradation behavior of 4Cz-IPN. (a) Reactions were performed with PC (1.0×10^{-4} M) and DIPEA (0.5 M) in CH_3CN under the illumination of two 3 W 455 nm LEDs for 2 h at RT. PC degradations were monitored *in situ* by TLC (EA:hexanes, 1:4 v/v). The left and right spots were collected before and after irradiation, and the middle spot was a co-spot. The photodegraded products were successfully isolated by column chromatography that gives ^{1}H NMR spectra, confirming that an ethyl substitution reaction occurred at the CN position. (b) Structural analysis of 4Cz-Et-BN with 2D ^{1}H NMR analyses combined with HRMS, MS (GC-FAB-HRMS): calculated for $C_{57}H_{38}N_5$ [M+H]$^+$: 792.3127; found as 792.3129.

Figure 2.20. Photodegradation behavior of 4Cz-IPN. (a) Reactions were performed with PC (1.0×10^{-4} M) and DIPMA (0.5 M) in CH_3CN under the illumination of two 3 W 455 nm LEDs for 2 h at RT. PC degradations were monitored *in situ* by TLC (EA:hexanes, 1:4 v/v). The left and right spots were collected before and after irradiation, and the middle spot was a co-spot. The photodegraded products were successfully isolated by column chromatography that gives ^{1}H NMR spectra, confirming that a methyl substitution reaction occurred at the CN position. (b) Structural analysis of 4Cz-Me-BN with 2D ^{1}H NMR analyses combined with HRMS, MS (GC-FAB-HRMS): calculated for $C_{56}H_{36}N_5$ [M+H]$^+$: 778.2971; found as 778.2980.

a) ■ *Photodegradation behavior of 4tCz-IPN*

b) ■ *HRMS spectrum of 4tCz-Me-BN and 4tCz-Et-BN mixture*

c) ■ *1D ^{1}H NMR spectrum of mixture of 4tCz-Me-BN and 4tCz-Et-BN*
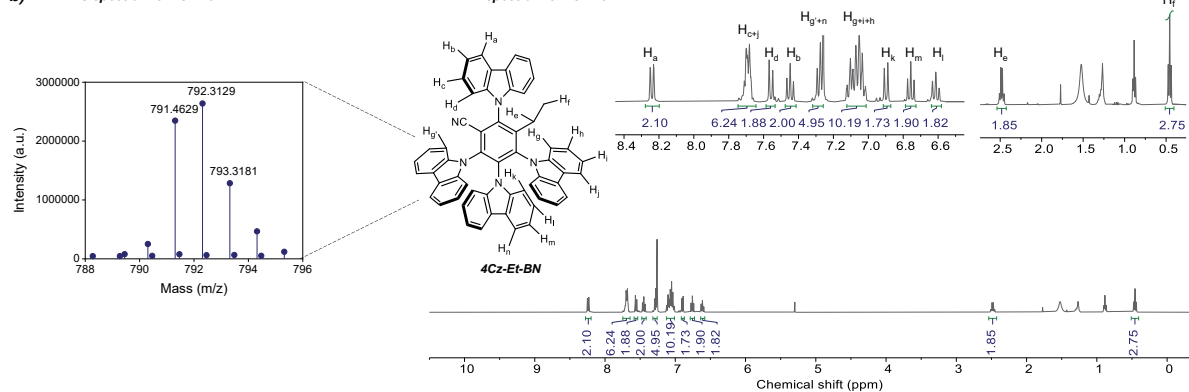
■ *2D COSY ^{1}H NMR spectrum*   ■ *2D NOESY ^{1}H NMR spectrum*
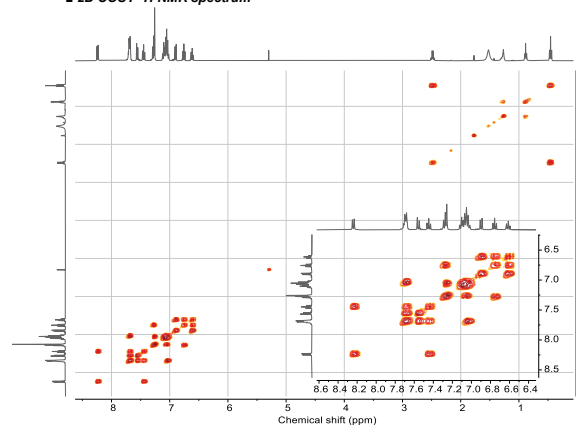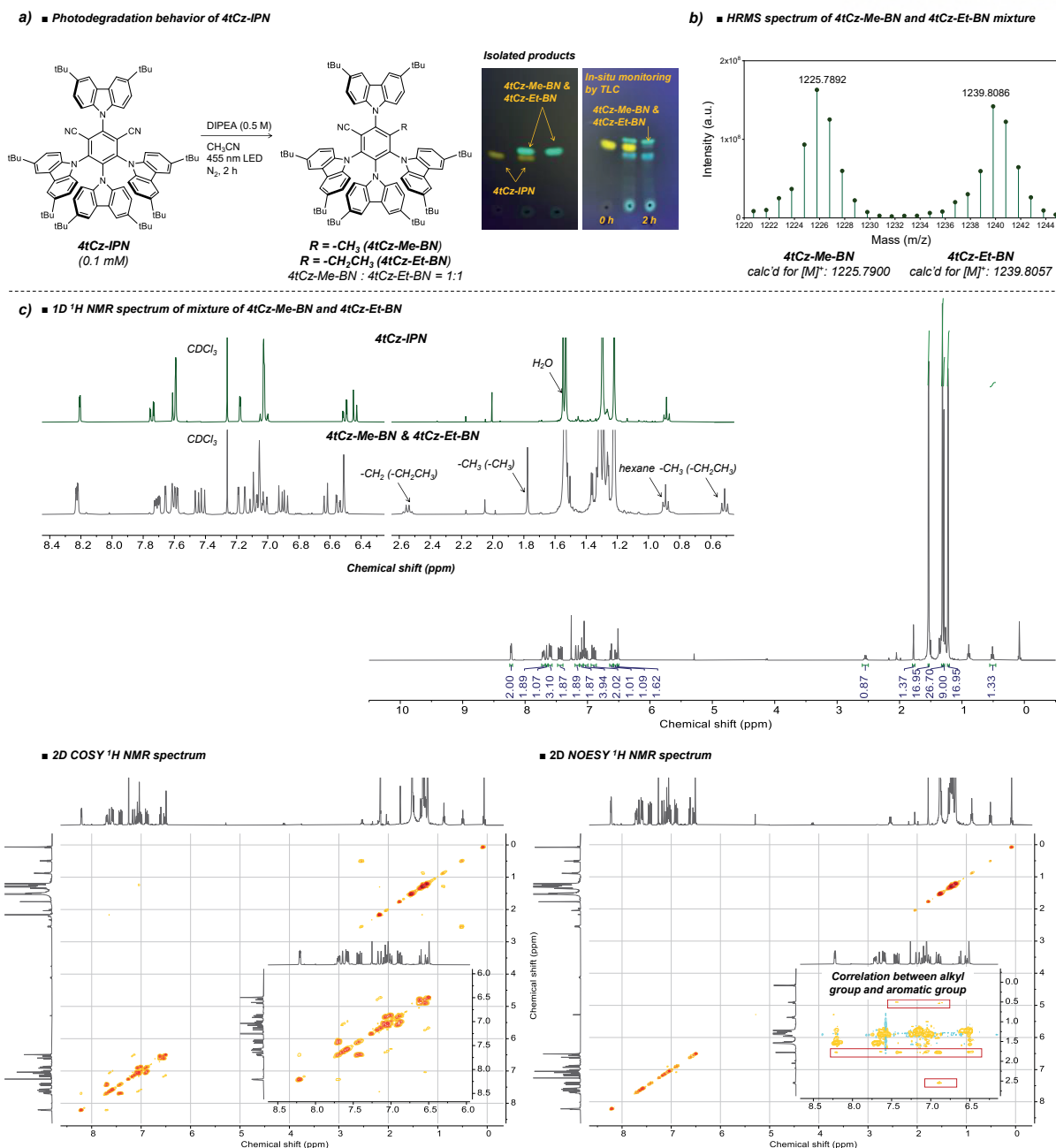
Figure 2.21. Photodegradation behavior of 4tCz-IPN. (a) Reactions were performed with PC (1.0 × 10^{-4} M) and DIPEA (0.5 M) in CH$_3$CN under the illumination of two 3 W 455 nm LEDs for 2 h at RT. PC degradations were monitored *in situ* by TLC (EA:hexanes, 5:95 v/v). The left and right spots were collected before and after irradiation, and the middle spot was a co-spot. (b, c) The mixture of photodegraded products was successfully isolated by column chromatography that gives ^{1}H NMR spectra, confirming that a methyl (or ethyl) substitution reaction occurred at the CN position combined with HRMS, MS (GC-FAB-HRMS): calculated for 4tCz-Me-BN (C$_{88}$H$_{99}$N$_5$) [M]$^+$: 1225.7900; found as 1225.7892, calculated for 4tCz-Et-BN (C$_{89}$H$_{101}$N$_5$) [M]$^+$: 1239.8057; found as 1239.8086.
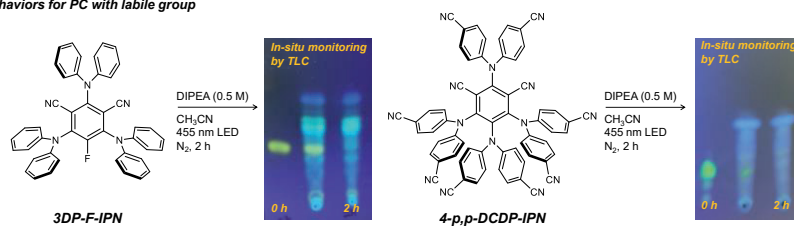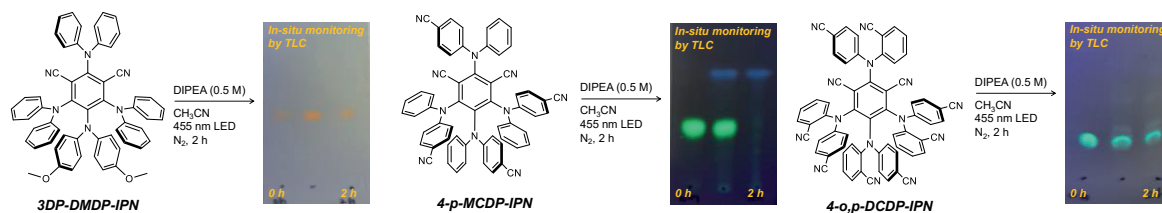
Figure 2.22. (a) Photodegradation behavior of PCs with the labile group, 3DP-F-IPN, and 4-p,p-DCDP-IPN. Reactions were performed with PC (1.0×10^{-4} M) and DIPEA (0.5 M) in CH_3CN under the illumination of two 3 W 455 nm LEDs for 2 h at RT. PC degradations were monitored *in situ* by TLC (EA:hexanes, 1:6 v/v for 3DP-F-IPN and acetone:hexanes, 2:3 v/v for 4-p,p-DCDP-IPN). The left and right spots were collected before and after irradiation, and the middle spot was a co-spot. (d) Photodegradation behavior of PCs' nongenerating PC$^{\bullet-}$, 3DP-DMDP-IPN, 4-p-MCDP-IPN, and 4-o,p-DCDP-IPN. Reactions were performed with PC (1.0×10^{-4} M) and DIPEA (0.5 M) in CH_3CN under the illumination of two 3 W 455 nm LEDs for 2 h at RT. PC degradations were monitored *in situ* by TLC (EA:hexanes, 1:1 v/v for 3DP-DMDP-IPN, EA:hexanes, 7:3 v/v for 4-p-MCDP-IPN and MeOH:$CHCl_3$ = 1:4 v/v for 4-o,p-DCDP-IPN). The left and right spots were collected before and after irradiation, and the middle spot was a co-spot.

2.3.5 Dehalogenation of Activated Aryl Halides

Considering the abovementioned experimental results, we assumed that the supra-efficient $PC^{\bullet-}$ generation of 4DP-IPN and its highly negative E_{red}^0(4DP-IPN) of -1.66 V would enable the highly efficient dehalogenation of aryl- and alkyl halides. To compare the catalytic performance of 4DP-IPN with that of the previously known PCs, we first investigated the viability of reducing 4-bromobenzonitrile ($E_{red}^0 = -1.83$ V), which was chosen as a substrate owing to its mild reactivity. The reaction conditions were optimized by irradiating a mixture of 4-bromobenzonitrile, 4DP-IPN (0.005 mol%), and tertiary amines in degassed acetonitrile using a 455 nm LED light at room temperature. Five equivalents of TEA prevented any conversion. However, 10 equivalents of DIPEA allowed the production of the reduction product, benzonitrile, after 8 h with a 100% yield (**Table 2.2**). This conclusion is consistent with the PL quenching tests, proving that the dehalogenation reaction must occur with the efficient $PC^{\bullet-}$ formation.

Table 2.2. Screening of conventional tertiary amines in photoredox reductive dehalogenation. Redox potential values are against SCE and referred to in the literature.[68,69]
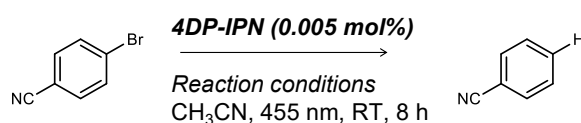
Entry	Reaction conditions	E_{ox}^0	Yield (%)
1	TEA (5 equiv.)	0.96[68]	0
2	TEA (10 equiv.)		5
3	TBA (5 equiv.)	0.88[69]	2
4	TBA (10 equiv.)		73
5	DIPEA (5 equiv.)	0.68[68]	75
6	DIPEA (10 equiv.)		100

Reactions were performed with 4-bromobenzonitrile (0.1 M), 4DP-IPN (0.005 mol%), and tertiary amines (10 equiv.) in CH_3CN (1 ml) under the illumination of two 3 W 455 nm LEDs for 8 h. All solutions were prepared inside the glovebox and degassed by bubbling with Ar. Yields were determined by GC coupled with FID using TMB as an internal standard.

■ *Fate of catalyst during dehalogenation reactions*
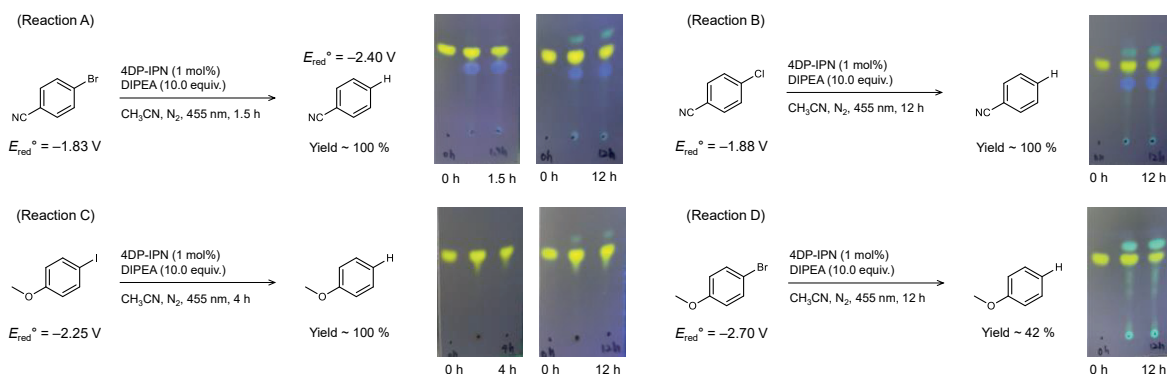
Figure 2.23. (a) The catalyst fate during dehalogenation reactions. Reactions were performed with substrates (0.1 M), DIPEA (10 equiv.), and 4DP-IPN (1 mol%, 1.0×10^{-3} M) in CH$_3$CN (1 ml) under the illumination of two 3 W 455 nm LEDs for several hours at RT. Yields were determined by ^{1}H NMR using TMB as an internal standard. PC degradation was monitored by *in situ* TLC with eluent conditions (EA:hexanes, 1:4 v/v). All redox potential values were referred to in the literature, where the potential values were measured against the standard calomel electrode (SCE).[86–88]

The 455 nm LED irradiation results were superior to those of the 515 nm LED irradiation (faster reaction kinetics), which is at odds with the UV–Vis test findings on the PC$^{\bullet-}$ photodegradation. This discrepancy probably resulted because the ET between the PC$^{\bullet-}$ and substrate occurred more quickly than the PC$^{\bullet-}$ photodegradation. We examined the photodegradation behavior of 4DP-IPN in real reactions to dehalogenate different aryl halides (**Figure 2.23**), in which 10 equivalents of DIPEA were employed as a sacrificial agent to verify our hypothesis. Aliquots of each reaction mixture were sampled at regular intervals to track the reaction production and the PC degradation. *In situ* TLC was monitored to follow the PC degradation because a small quantity of PC (1 mol%) was used, whereas ^{1}H NMR was used to trace the reaction.

When a minor quantity of the photodegradation product (4DP-Me-BN) occurred (**Figure 2.23: Reaction A**), a 100% yield for 4-bromobenzonitrile was achieved in 1.5 h, indicating that 4DP-IPN is an active PC for the 4-bromobenzonitrile dehalogenation. Interestingly, the dehalogenation process considerably slowed the PC degradation compared to DIPEA alone, which was most probably caused by the PC degradation competition with the dehalogenation process, as shown in **Figure 2.24**. In other words, the ET from 4DP-IPN$^{\bullet-}$ to 4-bromobenzonitrile was significantly faster than i) the 4DP-IPN$^{\bullet-}$ formation and ii) the substitution reaction to form 4DP-Me-BN, causing a major delay in the PC degradation. 4-Chlorobenzonitrile, 4-iodoanisole, and 4-bromoanisole (**Figure 2.23: Reactions B, C, and D,** respectively) were more difficult substrates whose dehalogenation reactions occurred at a faster rate, supporting our hypothesis.

■ *Competition of radical addition of PC vs ET process*
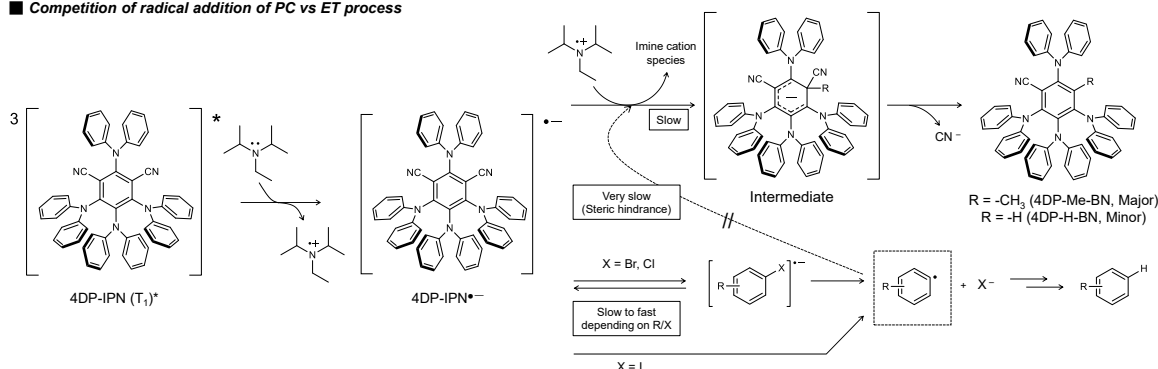
Figure 2.24. The proposed mechanistic pathways for the 4DP-IPN photodegradation in the presence of aryl halides.

We tested various PCs under optimal conditions. 4DP-IPN outperformed the other used PCs, as shown in **Table 2.3**. Ru(bpy)₃Cl₂ and Ru(phen)₃(PF₆)₂, which are commonly used as PCs for reductive cycles, gave very low yields of 13% and 0%, respectively, even at high catalyst loadings of 5 mol%. This was probably caused by the less negative reduction potential of the catalysts (E_{red}^0(Ru(bpy)$_3^{2+}$) = −1.33 V and E_{red}^0(Ru(phen)$_3^{2+}$) = −1.36 V) compared to that of 4DP-IPN (−1.66 V).[71] Rh6G and PDI employed as PCs for ConPET showed yields of 2% and 4%, respectively, at 5 mol% PC loadings. Although the one-electron-reduced forms of those PCs have highly negative excited state oxidation potentials (E_{ox}^*(PDI$^{•-}$) = −1.87 V and E_{ox}^*(Rh6G$^•$) = −2.40 V),[31,46] Rh6G$^•$ and PDI$^{•-}$ have low excited state population owing to their short excited-state lifetimes, probably resulting in ineffective ET with 4-bromobenzonitrile and low yields. In contrast, Ir(ppy)₃, known as a PC for oxidative cycles,[20] showed decent catalytic activity. However, to give comparable yields, it required 100 times higher PC loading (0.5 mol%) than that of 4DP-IPN. Despite the highly negative excited state oxidation potential of Ir(ppy)₃ (E_{ox}^*(Ir(ppy)₃) = −1.73 V), the comparatively short excited-state duration may have contributed to the higher needed Ir(ppy)₃ loading compared with that of 4DP-IPN. The range of various substituted aryl/alkyl halides with ground-state reduction potentials of less than −2.2 V was investigated in the presence of 4DP-IPN (0.001–0.05 mol%), which produced comparable reduction products in approximately quantitative quantities (**Table 2.4**, "Activated aryl/alkyl halides").

Table 2.3. Results of reductive dehalogenation of 4-bromobenzonitrile with different PCs.
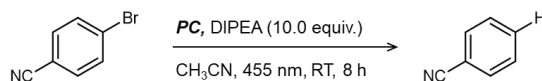
Entry	PC	PC loading (mol%)	Yield (%)
1	—	—	0
2	Ru(bpy)$_3$Cl$_2$	5	13
3	Ru(phen)$_3$(PF$_6$)$_2$	5	0
4	Rh6G	5	2
5[a]	PDI	5	0
6[a,b]	PDI	5	4
7	4Cz-IPN	5	75
8[a]	Ir(ppy)$_3$	5	100
9	Ir(ppy)$_3$	0.5	100
10	Ir(ppy)$_3$	0.05	26
11	Ir(ppy)$_3$	0.005	0
12	4DP-IPN	5	100
13	4DP-IPN	0.5	100
14	4DP-IPN	0.05	100
15	4DP-IPN	0.005	100
[†]16[c]	4DP-IPN	0.005	0
[†]17[d]	4DP-IPN	0.005	0

Reactions were performed with 4-bromobenzonitrile (0.1 M), PC (5–0.001 mol%), and DIPEA (10 equiv.) in CH$_3$CN (1 ml) under two 3 W 455 nm LEDs for 8 h. All solutions were prepared inside the glovebox and degassed by bubbling with Ar. [a]The reaction was performed in DMF because of the solubility. Control experiments were performed [b]with TEA instead of DIPEA [c]in the dark or [d]in the absence of DIPEA. Yields were determined by GC-FID or [†]^{1}H NMR using TMB as an internal standard.

At a higher 4DP-IPN concentration of 0.03 mol%, the reaction of 4-bromobenzonitrile gave a quantitative yield without degassing process (**Figure 2.25**), which enabled a facile gram-scaled reaction under ambient conditions without any preceding degassing (**Table 2.5**). To understand the origin of this high oxygen tolerance, the kinetics of the reaction with and without degassing were monitored. An inhibition period clearly appeared under non-degassed conditions but not under fully degassed conditions (**Figure 2.25**). These results imply that dissolved oxygen in the mixture solutions was fully consumed before starting the reductive dehalogenation reaction. According to the previous reports,[33,89] oxygen could be consumed through the generation of reactive oxygen species (i.e., $^1O_2$ and $O_2^{\bullet -}$) and their subsequent reaction with DIPEA and/or its cationic intermediates; indeed, in air, the oxygen tolerance was determined depending on the amount of DIPEA (**Table 2.4.**).
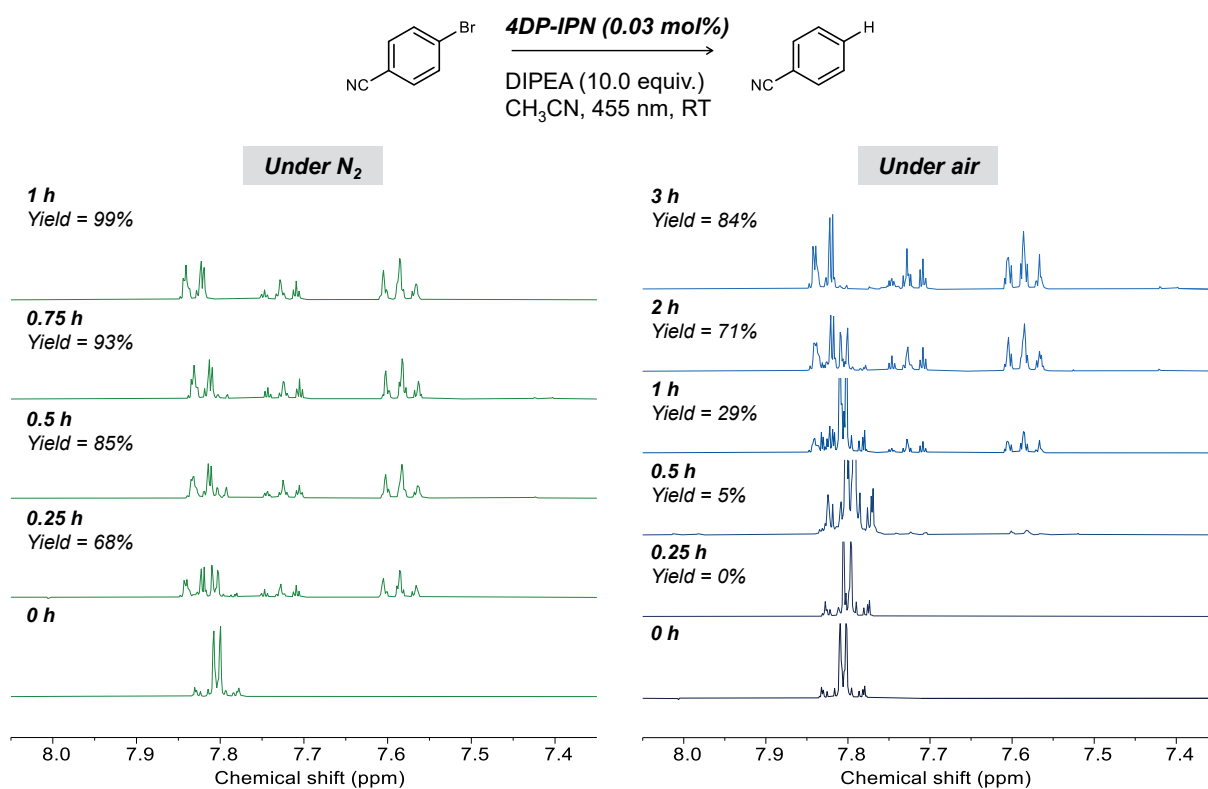
Figure 2.25. Estimation of O_2 effect in photoredox reductive dehalogenation. Reaction condition was the same described above for the general procedure, 4-bromobenzonitrile (0.2 mmol, 1 equiv.), DIPEA (10.0 equiv.) and 4DP-IPN (0.03 mol%) in CH_3CN (2 mL, 0.1 M of aryl halides) under illumination of two 3W 455 nm LEDs at RT. All the samples were prepared in situ and all of yields were determined by ^1H NMR using TMB as an internal standard (400 MHz, DMSO-d_6).

Table 2.4. Oxygen tolerance test for the dehalogenation of 4-bromobenzonitrile varying concentration of DIPEA.
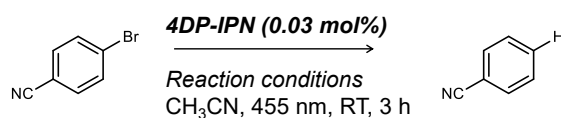
Entry	Reaction conditions	Yield (%)
1	DIPEA (2.0 equiv.) under N_2	62
2	DIPEA (2.0 equiv.) under air	0
3	DIPEA (5.0 equiv.) under air	12
4	DIPEA (10.0 equiv.) under air	84

Reactions were performed with 4-bromobenzonitrile (0.1 M), 4DP-IPN (0.03 mol%), DIPEA (2.0-10.0 equiv.) in CH_3CN (1 mL) under two 3W 455 nm LEDs for 3 hours under air atmosphere in the closed glass vial. All solutions were prepared outside under ambient conditions. Yields were determined by ^1H NMR using TMB as an internal standard.

Table 2.5. Results of reductive dehalogenation of different aryl/alkyl halides in the presence of 4DP-IPN as a PC.

■ Reaction conditions

Gram-scaled reaction

Reactions were performed with substrates (0.1 M), DIPEA (10 equiv.), and 4DP-IPN (0.005 mol%) in CH$_3$CN (1 ml) under the illumination of two 3 W 455 nm LEDs for 6–48 h at RT. The gram-scale reaction was performed with 4-bromobenzonitrile (3 g, 16.48 mmol), DIPEA (10 equiv.), and 4DP-IPN (0.01 mol%) in CH$_3$CN (0.55 M) with irradiation by four 3 W 455 nm LEDs under ambient conditions without any degassing process. The reaction was performed with [a]0.01, [b]0.05, [c]0.5, and [d]5 mol% of 4DP-IPN and [i]illumination by four 3 W 455 nm LEDs. Injection of [f]1.5 and [g]3 mol% of 4DP-IPN was divided over three additions every 16 h during the reaction. Yields were determined by GC-FID or [†]^{1}H NMR using TMB as an internal standard. All redox potential values were referred to in the literature where the potential values were measured against SCE.[87,88,90–93]

44

2.3.6 Dehalogenation of Inactivated Aryl Halides

The dehalogenation of inactive aryl/alkyl halides was then investigated, and the substrate E_{red}^0 values ranged widely from -2.2 V to -3.0 V, which was predicted to be challenging for traditional photoredox catalysis. Although the theoretical energy barrier was quite high, moderate to high yields were mainly achieved with larger PC loadings (0.5–5 mol%). Therefore, we assumed that ConPET participated in the dehalogenation of inactivated halides. The excited state oxidation potential of 4DP-IPN$^{\cdot-}$ was calculated as -3.38 V (eq. 4), corresponding to the D_2 state on the Koopmans theorem. This corresponds to an energy of -1.30 eV. The (TD)DFT computations indicate that the D_1 state may also influence ConPET. However, the D_2 state was probably responsible for ConPET, considering the energies and associated reducing capabilities (i.e., E_{ox}^* (4DP-IPN$^{\cdot-}$ at D_1) = -2.51 V). The excited state lifetime of D_2 was predicted to be long enough because the energy difference between the two molecules (0.87 eV) was close to that between D_1 and D_0 (0.85 eV, **Figure 2.26**). Without considering any potential barrier to internal conversion *via* conical intersections, which might stabilize the D_2 state, this should effectively slow down the internal conversion from D_2, increasing the D_2 lifetime:

$$E_{ox}^*(PC^{\cdot-}) = -E_{0\cdot0}(PC^{\cdot-}) + E_{red}^0(PC). \qquad \text{(eq. 4)}$$

Therefore, the inactivated aryl/alkyl halides could be reduced because of the excited state oxidation potential of 4DP-IPN$^{\cdot-}$. Even with greater PC loadings, aryl chloride exhibited lower yields than aryl bromide but with identical reduction potentials (i.e., chlorobenzene *vs*. 4-bromoanisole, see **Table 2.4**) owing to the strong C-Cl bond strength to slow down the bond dissociation of reduced aryl chloride, allowing BET to occur from the anion to PC or DIPEA derivatives.

a) ■ Energy diagram of 4DP-IPN

$D_2{}^*$

D_0

S_0

$E_{00,exp}(PC^{•-}) = 1.72$ eV

$E_{vertical\ transition,\ theo} = 1.91$ eV
$(D_0 \rightarrow D_2)$

$E_{red,exp}(PC^{•-}) = 3.02$ eV
(i.e., -1.66 V vs SCE)

$E_{ox,exp}(PC^{•-})^* = 1.30$ eV (i.e., -3.38 V vs SCE)

b) ■ TD-DFT calculation of 4DP-IPN

4DP-IPN

Calculated UV-Vis absorption spectrum

ε axis: 5×10^4, 4×10^4, 3×10^4, 2×10^4, 1×10^4

Wavelength (nm): 200, 300, 400, 500, 600, 700, 800

Oscillator strength (f): 0.3, 0.2, 0.1, 0.0

S_6: 2.92 eV
H−1→L+1 (87%)
H→L+1 (11%)
f = 0.009 — LUMO+1

S_5: 2.83 eV
H−1→L+1 (11%)
H→L+1 (85%)
f = 0.026 — LUMO

S_4: 2.81 eV
H−3→L (98%)
f = 0.040 — HOMO

S_3: 2.65 eV
H−2→L (97%)
f = 0.036 — HOMO−1

S_2: 2.52 eV
H−1→L (98%)
f = 0.037 — HOMO−2

S_1: 2.39 eV
H→L (98%)
f = 0.070 — HOMO−3

S_0

c) ■ TD-DFT calculation of 4DP-IPN•−

4DP-IPN•−

Calculated UV-Vis absorption spectrum

ε axis: 2.0×10^4, 1.5×10^4, 1.0×10^4, 5.0×10^3, 0.0

Wavelength (nm): 500, 1000, 1500

Oscillator strength (f): 0.20, 0.15, 0.10, 0.05, 0.00

Inset: 0.008, 0.006, 0.004, 0.002; 1200, 1400, 1600

HONTO → LUNTO

$D_0 \rightarrow D_6$ 99.9% D_6: 2.05 eV   f = 0.013
$D_0 \rightarrow D_5$ 99.8% D_5: 2.00 eV   f = 0.004
$D_0 \rightarrow D_4$ 99.4% D_4: 1.99 eV   f = 0.027
$D_0 \rightarrow D_3$ 99.5% D_3: 1.96 eV   f = 0.002
$D_0 \rightarrow D_2$ 99.9% D_2: 1.91 eV   f = 0.006
$D_0 \rightarrow D_1$ 99.5% D_1: 0.85 eV   f = 0.004

D_0

Figure 2.26. (a) Energy diagram of 4DP-IPN derived from the experiments and time-dependent density functional theory (TD-DFT) calculations. TD-DFT results of (b) 4DP-IPN and (c) 4DP-IPN•−. TD-DFT calculations were performed with the B3LYP functional and 6−311++G* basis set. Using optimized geometries (S_0 and D_0), vertical transition energies were calculated in the CH_3CN solution employing a polarizable continuum model (PCM). The percentage contributions of each transition were evaluated by $C_i^2 * 2 * 100$ (%), where C_i is the excitation coefficient for each vertical transition in a closed-shell system, or $\alpha / 2 * 100$ (%), where α is a paired coefficient in a natural transition orbital (NTO) in the open-shell system. However, the theoretical evidence indicates the appearance of a near-infrared (NIR) band for the PC•−, which corresponded to the D_1 state (SOMO→LUMO), independent of the chosen DFT functional. At the B3LYP level of theory, it appeared at 1,454 nm. Therefore, we thus recorded the absorption spectrum in the NIR range to 1,500 nm but did not find evidence for such absorption in this range. However, an absorption band might have been shown at a wavelength >1,500 nm but was not detected. Nonetheless, the energy difference between the bands at 1,450 and 1,600 nm, for example, is only ~0.1 eV, within the error of the DFT calculations.

46

Furthermore, the semiquantitative quenching tests for 4-bromoanisole confirmed that ConPET was involved (**Figure 2.27**). The prepared 4DP-IPN$^{\bullet-}$ solution changed color from dark green to yellow in a matter of seconds when an excess quantity of 4-bromobenzonitrile was added. However, the 4DP-IPN$^{\bullet-}$ solution showed no noticeable color change with an excess amount of 4-bromoanisole, indicating that a multiphoton excitation mechanism and quick ET between 4DP-IPN$^{\bullet-}$ and 4-bromoanisole may be excluded (i.e., ConPET). However, the ConPET procedure was not particularly effective, given the low-to-moderate yields of inactivated aryl chlorides (**Table 2.5**). This was presumably caused by the short excited-state lifetime of 4DP-IPN$^{\bullet-}$.[47] Other possible pathways, such as the XAT mechanism, by α-aminoalkyl radicals recently proposed by Leonori's group,[57] cannot be excluded. There is an ongoing study on the dynamics of the excited states in PC$^{\bullet-}$ and connected ConPET processes.
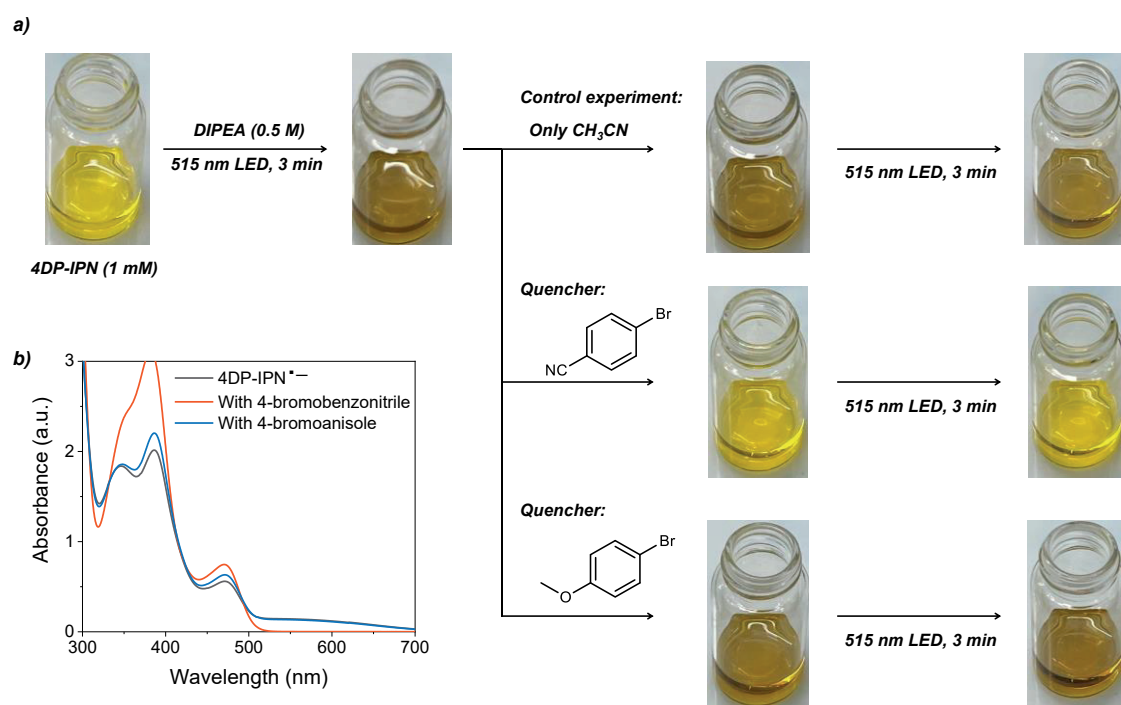
Figure 2.27. Evaluation of PET the process in photoredox reductive dehalogenation. (a) Inside a glovebox using flame-dried glass vials, the radical anion of 4DP-IPN (1.0×10^{-3} M) was generated with DIPEA (0.5 M) in CH$_3$CN (2 ml) under the illumination of a 3 W 515 nm LED for 3 min, and the aryl bromides solution (0.1 M) was added as a quencher in CH$_3$CN (0.2 ml). Subsequently, the added solutions were re-illuminated by a 3 W 515 nm LED for 3 min. All pictures were obtained immediately without any additional delay. (b) UV–Vis absorption spectra of 4DP-IPN$^{\bullet-}$ (1.0×10^{-4} M, orange line) in the presence of aryl halide (1.0×10^{-2} M) generated with DIPEA (0.5 M) in CH$_3$CN under the illumination of two 3 W 515 nm LEDs for 3 min.
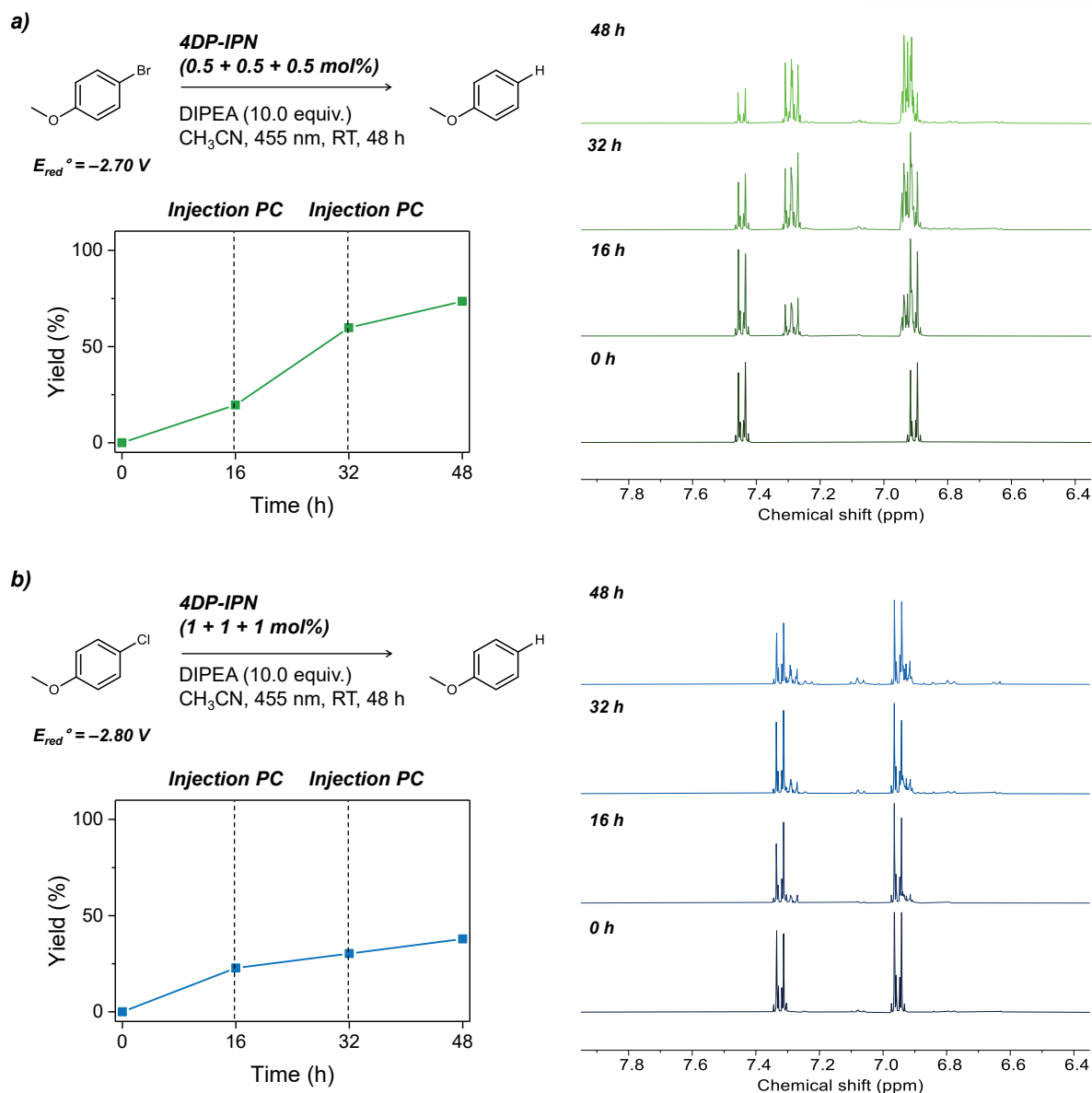
Figure 2.28. Subsequential addition of PC into photoredox reductive dehalogenation. Reaction condition was similar with general procedure, aryl halides (0.2 mmol, 1 equiv.), DIPEA (10.0 equiv.) and (a) 0.5 mol% of 4DP-IPN, (b) 1 mol% of 4DP-IPN in CH_3CN (2 mL, 0.1 M of aryl halides) under illumination of four 3W 455 nm LEDs at RT. (a) 0.5 mol% of 4DP-IPN and (b) 1 mol% of 4DP-IPN were additionally injected every 16 hours. To monitor yield and conversion, all the samples were prepared in situ and all of yields were determined by ^{1}H NMR using TMB as an internal standard (400 MHz, DMSO-d_6).

2.4 Conclusion

In conclusion, creating supra-efficient PCs with primarily negative reduction potentials was possible. We showed that the highly efficient $PC^{\bullet-}$ synthesis can be made by cyanoarene-based PCs with tightly twisted donor–acceptor structures, attributed to their capacity to efficiently populate T_1, which is long-lived because of weak SOC and adequately positive excited state reduction potentials. Moreover, using a PC with highly negative $E_{red}^0(PC)$, 4DP-IPN, the $PC^{\bullet-}$ degradation of 4DP-IPN was analyzed. We further investigated the PC degradation in the actual dehalogenation reactions with different substrates, providing a great insight into the photoredox catalysis performed by cyanoarene-based PCs. This insight led to the effective reductive dehalogenation of aryl/alkyl halides at extremely low PC loadings as small as 0.001 mol%. We hope our study will improve the knowledge about the formation, decomposition, and photochemical and electrochemical properties $PC^{\bullet-}$. Our findings also open the door to a thorough comprehension of the reductive cycles in fully organic visible-light-driven photoredox catalysis, which may be used to address several difficult problems in a range of photoredox-mediated organic reactions and polymerizations.

Chapter 3. Application to Synthesis of Pressure-Sensitive Adhesive

This chapter was written based on the publication in Adv. Mater.[62]

3.1 Introduction

Adhesives are the most crucial parts of a flexible electrical gadget. In addition to the typical function of combining two things,[94] adhesives can prevent the device destruction by reducing the tensile and compressive stresses produced when the device deforms. Moreover, the adhesive must possess extra practical qualities depending on the final product. For instance, it is expected to have optical transparency,[95] electrical and thermal conductivity,[96] biocompatibility,[97,98] biodegradability,[99,100] and other properties. Notably, in flexible electronics, the recently developed foldable display demonstrates the need for advanced adhesives, which are essential in the dissipation of tension to prevent the films from delaminating, warping, or both, even under significant external deformations.[101,102] A revolutionary technique was created to minimize the screen's power consumption by 25% for the present foldable display. The current foldable display features a special panel design, which eliminates the need for an extra polarizing layer that typically prevents the screen from reflecting outside UV radiation (**Figure 3.1**).[103] Intriguingly, this technical advancement necessitates using an adhesive with UV-blocking properties to act as the polarizer and shield the panel from UV rays from the outside. Therefore, standard UV-based synthetic processes are inadequate to synthesize the acrylic PSA in order to give the adhesive UV-blocking properties.

■ *UV-blocking issue of foldable OLEDs*
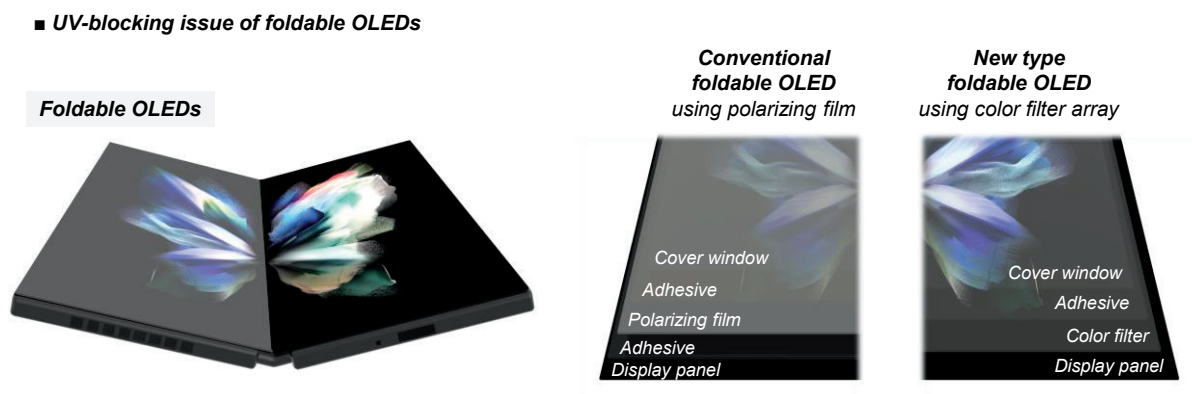
Figure 3.1. Device structure of a foldable smartphone with conventional and advanced OLED panels.

A novel acrylic resin that can be successfully cured by visible-light irradiation would be a great way to address this problem. In addition, the new system would better resolve the fundamental problems

with the existing UV-curing systems, namely, their oxygen sensitivity.[104] Herein, we created a novel acrylic resin that can be successfully cured by visible light without the need for oxygen removal and first-ever UV-blocking adhesives, which can be used in flexible displays. Most crucially, a new PC and a set of additives that enable sufficiently quick curing under visible light when UV absorbers are present are given. Because of the PC's great catalytic activity, UV-blocking adhesive films were only prepared using a tiny amount (10 ppm relative to monomers). Accordingly, films displayed extremely high optical transparency in the visible light region. The roles of tertiary amine are not restricted to being sacrificial reductants because they may function as initiators, oxygen scavengers, and crosslinkers, as shown by screening numerous amine-based reductants. Understanding the amine function enabled us to improve the structure of amine-based reductants, reducing the need for additives (e.g., an external crosslinker, initiator, or both) and increasing the curing pace. Additionally, we observed high oxygen-tolerance behavior with a particular combination of PC and sacrificial reductants, which was seen only in systems using special agents, such as boron derivatives,[105,106] thiol derivatives,[107,108] and chain transfer agent.[109,110] Experimental investigations and quantum chemical computations are also used to provide a mechanism for the oxygen tolerance. According to our analysis, this method can be widely used in various applications that require a highly effective visible light-curing procedure, not just the production of UV-blocking adhesives.

3.2 Experimental

3.2.1 Materials

All chemicals (i.e., monomers and UV absorber 2) and organic solvents were purchased commercially and used without further purification in Aldrich, TCI, and Alfa Aesar. For all acrylic monomers, the inhibitor was removed by basic alumina (Aldrich). Other cyanoarene-based PCs were prepared according to the previously reported procedures.[11] The synthetic procedures and structural PC characterization are fully described in **Appendix 1**.

3.2.2 General Procedure

3.2.2.1 General Procedure for Measurements of PET Rate Constant

Outside the glove box, a sealable quartz cuvette was charged with PC (1.0×10^{-4} M) and tertiary amines in 3 ml of anhydrous EA. Afterward, the quartz cuvette was capped with a rubber septum and sealed with parafilm. The reaction batches were purged with N_2 (99.999%) for 10 min outside the glove box. Subsequently, the PL decays of reaction solutions using TSCPC techniques were recorded to monitor the lifetime change of PL and the tertiary amine concentration. The rate constants of PET were evaluated using the Stern–Volmer relationship. In preparation for the reaction, the PC pre-prepared stock solutions were used for higher result reproducibility.

3.2.2.2 General Procedure for Bulk Polymerization and Film Curing

The PSA samples were prepared in two steps: i) bulk polymerization and ii) PSA film curing. In bulk polymerization, some acrylic monomers were polymerized to prepolymer containing mixture of linear polymer chains and unreacted monomers (**Figure 3.2**). Bulk polymerization was performed in a vial (20 ml glass scintillation vial, Kimble®), and the weight of the monomer mixture was fixed at 5 g. Two bulb-type blue LEDs (MR16, wavelength: 455 nm, watt: 9 W) were used in bulk polymerization, and the light intensity of one bulb was approximately 50 mW/cm^2 (455 nm, **Figure 3.3(a)**). Bulk polymerization conversion was gravimetrically evaluated.

In film curing, after bulk polymerization, the prepolymer was coated into a film form and then cured by a blue LED. The thickness of the cured adhesive film was set as ca. 50 μm. Two string-type blue LEDs (wavelength: 452 nm, watt: 3 W) were used. When both LEDs were turned on, the light intensity observed at the film's center was approximately 15 mW/cm^2 (452 nm, **Figure 3.3(b)**). Different UV setups were used for bulk polymerization and film curing when performing photopolymerization using UV light. Two UV handlamps (model: VL-4LC, wavelength: 365 nm, watt: 4 W) were used for bulk polymerization, and the light intensity of one lamp was approximately 0.5 mW/cm^2 (365 nm, **Figure**

3.3(c)). Four string-type UV LEDs (wavelength: 373 nm, watt: 1.7 W) were employed in film curing. When all LEDs were turned on, the light intensity observed at the film's center was approximately 6 mW/cm^2 (373 nm, **Figure 3.3(d)**). Light intensity (mW/cm^2) at 455, 452, 373, and 365 nm was measured using an energy meter (PM100D, Thorlabs, USA, **Figure 3.3(e)**). Because the energy meter detects the intensity of light's full spectrum rather than light with a single wavelength, the actual light intensity with a single wavelength (455, 452, or 373 nm) is much lower than the measured value (**Figure 3.3(f)**). The portion of single wavelength light was obtained from a range of peak energy ± 0.15% (in eV) to evaluate light intensity with a single wavelength. The single wavelength intensity was not evaluated because of the low intensity of the UV hand lamp and high noise.
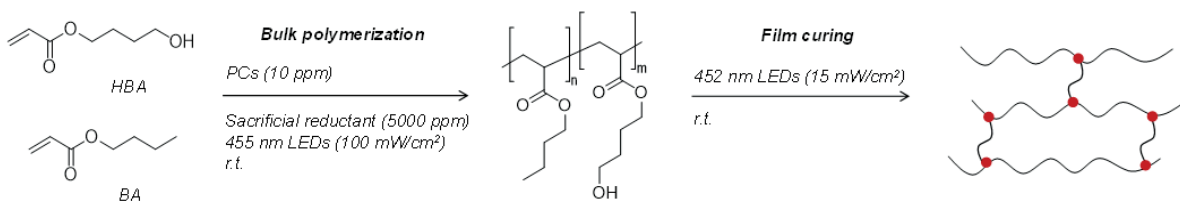
Figure 3.2. The preparation process of pressure-sensitive adhesive (PSA) samples: bulk polymerization and film curing.
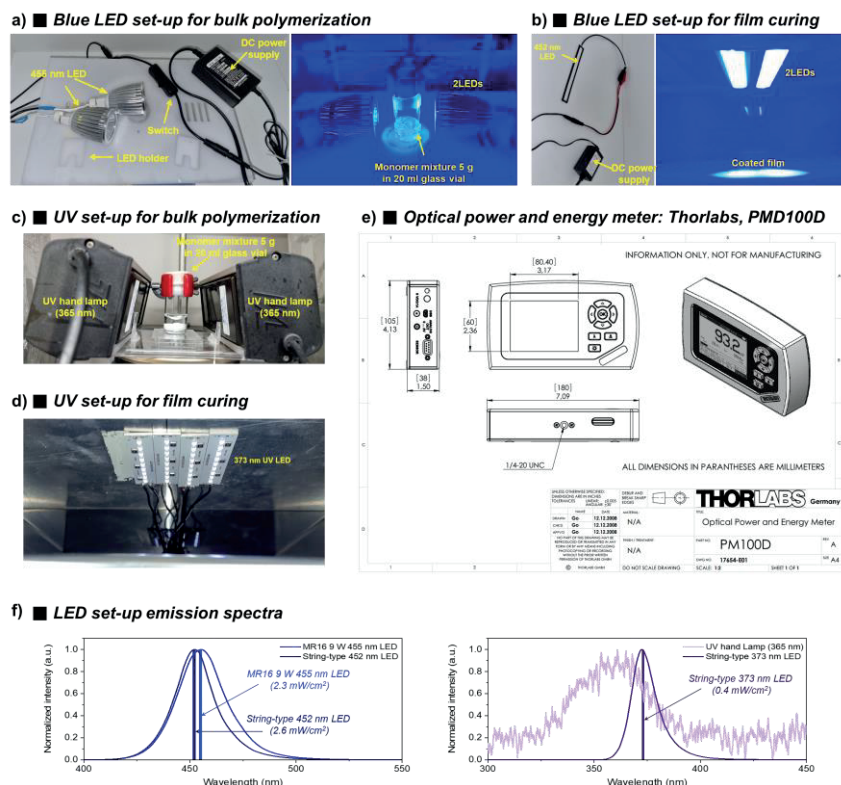
Figure 3.3. Experimental setup for bulk polymerization and film curing. Blue LED setup for (a) bulk polymerization and (b) film curing. UV setup for (c) bulk polymerization and (d) film curing. (e) Energy meter for the evaluation of light intensity. (f) LED setup emission spectra.

53
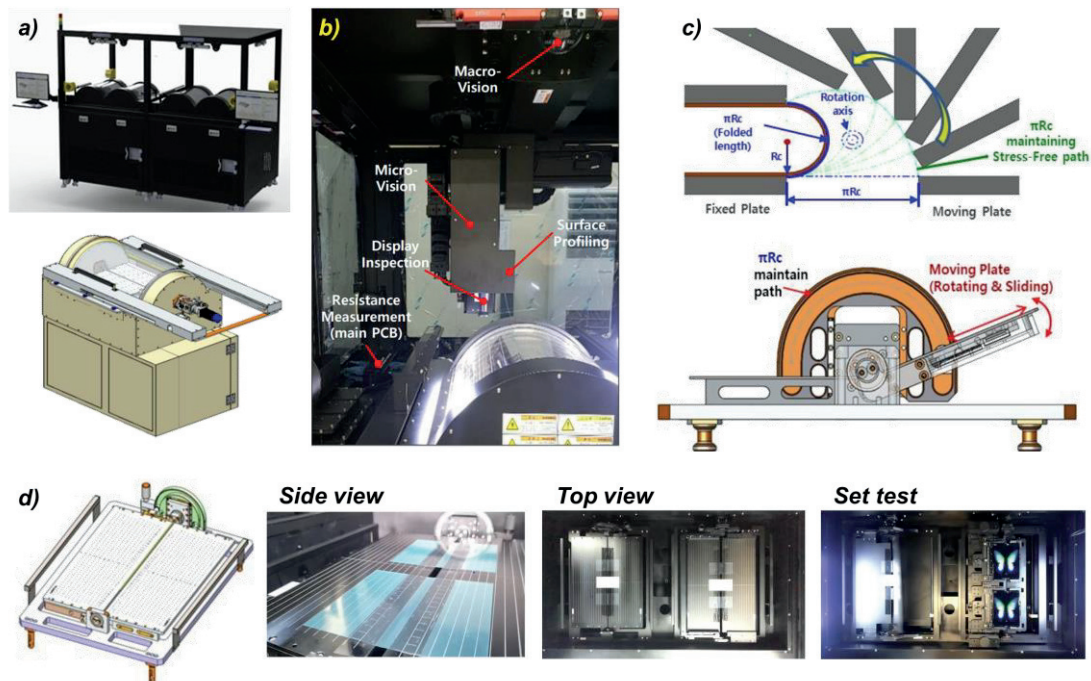
Figure 3.4. Dynamic folding test instrument: (a) outside and (b) inside view. (c) Schematic illustration for folding procedure. (d) Appearance of the used folding plate (left scheme, side view, and top view) and customized folding plate for the set test (right picture).

3.2.2.3 Dynamic Folding Test of PSA Samples

Customized equipment (Foldy-200, FlexiGO, Republic of Korea, **Figure 3.4**) was used to evaluate folding durability.[111] The attached specimen was folded inward during our dynamic folding test, and the apparatus we employed allowed us to maintain the folded length throughout the dynamic folding test (**Figure 3.4(c)**). Inspection techniques (e.g., microvision, macrovision, display inspection, and surface profiling) were used to assess the folding durability qualitatively and quantitatively (**Figure 3.3(b)**). We used the folding plate to examine film-type specimens, which can hold ten specimens per chamber. It is feasible to assess the assembled foldable smartphone's folding durability if the folding plate is manufactured to demand (set test in **Figure 3.4(d)**).

54

3.3 Results and Discussion

3.3.1   Design Strategy

Visible light has been extensively used as an energy source in various chemical processes since the pioneering work on photoredox catalysis by MacMillan,[2,23] Stephenson,[4] and Yoon.[3,24] This approach was then merged with ordinary polymerization reactions, significantly developing PET-based visible light-driven polymerization procedures between PC and substrate.[11,15,16] Despite the recent significant efforts, the development of a visible light-curing resin system to produce UV-blocking adhesives remains challenging because of i) the high loading of the colored PC, which lowers the optical transparency of the resultant adhesive;[112] ii) the use of additives that are colored, contain sulfur or halogen atoms, or both,[2,18,64] which are not permitted for use in electronic devices; iii) the slower curing rate compared to that of a UV-light/photoinitiator system; and iv) the ambiguous oxygen tolerance. The reaction conditions considerably impact the amount of oxygen a photoredox-mediated polymerization can tolerate.[104]

Figure 3.5. Proposed mechanism for photocatalyzed visible-light-driven free radical polymerization in the presence of sacrificial reductants.

A visible light-curing system with a sufficiently fast polymerization rate, even at ppm-level PC loading, is necessary to provide optical clarity in the visible region and a sufficiently high curing rate. Accordingly, we developed a PC that successfully produces long-lived T_1 excited states. The T_1 population, which has a long lifetime to permit effective PET, plays a critical role in photoredox catalysis.[5,13] Additionally, the T_1 excited state is less vulnerable to BET, which lowers the catalyst's effectiveness.[5]

A reductive quenching cycle was chosen as the mechanistic pathway for the visible light curing of the system to remove further additives and assure oxygen tolerance (**Figure 3.5**). In this situation, tertiary amines may be ideal sacrificial reductants because they may act as initiators and oxygen scavengers. A $PC^{\bullet-}$ and tertiary amine radical cation ($R_3N^{\bullet+}$) result from the first PET reaction in the reductive cycle between the PC and the amine-based sacrificial reductant. Subsequently, to generate α-amino radical species, $R3N^{\bullet+}$ loses a proton (H+), which serves as the free radical polymerization initiator.[104] Additionally, tertiary amines lessen oxygen inhibition. They can interact with inert peroxyl radicals created by oxygen interaction with the developing radical species to change them into active α-amino radical species.[113,114] Furthermore, an ET reaction between $PC^{\bullet-}$ and O_2 regenerates the ground-state PC,[115,116] allowing the catalytic cycle to proceed smoothly.

Four cyanoarene-based PCs were designed based on a strongly twisted donor–acceptor (D–A) structure to generate a long-lived T_1 excited state and drive the reductive quenching PC cycle (**Figure 3.6**). Such PCs could efficiently generate long-lived T_1 because they can fulfill the conditions of a small ΔE_{ST} and the orthogonality rule.[11] According to previous studies conducted by our group[11,61–64] and others,[58,60] 4Cz-IPN and 4DP-IPN were considered exemplary PCs in the D–A structure owing to their remarkably high photocatalytic activity in various chemical processes involving a reductive or oxidative cycle. Furthermore, to enable PET between the PC and amine-based sacrificial reductant and improve the catalytic efficacy, we designed two additional PCs with noticeably lower HOMO energy. The lowered HOMO energy of PC enhances the $-\Delta G_{PET}$ and hence the ET rate because the PET between PC and the sacrificial reducing agent is often situated in the Marcus "normal region."[17] As the HOMO is localized in the donor moiety of the strongly twisted D–A type structure, for efficient visible-light absorption, we added a potent electron-withdrawing group (i.e., the CN group) to the donor group to lower the HOMO energy (**Figure 3.6**). A full description of the synthesis and characterization of PCs is provided in **Appendix 1**. According to our predictions, the change in donor moieties increased $E_{red}^*(PC)$, consistent with the trend of the HOMO energy of PCs predicted by DFT calculations (**Figure 3.6**). Furthermore, four tertiary amines with different oxidation potentials were selected as sacrificial reductants (**Figure 3.6**).

■ *PC design appropriate for a reductive quenching cycle*

HOMO decrease: Better PET from reductants

4DP-IPN
$E_{red}^{*}(S_1) = 0.89\ V$
$E_{red}^{*}(T_1) = 0.72\ V$
L −2.56
H −5.61

4Cz-IPN
$E_{red}^{*}(S_1) = 1.56\ V$
$E_{red}^{*}(T_1) = 1.47\ V$
L −2.98
H −6.05

4-o,p-DCDP-IPN
$E_{red}^{*}(S_1) = 1.57\ V†$
$E_{red}^{*}(T_1) = 1.21\ V†$
L −3.07
H −6.38

4-p,p-DCDP-IPN
$E_{red}^{*}(S_1) = 1.50\ V$
$E_{red}^{*}(T_1) = 1.33\ V$
L −3.39
H −6.51

HOMO decrease: Less PET to PCs

DIPEA
$E_{ox}^{o} = 0.62\ V†$
L −0.21
H −5.52

TEA
$E_{ox}^{o} = 0.75\ V†$
L −0.18
H −5.79

DMBA
$E_{ox}^{o} = 0.89\ V†$
L −0.58
H −6.11

DMAEAc
$E_{ox}^{o} = 0.96\ V†$
L −0.24
H −6.24

Energy (eV)

Figure 3.6. Molecular structures and experimentally evaluated redox potentials of photoredox catalysts (PCs) and sacrificial reductants. Calculated HOMO and LUMO energies of each PC and reductant are also shown. The ground redox potentials (E_{red}^{0} and E_{ox}^{0}) were measured against the standard calomel electrode in CH$_3$CN using CV cycle. The excited reduction potential (E_{red}^{*}) was obtained from $E_{red}^{*} = E_{00} - E_{red}^{0}$. $E_{00}(S_1)$ and $E_{00}(T_1)$ were evaluated from the onset of photoluminescence (PL) and gated PL spectra of PCs in EA at 65 K, respectively. †The redox potentials of the ground state were evaluated from the half-peak potentials ($E_{p/2}^{0}$) owing to their irreversible CV cycle.

57

3.3.2 Bulk Polymerization

Herein, we investigated the visible-light-driven bulk polymerization of acrylic monomers, the initial stage in adhesive production, using the four PCs and sacrificial reductants. Notably, acrylic adhesives are often made *via* photomediated bulk polymerization of acrylic monomers, followed by a photoinduced method for film curing. n-Butyl acrylate (BA) and 4-hydroxybutyl acrylate (HBA) were chosen as monomers because they provide appropriate adhesives for a foldable display; HBA provides adhesives with cohesive strength, BA is a monomer with a low glass transition temperature (T_g) that provides them with great flexibility even at low temperatures. As a control experiment, we first conducted bulk polymerization of a mixture of BA and HBA using a conventional UV-photoinitiator (i.e., 1,000 ppm of irgacure 184) under argon atmosphere and UV-light illumination (365 nm, 8 W, 20 s) (**Table 3.1**). Continuous light irradiation provided poly(BA−co−HBA) with a moderate conversion (5.22%) and high molecular weight ($Mn = 1,319$ kg mol^{-1}). No polymerization occurred when the same process was performed without degassing, indicating that traditional photoinitiator-mediated photocuring of the BA/HBA combination is not oxygen-tolerant as anticipated.

We performed the same polymerization using 10 ppm of each prepared PC in the presence of DMAEAc (5,000 ppm), selected as the sacrificial reductant, under argon atmosphere and 455 nm LED irradiation to assess the catalytic performances of the generated PCs (18 W, 30 s; **Table 3.2**). Significantly different results were obtained for several PCs. Surprisingly, 4Cz-IPN showed the highest catalytic performance (*vide infra*). In reality, it was anticipated that PCs with lower HOMO energies would perform better. Except for 4Cz-IPN and 4-p,p-DCDP-IPN, none of the PCs underwent polymerization under the ambient conditions reported in **Table 3.2**. Although 4-p,p-DCDP-IPN showed strong oxygen-acceleration behavior and the monomer conversion was significantly enhanced in the presence of oxygen from 6.1% to 24.0%, it experienced solubility concerns in the monomer mixture (**Figure 3.7**). The 4Cz-IPN achieved the best performance among PCs with no solubility problems. It offered a very high conversion (23.0%) even under ambient conditions, which was only marginally lower than the conversion achieved in an argon atmosphere. Furthermore, identical bulk polymerization was performed in an oxidative quenching cycle for comparison, using alkyl bromide as an initiator instead of DMAEAc (**Table 3.1**). The reductive quenching cycle is preferable in this scenario because no polymerization occurred under ambient conditions.

4DP-IPN   *4Cz-IPN*   *4-o,p-DCDP-IPN*   *4-p,p-DCDP-IPN*
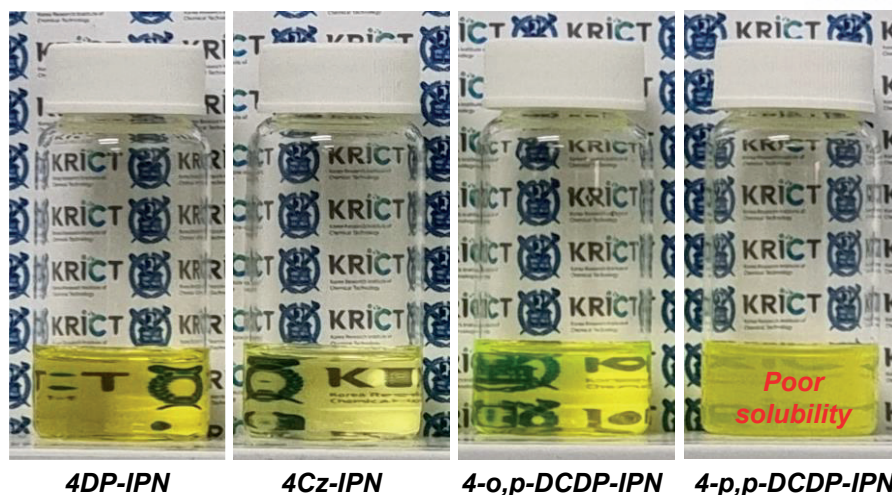
Figure 3.7. Photos of monomer mixtures containing 10 ppm of PC (6.9 × 10^{-5} M). Monomer composition was fixed as [BA]:[HBA] = 80:20.

The 4Cz-IPN performance at 10 ppm was then examined in relation to the impacts of the sacrificial reductants (**Table 3.2**). DMAEAc achieved the greatest conversion among the four reductants (DIPEA, TEA, DMBA, and DMAEAc) in the ambient and inert environments. Because DMAEAc has the lowest HOMO energy among the amines (**Figure 3.6**), PET from DMAEAc was expected to be the slowest. However, the results completely contradicted our predictions. When the reaction was performed without degassing, the DIPEA with the greatest HOMO energy performed poorly, and no polymers were produced.

59

Table 3.1. Results of PC-mediated bulk polymerization using oxidative quenching cycle. Monomer composition was fixed as [BA]:[HBA] = 80:20.
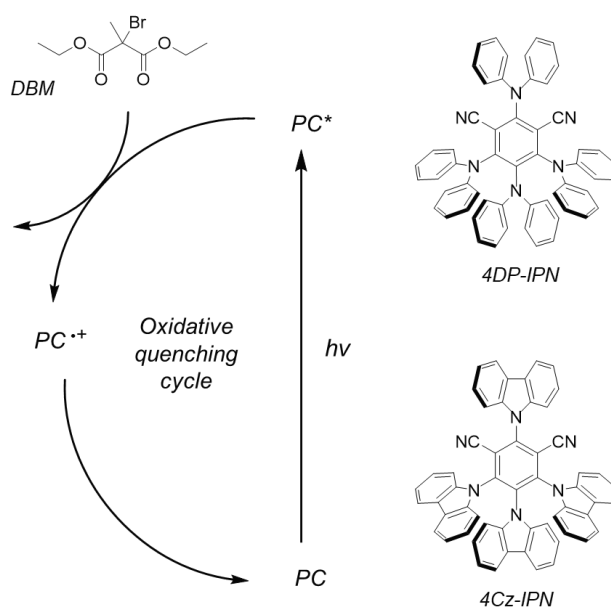
Entry	PC/PI	Atm.	Conversion (%)	M_n (kg/mol)	PDI
1[a]	4DP-IPN	Air	0	—	—
2[a]	4DP-IPN	Argon	23.89	425	1.40
3[a]	4Cz-IPN	Air	0	—	—
4[a]	4Cz-IPN	Argon	3.79	366	1.40
5[b]	Irgacure 184	Air	0	—	—
6[b]	Irgacure 184	Argon	5.22	1319	1.13

[a]PC content: 10 ppm, reaction time: 30 s (455 nm, 100 mW/cm^2), oxidant (diethyl 2-bromo-2-methylmalonate, DBM) content: 1,000 ppm. [b]Photoinitiator (PI, Irgacure 184) content: 1,000 ppm, reaction time: 20 s (365 nm, 1 mW/cm^2).

Table 3.2. Bulk polymerization results with various PCs and reductants. Monomer mixture composition was fixed as follows: [BA]:[HBA]:[reductants]:[PC] = 80:20:0.5:0.001. Bulk polymerization was conducted by blue LED (455 nm, 18 W, 30 s) under argon or air conditions. Conversion was gravimetrically evaluated.
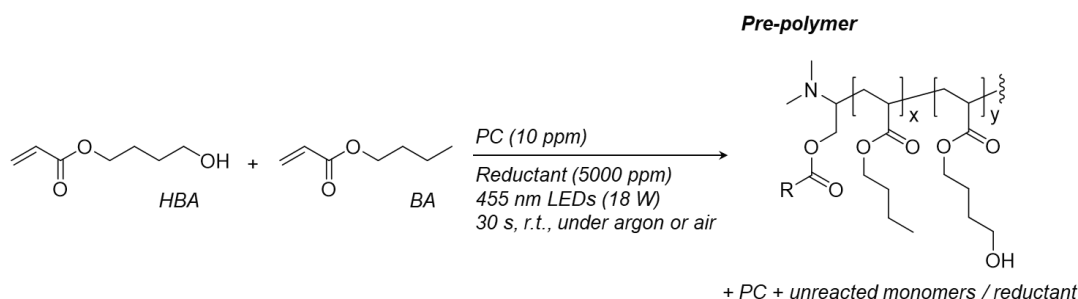
Entry	PC (10 ppm)	Reductant (5,000 ppm)	Conversion (%)	
			Under argon	Under air
1	—	—	No separable polymer	No separable polymer
2	—		No separable polymer	No separable polymer
3	4DP-IPN		6.7	No separable polymer
4	4Cz-IPN	DMAEAc	20	23
5	4-o,p-DCDP-IPN		1.3	No separable polymer
6	4-p,p-DCDP-IPN		6.1	24
7		—	3.8	No separable polymer
8	4Cz-IPN	DIPEA	4	No separable polymer
9		TEA	18.8	14.8
10		DMBA	11.2	15.7

3.3.3 Origin of the Catalytic Performance

Mechanistic experiments were performed to figure out the reason for the unexpected findings in bulk polymerization: i) 4Cz-IPN showed better catalytic performance than other PCs with lower HOMO energies, ii) DMAEAc with the lowest HOMO energy was the best sacrificial reductant among the amines, and iii) strong oxygen-tolerance behavior was observed for 4Cz-IPN in the presence of DMAEAc.

When the sacrificial reductant is fixed, the PET and BET between the PC and sacrificial reductant are the only factors affecting the catalytic performance. The PET rate is described by the following equation:

$$v_{PET} = v_{PET} \ [PC^*][Q], \tag{eq. 4}$$

where [PC*] is the PC concentration in the excited state and [Q] is the sacrificial reductant concentration. First, PL decay quenching studies were used to track the PET from the sacrificial electron donor (DMAEAc) to the PC to identify k_{PET} in different systems. Due to similar polarity with acrylate, EA was used as a solvent for photophysical investigations to account for the acrylic polymerization results. 4-p,p-DCDP-IPN was excluded from this investigation because of the aforementioned solubility problem. Most PCs displayed a PL with two components of around millisecond and microsecond lifetimes in the Ar atmosphere in the absence of DMAEAc (**Figure 3.11**, inset). According to a previous report,[117] the short and long components are attributed to PF and DF, respectively. DF is produced by a RISC from its lowest T_1 to its lowest S_1 excited state. In addition, long-lived T_1 generation is inefficient, considering the weak DF component and fast decay time reported for 4-o,p-DCDP-IPN.

The lifetime of each PC's DF component was shortened when DMAEAc existed, indicating that the T_1 of PCs is critical in the PET event (**Figure 3.8**). No emission quenching was observed for 4-o,p-DCDP-IPN, even at a high DMAEAc concentration, because it has a negligible delayed component. The PET rate constant grew with increasing $-\Delta G_{PET}$, corresponding with the Marcus "normal region" behavior, considering the excited-state reduction potentials of PCs ($E_{red}^*(T_1$, 4DP-IPN) = 0.72 V and $E_{red}^*(T_1$, 4Cz-IPN) = 1.47 V).[17] Hence, the very small k_{PET} value of 4DP-IPN results from its smallest $-\Delta G_{PET}$.
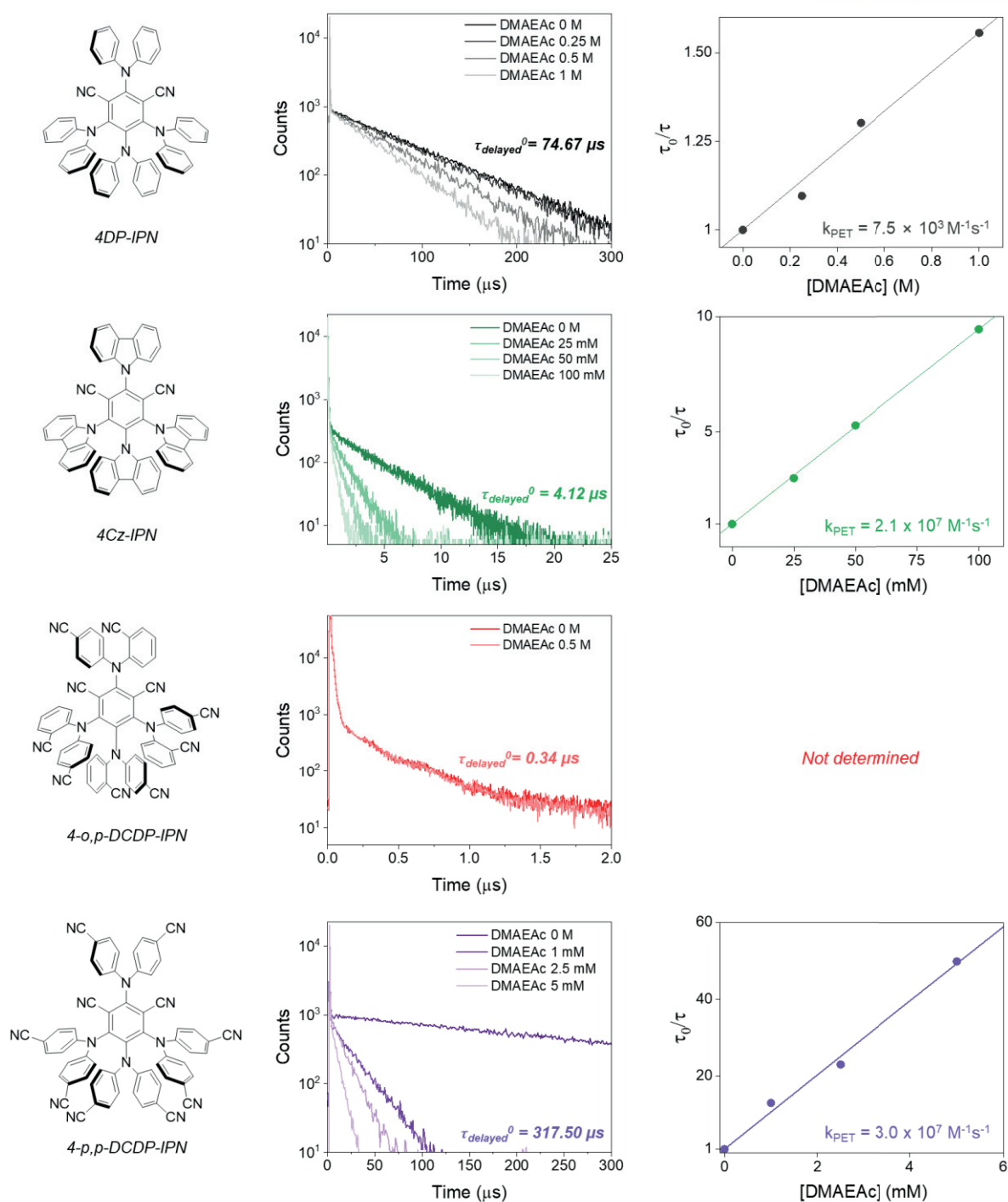
Figure 3.8. Chemical structures (left), PL decay (center), and Stern–Volmer plots (right) of delayed fluorescence of PCs quenched by DMAEAc. Generally, PL decay at RT spectra was obtained from the degassed solutions of PCs (1.0×10^{-5} M) in EA, varying the concentration of DMAEAc. In the case of 4-o,p-DCDP-IPN, no change occurred at even high DMAEAc concentrations. Thus, the ET rate constant was not determined.
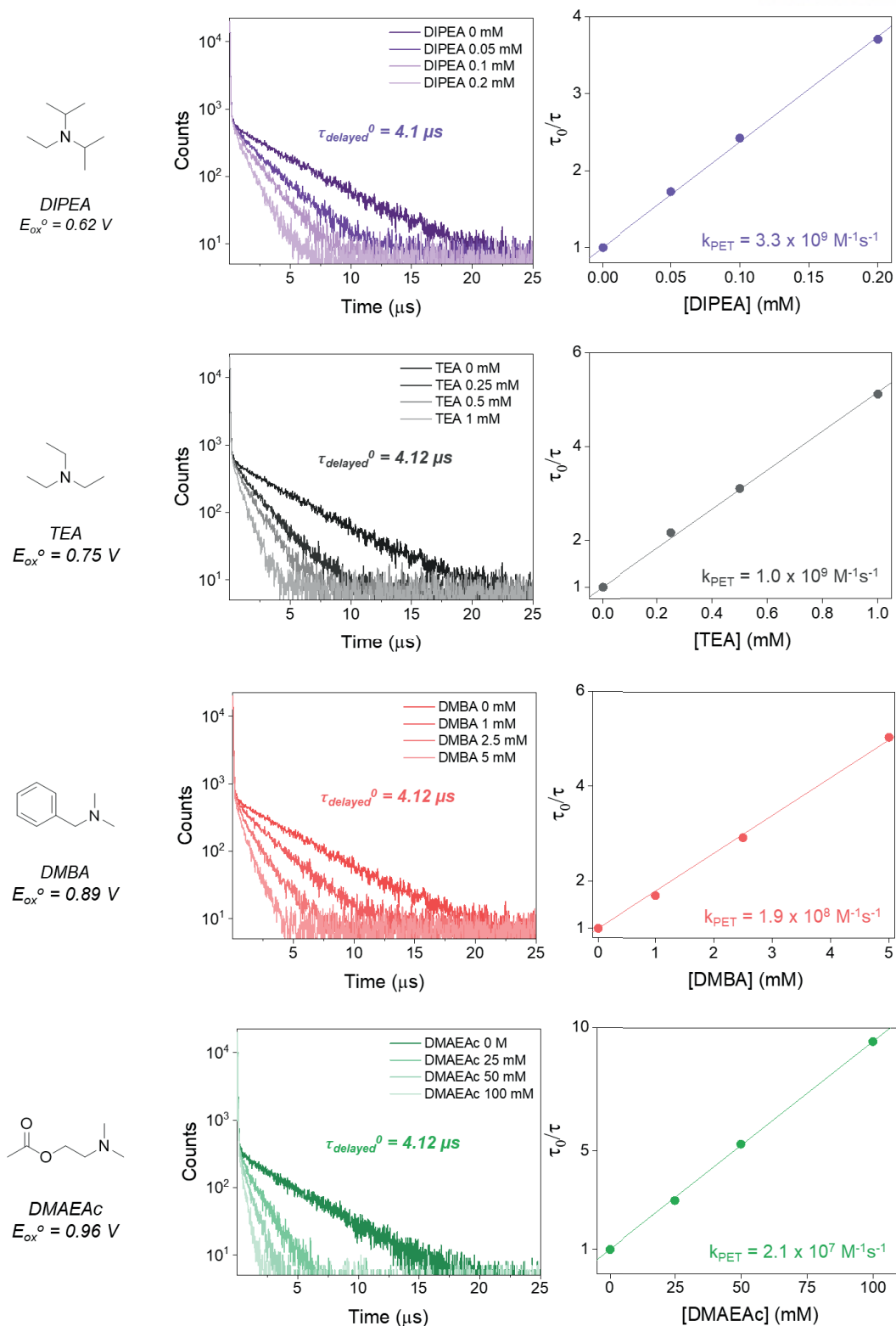
Figure 3.9. Chemical structures (left) of various reductants and PL decay (center) and Stern–Volmer plots (right) of delayed fluorescence of 4Cz-IPN quenched by the various reductants, respectively. Generally, PL decay at RT spectra was obtained from the degassed solutions of 4Cz-IPN (1.0×10^{-5} M) in EA, varying the reductant concentrations.
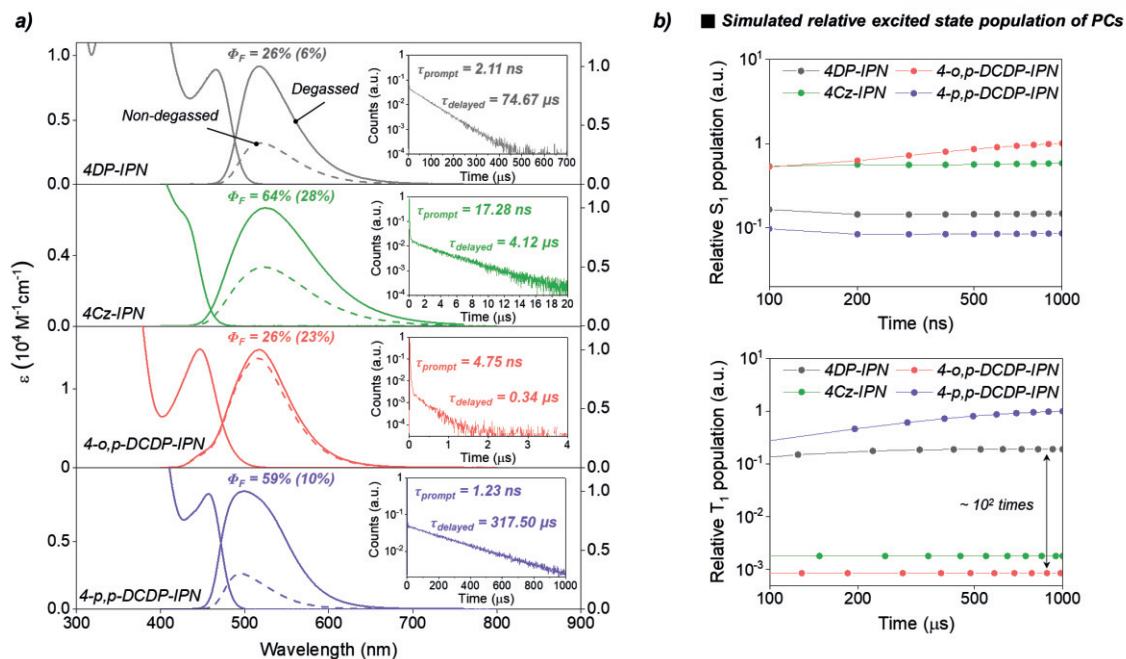
Figure 3.10. (a) UV–Vis absorption and steady-state PL emission spectra of PCs (1.0×10^{-5} M) in EA at RT. The PL decay of prompt and delayed fluorescence of PCs are indicated in the inset. Generally, PL emission spectra were obtained from the degassed solution of PC by purging with N_2 gas for 10 min. The quantum yields of PL (Φ_F) of PCs were determined by relative Φ_F to coumarin 153 (1.0×10^{-5} M) in ethanol solution.[118] The values between parentheses correspond to Φ_F of degassed solutions. (b) Kinetic simulation results for the relatively excited singlet (S_1) (left) and triplet state (T_1) (right) population, referred to as the total concentration, of PCs (6.9×10^{-5} M) under the continuous 455 nm irradiation (see the SI for the more detail).
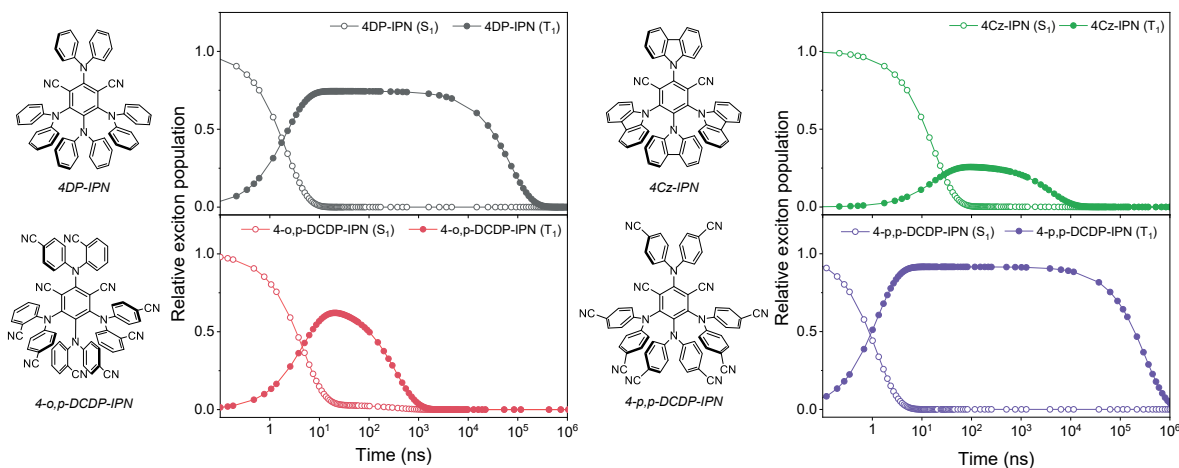
Figure 3.11. Chemical PC structures and their analytical model for exciton dynamics generated by single pulsed 455 nm photoexcitation in EA at RT. The photophysical rate constants were obtained from **Table 3.3**, and extinction coefficients were obtained from UV-Vis absorption spectra in EA at RT.

We attempted to estimate the effective excited-state concentrations of 4Cz-IPN, 4DP-IPN, and 4-o,p-DCDP-IPN because the PET rate is determined by (eq. 4). We used the rate constants obtained from our experiments to model the time-dependent excited-state concentrations of the PCs under 455 nm irradiation (**Figure 3.10(b), Figure 3.11 and Table 3.3**; see **Appendix 4** for the simulation details and the rate equations employed). The relative T_1 concentrations of 4Cz-IPN and 4DP-IPN in the photostationary state were approximately 10 and 100 times greater than those of 4-o,p-DCDP-IPN, respectively. Compared to 4Cz-IPN or 4DP-IPN, 4-o,p-DCDP-IPN showed less success in the generation of long-lived T_1. The findings of these kinetic simulations properly explain the greatest catalytic performance of 4Cz-IPN (i.e., a high excited-state population and moderate k_{PET}).
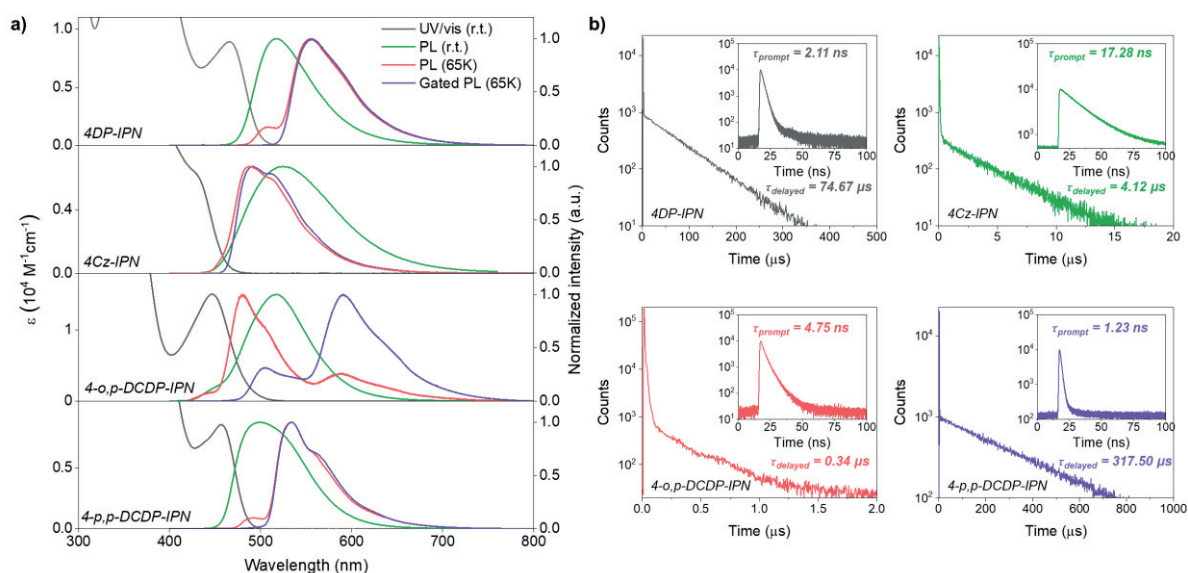
Figure 3.12. Photophysical properties of PCs, including UV–Vis absorption and photoluminescence (PL) emission spectra. (a) UV–Vis absorption (at RT), steady-state PL (at RT), PL (at 65 K), and gated PL (at 65 K) spectra of 4DP-IPN, 4Cz-IPN, 4-o,p-DCDP-IPN, and 4-p,p-DCDP-IPN in EA (1.0×10^{-5} M). (b) PL decay of prompt (inset) and delayed component of 4DP-IPN, 4Cz-IPN, 4-o,p-DCDP-IPN, and 4-p,p-DCDP-IPN in EA (1.0×10^{-5} M). Delayed PL decay spectra were obtained at RT after the degassing process by N_2 gas for 10 min. However, prompt PL decay was obtained without the degassing process.

Table 3.3. Photophysical properties of PCs in EA. The photophysical rate constants were derived by experimental and computational methods in this work, followed by the procedure that our group studied.

4DP-IPN, 4Cz-IPN, 4-o,p-DCDP-IPN, 4-p,p-DCDP-IPN
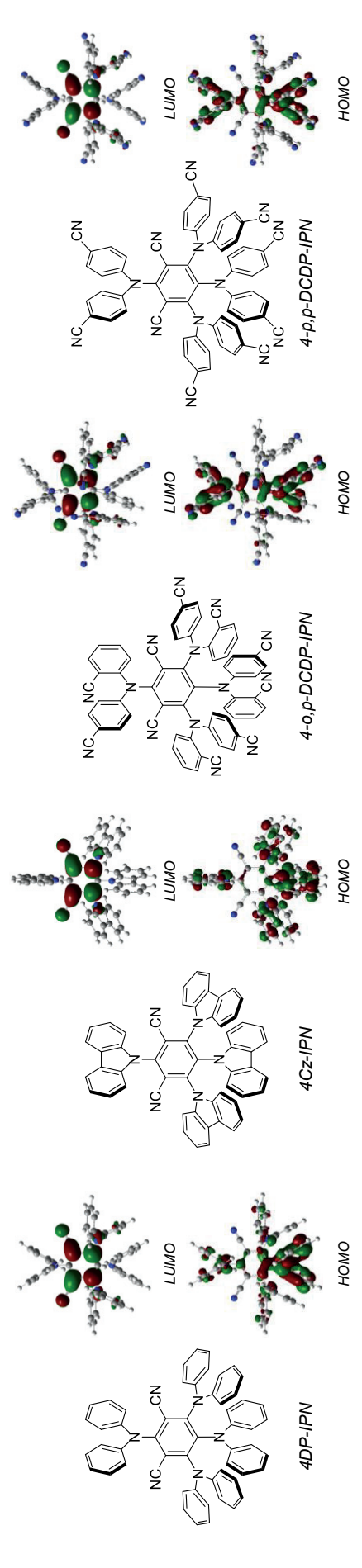
PC	$E_{00}(S_1)$ (eV)[a]	$E_{00}(T_1)$ (eV)[b]	τ_{prompt} (ns)	$\tau_{delayed}$ (µs)	$\lambda_{max,abs}$ (nm)	$\lambda_{max,em}$ (nm)	$f_{S0 \to S1}$ [c]	Φ_F	Φ_{ISC}	$k_{r,S1}$ (10^7 s^{-1})	$k_{nr,S1}$ (10^7 s^{-1})	k_{ISC} (10^8 s^{-1})	$k_{r,T1}$ (s^{-1})	$k_{nr,T1}$ (s^{-1})	k_{RISC} (10^5 s^{-1})
4DP-IPN	2.55	2.38	2.11	74.67	465	518	0.0750	0.26	0.75	3.1	8.9	3.5	—	—	0.55
4Cz-IPN	2.77	2.68	17.28	4.12	422	524	0.0742	0.64	0.26	2.7	1.5	0.15	—	—	3.3
4-o,p-DCDP-IPN	2.94	2.58	4.75	0.34	446	517	0.0425	0.26	0.69	1.7	4.9	1.4	—	—	93
4-p,p-DCDP-IPN	2.63	2.46	1.23	317.50	457	499	0.0873	0.59	0.92	4	2.8	7.4	—	—	0.37

E_{00} were extracted from the [a]onset of PL and [b]onset of gated PL in EA at 65 K, respectively. The onsets were obtained by tangential methods, i.e., tangent intersection, set at the high energy slope of the spectrum, with the x-axis. [c]Oscillator strengths were obtained by the TD-DFT calculation.

The PET from different amine reductants to 4Cz-IPN was observed to determine how the amine-based additive affected the BA/HBA mixture polymerization (**Figure 3.9**). As predicted, the rate constant of PET was measured in a Marcus normal region. DMAEAc showed the slowest PET (k_{PET} = 2.1 × 107 $M^{-1}s^{-1}$ and E_{ox}^{0}(DMAEAc) = 0.96 V), which contrasts the rapid conversion during bulk polymerization. Therefore, we assumed that instead of an initial PET event, the rate-determining step might be the generation of α-amino radical species from the one-electron oxidized amine reductant. We estimated the free energy profiles along the reaction pathway for the generation of the α-amino radicals of DMAEAc and DIPEA to evaluate this notion (**Figure 3.14(a)**, lower part). The mechanistic route with low activation energy (path B) is the one where another amine involves in proton transfer process.[83,85]Additionally, in path B, the activation barrier for the amino radical formation of DMAEAc was significantly lower (10.15 kcal mol^{-1}) than that for the α-amino radical formation of DIPEA (22.49 kcal mol^{-1}), showing that the α-amino radical generation is essential for the whole photomediated polymerization process.

Furthermore, the role of oxygen in bulk polymerization was studied (**Table 3.1 and Table 3.2**). As mentioned above, tertiary amines can change inactive peroxyl radicals into reactive amino radical species, reducing oxygen inhibition in photoinduced free radical polymerizations.[104] Therefore, we calculated the bond dissociation energies (BDEs) for the α-hydrogen of DMAEAc and DIPEA. As shown in **Figure 3.14(b)**, DMAEAc exhibited a BDE of α-hydrogen (85.36 kcal mol^{-1}) higher than DIPEA (86.98 kcal mol^{-1}), which is consistent with the observed oxygen effect. These findings strongly imply that producing amino radical species from peroxyl radicals is necessary to develop oxygen tolerance. Additionally, PCs considerably impact the behavior related to oxygen tolerance. The presence of oxygen significantly reduced the PL lifetimes of PCs (**Figure 3.15**), indicating that electron/energy transfer between $^{3}PC^{*}$ and oxygen, followed by the generation of reactive oxygen species, such as singlet oxygen ($^{1}O_2$) (**Figure 3.16**), superoxide radical anion ($O_2^{\bullet-}$), and hydroperoxyl radical. These reactive oxygen species may react with tertiary amines and cause oxygen-tolerant behavior, maintaining polymerization. For example, the generated superoxide radical anion ($O_2^{\bullet-}$) can accelerate the initiation step by i) facilitating the formation of α-amino radical species,[34] ii) generating reactive radical species such as hydroperoxyl radical (**Figure 3.5**).[119] Our DFT simulations revealed the viability of this strategy. However, its intricacy makes it quite challenging to fully comprehend this behavior. Hence, further investigation is being conducted.
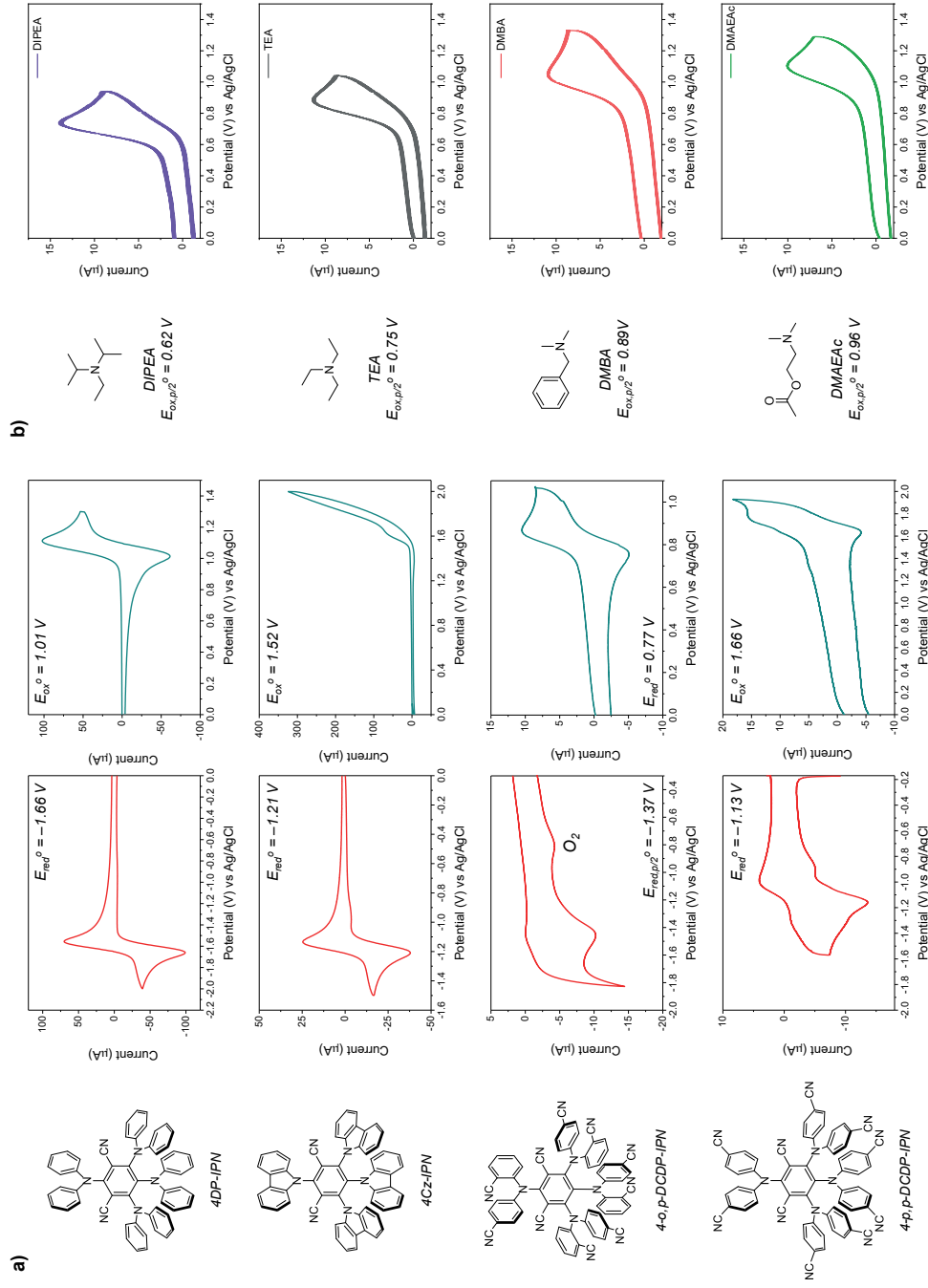
Figure 3.13. Chemical structures (left) and CV spectra (right) of (a) PCs and (b) reductants studied in this work. CV spectra were obtained in CH₃CN (2.0 × 10⁻⁴ M) (1.0 × 10⁻³ M for 4-o,p-DCDP-IPN) at RT after the degassing process by argon for 15 min. The potentials were evaluated for the reversible CV cycle as their half-potentials ($E_{1/2}^0$). However, for the irreversible CV cycle, the potentials were obtained from their half-peak potentials ($E_{p/2}^0$).[86]

69

Figure 3.14. (a) Proposed mechanistic pathway for the formation of α-amino radical from radical cation of tertiary amines (upper part) and the DFT calculation results for energy profiles of each pathway (lower part). (b) Proposed mechanistic pathway for the oxygen tolerance of bulk polymerization in the presence of tertiary amines and the bond dissociation energy (BDE) of α-C–H of DMAEAc and DIPEA.

70
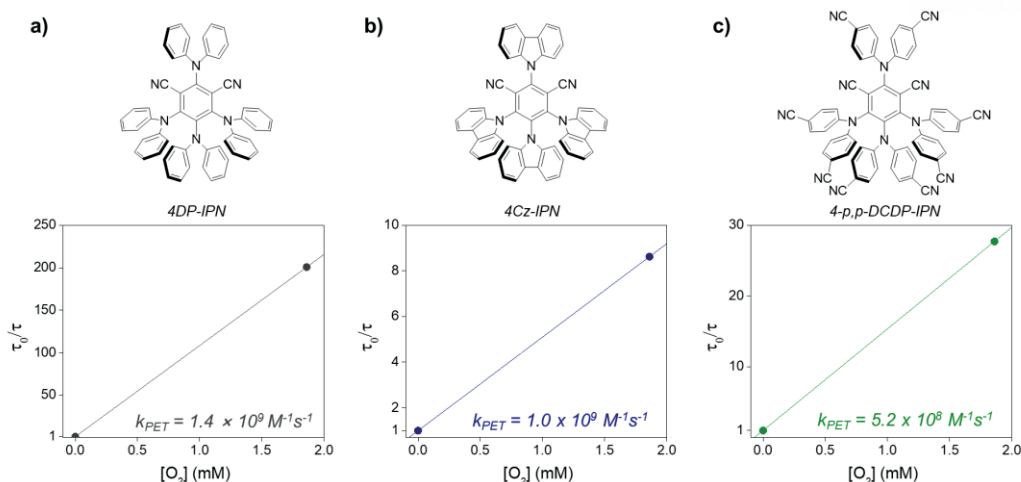
Figure 3.15. Chemical structures and Stern–Volmer plots of delayed fluorescence of (a) 4DP-IPN, (b) 4Cz-IPN, and (c) 4-p,p-DCDP-IPN quenched by air, respectively. Generally, PL decay at RT spectra was obtained from the degassed and non-degassed solutions of PCs (1.0×10^{-5} M) in EA. 4-o,p-DCDP-IPN was excluded because of its weak delayed fluorescence. The oxygen concentration in EA at air saturation was referred to in the literature.
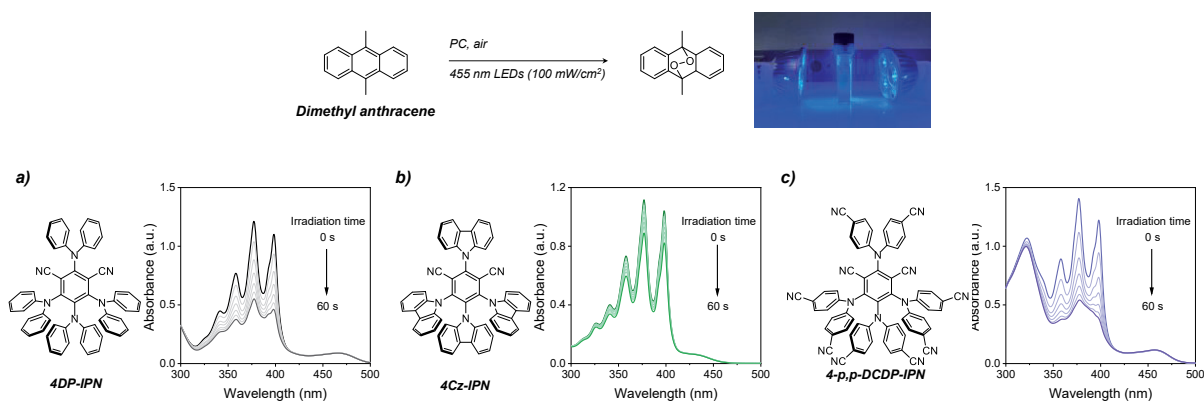
Figure 3.16. Investigation of singlet oxygen formation by PCs. Experiments were performed with dimethyl anthracene (1.0×10^{-4} M) in EA in the presence of (a) 4DP-IPN (1.0×10^{-5} M), (b) 4Cz-IPN (1.0×10^{-5} M), and (c) 4-p,p-DCDP-IPN (1.0×10^{-5} M) under the illumination of blue LED (6 W 455 nm, 100 mW/cm^2, 0–60 s) without any degassing process.

3.3.4 Synthesis of UV-Blocking PSA

Finally, using the ideal ratio of PC and reductants, namely, 4Cz-IPN and the mixture of DMAEAc/DMAEA, we investigated the visible-light-curing of the prepolymer mixtures of the BA and HBA to prepare acrylic PSA films. The optimization description and mechanical properties of the PSA film were fully described in the publications.[62] Notably, because PC is recycled throughout the catalytic cycle in the prepolymer preparation, our PC system does not require additional PC, unlike the traditional UV-curing procedure which requires extra photoinitiators. Moreover, a crosslinker for film curing, such as poly(ethylene glycol) diacrylate, was not used in this procedure. Alternatively, DMAEA was used as a part of a "hybrid reductant," giving sufficient crosslinking degree because DMAEA has a similar chemical structure with DMAEAc. As it is expected to have similar chemical/electrical properties to DMAEAc, and DMAEA was composed of 40% or 60% of the total reductants.

Film curing rates were best at 10 ppm of 4Cz-IPN and 5,000 ppm of DMAEAc, similar to the bulk polymerization process, and 91.6% conversion was attained in 3 min under 455 nm LED irradiation. Subsequently, two UV absorbers were added to the optimal prepolymer for the target PSA to achieve the desired UV-blocking capabilities. Among the different types of UV absorbers,[120] we used a cyanoacrylate-based UV absorber (i.e., UV absorber 1, 2) with excellent compatibility with the acrylic monomers. We successfully produced the desired PSA film under blue light LED irradiation (452 nm). The produced UV-blocking PSA had an outstanding transmission in the visible light region ($T_{452\,nm}$ ~ 100%) while effectively blocking the UV light ($T_{373\,nm}$ = 1.2%, **Figure 3.17(b)**).
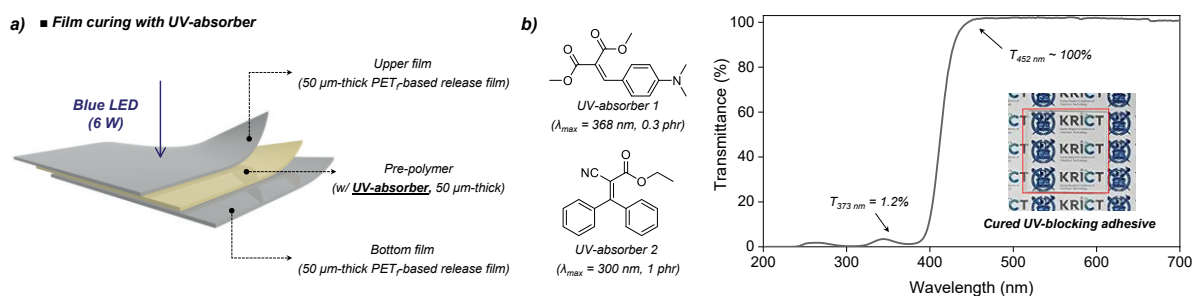
Figure 3.17. (a) Scheme for film curing step of UV-blocking PSA. (b) Chemical structures of UV-absorbers used in this work and UV–Vis absorption spectra of cured UV-blocking PSA.

Subsequently, we performed dynamic folding experiments to determine whether our UV-blocking PSA samples were appropriate for a foldable display (**Figure 3.18**). The structure of the folding test specimen was designed with reference to the actual foldable smartphone (**Figure 3.18(d)**).[102] The curvature radius and the folding cycle were fixed at 1.5 mm and 0.5 Hz, respectively. Tests were performed under three conditions to emulate the actual usage environment of a foldable smartphone: room temperature (25°C for 200,000 cycles), low temperature (−20°C for 30,000 cycles), and high

temperature with high humidity (60°C and 93% humidity for 50,000 cycles). Interestingly, our UV-blocking PSA samples with 60% DMAEA showed exceptional folding endurance under all conditions, almost meeting the requirements for foldable displays. Nevertheless, we produced a UV-blocking PSA that performed incredibly well using only a minimal monomer composition and no functional additions, such as those that increase flexibility. A more complicated composition with functional additives and monomers may be used in the future to produce excellent UV-blocking PSA.
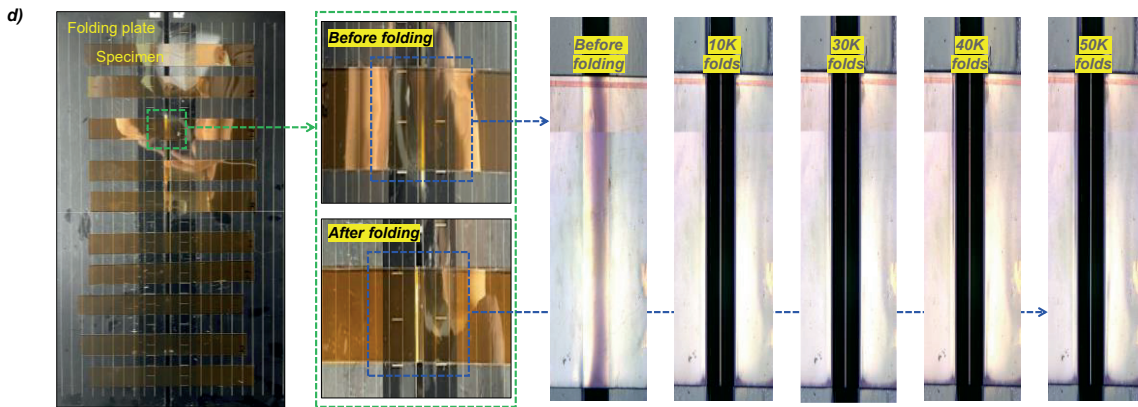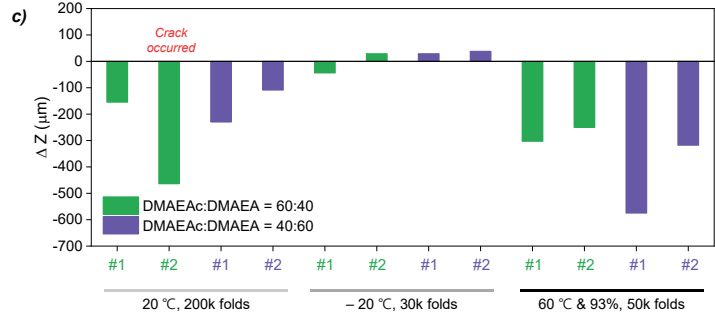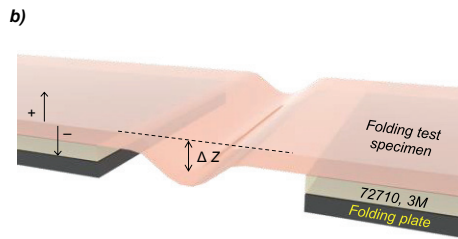
Figure 3.18. (a) Procedure of dynamic folding test and (b) quantitative evaluation of folding durability. (c) Dynamic folding test results of UV-blocking PSA samples. (d) Photos of mounted test specimens (left) and images of the folded region according to folding cycles (right).

3.4 Conclusion

To produce UV-blocking optically transparent adhesives for foldable displays, we designed and validated a revolutionary and highly efficient visible-light-curing resin system. The development of the UV-blocking PSA film worked best with the mixture of 4Cz-IPN and DMAEAc after assessing various PCs and reductants with different attributes. This mixture had a fast PET rate resulting from the good generation of T_1 excited states and appropriate redox potentials, efficient generation of α-amino radical species, and sufficient solubility in acrylic monomers to achieve the best curing performance with high oxygen tolerance. After determining the ideal ratio between PC (i.e., 10 ppm) and reductant (i.e., 5000 ppm), we used a mixed reductant system (i.e., hybrid reductants) to precisely regulate the crosslinking degree. The reductant comprised DMAEAc and DMAEA, and the PSA with 40% or 60% DMAEA had an appropriate degree of crosslinking and adequate mechanical properties. Finally, we produced a PSA blocking the UV light less than 400 nm by adding UV absorbers to the PSA composition we refined. After dynamic folding testing at several temperatures (25°C, −20°C, and 60°C with 93% humidity), the UV-blocking PSA containing 60% DMAEA demonstrated good folding endurance without any faults, practically meeting the requirements for commercial foldable displays. Accordingly, UV-blocking PSA was effectively created from two acrylic monomers using three additives (PC, reductant, and UV absorber). However, more functional additives might be used to expand utilization scope of PSA. Furthermore, the production of UV-blocking PSA is only one application for the suggested visible-light-curing technique. Other systems can also be developed using our system, such as optically transparent resins, dental resins, and 3D and 4D printed materials.

Chapter 4. Conclusions of Dissertation

In this dissertation, the design strategies for highly efficient visible-light-driven photoredox catalysis were studied. After screening various cyanoarenes, one of the purely organic TADF compounds, such as PC, the origin of the efficient formation of the PC radical anion was revealed: i) capacity to efficiently populate the PC in the T_1 excited state and ii) adequately positive excited reduction potentials. Furthermore, we observed the photodegradation behavior of cyanoarene-based PCs and noticed that photodegradation is essentially mediated by the $PC^{\bullet-}$ formation, and the photodegrade adduct depends on the electronic and structural PC properties. For more details about the formation and degradation of $PC^{\bullet-}$ in actual photoredox catalysis, we conducted a reductive dehalogenation reaction of aryl halides as a model and revealed that the photodegradation behavior of PCs depends on the rate of ET process to different target substrates. Based on this understanding of the formation and degradation of PCs, using PC with highly negative $E_{red}^0(PC)$, 4DP-IPN, highly effective reductive dehalogenation of aryl/alkyl halides was realized at extremely low PC loadings as small as 0.001 mol%. Subsequently, to demonstrate our visible-light-driven system, we applied our strategies for the well-formation of $PC^{\bullet-}$ to the production of UV-blocking, optically transparent adhesives for foldable displays. The UV-blocking PSA cannot be prepared under UV-light irradiation. However, visible-light-irradiation is an optimal solution to synthesize the adhesive combined with excellent oxygen tolerance. From the mechanistic studies on acrylic bulk polymerization, we observed that PC with an efficient generation of T_1 excited states and appropriate redox potentials is required to successfully prepare PSA. Furthermore, inadequate sacrificial reductants are essential to efficiently generate initiating species, α-amino radical species. This indicate that the rate-determining step for polymerization is the generation of α-amino radical species, not the rate of the initial PET process. After optimizing the PSA preparation for an appropriate degree of crosslinking and mechanical properties, we finally produced a UV-light blocking PSA combined with adding UV-absorbers to the PSA composition. Notably, our UV-blocking PSA synthetic system comprises only three components (PC, sacrificial reductant, and UV-absorber). Furthermore, dynamic folding testing of the optimized PSA was performed at several temperatures (25°C, −20°C, and 60°C with 93% humidity), meeting practical requirements for commercial foldable displays.

This dissertation mainly studied the reductive quenching cycle of PC, mediated by the PC radical anion, and our findings have opened the door to a thorough comprehension of the reductive cycles in purely organic visible-light-driven photoredox catalysis. We hope that our study will improve the knowledge about i) the formation and degradation behavior of $PC^{\bullet-}$ and ii) the oxidized sacrificial reductant species generated after the PET process to address several difficult problems in a range of photoredox-mediated organic reactions and polymerizations.

75

Appendix 1. Syntheses of cyanoarene-based PCs
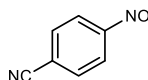
4-nitrosobenzonitrile: A solution of 4-aminobenzonitrile (2.0 g, 16.9 mmol), potassium peroxymonosulfate (20.8 g, 33.86 mmol) in CH_2Cl_2 (56 mL) and water (200 mL) was rigorously stirred for 3 hours under ambient conditions. After 3 hours, the organic layers were extracted by 1 M HCl aqueous solution (50 mL), neutralized by saturated $NaHCO_3$ aqueous solution (60 mL) and washed by brine 3 times. Subsequently, the organic layers were dried over $NaSO_4$ and concentrated under reduced pressure. The collected crude product was a gray greenish solid and used for next synthesis of **4-monocyanodiphenylamine** without further purification. Data were in full agreement with those reported in literature.[121] ^{1}H NMR (400 MHz, $CDCl_3$): δ 7.97 (br s, 4H).
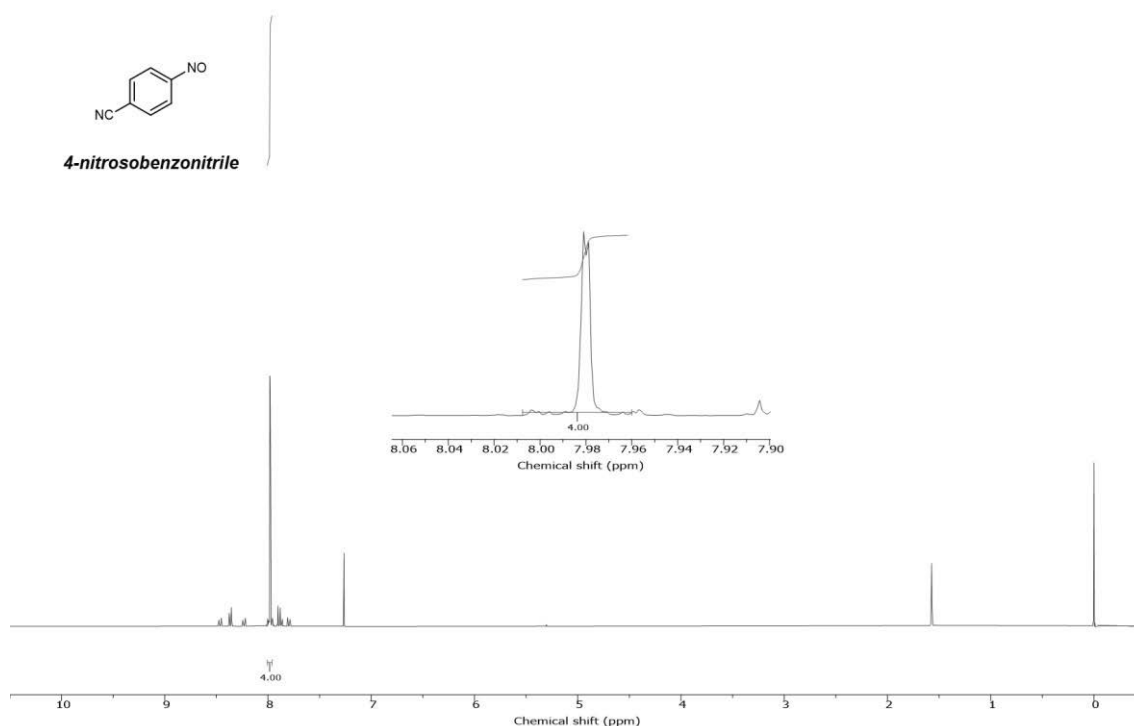
Figure A1.1 ^{1}H NMR data of 4-nitrosobenzonitrile at RT (400 MHz, $CDCl_3$).
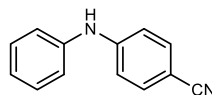
4-monocyanodiphenylamine: For the synthesis, a procedure using metal-free Chan-Evans-Lam coupling was followed.[122] A solution of **4-nitrosobenzonitrile** (1.0 g, 7.57 mmol), phenylboronic acid (1.38 g, 11.4 mmol) and triethyl phosphite (1.51 g, 9.10 mmol) in anhydrous THF (20 mL) was stirred for 1 hour under ambient conditions. After 1 hour, the reaction mixture was filtered through a small plug of silica (EA:hexanes, 1:9 v/v). After the filtration, the mixture was further purified by column chromatography on silica gel with gradient CH_2Cl_2/hexanes mixtures to give pure product as yellow solid. Data were in full agreement with those reported in literature.[123] ^1H NMR (400 MHz, $CDCl_3$): δ 7.4 –7.42 (m, 2H), 7.39–7.30 (m, 2H), 7.20–7.13 (m, 2H), 7.13–7.08 (m, 1H), 6.99–6.93 (m, 2H), 6.24 (s, 1H).
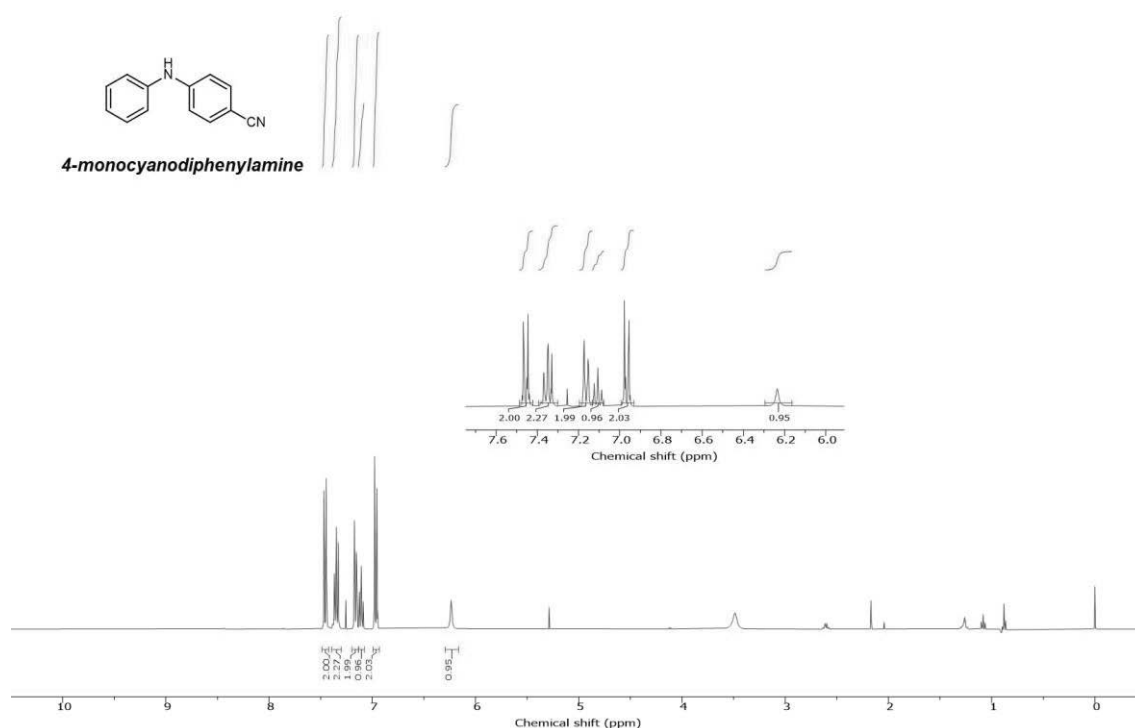
Figure A1.2 ^1H NMR data of 2,4′-dicyanodiphenylamine at RT (400 MHz, $CDCl_3$).
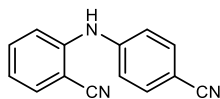
2,4'-dicyanodiphenylamine: A solution of potassium tert-butoxide (1.39 g, 12.39 mmol), 2-aminobenzonitrile (1.17 g, 9.91 mmol) in anhydrous DMSO (15 mL) was stirred for 1 hour at RT under a N_2 atmosphere. After 1 hour, 4-fluorobenzonitrile (1.2 g, 16.5 mmol) dissolved in DMSO (5 mL) was slowly added to the reaction mixture and stirred further at RT for 24 hours. Afterwards, distilled water was poured into the reaction mixture to quench the excess potassium tert-butoxide and to precipitate the crude product, which was further purified by reprecipitation in MeOH/water to give pure product as pale red solid (0.98 g, 45%). Data were in full agreement with those reported in literature.[124] ^{1}H NMR (400 MHz, CDCl$_3$): δ 7.60 (dd, 3H), 7.55–7.48 (m, 1H), 7.42 (dd, 1H), 7.20–7.14 (m, 2H), 7.08 (td, 1H), 6.57 (s, 1H).
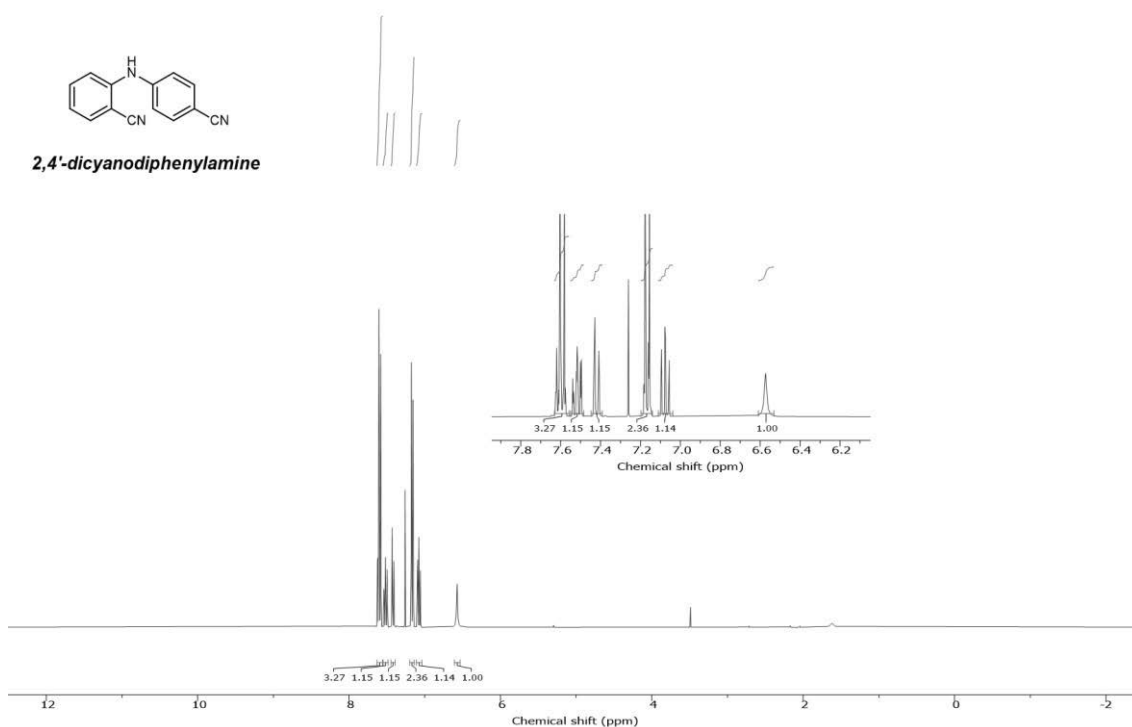
Figure A1.3 ^{1}H NMR data of 2,4′-dicyanodiphenylamine at RT (400 MHz, CDCl$_3$).
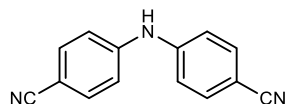
4,4′-dicyanodiphenylamine: A solution of potassium tert-butoxide (2.22 g, 19.8 mmol), 4-aminobenzonitrile (1.95 g, 16.5 mmol) in anhydrous DMSO (30 mL) was stirred for 1 hour at RT under N_2 atmosphere. After 1 hour, 4-fluorobenzonitrile (2.0 g, 16.5 mmol) dissolved in DMSO (10 mL) was slowly added to the reaction mixture and stirred further at RT overnight. Afterwards, distilled water was poured into the reaction mixture to quench the excess potassium tert-butoxide and to precipitate the crude product, which was further purified by reprecipitation in MeOH/water to give pure product as pale red solid (1.74 g, 48%). Data were in full agreement with those reported in literature.[125] ^{1}H NMR (400 MHz, CDCl$_3$): δ 7.62–7.57 (dt, 4H), 7.18–7.15 (dt, 4H), 6.38–7.15 (s, 1H).
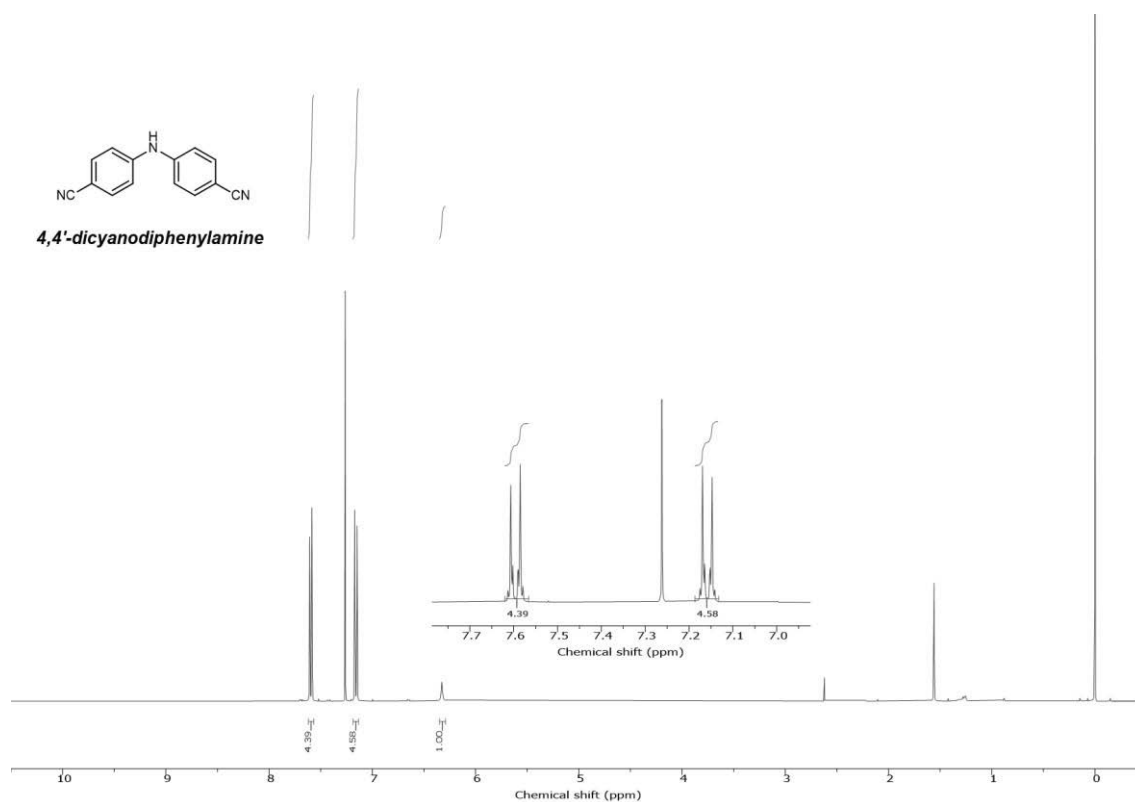
Figure A1.4 ^{1}H NMR data of 4,4′-dicyanodiphenylamine at RT (400 MHz, CDCl$_3$).
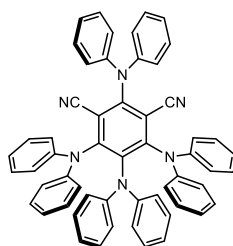
4DP-IPN: A solution of NaH (60% in mineral oil, 0.477g, 11.94 mmol) and diphenylamine (1.48 g, 8.75 mmol) in anhydrous DMAc (5 mL) was stirred for 30 min in ice bath under N_2 atmosphere. After 30 min, 2,4,5,6-tetrafluoroisophthalonitrile (0.4 g, 1.99 mmol) dissolved in DMAc (5 mL) was slowly added to the reaction mixture and stirred further at 100 °C for 10 h. Afterwards, distilled water (2 mL) was poured into the reaction mixture to quench the excess NaH and, methanol was added to precipitate the crude product, which was further purified by column chromatography on silica gel (CH_2Cl_2:hexanes, 2:3 v/v) to give pure product as yellow solid (1.32 g, 83%). Data were in full agreement with those reported in literature.[11] ^{1}H NMR (400 MHz, DMSO-D_6): δ 7.31 7.21 (m, 8H), 7.10–7.05 (t, 8H), 7.03–6.97 (t. 2H), 6.91–6.75 (m, 16H), 6.68–6.62 (m, 6H).
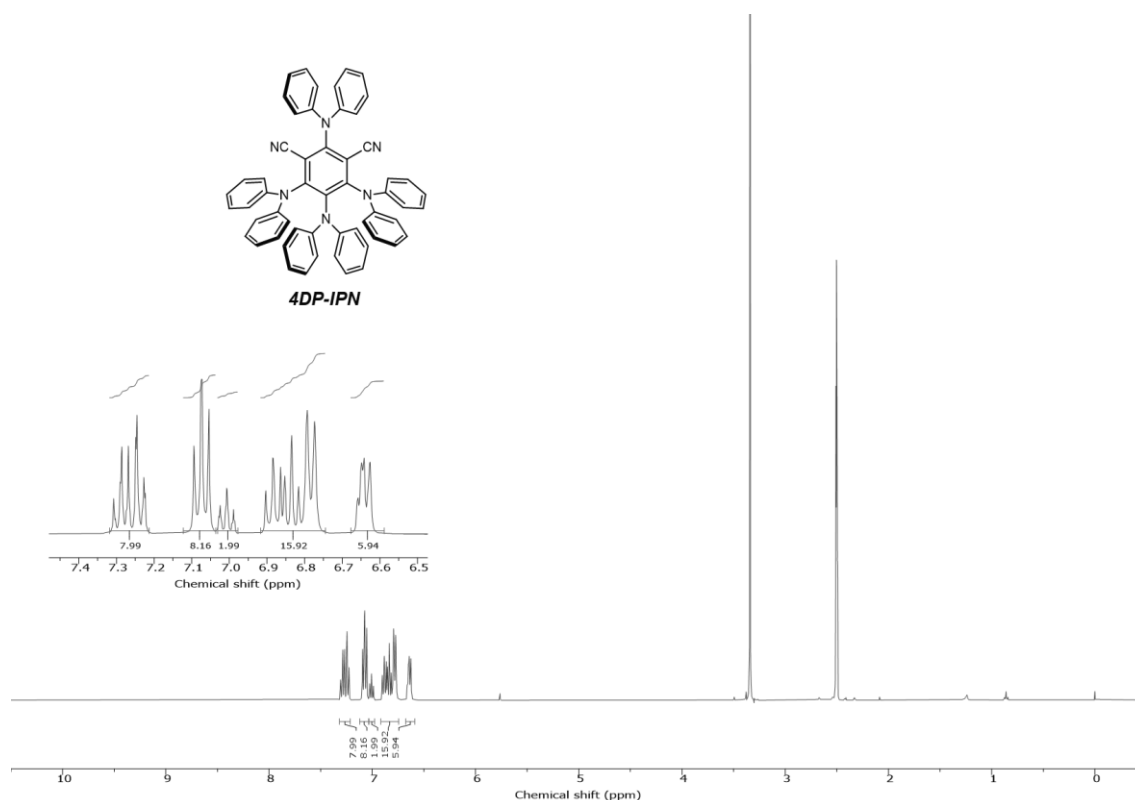
Figure A1.5. ^{1}H NMR data of 4DP-IPN at RT (400 MHz, DMSO-d_6).
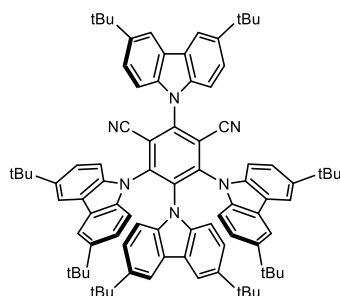
4tCz-IPN: A solution of *t*-BuOK (0.193 g, 1.72 mmol) and 3,6-di-tert-butyl-9H-carbazole (0.400 g, 1.43 mmol) in anhydrous THF (40 mL) was stirred for 30 min in ice bath under N_2 atmosphere. After, 2,4,5,6-tetrafluoroisophthalonitrile (0.057 g, 0.28 mmol) was slowly added to the reaction mixture and stirred further for 12 h. After completion of the reaction, distilled water (2 mL) was poured into the reaction mixture to quench the excess NaH. The resulting solution was concentrated under reduced pressure followed by washing several times with water and ethanol to yield the crude product, which was purified by column chromatography on silica gel (CH_2Cl_2:hexanes, 2:1 v/v) to give pure product (0.160 g, 45%). Data were in full agreement with those reported in literature.[1] ^{1}H NMR (400 MHz, $CDCl_3$): δ 8.21 (d, 2H), 7.74 (dd, 2H), 7.61–7.59 (m, 6H), 7.18 (d, 2H), 7.05–7.00 (m, 8H), 6.51 (dd, 2H), 6.44 (d, 2H), 1.53 (s, 18H), 1.30 (s, 36H), 1.22 (s, 18H).
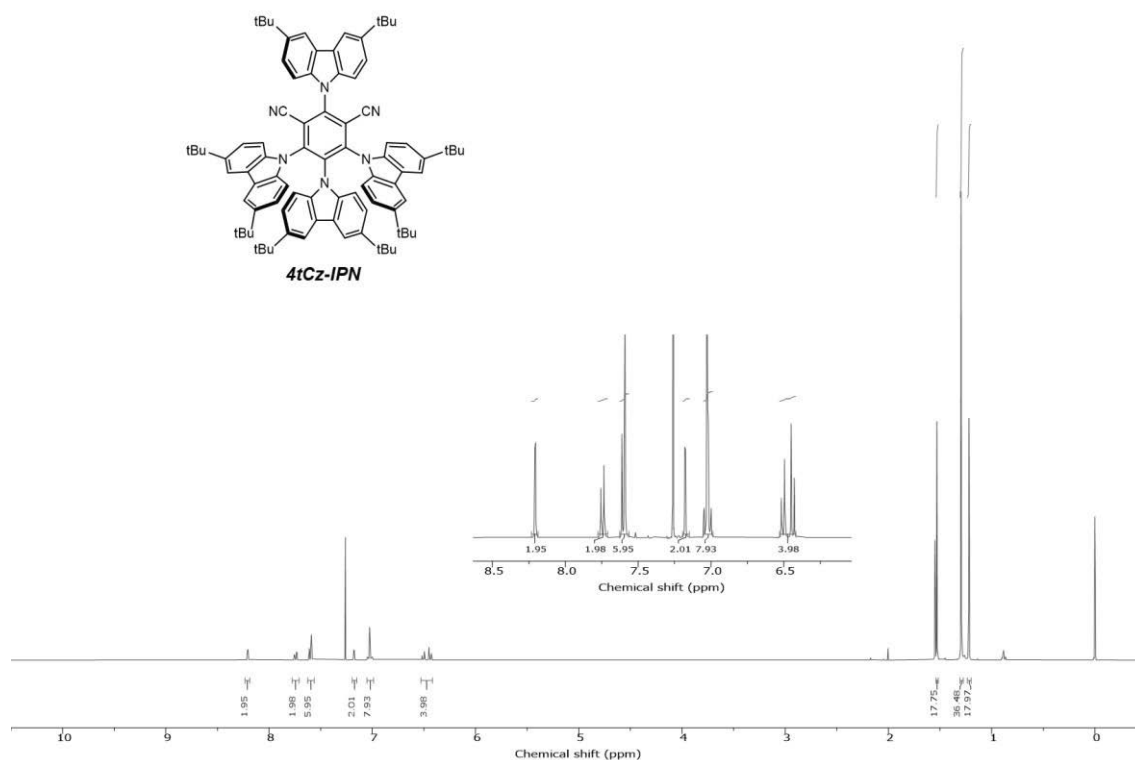
Figure A1.6 ^{1}H NMR data of 4tCz-IPN at RT (400 MHz, $CDCl_3$).
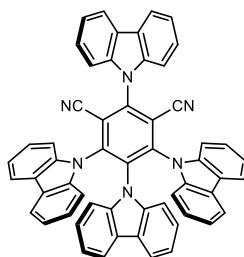
4Cz-IPN: A solution of NaH (60% in mineral oil, 0.738 g, 18.45 mmol) and carbazole (2.16 g, 12.30 mmol) in anhydrous THF (40 mL) was stirred for 30 min in ice bath under N_2 atmosphere. After, 2,4,5,6-tetrafluoroisophthalonitrile (0.5 g, 2.46 mmol) was slowly added to the reaction mixture and stirred further for 12 h. After completion of the reaction, distilled water (2 mL) was poured into the reaction mixture to quench the excess NaH. The resulting solution was concentrated under reduced pressure followed by washing several times with water and ethanol to yield the crude product, which was purified by column chromatography on silica gel (CH_2Cl_2:hexanes, 2:1 v/v) to give pure product (1.48 g, 93%) Data were in full agreement with those reported in literature.[1,126,127] ^{1}H NMR (400 MHz, CDCl3): δ 8.22 (dt, 2H), 7.74–7.67 (m, 8H), 7.49 (ddd, 2H), 7.33 (dt, 2H), 7.23–7.21 (m, 4H), 7.12–7.05 (m, 8H), 6.82 (td, 4H), 6.63 (ddd, 2H).
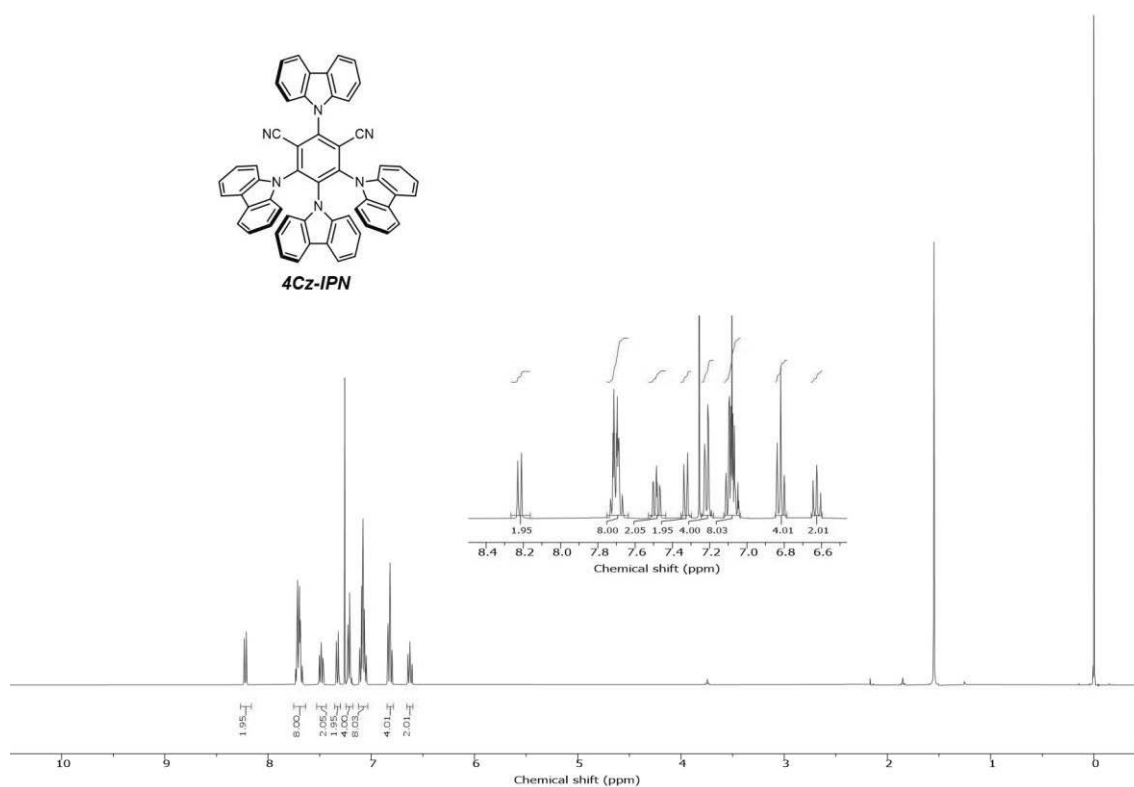
Figure A1.7 ^{1}H NMR data of 4Cz-IPN at RT (400 MHz, CDCl$_3$).
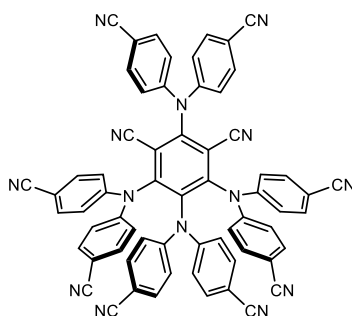
4-p,p-DCDP-IPN: A solution of NaH (60% in mineral oil, 0.120 g, 3 mmol) and **4,4′-dicyanodiphenylamine** (0.548 g, 2.5 mmol) in anhydrous DMAc (5 mL) was stirred for 30 min in ice bath under N_2 atmosphere. After 30 min, 2,4,5,6-tetrafluoroisophthalonitrile (0.1 g, 0.5 mmol) dissolved in DMAc (5 mL) was slowly added to the reaction mixture and stirred further at 60 ℃ for 12 h. Afterwards, distilled water (2 mL) was poured into the reaction mixture to quench the excess NaH and, methanol was added to precipitate the crude product, which was further purified by reprecipitation in CH2Cl2//EA to give pure product as yellow solid (0.140 g, 28%). ^{1}H NMR (400 MHz, acetone-d_6): δ 7.87–7.81 (d, 4H), 7.70–7.62 (d, 8H), 7.55–7.48 (td. 8H), 7.20–7.15 (d, 8H), 7.10–7.03 (d, 4H). MS (GC-FAB-HRMS): calculated for $C_{64}H_{33}N_{14}$ [M+H]$^+$: 997.3013; found as 997.3005.
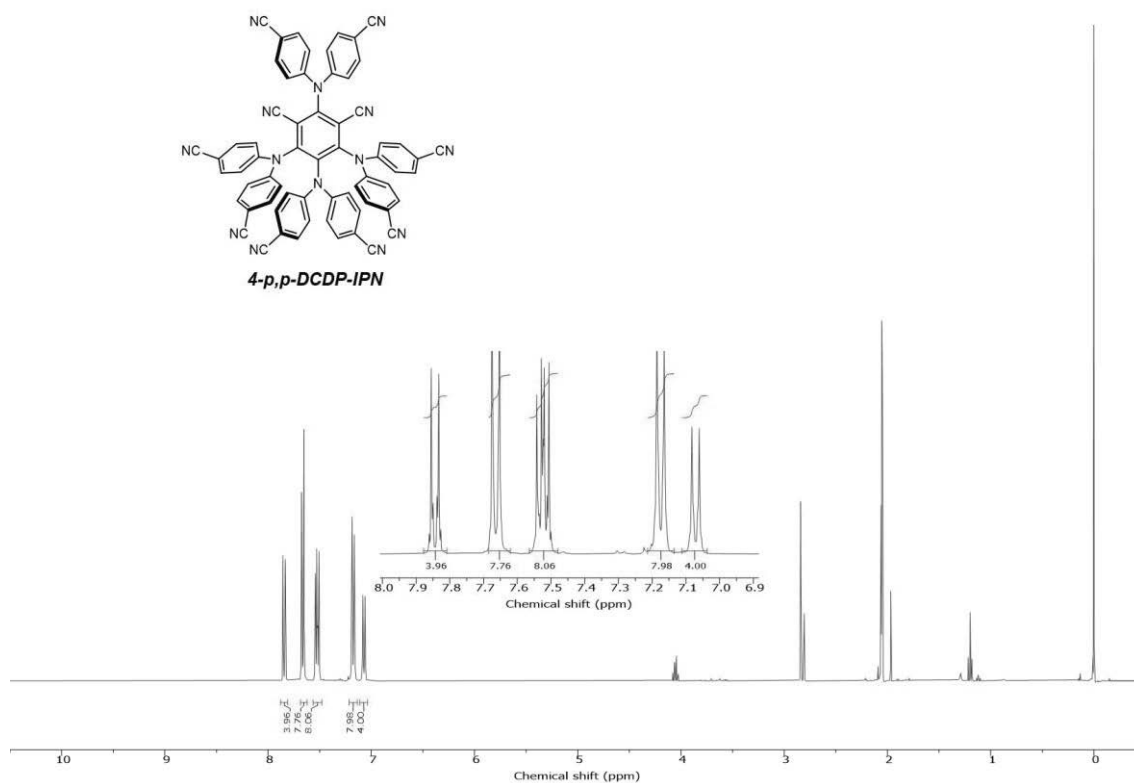
Figure A1.8 ^{1}H NMR data of 4-p,p-DCDP-IPN at RT (400 MHz, acetone-d_6).
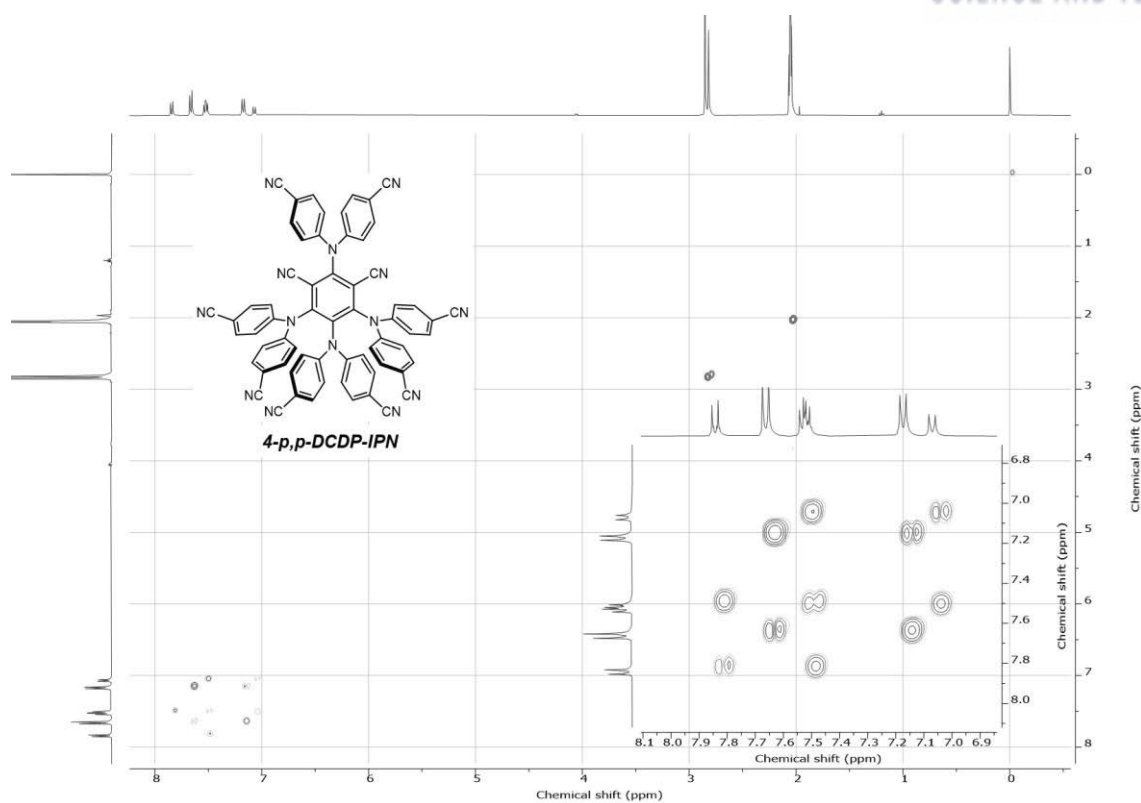
Figure A1.9 COSY NMR data of 4-p,p-DCDP-IPN at RT (400 MHz, acetone-d_6).
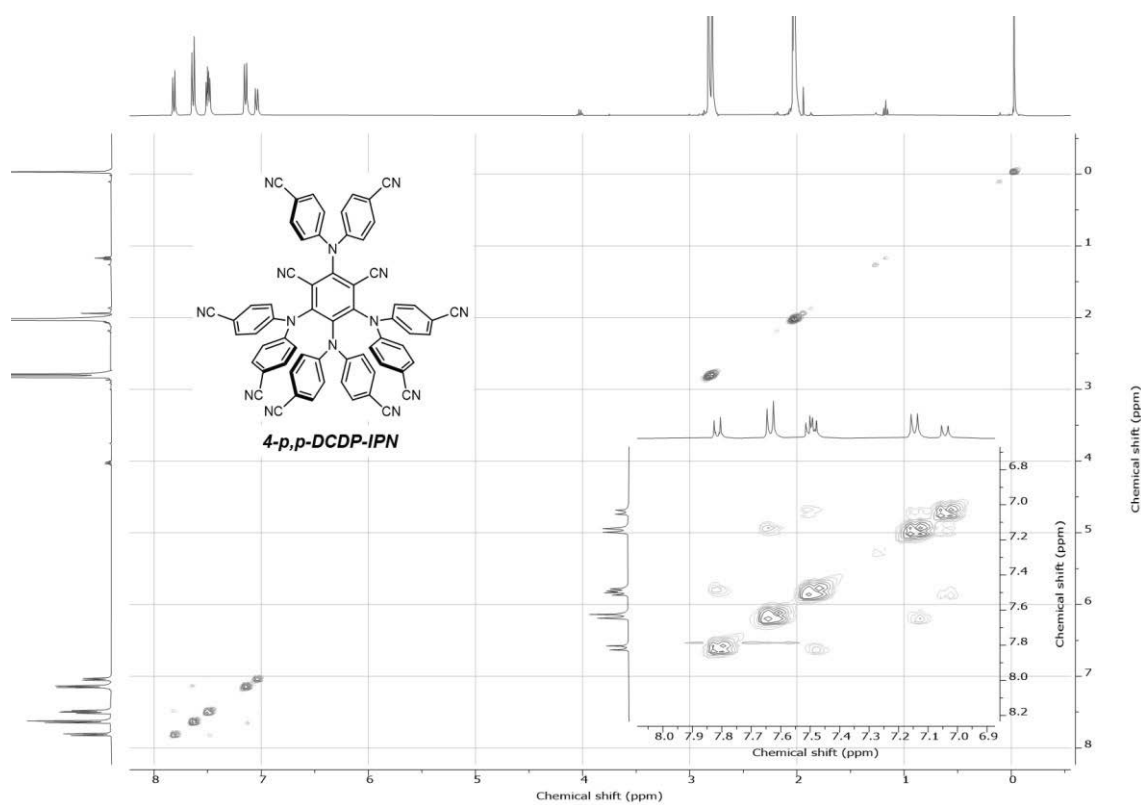
Figure A1.10. NOESY NMR data of 4-p,p-DCDP-IPN at RT (400 MHz, acetone-d_6).
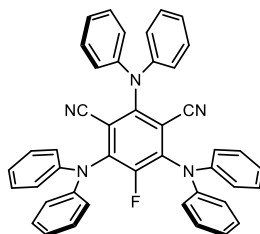
3DP-F-IPN: A procedure similar to the synthesis of **4Cz-IPN** is followed. A solution of potassium tert-butoxide (2.424 g, 21.6 mmol), diphenylamine (3.03 g, 18.0 mmol) in anhydrous DMAc (20 mL) was stirred for 2 hours in ice bath under N_2 atmosphere. After 2 hours, 2,4,5,6-tetrafluoroisophthalonitrile (1.2 g, 6.0 mmol) dissolved in DMAc (5 mL) was slowly added to the reaction mixture and stirred further at RT for 48 hours. Afterwards, distilled water (2 mL) was poured into the reaction mixture to quench the excess potassium tert-butoxide and, methanol was added to precipitate the crude product, which was further purified by recrystallization in $CHCl_3$/MeOH to give pure product as yellow solid (1.02 g, 26%). Data were in full agreement with those reported in literature.[128] ^{1}H NMR (400 MHz, $CDCl_3$): δ 7.29–7.22 (m, 12H), 7.09–7.02 (m, 6H), 7.02–6.95 (m, 12H).
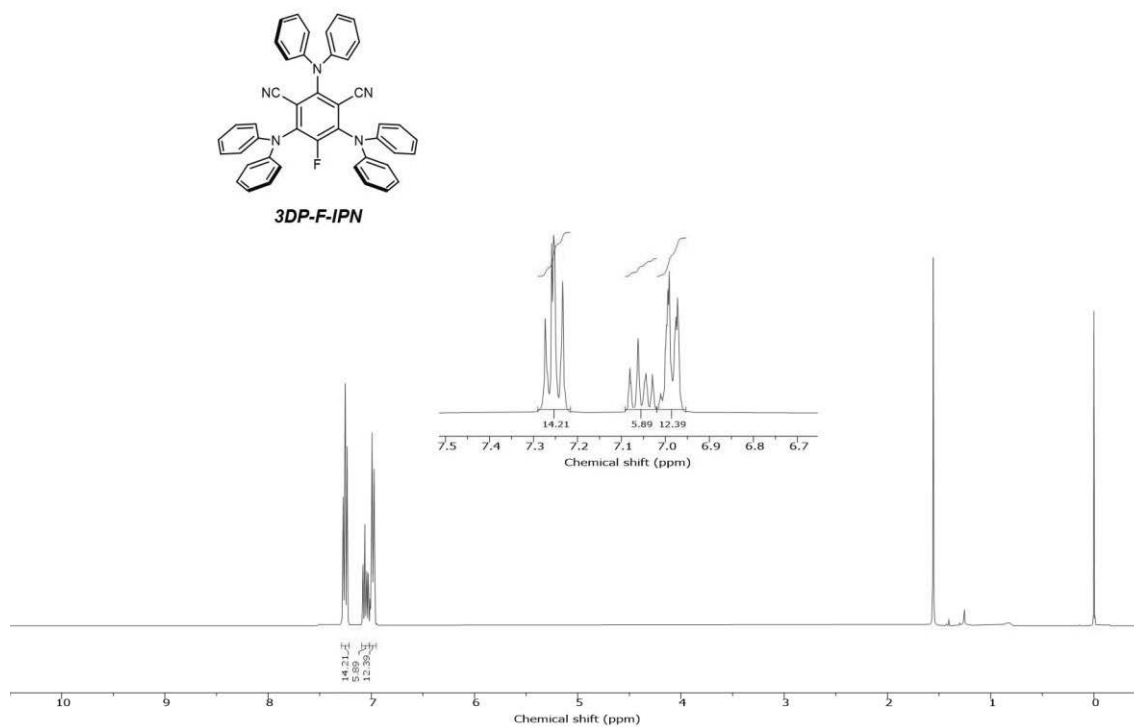
Figure A1.11 ^{1}H NMR data of 3DP-F-IPN at RT (400 MHz, $CDCl_3$).
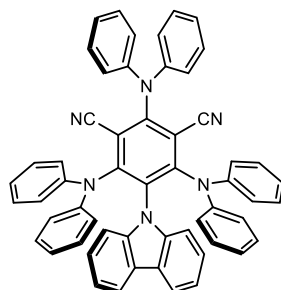
3DP-Cz-IPN: A solution of potassium tert-butoxide (0.124 g, 1.10 mmol), carbazole (0.154 g, 0.927 mmol) in anhydrous DMAc (5 mL) was stirred for 1 hour in ice bath under N_2 atmosphere. After 1 hour, **3DP-F-IPN** (0.5 g, 0.772 mmol) dissolved in DMAc (5 mL) was slowly added to the reaction mixture and stirred further at 70 °C for 6 hours. Afterwards, distilled water (2 mL) was poured into the reaction mixture to quench the excess potassium tert-butoxide and, methanol was added to precipitate the crude product, which was further purified by column chromatography on silica gel with gradient CH_2Cl_2/hexanes mixtures to give pure product as yellow solid. ^{1}H NMR (400 MHz, $CDCl_3$): δ 7.55–7.50 (d, 2H), 7.40–7.35 (t, 4H), 7.20–7.15 (d, 4H), 7.14–7.08 (t, 2H), 7.07–7.03 (t, 2H), 6.98– 6.88 (dt, 4H), 6.80–6.71 (t, 8H), 6.65–6.58 (t, 4H), 6.48–6.40 (t, 8H). MS (GC-FAB-HRMS): calculated for $C_{56}H_{39}N_6$ [M+H]$^+$: 795.3236; found as 795.3231.
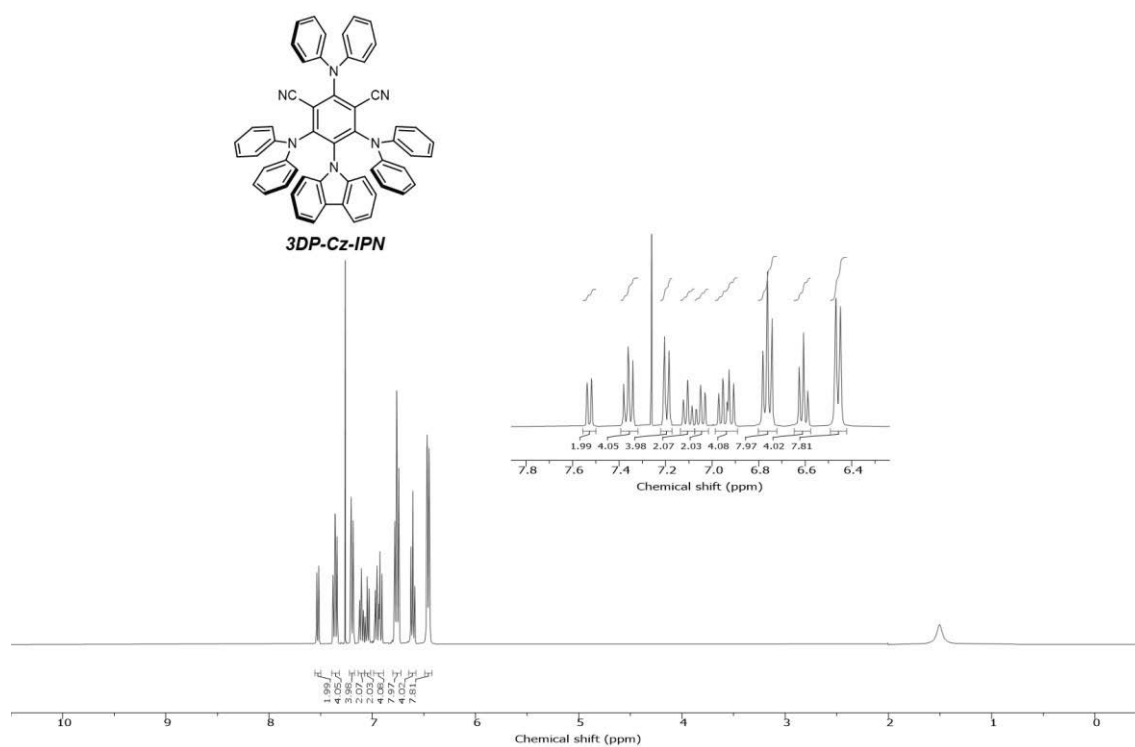
Figure A1.12 ^{1}H NMR data of 3DP-Cz-IPN at RT (400 MHz, $CDCl_3$).
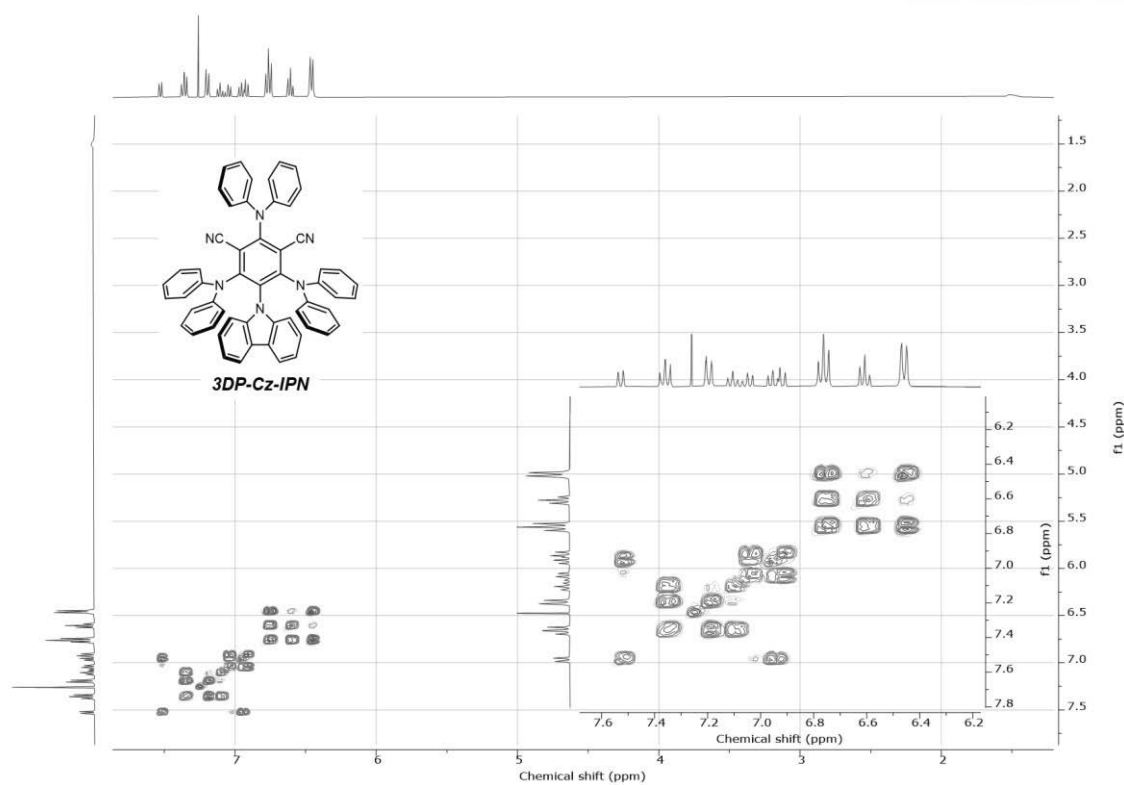
Figure A1.13 COSY NMR data of 3DP-Cz-IPN at RT (400 MHz, CDCl$_3$).
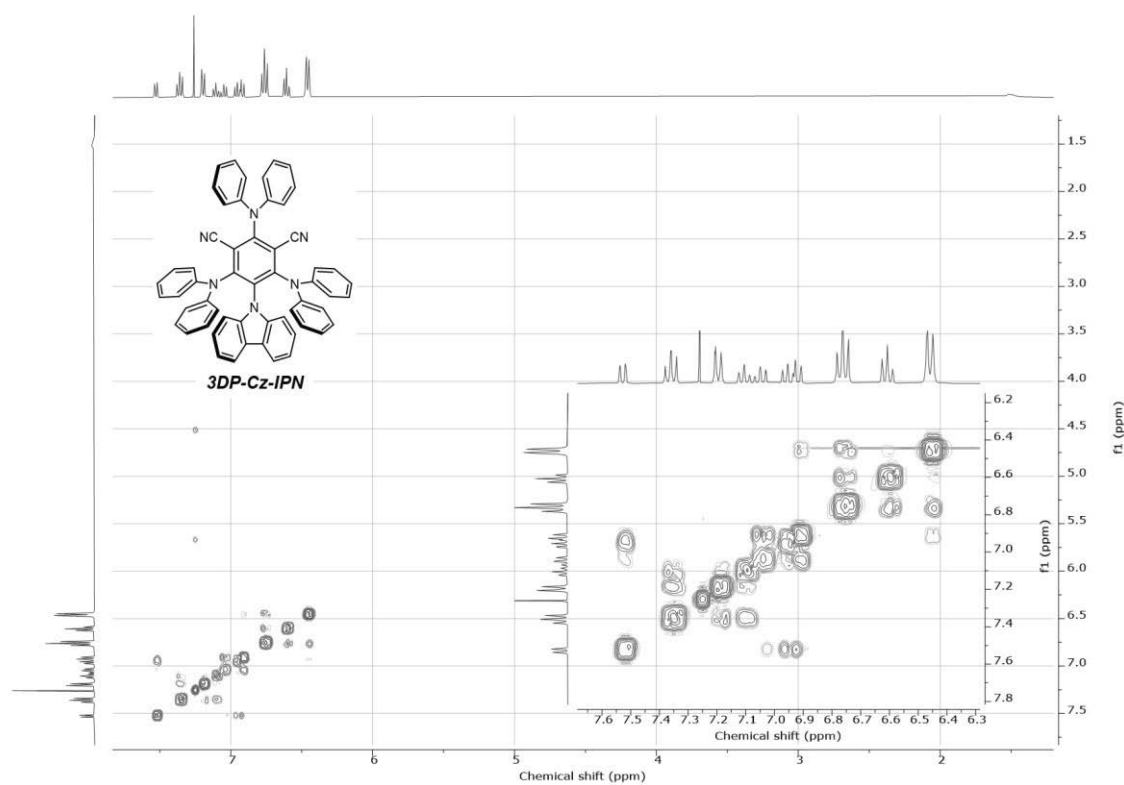
Figure A1.14 NOESY NMR data of 3DP-Cz-IPN at RT (400 MHz, CDCl$_3$).
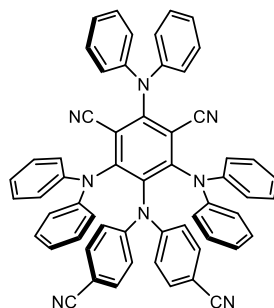
3DP-DCDP-IPN: A solution of sodium hydride (0.060 g, 1.50 mmol) and **4,4′-dicyanodiphenylamine** (0.202 g, 0.922 mmol) in anhydrous DMF/DMSO (3/7) (10 mL) was stirred for 1 hour in ice bath under N_2 atmosphere. After 1 hour, **3DP-F-IPN** (0.5 g, 0.772 mmol) was slowly added to the reaction mixture and stirred further at 120 °C for 17 hours. Afterwards, distilled water (2 mL) was poured into the reaction mixture to quench the excess NaH and, methanol was added to precipitate the crude product, which was further purified by column chromatography on silica gel with gradient CH_2Cl_2/hexanes mixtures to give pure product as yellow solid (0.117 g, 18%). ^1H NMR (400 MHz, DMSO-d_6): δ 7.40–7.35 (d, 4H), 7.30–7.25 (d, 8H), 7.13–7.07 (t, 8H), 7.05–7.00 (q, 2H), 6.90–6.75 (m, 16H). MS (GC-FAB-HRMS): calculated for $C_{58}H_{39}N_8$ [M+H]$^+$: 847.3298; found as 847.3290.
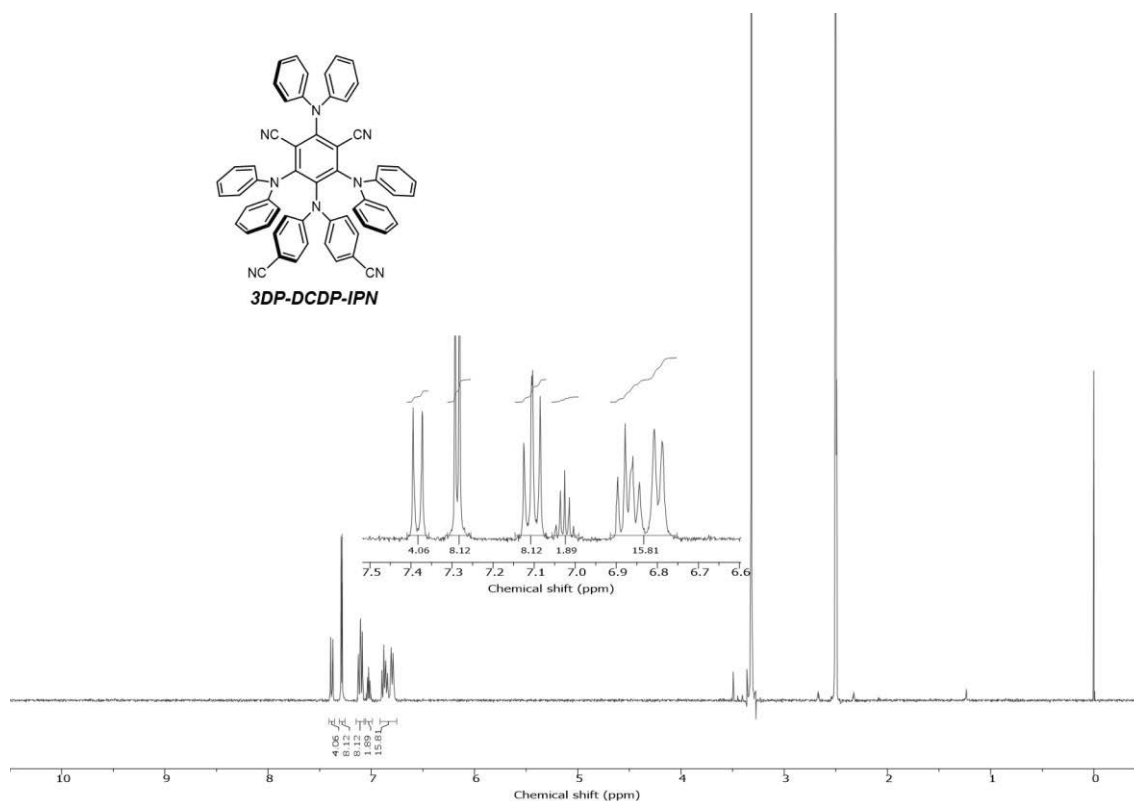
Figure A1.15 ^1H NMR data of 3DP-DCDP-IPN at RT (400 MHz, DMSO-d_6).
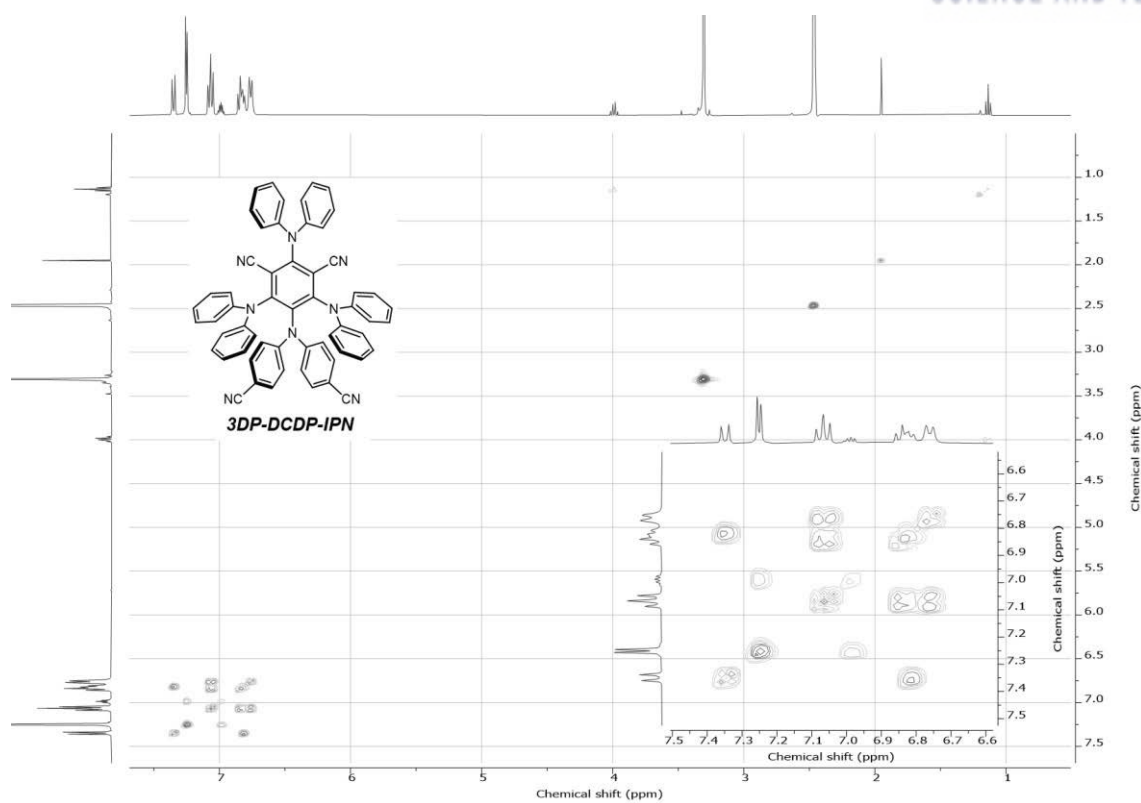
Figure A1.16 COSY NMR data of 3DP-DCDP-IPN at RT (400 MHz, DMSO-d$_6$).
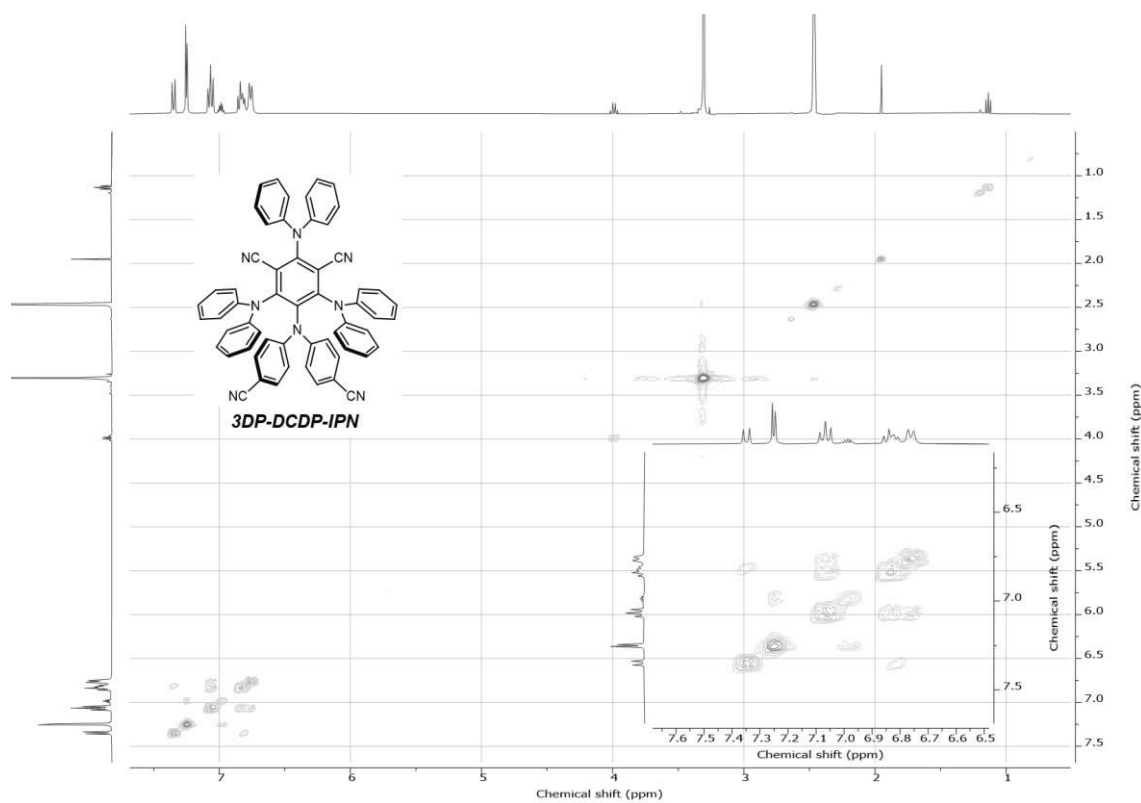
Figure A1.17 NOESY NMR data of 3DP-DCDP-IPN at RT (400 MHz, DMSO-d$_6$).
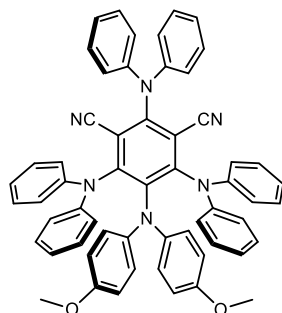
3DP-DMDP-IPN: A solution of sodium hydride (0.037 g, 0.926 mmol) and 4,4'-dimethoxydiphenylamine (0.127 g, 0.556 mmol) in anhydrous DMF/DMSO (3/7) (10 mL) was stirred for 0.5 h in ice bath under N_2 atmosphere. After 1 hour, 3DP-F-IPN (0.3 g, 0.463 mmol) was slowly added to the reaction mixture and stirred further at 120 °C for 16 hours. Afterwards, distilled water (2 mL) was poured into the reaction mixture to quench the excess sodium hydride and methanol was added to precipitate the crude product, which was further purified by column chromatography on silica gel with gradient CH_2Cl_2/hexanes mixtures to give the pure product as reddish orange powder. ^{1}H NMR (400 MHz, CDCl$_3$): δ 7.25 (d, 4H), 7.07 (m, 12H), 7.00 (t, 2H), 6.87 (t, 4H), 6.70 (d, 8H), 6.46–6.38 (m, 8H), 3.60 (s, 6H). MS (GC-FAB-HRMS): calculated for $C_{58}H_{45}N_6O_2$ [M+H]$^+$: 857.3604; found as 857.3602.
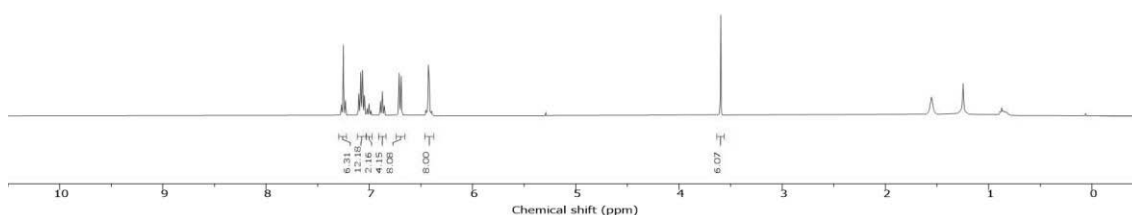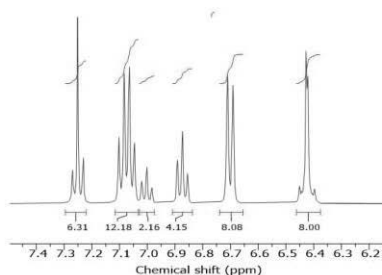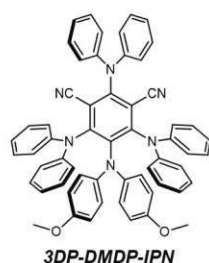
Figure A1.18 ^{1}H NMR data of 3DP-DMDP-IPN at RT (400 MHz, DMSO-d$_6$).

90
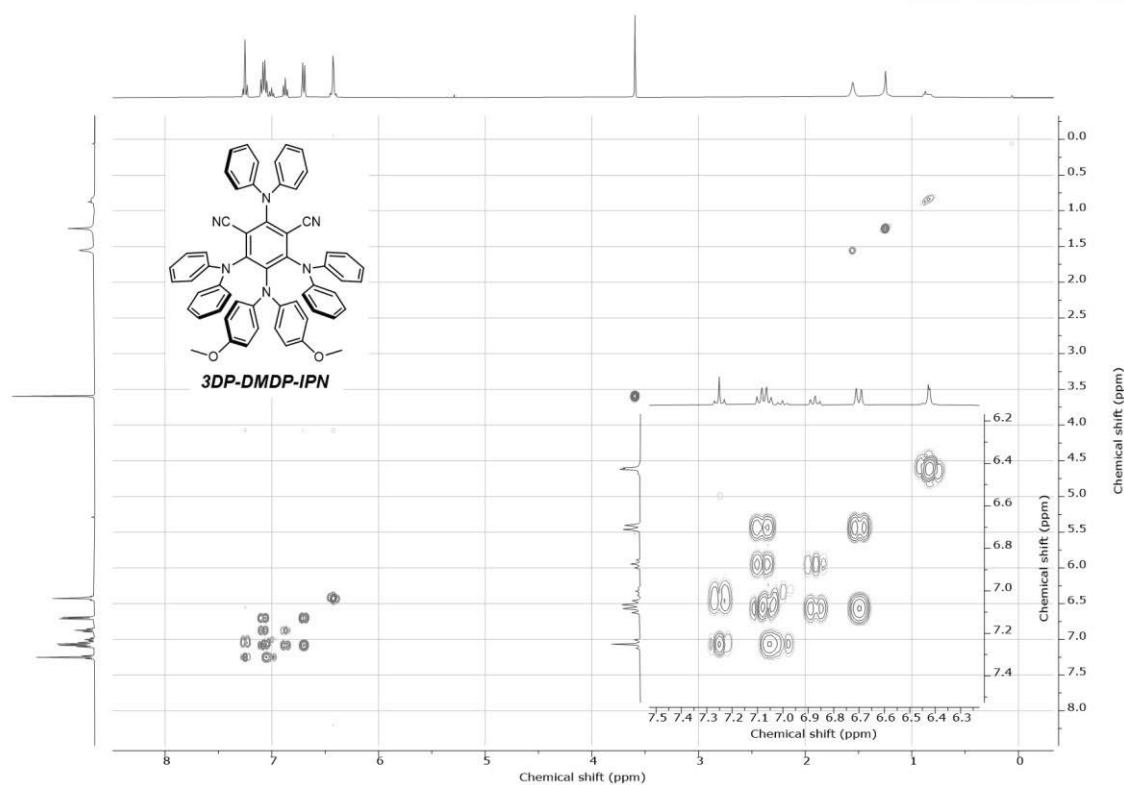
Figure A1.19 COSY NMR data of 3DP-DMDP-IPN at RT (400 MHz, DMSO-d$_6$).
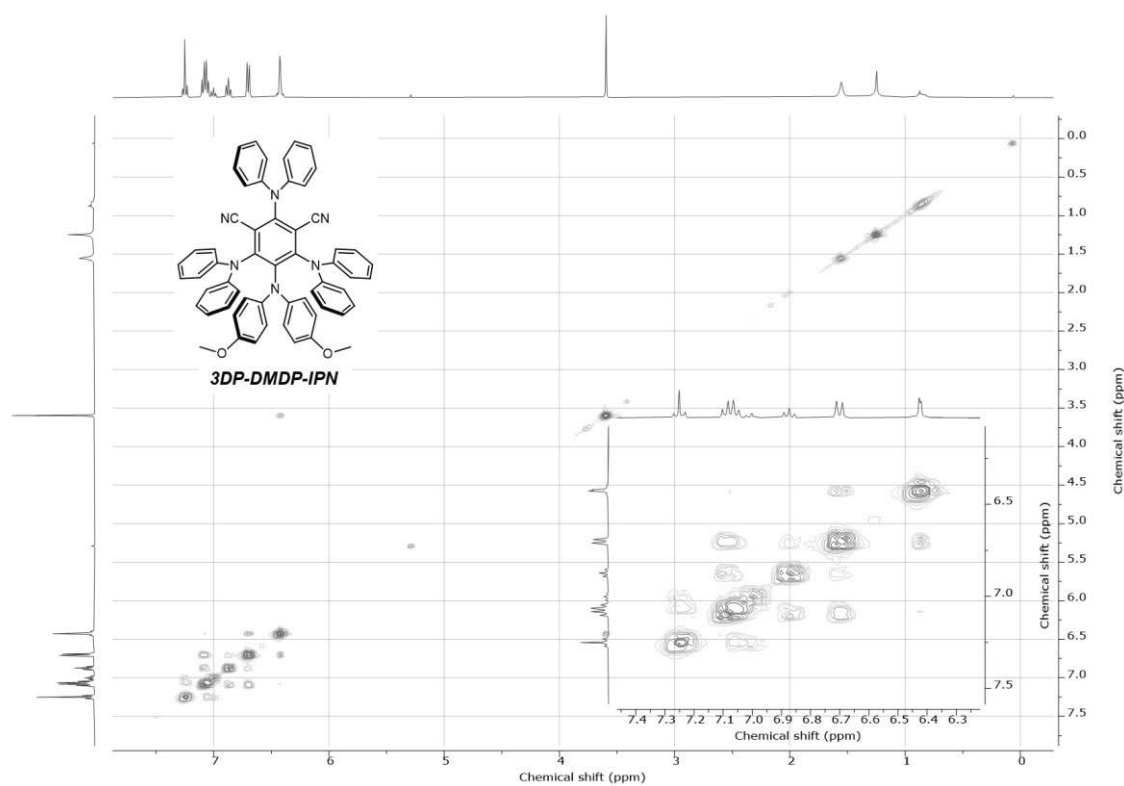
Figure A1.20 NOESY NMR data of 3DP-DMDP-IPN at RT (400 MHz, DMSO-d$_6$).
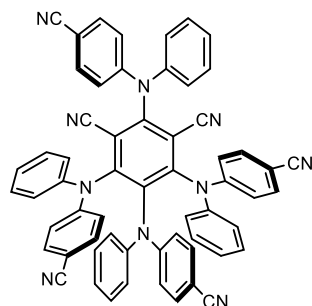
4-p-MCDP-IPN: A solution of potassium tert-butoxide (0.741 g, 6.6 mmol), **4-cyanodiphenylamine** (0.855 g, 4.4 mmol) in anhydrous DMSO (5 mL) was stirred for 1 hour in ice bath under N_2 atmosphere. After 1 hour, 2,4,5,6-tetrafluoroisophthalonitrile (0.2 g, 1.0 mmol) dissolved in DMSO (5 mL) was slowly added to the reaction mixture and stirred further at 60 ℃ overnight. Afterwards, distilled water (2 mL) was poured into the reaction mixture to quench the excess potassium tert-butoxide and, methanol was added to precipitate the crude product, which was further purified by washing with CH_2Cl_2 to give pure product as yellow solid. ^{1}H NMR (400 MHz, acetone-d_6): δ 7.64–7.57 (m, 8H), 7.39 (dd, 8H), 7.34–7.24 (m, 8H), 7.24–7.09 (m, 12H). MS (MALDI-TOF-LRMS): calculated for $C_{60}H_{36}N_{10}$ [M+H]$^+$: 897.3203; found as 897.9657. MS (GC-FAB-HRMS): not found.
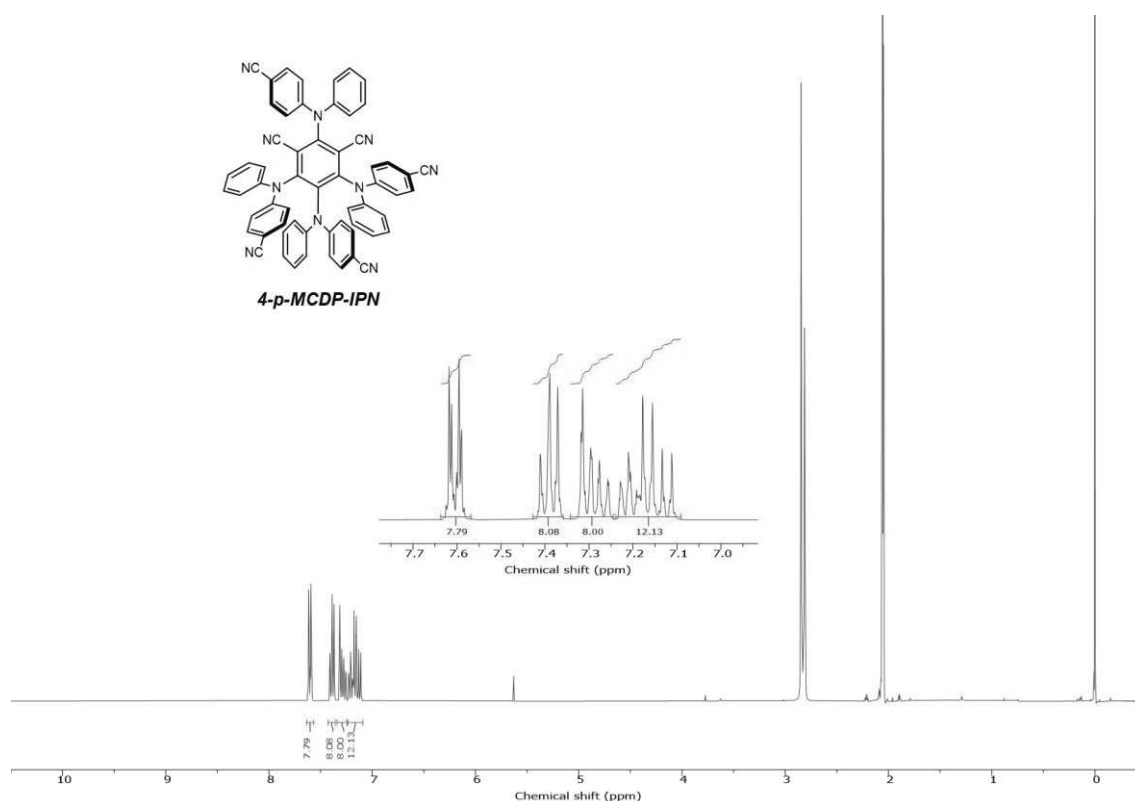
Figure A1.21 ^{1}H NMR data of 4-p-MCDP-IPN at RT (400 MHz, acetone-d_6).

92
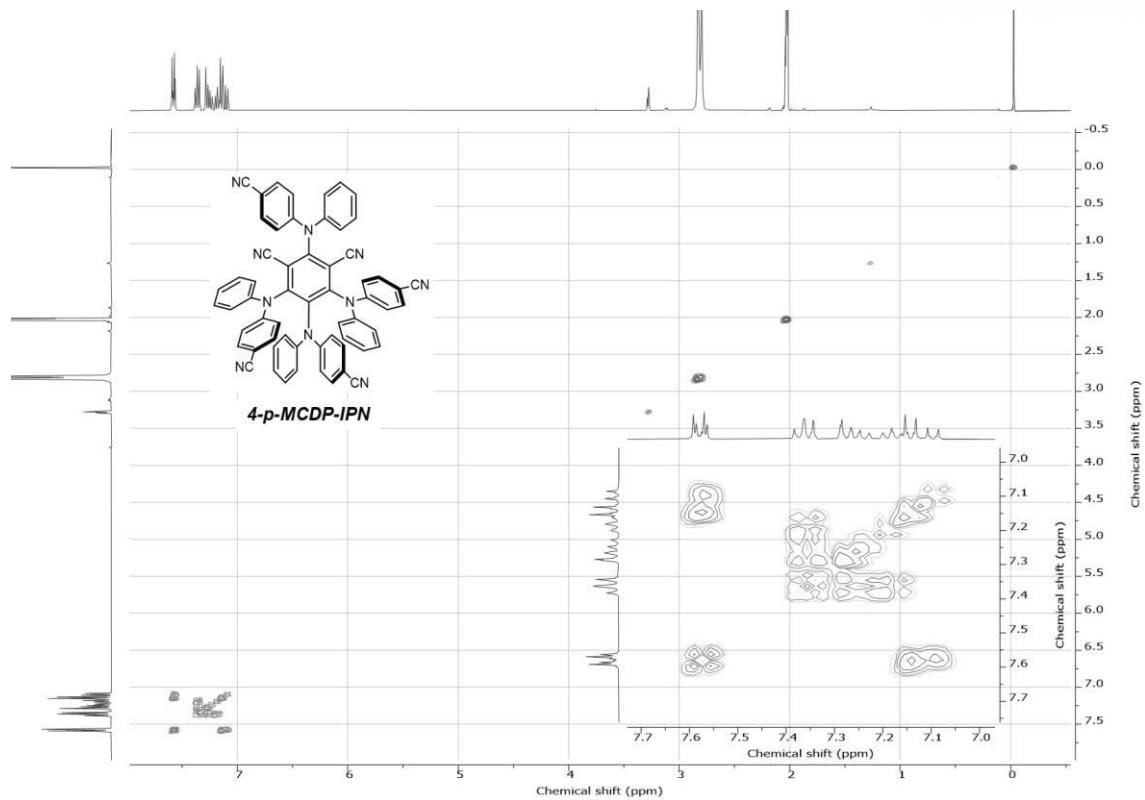
Figure A1.22 COSY NMR data of 4-p-MCDP-IPN at RT (600 MHz, acetone-d_6).
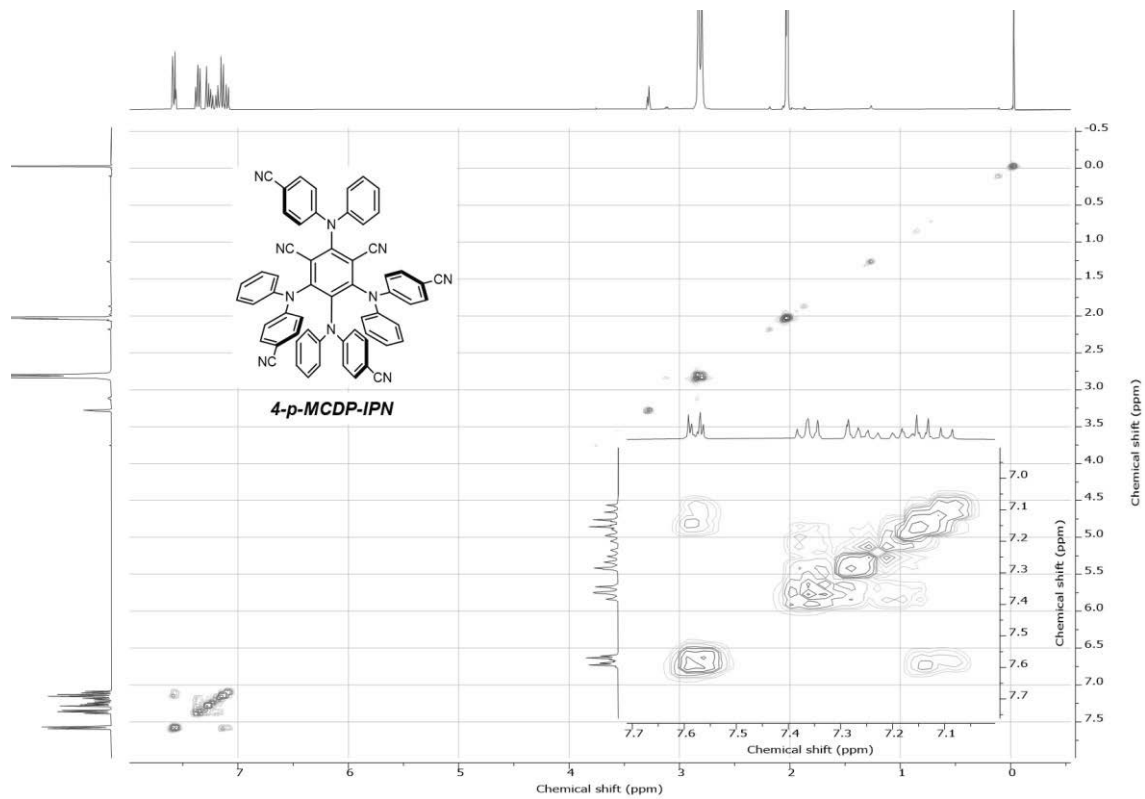
Figure A1.23 NOESY NMR data of 4-p-MCDP-IPN at RT (400 MHz, acetone-d_6).
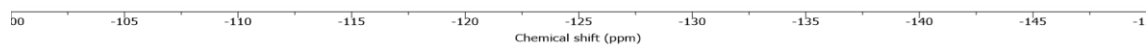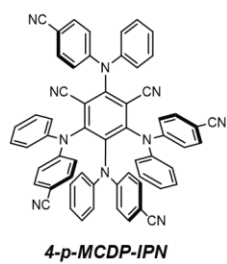
4-p-MCDP-IPN

Figure A1.24 ^{19}F NMR data of 4-p-MCDP-IPN at RT (565 MHz, DMSO-d$_6$).
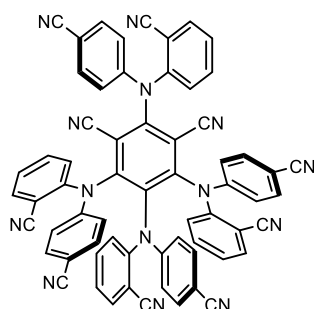
4-o,p-DCDP-IPN: A solution of NaH (60% in mineral oil, 0.120g, 3 mmol) and **2,4′-dicyanodiphenylamine** (0.548g, 2.5 mmol) in anhydrous DMAc (3 mL) was stirred for 30 min in ice bath under N_2 atmosphere. After 30 min, 2,4,5,6-tetrafluoroisophthalonitrile (0.1 g, 0.5 mmol) dissolved in DMAc (2 mL) was slowly added to the reaction mixture and stirred further at 60 °C for 6 hours. Afterwards, distilled water (2 mL) was poured into the reaction mixture to quench the excess NaH. The organic layers were extracted by EA and brine 3 times. Subsequently, the organic layers were dried over $NaSO_4$ and concentrated under reduced pressure which was further purified by column chromatography on silica gel with gradient CH_2Cl_2/hexanes mixtures to give pure product as reddish orange solid. ^{1}H NMR (400 MHz, acetone-d_6): δ 7.68–7.56 (m, 8H), 7.51 (d, 8H), 7.45 (d, 1H), 7.36 (d, 3H), 7.26–7.15 (m, 7H), 7.07 (d, 5H). MS (GC-FAB-HRMS): not found.
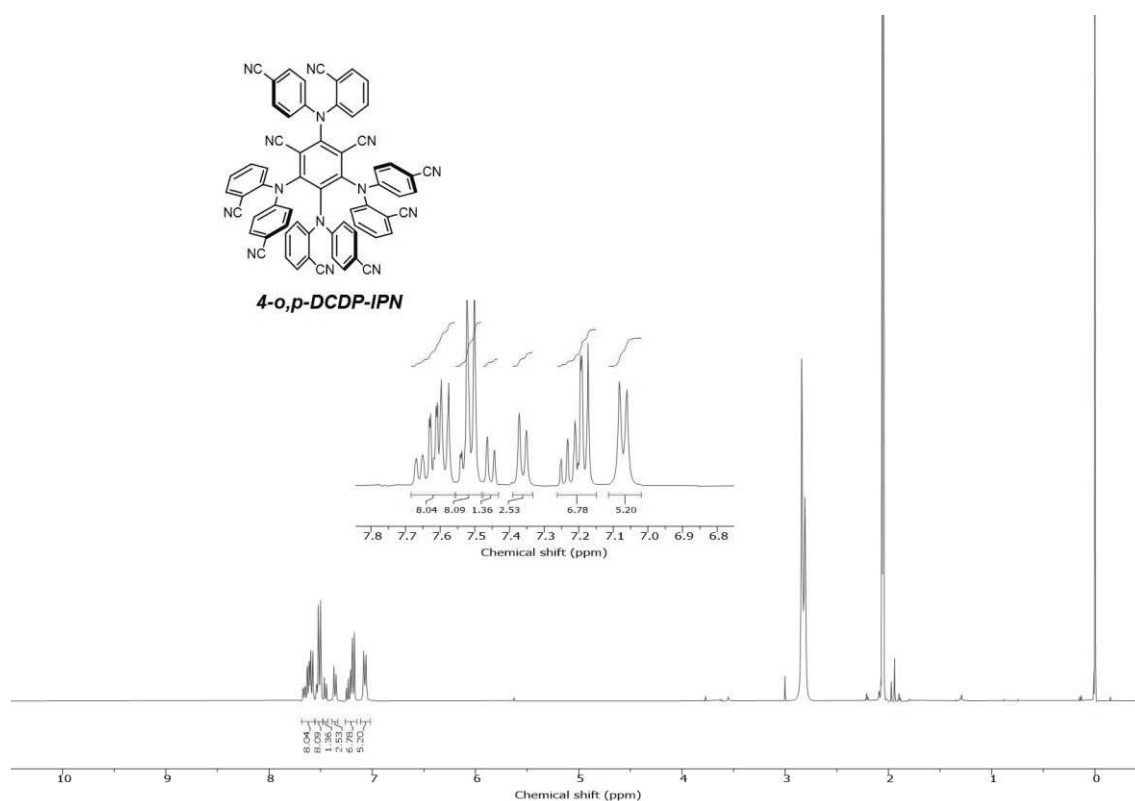
Figure A1.25 ^{1}H NMR data of 4-o,p-DCDP-IPN at RT (400 MHz, acetone-d_6).

95
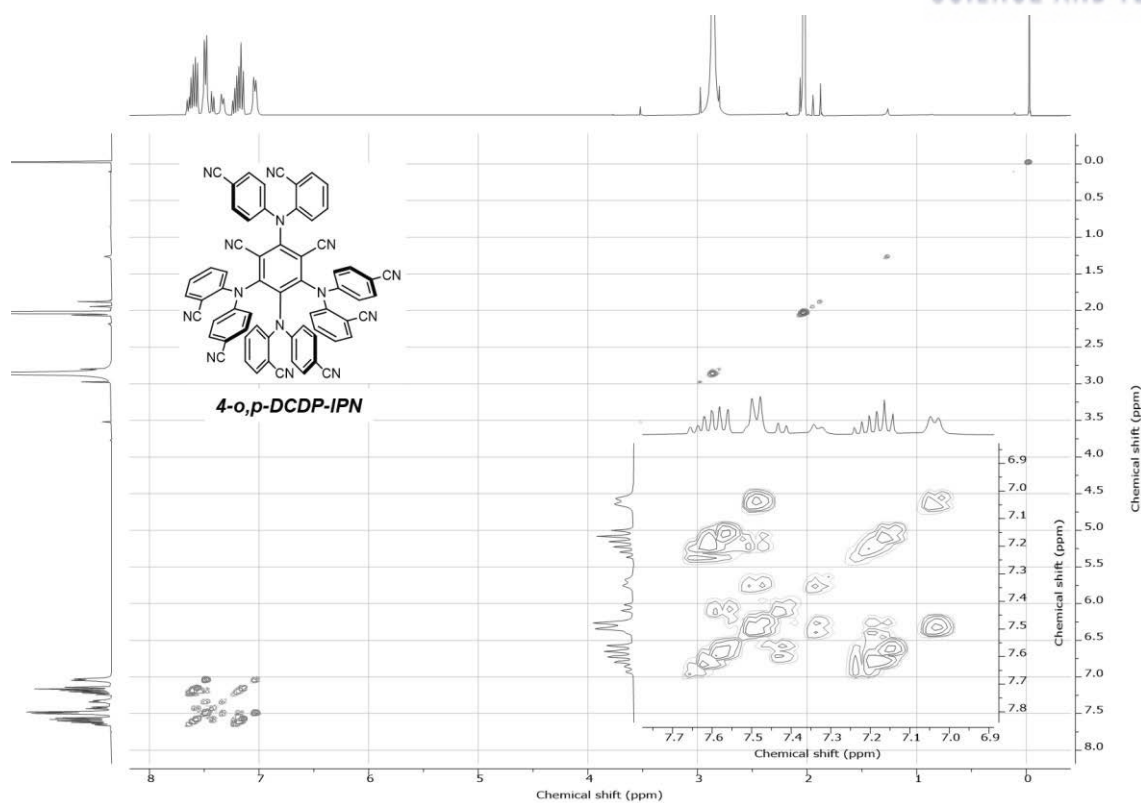
Figure A1.26 COSY NMR data of 4-o,p-DCDP-IPN at RT (400 MHz, acetone-d$_6$).
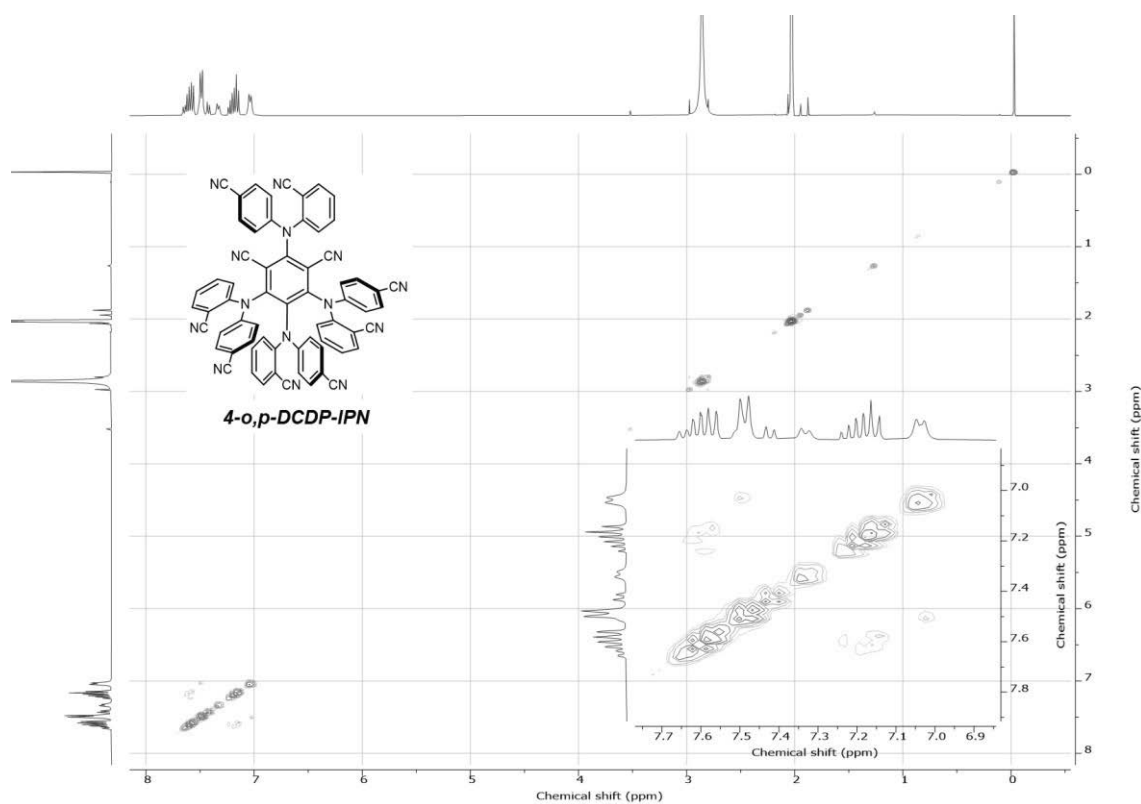
Figure A1.27 NOESY NMR data of 4-o,p-DCDP-IPN at RT (400 MHz, acetone-d$_6$).
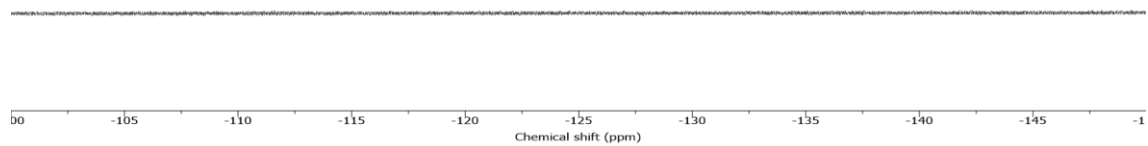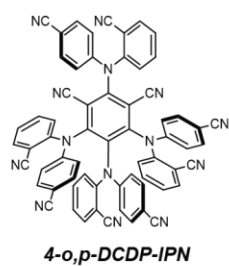
4-o,p-DCDP-IPN

Figure A1.28 ^{19}F NMR data of 4-o,p-DCDP-IPN at RT (565 MHz, acetone-d$_6$).

Appendix 2. Characterization of cyanoarene-based PCs

Photophysical characterization of cyanoarene-based PCs

 UV-Vis absorbance measurements were performed with a V-770 JASCO UV-Vis-NIR spectrometer. Steady-state PL emission spectra at RT were obtained using a HORIBA Jobin Yvon Fluoromax-4 spectrofluorimeter equipped with a 150 W Xe short arc lamp and Hamamatsu R928P PMT detector; the emission spectra were corrected for the sensitivity of the photomultiplier. PL decay measurements were carried out by the TCSPC technique. The excitation source was a 377 nm pulsed diode laser (LDH series PicoQuant) of pulse width (FWHM) < 49 ps. A NanoHarp−250 TCSPC event timer with 25 ns time resolution was employed to measure decays of delayed fluorescence. For temperature-dependent PL studies a Picoquant LDH−D−C−405 pulsed diode laser and a Picoquant HydraHarp−400 TCSPC event timer with 1 ps time resolution were used to measure the decays of the PF, and a 355 nm Nd:YAG laser with a pulse width of 300 ps (Teemphotonics) and a Picoquant TimeHarp 260 nano TCSPC electronics with 1 ns resolution were employed on short (nanosecond to microsecond) and long (microsecond to second) time scales, respectively. Low-temperature PL was dispersed in wavelength using an Acton SP2500 spectrometer and detected either by a Princeton Instruments Spec10:400BR CCD camera or by a low dark current hybrid photomultiplier (PMA 06, PicoQuant), both attached to the spectrometer. Gated PL spectra were acquired with a delay of 250 ms, using a cw 405 nm laser module with TTL modulation input (maximum modulation frequency 20 kHz) and suitable triggering of the CCD. Trigger pulses for the laser and the CCD camera were provided by a Stanford Research Systems DG645 pulse and delay generator with 5 ps resolution. The PL decay time fitting procedure was carried out by using the Fluofit software (PicoQuant).

Electrochemical characterization of cyanoarene-based PCs

 CV experiments were carried out with a VersaSTAT3-200 (Princeton Applied Research) using a one compartment electrolysis cell consisting of a glassy carbon working electrode, a platinum wire counter electrode, and a quasi Ag_+/Ag (sat. KCl aqueous solution) reference electrode bought from AT FRONTIER (Part No. R303). Specifically, the electrode is a silver wire that is coated with a thin layer of silver chloride and an insulated lead wire connects the silver wire with measuring instrument. The electrode also consists of a porous plug on the one end which will allow contact between the field environment with the silver chloride electrolyte. Saturated potassium chloride is added inside the body of the electrode to stabilize the silver chloride concentration and in this condition the electrode's reference potential is known to be +0.197 V at 25 °C. The measurements were done in 0.2 mM CH_3CN solution with 0.1 M tetrabutylammonium hexafluorophosphate (n-Bu_4NPF_6, Aldrich, Electrochemical grade) as supporting electrolyte at a scan rate of 100 mV/s. The redox potential was calibrated after

each experiment against the ferrocenium/ferrocene couple (Fc+/Fc), which allowed conversion of all potentials to the aqueous SCE scaled by using E^0 (Fc+/Fc) = 0.42 V vs SCE in CH_3CN. The working solution was degassed with Ar for 15 min before measurement and then kept under a positive Ar pressure during the measurement.

Appendix 3. Computational details

Density functional theory (DFT) and time-dependent (TD) DFT calculations were performed with the B3LYP functional and 6–311++G* basis set, as all implemented in the Gaussian16 program package. The geometries (S_0 and D_0) optimization and single point energies were calculated in CH_3CN (or EA) solution employing the polarizable continuum model. In all geometry optimization calculations, frequency calculations were performed both to verify that geometries were true minima and to obtain free energies at 298.15 K. To obtain the calculated UV-Vis absorption spectrum of the neutral (S_0) and radical anion (D_0) species, vertical transition energies for the first 60 excited states were obtained by single-point calculations on the optimized S_0 and D_0 geometries, respectively. Molecular orbital topologies were obtained by employed in Gaussian09w and plotted with GaussView 6.0. To derive calculated redox potentials, the Gibbs free energies, $\Delta G_{solv}^{\circ,redox}$, between radical and neutral species were converted to SCE by a given process, $E_{redox,SCE}^{\circ}$ (V vs SCE) $= E_{redox}^{\circ}(eV) - 4.68\ eV$. The geometries of transition state were optimized with QST3 using the STQN method and all optimized geometries of transition state were verified with single imaginary frequency and individual intrinsic reaction coordinate calculations. The Gibbs free energy and enthalpy with relevant standard state reference were obtained from following relations.[129]

$$G^0 \text{ (298.15 K, 1 M)} = G^0{}^* \text{ (298.15 K, 1 atm)} + 1.89 \text{ kcal/mol}$$

$$H^0 \text{ (298.15 K, 1 M)} = H^0{}^* \text{ (298.15 K, 1 atm)} + 0.59 \text{ kcal/mol.}$$

In fact, we have done comparisons with different functionals (including CAM-B3LYP, M06-2X and wB97XD), and we saw very different behaviors for absolute and relative energies of the S_2 and T_n states (and in particular with respect to the ΔE_{ST}) as well as for the state descriptions. The B3LYP functional was chosen because if its good performance of the ΔE_{ST} with respect to experiment as shown by us earlier.[11] For the calculated radical anion absorption, the lowest excited state was actually calculated to be lower with CAM-B3LYP and M06-2X in comparison with B3LYP, so that the latter method still appears quite reasonable to describe the electronic nature of ground and excited states properties for both the neutral and the radical anion species.

Appendix 4. Kinetic simulation

To analyze quantitatively exciton dynamics of selected PCs, we visualized the excited state concentration of PCs benchmarked by Adachi group.[130] The concentration of S_1 and T_1 can be described by following system of ordinary differential equations (ODE).

$$\frac{d[S_1]}{dt} = k_{RISC}[T_1] - \left(k_{ISC} + k_{r,S_1} + k_{nr,S_1}\right)[S_1]$$

$$\frac{d[T_1]}{dt} = k_{ISC}[S_1] - (k_{RISC} + k_{r,T_1} + k_{nr,T_1})[T_1]$$

where k_{ISC}, k_{RISC}, $k_{r,S1}$, $k_{r,T1}$, $k_{nr,S1}$ and $k_{nr,T1}$ denote the rate constants of ISC, RISC, radiative decay from $^1PC^*$ (S_1), radiative decay from $^3PC^*$ (T_1), non-radiative decay from S_1, and non-radiative decay from T_1, respectively. These coupled nonlinear rate equations enable to trace time-dependent decay of the S_1 and T_1 state generated by single pulsed-photoexcitation and the ODEs were solved using ODE15s solvers implemented in the Matlab program package.

Evaluation of $k_{r,S1}$, $k_{nr,S1}$, k_{ISC} and k_{RISC}

The general TADF kinetics can be obtained from the differential equations for the singlet and triplet excited state (S_1, T_1) deactivation.

$$\frac{d[S_1]}{dt} = -k_S \cdot [S_1] + k_{RISC} \cdot [T_1] + \alpha \cdot I \qquad \text{(eq. A1)}$$

$$\frac{d[T_1]}{dt} = k_{ISC} \cdot [S_1] - k_T \cdot [T_1] \qquad \text{(eq. A2)}$$

where $k_S = k_{r,S1} + k_{nr,S1} + k_{ISC}$, $k_T = k_{r,T1} + k_{nr,T1} + k_{RISC}$, I is the intensity of excitation, and α is the absorption coefficient; the solutions are

$$S_1(t) = \frac{S_1(0)}{A_2 - A_1}[(A_2 - k_S)\,exp(-A_1 t) + (k_S - A_1)\,exp(-A_2 t)] \qquad \text{(eq. A3)}$$

$$T_1(t) = \frac{S_1(0) \cdot k_{ISC}}{A_2 - A_1}[exp(-A_1 t) - exp(-A_2 t)] \qquad \text{(eq. A4)}$$

and the total intensity is obtained as

$$I(t) = k_{r,S_1} S_1(t) + k_{r,T_1} T_1(t) \qquad \text{(eq. A5)}$$

$$I(t) = \frac{S_1(0)}{A_2 - A_1} \left[\left(k_{r,S_1}(A_2 - A_S) + k_{r,T_1} k_{ISC} \right) exp(-A_1 t) + \left(k_{r,S_1}(k_S - A_1) - k_{r,T_1} k_{ISC} \right) exp(-A_2 t) \right] \qquad \text{(eq. A6)}$$

The exponents $A_{1,2}$ (which correspond to the reciprocal values of the prompt/delayed PL lifetime constants, $i.e.$, $\tau_{PF,DF}^{-1}$, respectively) are given by

$$A_{1,2} = \frac{1}{2} \left(k_S + k_T \mp (k_T - k_S) \sqrt{1 + 4 \cdot k_{ISC} k_{RISC}/(k_T - k_S)^2} \right) \qquad \text{(eq. A7)}$$

The total PL quantum yield Φ_{PL} is given as the sum of fluorescence and phosphorescence quantum yields ($\Phi_{PL} = \Phi_F + \Phi_{PH}$), where Φ_F consists of a prompt fluorescence (Φ_{PF}) and delayed fluorescence (Φ_{DF}) part; the prompt part is defined by

$$\Phi_{PF} = \frac{k_{r,S_1}}{k_S} \qquad \text{(eq. A8)}$$

In the presence of large number of TADF cycles, the total Φ_F (along with Φ_{PH}) under steady state is obtained as,[131]

$$\Phi_F = \Phi_{PF} \frac{1}{(1 - \eta_{ISC} \cdot \eta_{RISC})} \qquad \text{(eq. A9)}$$

where $\eta_{ISC} = k_{ISC}/k_S$ and $\eta_{RISC} = k_{RISC}/k_T$ are the efficiencies for ISC and RISC, respectively. Similarly, Φ_{PH} is obtained as

$$\Phi_{PH} = \frac{\eta_{ISC} k_{PH}}{k_T (1 - \eta_{ISC} \cdot \eta_{RISC})} \qquad \text{(eq. A10)}$$

The condition for strong TADF emitters translates to $k_{RISC} \gg k_{r,T1}$, $k_{nr,T1}$, so that $\eta_{RISC} \approx 1$; the phosphorescence lifetime of 4DP-IPN at 65 K is about 407 ms, therefore, the sum of $k_{r,T1}$ and $k_{nr,T1}$ is about 2.5 s^{-1} at 65 K. This simplifies eq. (S17) to

$$\Phi_F = \frac{\Phi_{PF}}{(1 - \eta_{ISC} \cdot \eta_{RISC})} \approx \frac{\Phi_{PF}}{(1 - \eta_{ISC})} = \frac{k_S \Phi_{PF}}{(k_{r,S_1} + k_{nr,S_1})} = \frac{k_{r,S_1}}{(k_{r,S_1} + k_{nr,S_1})} \qquad \text{(eq. A11)}$$

Furthermore, for TADF compounds with a non-negligible $\Delta E_{ST} \gtrsim 0.1$ eV (which is indeed the case for the 4DP-IPN as discussed further up), RISC is much smaller than ISC; $i.e.$ $k_{RISC} \ll k_{ISC}$. Under these

conditions, with a Taylor expansion ($y = \sqrt{1+x} \approx 1 + \frac{x}{2}$ for x << 1), the solutions for $A_{1,2}$ simplify to

$$A_1 = \tau_{PF}{}^{-1} = \frac{1}{2}\left(k_S + k_T - (k_T - k_S)\sqrt{1 + 4 \cdot k_{ISC}k_{RISC}/(k_T - k_S)^2}\right) = k_S - \frac{k_{ISC}k_{RISC}}{k_T - k_S} \approx k_S \qquad \text{(eq. A12)}$$

$$A_2 = \tau_{DF}{}^{-1} = \frac{1}{2}\left(k_S + k_T + (k_T - k_S)\sqrt{1 + 4 \cdot k_{ISC}k_{RISC}/(k_T - k_S)^2}\right) = k_T\left(1 - \frac{k_{ISC}k_{RISC}}{k_T k_S}\right) \approx k_{RISC}(1 - \eta_{ISC}) \qquad \text{(eq. A13)}$$

Finally, the radiative rate constant k_{r,S_1} can be estimated from the Strickler-Berg formula, which in its simplified form reads,[78,79]

$$k_{r,S_1,\text{SB}} = 0.667(s^{-1}cm^2)\frac{E_{\text{F,vert}}^3}{E_{\text{A,vert}}}n^2 f = 4.34 \cdot 10^7 (s^{-1}\text{eV}^{-2})\frac{E_{\text{F,vert}}^3}{E_{\text{A,vert}}}n^2 f \qquad \text{(eq. A14)}$$

where f is the TD-DFT calculated oscillator strength of vertical absorption, n is the refractive index of solvent and E is the energy of vertical absorption and emission respectively for the lowest energetic CT transition.

In summary, the photophysical rate constants of PCs in jablonski diagram were evaluated by experimental (*i.e.*, prompt/delayed fluorescence decays) and computational method (*i.e.*, TD-DFT), which each relation is simplified to

$$k_{r,S_1} = 4.34 \cdot 10^7 (s^{-1}\text{eV}^{-2})\frac{E_{\text{F,vert}}^3}{E_{\text{A,vert}}}n^2 f \qquad \text{(eq. A15)}$$

$$k_{\text{nr},S_1} = \frac{k_{r,S_1}}{\Phi_F} - k_{r,S_1} = k_{r,S_1}\left(\frac{1}{\Phi_F} - 1\right) \qquad \text{(eq. A16)}$$

$$k_{\text{ISC}} = \tau_{PF}{}^{-1} - \frac{k_{r,S_1}}{\Phi_F} \qquad \text{(eq. A17)}$$

$$k_{\text{RISC}} = \frac{\tau_{DF}{}^{-1}}{1 - k_{ISC}\tau_{PF}} \qquad \text{(eq. A18)}$$

where f, n, E, Φ_F, τ_{PF}, and τ_{DF} have been defined earlier.

Appendix 5. GC and NMR data of dehalogenation products
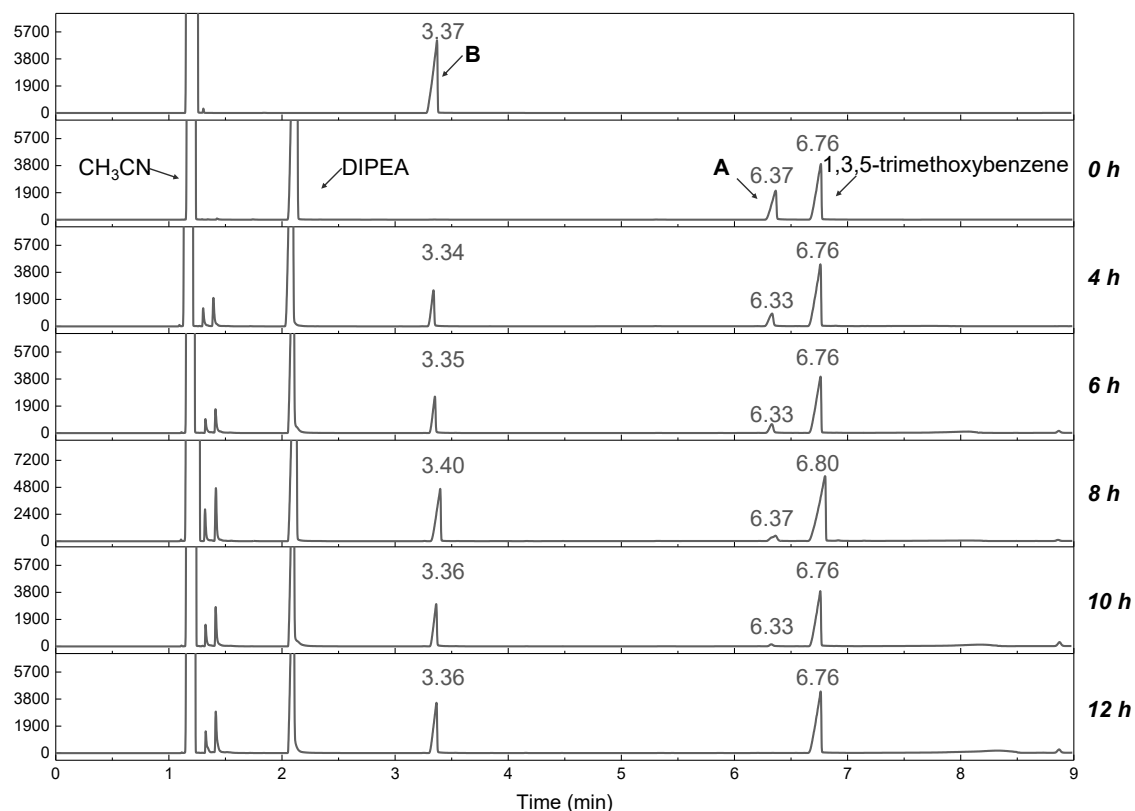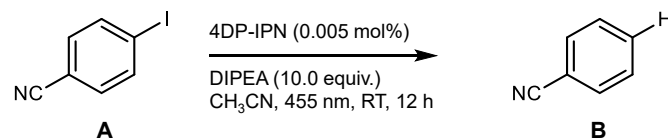
Figure A5.1 Gas chromatography (GC-FID) spectra for photoredox reductive dehalogenation of 4-iodobenzonitrile. Yield was measured by GC-FID using TMB as an internal standard.

Substrate screening (4-iodobenzonitrile), 0 h

^{1}H NMR (400 MHz, DMSO-d$_6$):
δ 8.00–7.96 (d, 2H), 7.62–7.58 (d, 2H)

Substrate screening (4-iodobenzonitrile), 12 h
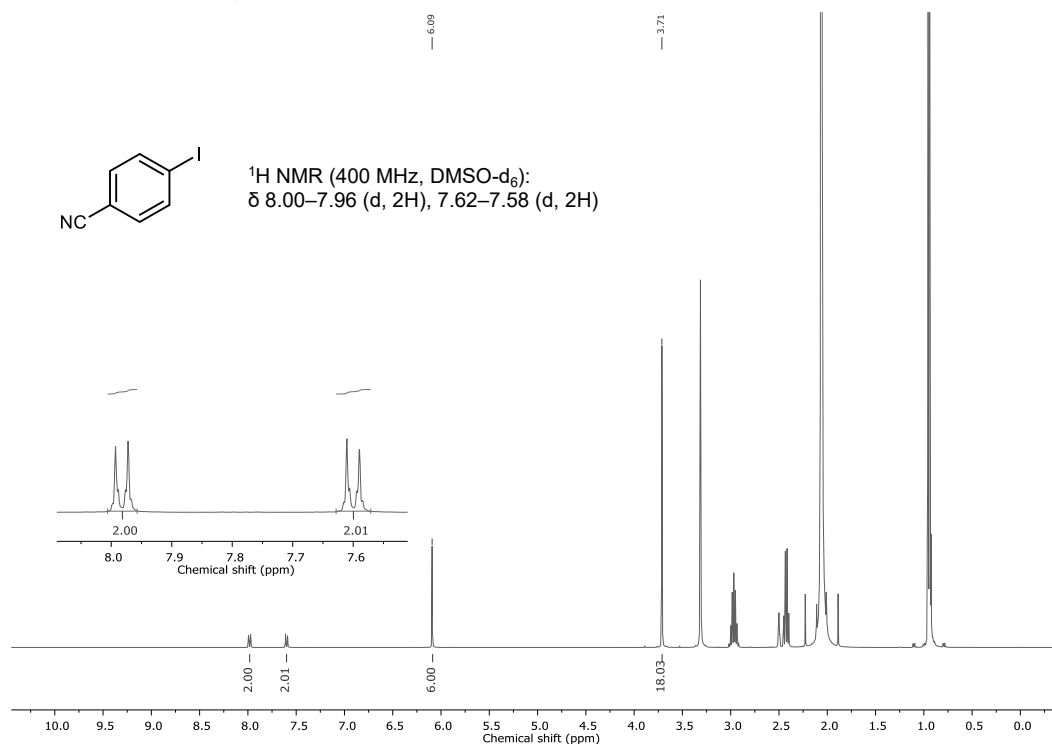
^{1}H NMR (400 MHz, DMSO-d$_6$):
δ 7.84–7.81 (m, 2H), 7.75–7.70 (tt, 1H),
7.62–7.56 (t, 2H)
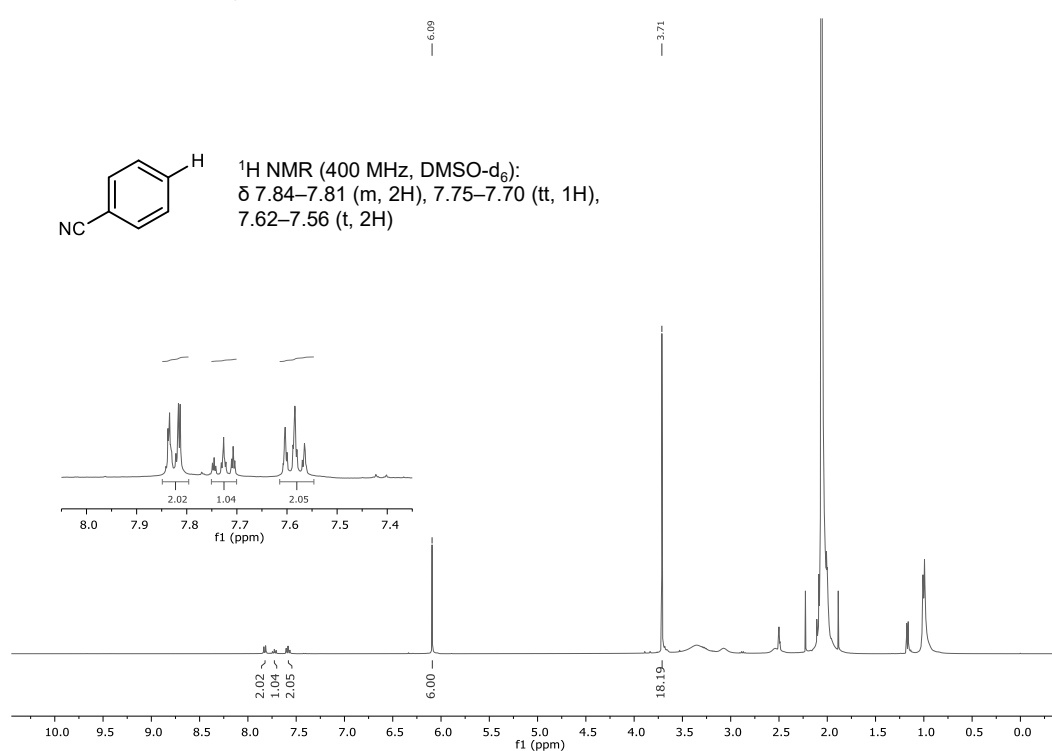
Figure A5.2 ^{1}H NMR data of photoredox reductive dehalogenation for 4-iodobenzonitrile (400 MHz, DMSO-d$_6$); TMB: δ 6.09 (s, 3H), 3.71 (s, 9H).

Figure A5.3 GC-FID spectra of photoredox reductive dehalogenation for 3-iodobenzonitrile. Yield was measured by GC-FID using TMB as an internal standard.

Substrate screening (3-iodobenzonitrile), 0 h

^{1}H NMR (400 MHz, DMSO-d_6):
δ 8.24–8.23 (t, 1H), 8.10–8.08
(dd, 1H), 7.87–7.84 (dd, 1H),
7.38–7.34 (t, 1H)

Substrate screening (3-iodobenzonitrile), 24 h

^{1}H NMR (400 MHz, DMSO-d_6):
δ 7.84–7.81 (m, 2H), 7.75–7.70 (tt, 1H),
7.62–7.56 (t, 2H)

Figure A5.4 ^{1}H NMR data of photoredox reductive dehalogenation for 3-iodobenzonitrile (400 MHz, DMSO-d_6); TMB: δ 6.09 (s, 3H), 3.71 (s, 9H).

Figure A5.5 GC-FID spectra of photoredox reductive dehalogenation for 2-iodobenzonitrile. Yield was measured by GC-FID using TMB as an internal standard.

Substrate screening (2-iodobenzonitrile), 0 h

^{1}H NMR (400 MHz, DMSO-d$_6$):
δ 8.07–8.05 (dd, 1H), 7.85–7.82 (dd, 1H),
7.61–7.57 (td, 1H), 7.47–7.42 (td, 1H)

Substrate screening (2-iodobenzonitrile), 24 h

^{1}H NMR (400 MHz, DMSO-d$_6$):
δ 7.84–7.81 (m, 2H), 7.75–7.70 (tt, 1H), 7.62–
7.56 (t, 2H)

Figure A5.6 ^{1}H NMR data of photoredox reductive dehalogenation for 2-iodobenzonitrile (400 MHz, DMSO-d$_6$); TMB: δ 6.09 (s, 3H), 3.71 (s, 9H).
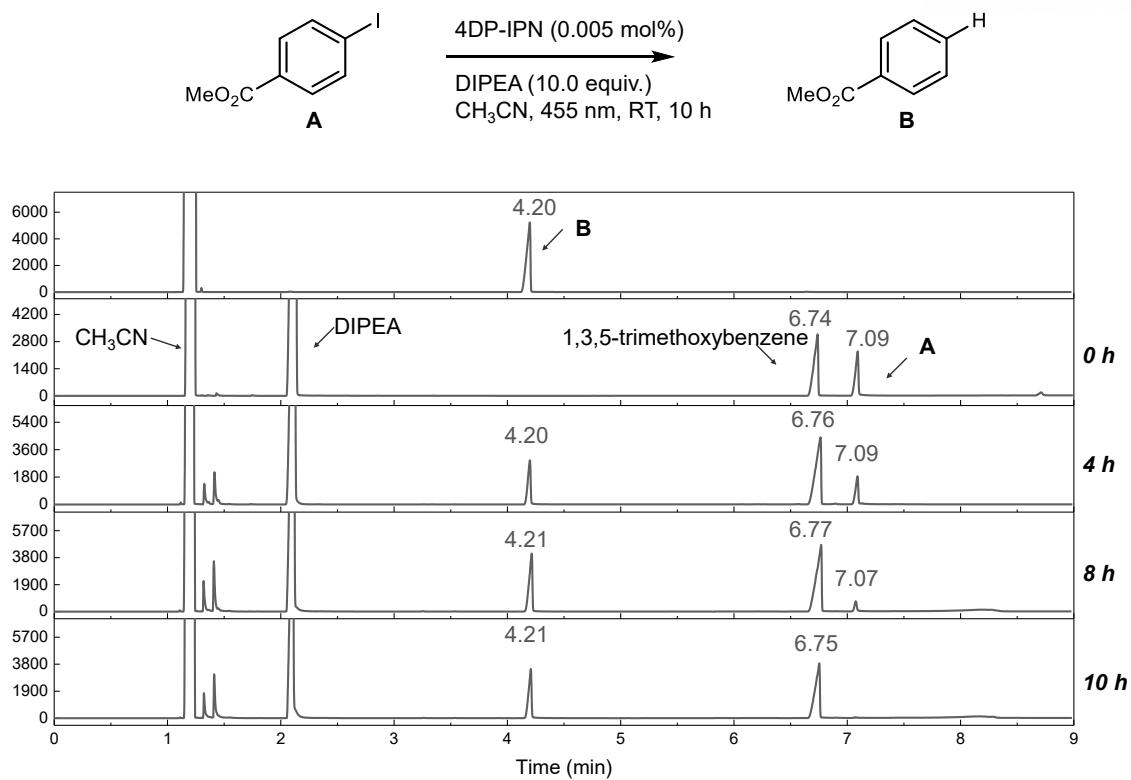
Figure A5.7 GC-FID spectra of photoredox reductive dehalogenation for methyl-4-iodobenzoate. Yield was measured by GC-FID using TMB as an internal standard.

Substrate screening (methyl 4-iodobenzoate), 0 h

^{1}H NMR (400 MHz, DMSO-d$_6$):
δ 7.93-7.90 (m, 2H), 7.73–7.70 (m, 2H),
3.85 (s, 3H)

Substrate screening (methyl 4-iodobenzoate), 10 h
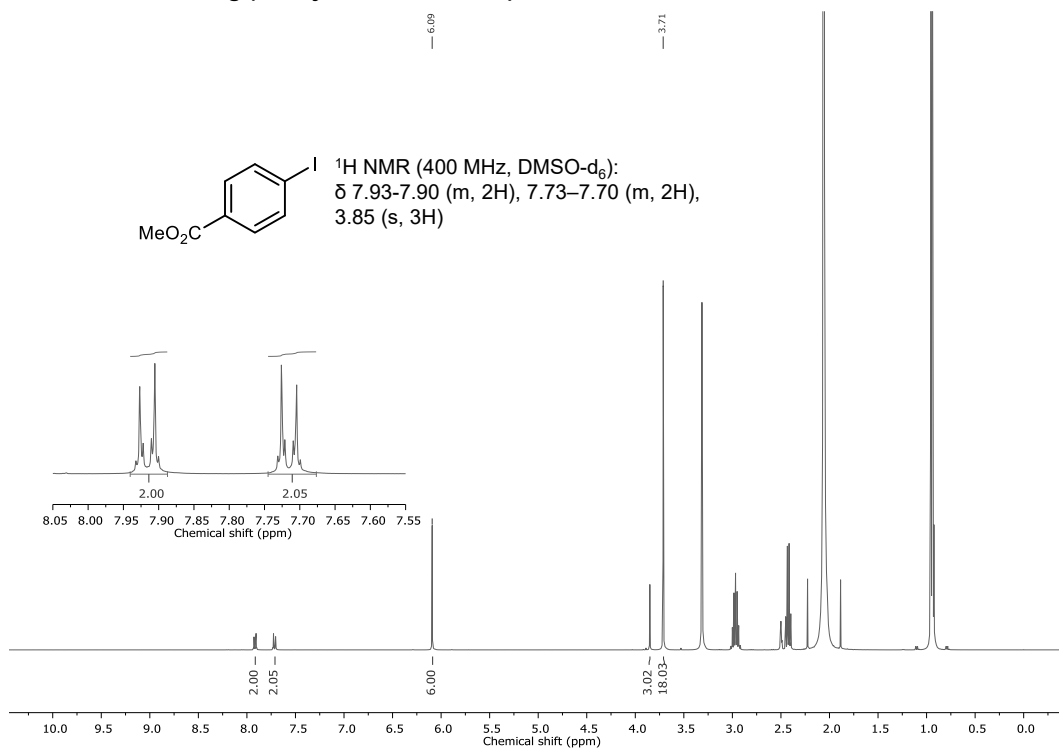
^{1}H NMR (400 MHz, DMSO-d$_6$):
δ 7.99–7.97 (m, 2H), 7.68–7.63 (tt, 1H),
7.55–7.50 (t, 2H), 3.86 (s, 3H)

Figure A5.8 ^{1}H NMR data of photoredox reductive dehalogenation for methyl 4-iodobenzoate (400 MHz, DMSO-d$_6$); TMB: δ 6.09 (s, 3H), 3.71 (s, 9H).

111

Figure A5.9 GC-FID spectra of photoredox reductive dehalogenation for methyl-3-iodobenzoate. Yield was measured by GC-FID using TMB as an internal standard.

Substrate screening (methyl 3-iodobenzoate), 0 h

^{1}H NMR (400 MHz, DMSO-d$_6$):
δ 8.26 (s, 1H), 8.03–8.00 (d, 1H), 7.98-7.96 (d, 1H),
7.36-7.32 (t, 1H), 3.86 (s, 3H)

Substrate screening (methyl 3-iodobenzoate), 10 h

^{1}H NMR (400 MHz, DMSO-d$_6$):
δ 7.99–7.97 (m, 2H), 7.68–7.63 (tt, 1H),
7.55–7.50 (t, 2H), 3.86 (s, 3H)

Figure A5.10 ^{1}H NMR data of photoredox reductive dehalogenation for methyl 3-iodobenzoate (400 MHz, DMSO-d$_6$); TMB: δ 6.09 (s, 3H), 3.71 (s, 9H).

Figure A5.11 GC-FID spectra of photoredox reductive dehalogenation for methyl-2-iodobenzoate. Yield was measured by GC-FID using TMB as an internal standard.

Substrate screening (methyl 2-iodobenzoate), 0 h

^{1}H NMR (400 MHz, DMSO-d$_6$):
δ 8.03-8.00 (dd, 1H), 7.74–7.71 (dd, 1H),
7.53-7.48 (td, 1H), 7.30-7.26 (td, 1H), 3.86 (s, 3H)

Substrate screening (methyl 2-iodobenzoate), 24 h

^{1}H NMR (400 MHz, DMSO-d$_6$):
δ 7.99–7.97 (m, 2H), 7.68–7.63 (tt, 1H),
7.55–7.50 (t, 2H), 3.86 (s, 3H)

Figure A5.12 ^{1}H NMR data of photoredox reductive dehalogenation for methyl 2-iodobenzoate (400 MHz, DMSO-d$_6$); TMB: δ 6.09 (s, 3H), 3.71 (s, 9H).

115

Figure A5.13 GC-FID spectra of photoredox reductive dehalogenation for 4-iodobenzaldehyde. Yield was measured by GC-FID using TMB as an internal standard.

Substrate screening (4-iodobenzaldehyde), 0 h

^{1}H NMR (400 MHz, DMSO-d$_6$):
δ 10.02 (s, 1H), 8.03-7.99 (m, 2H), 7.69-7.65 (m, 2H)

Substrate screening (4-iodobenzaldehyde), 24 h

^{1}H NMR (400 MHz, DMSO-d$_6$):
δ 10.02 (s, 1H), 7.93-7.91 (m, 2H),
7.74-7.70 (m, 1H), 7.63-7.61 (m, 2H)

Figure A5.14 ^{1}H NMR data of photoredox reductive dehalogenation for 4-iodobenzaldehyde (400 MHz, DMSO-d$_6$); TMB: δ 6.09 (s, 3H), 3.71 (s, 9H).

117
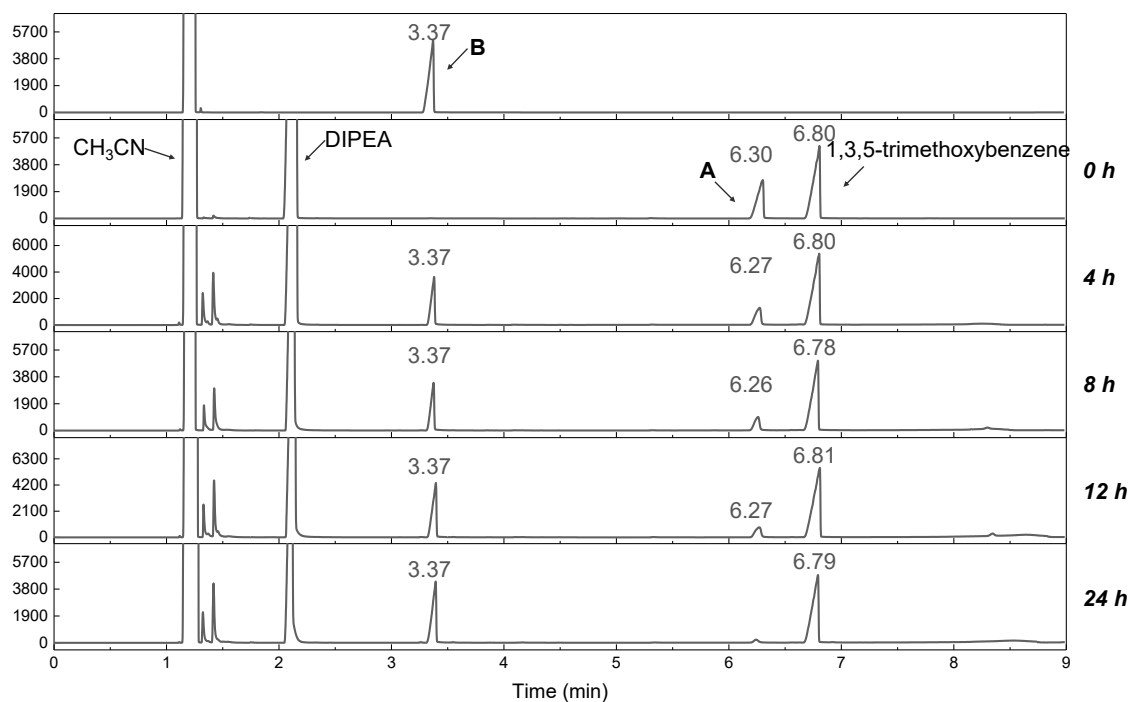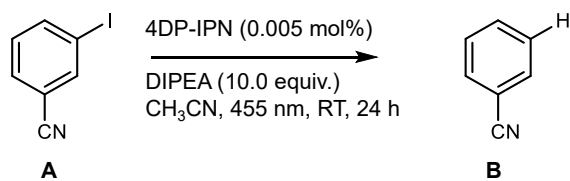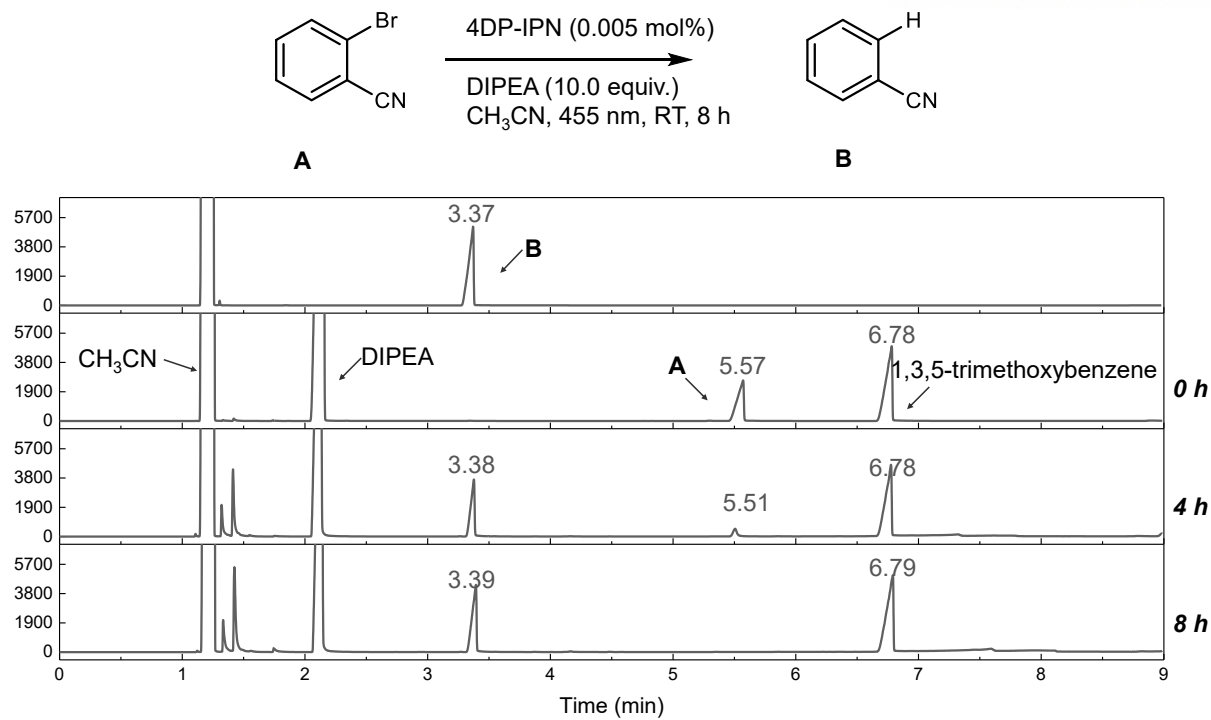
Figure A5.15 GC-FID spectra of photoredox reductive dehalogenation for 2-bromobenzonitrile. Yield was measured by GC-FID using TMB as an internal standard.

Substrate screening (2-bromobenzonitrile), 0 h

^{1}H NMR (400 MHz, DMSO-d$_6$):
δ 7.94–7.92 (dd, 1H), 7.89–7.87 (dd, 1H),
7.67–7.63 (td, 1H), 7.61–7.57 (td, 1H)

Substrate screening (2-bromobenzonitrile), 8 h

^{1}H NMR (400 MHz, DMSO-d$_6$):
δ 7.84–7.81 (m, 2H), 7.75–7.70 (tt, 1H), 7.62–
7.56 (t, 2H)

Figure A5.16 ^{1}H NMR data of photoredox reductive dehalogenation for 2-bromobenzonitrile (400 MHz, DMSO-d$_6$); TMB: δ 6.09 (s, 3H), 3.71 (s, 9H).
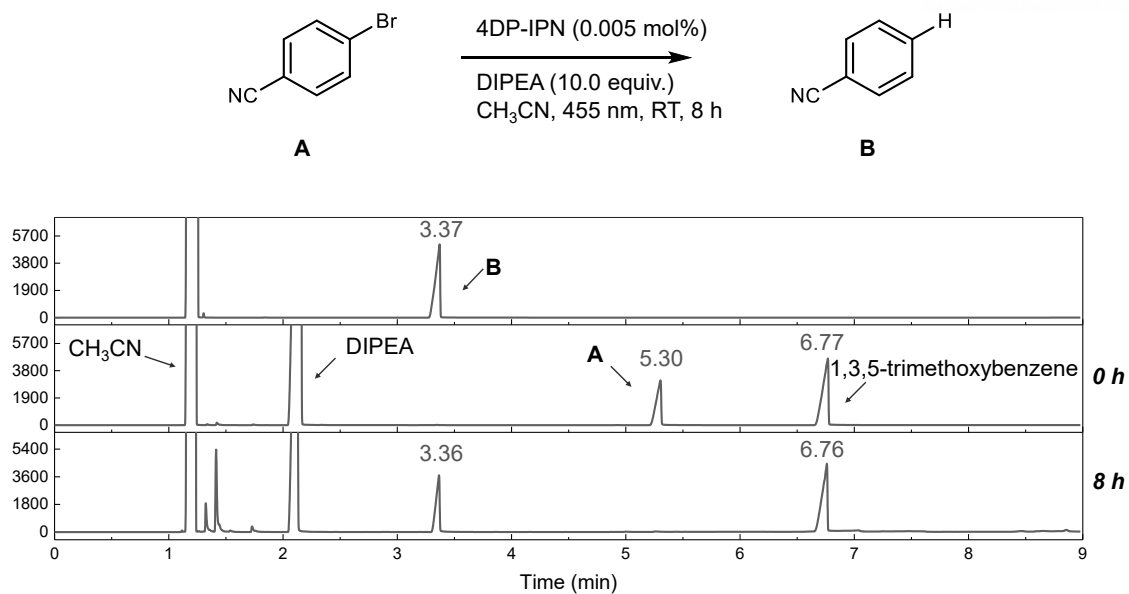
Figure A5.17 GC-FID spectra of photoredox reductive dehalogenation for 4-bromobenzonitrile. Yield was measured by GC-FID using TMB as an internal standard.
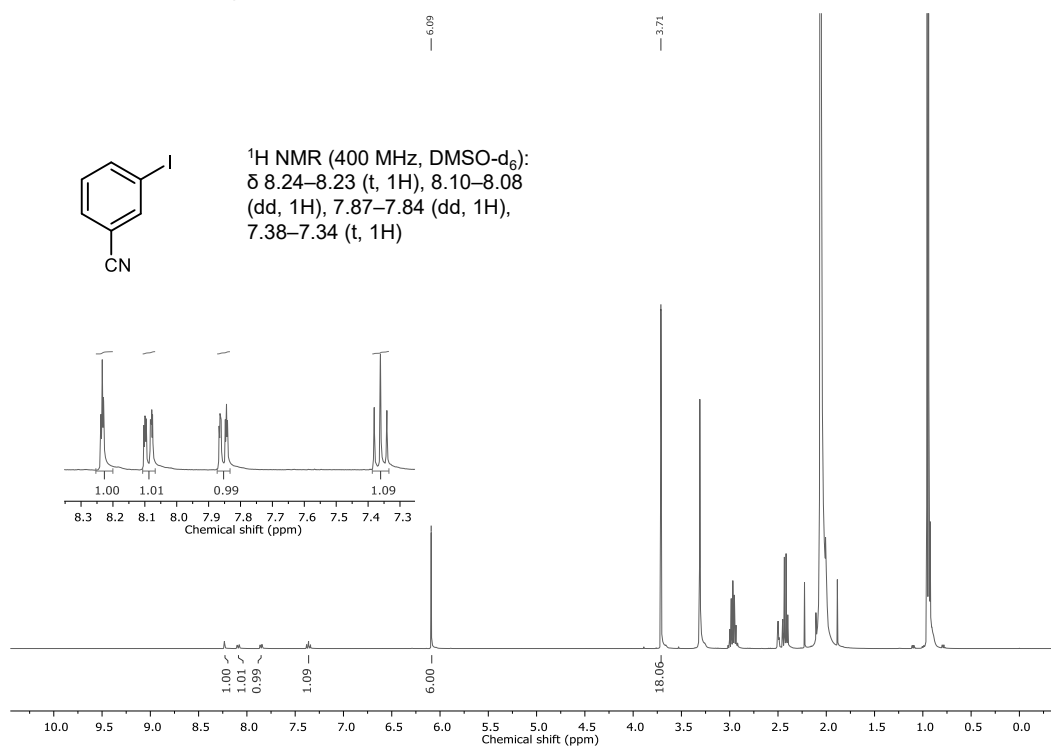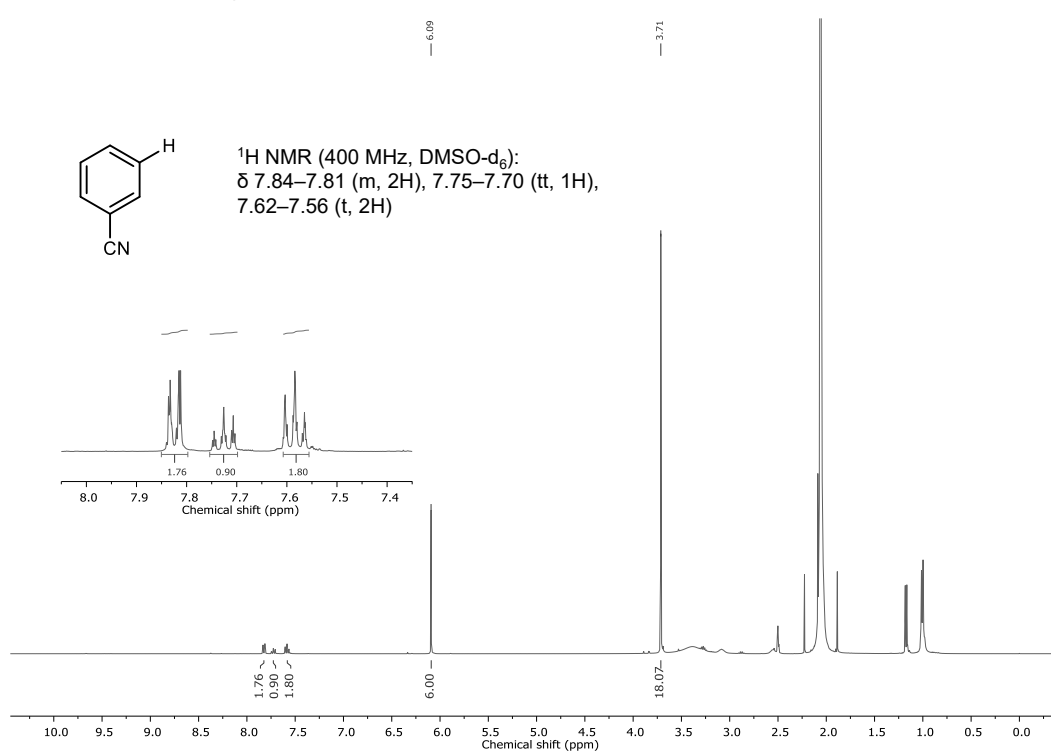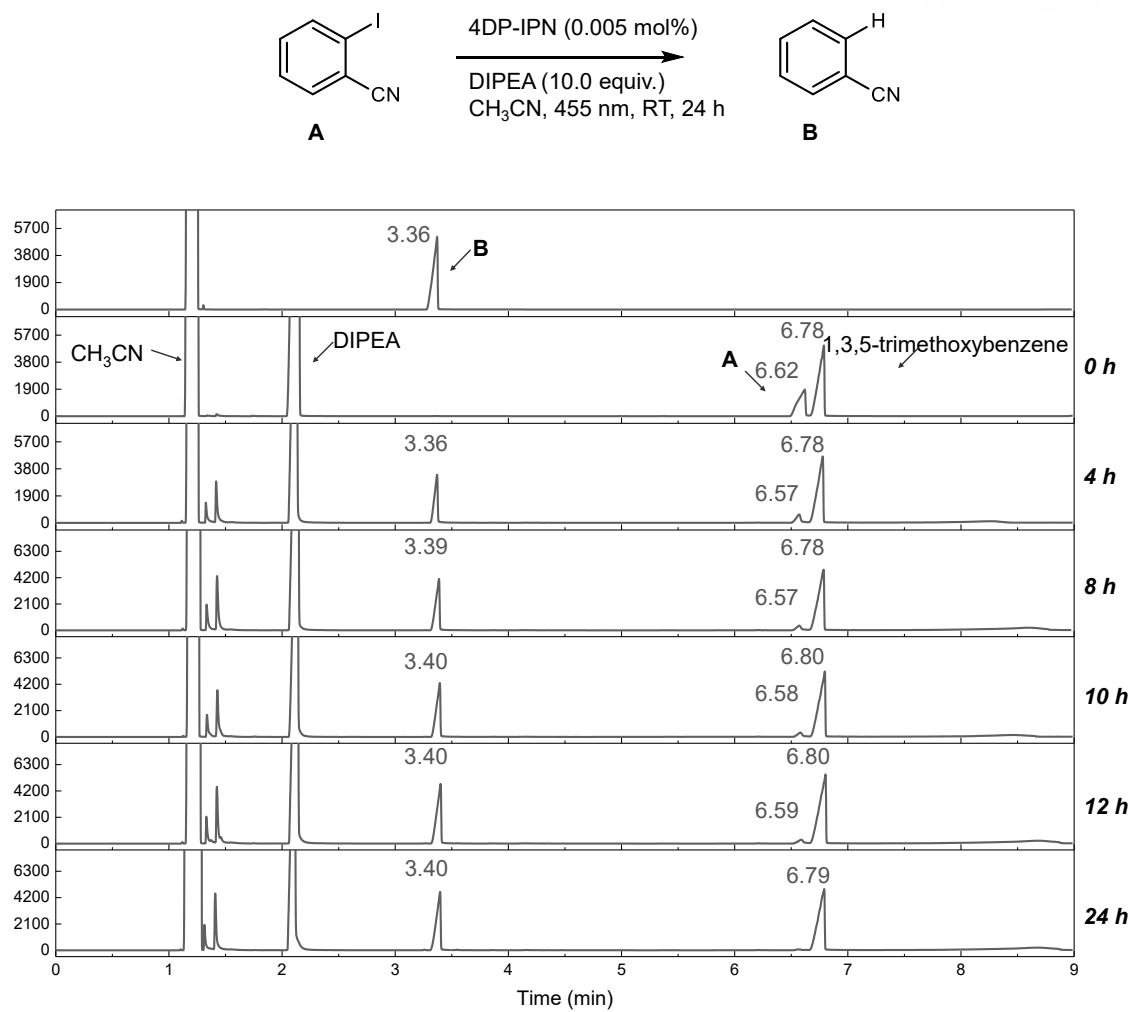
Substrate screening (4-bromobenzonitrile), 0 h

^{1}H NMR (400 MHz, DMSO-d$_6$):
δ 7.83–7.77 (m, 4H)

Substrate screening (4-bromobenzonitrile), 8 h

^{1}H NMR (400 MHz, DMSO-d$_6$):
δ 7.84–7.81 (m, 2H), 7.75–7.70 (tt, 1H), 7.62–7.56 (t, 2H)

Figure A5.18. ^{1}H NMR data of photoredox reductive dehalogenation for 4-bromobenzonitrile (400 MHz, DMSO-d$_6$); TMB: δ 6.09 (s, 3H), 3.71 (s, 9H).
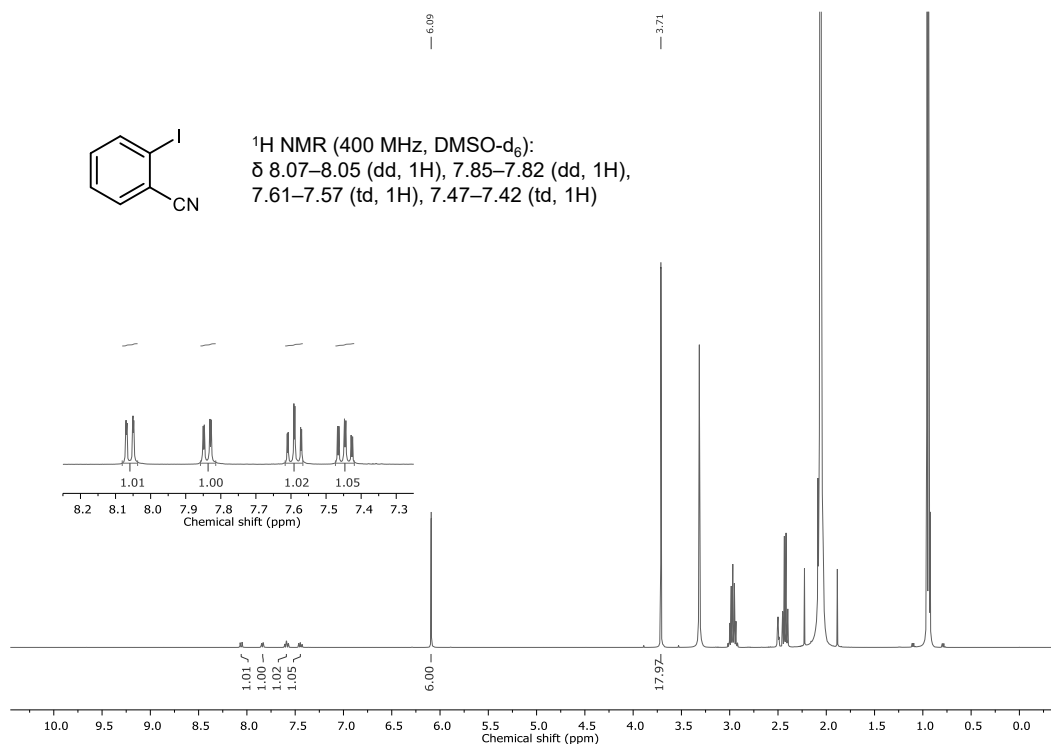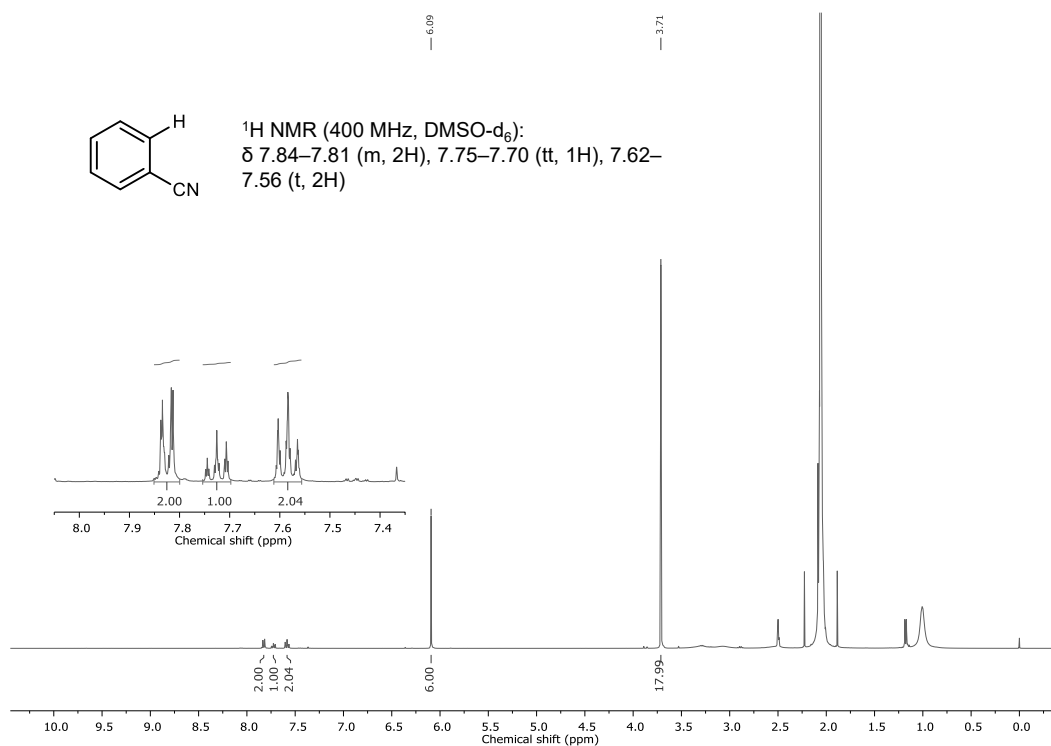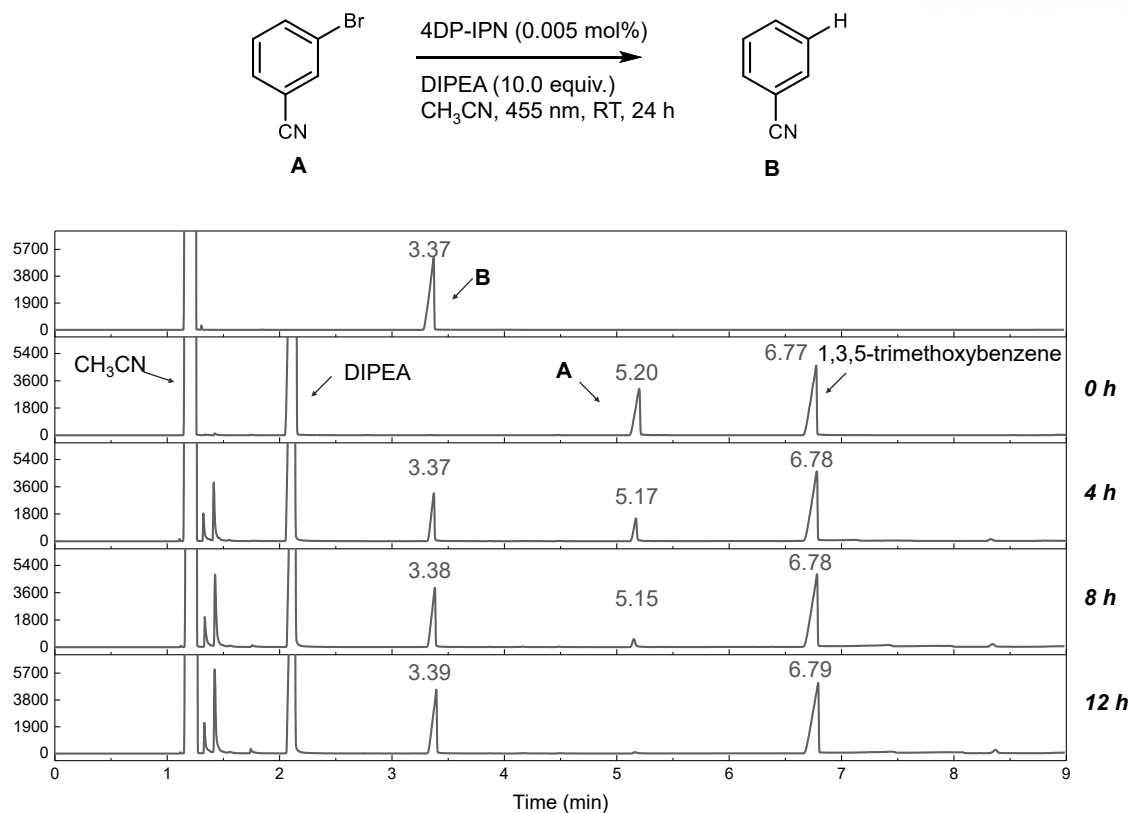
Figure A5.19 GC-FID spectra of photoredox reductive dehalogenation for 3-bromobenzonitrile. Yield was measured by GC-FID using TMB as an internal standard.

Substrate screening (3-bromobenzonitrile), 0 h

^{1}H NMR (400 MHz, DMSO-d$_6$):
δ 8.13–8.12 (t, 1H), 7.95–7.92 (dd, 1H),
7.87–7.84 (dt, 1H), 7.55–7.51 (t, 1H)

Substrate screening (3-bromobenzonitrile), 12 h
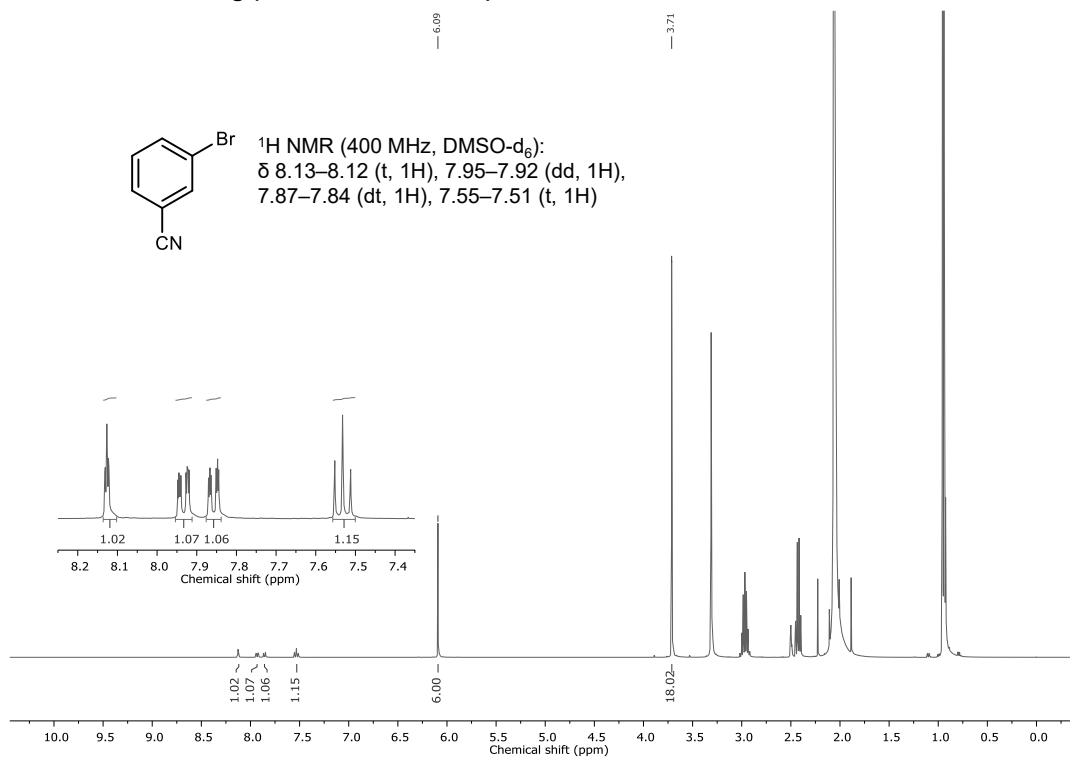
^{1}H NMR (400 MHz, DMSO-d$_6$):
δ 7.84–7.81 (m, 2H), 7.75–7.70 (tt, 1H),
7.62–7.56 (t, 2H)
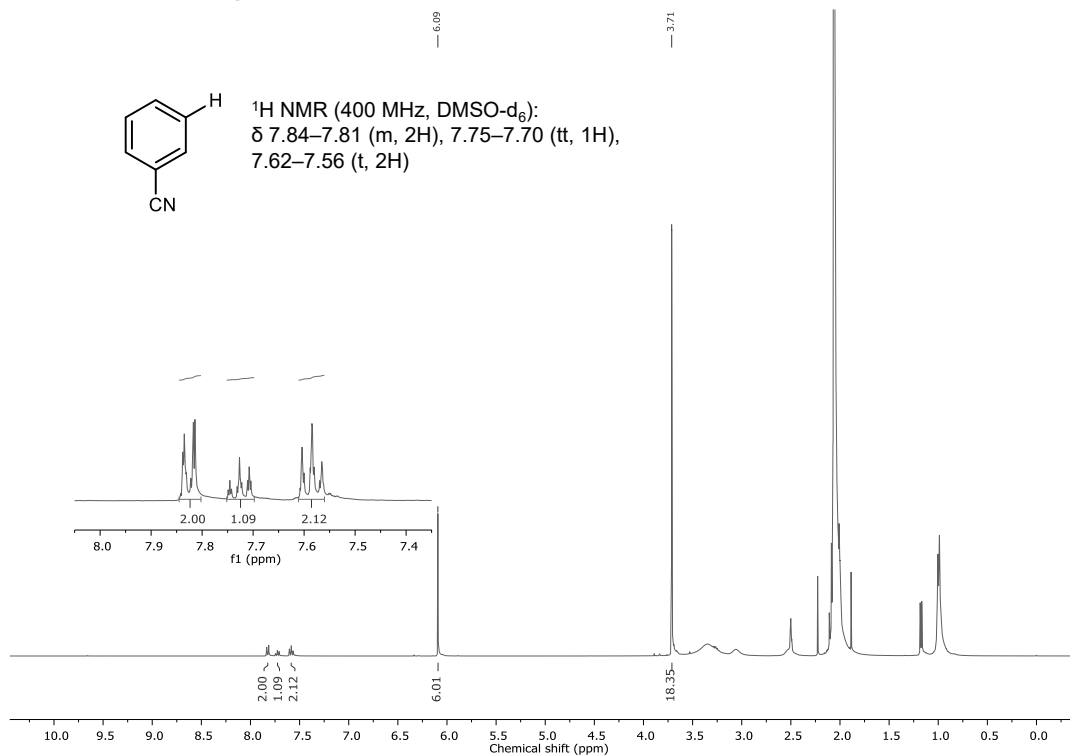
Figure A5.20 ^{1}H NMR data of photoredox reductive dehalogenation for 3-bromobenzonitrile (400 MHz, DMSO-d$_6$); TMB: δ 6.09 (s, 3H), 3.71 (s, 9H).

Figure A5.21 GC-FID spectra of photoredox reductive dehalogenation for 1-iodododecane. Yield was measured by GC-FID using TMB as an internal standard.

Substrate screening (1-iod_odecane), 0 h

H$_3$C $\overset{\text{I}}{\underset{11}{\bigvee}}$ ^{1}H NMR (400 MHz, CDCl$_3$):
δ 3.20-3.17 (t, 2H), 1.86-1.78 (q, 2H),
1.42-1.21 (m, 18H), 0.93-0.85 (t, 3H)

Substrate screening (1-iodododecane), 6 h

H$_3$C $\overset{\text{H}}{\underset{11}{\bigvee}}$ ^{1}H NMR (400 MHz, CDCl$_3$):
δ 1.34-1.23 (m, 20H), 0.90-0.86 (t, 6H)

Figure A5.22 ^{1}H NMR data of photoredox reductive dehalogenation for 1-iodododecane (400 MHz, CDCl$_3$); TMB: δ 6.09 (s, 3H), 3.71 (s, 9H).
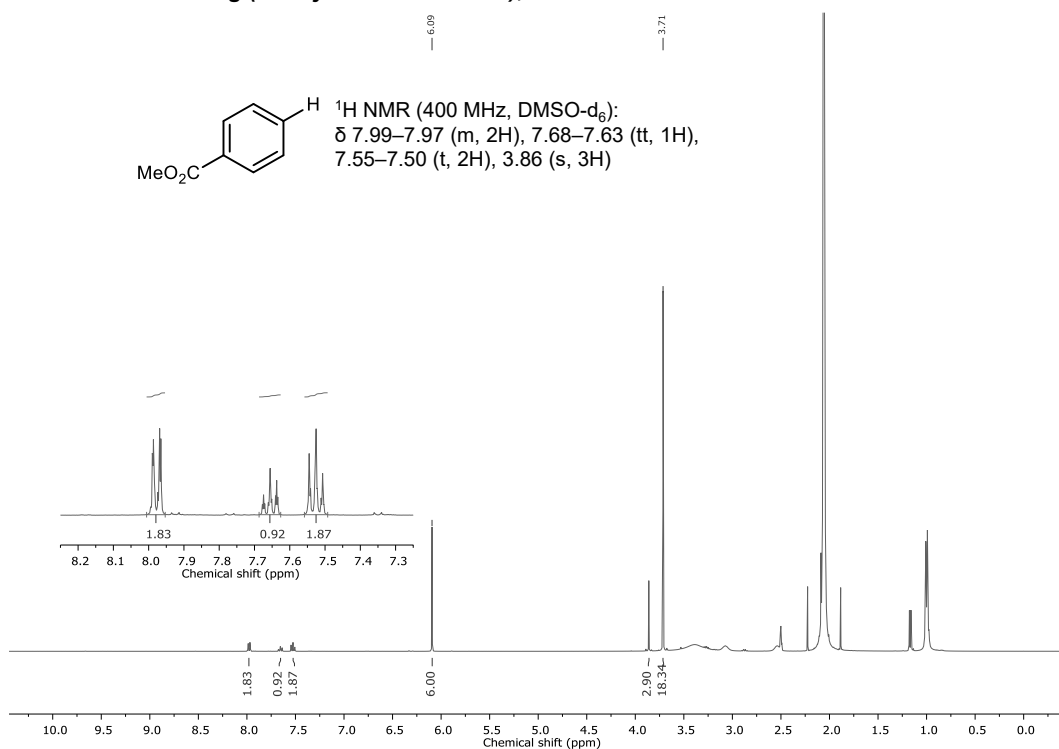
125
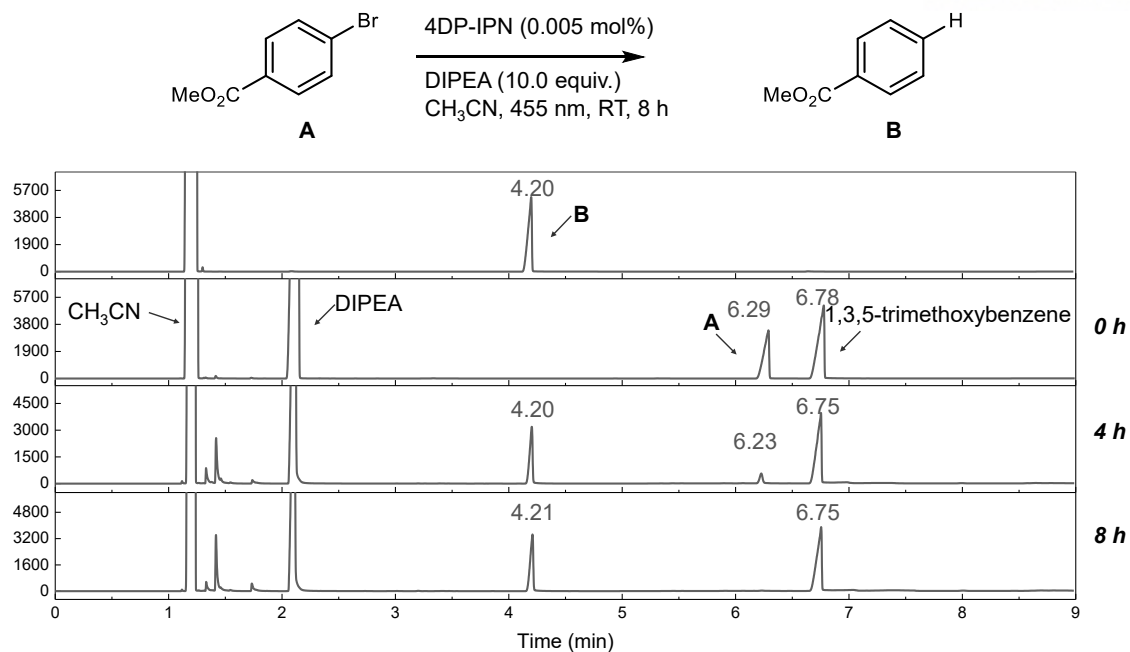
Figure A5.23 GC-FID spectra of photoredox reductive dehalogenation for methyl 4-bromobenzoate. Yield was measured by GC-FID using TMB as an internal standard.
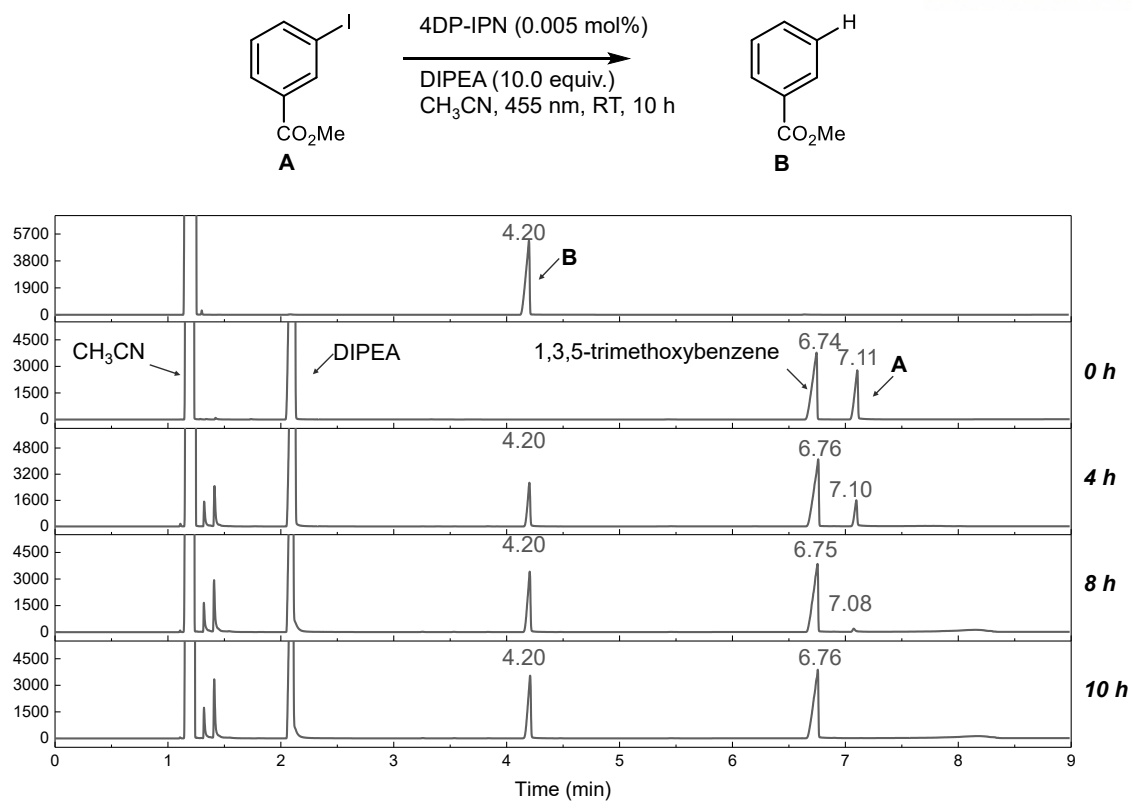
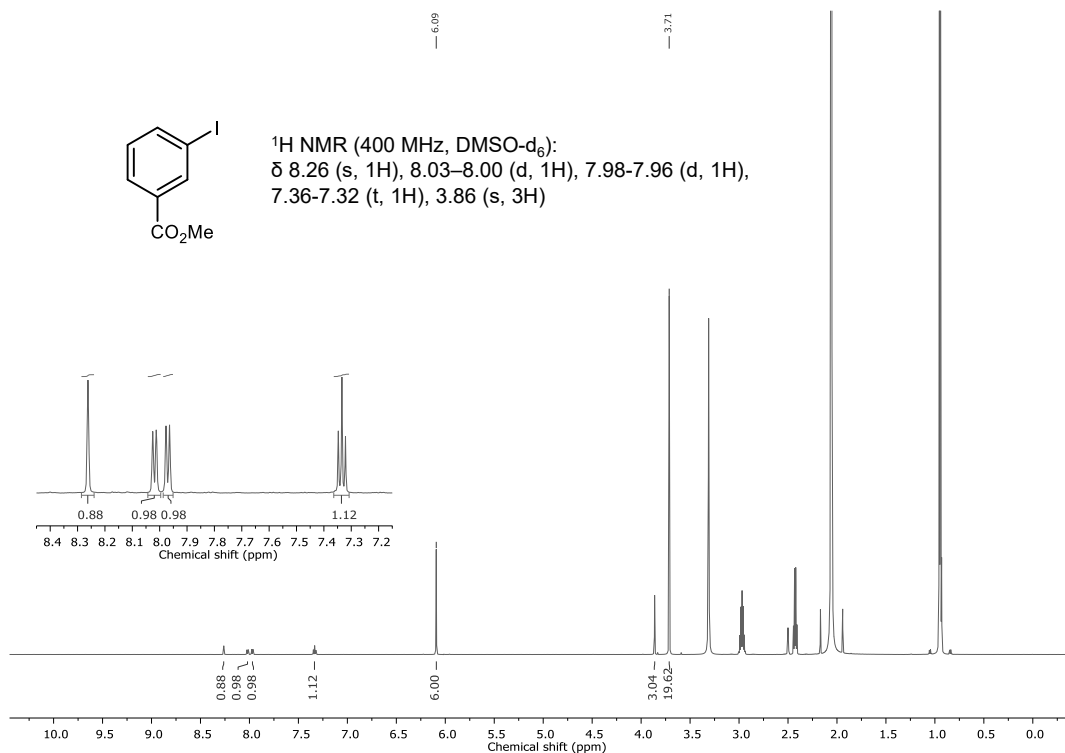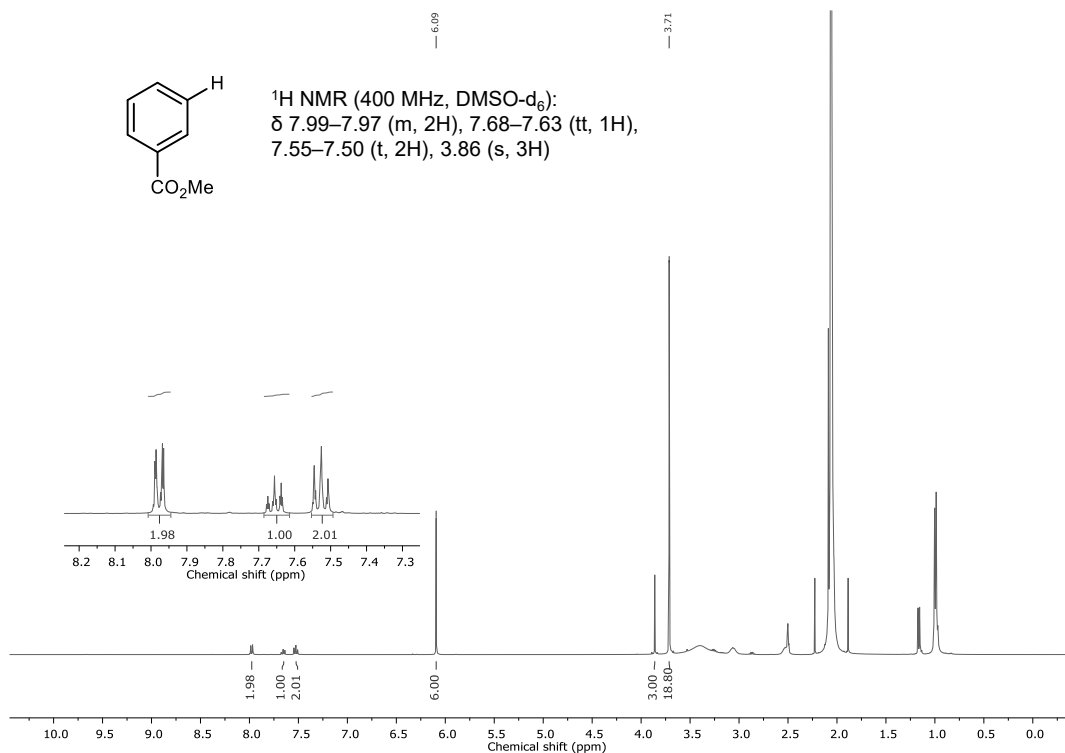*Substrate screening (methyl 4-bromobenzoate), 0 h*

^{1}H NMR (400 MHz, DMSO-d$_6$):
δ 8.00–7.85 (dd, 2H), 7.75–7.70
(dd, 2H), 3.7 (s, 3H)

Substrate screening (methyl 4-bromobenzoate), 8 h
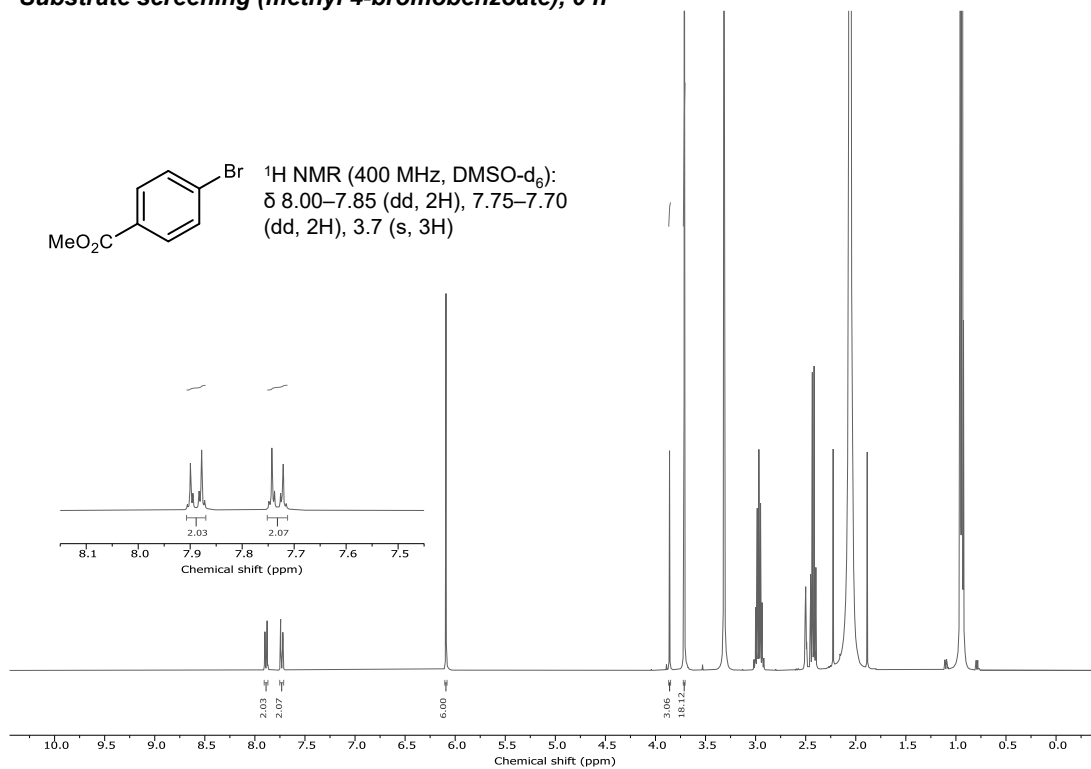
^{1}H NMR (400 MHz, DMSO-d$_6$):
δ 7.99–7.97 (m, 2H), 7.68–7.63 (tt, 1H),
7.55–7.50 (t, 2H), 3.86 (s, 3H)
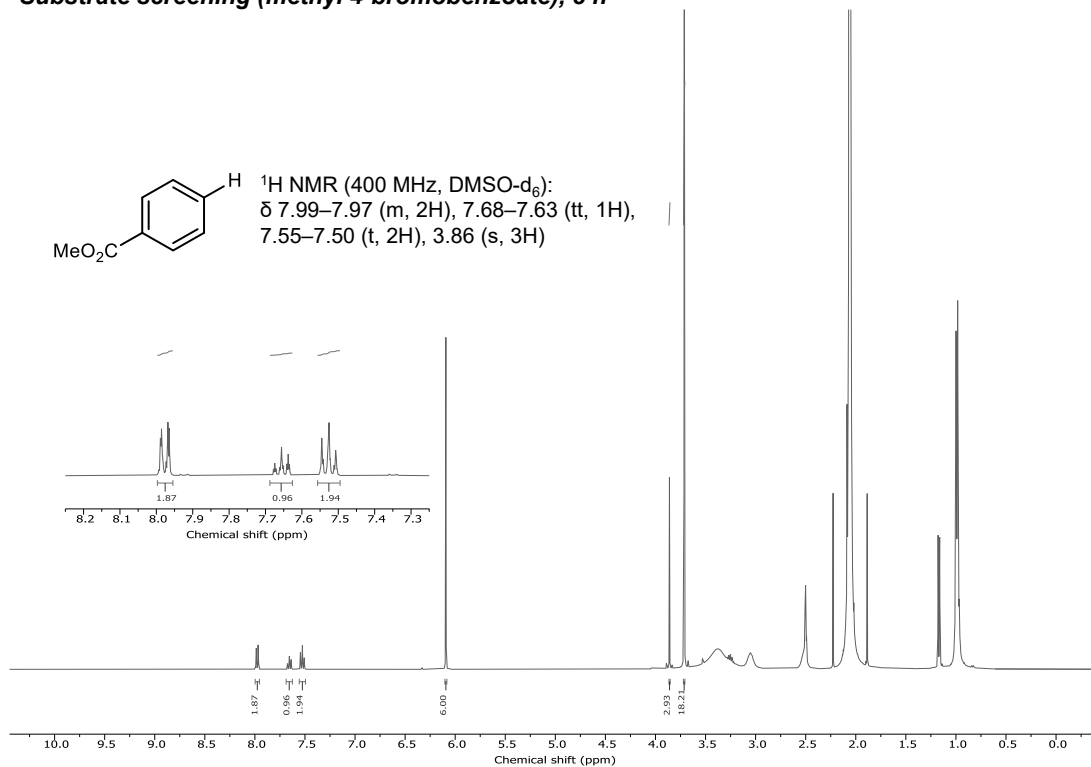
Figure A5.24 ^{1}H NMR data of photoredox reductive dehalogenation for methyl 4-bromobenzoate (400 MHz, DMSO-d$_6$); TMB: δ 6.09 (s, 3H), 3.71 (s, 9H).
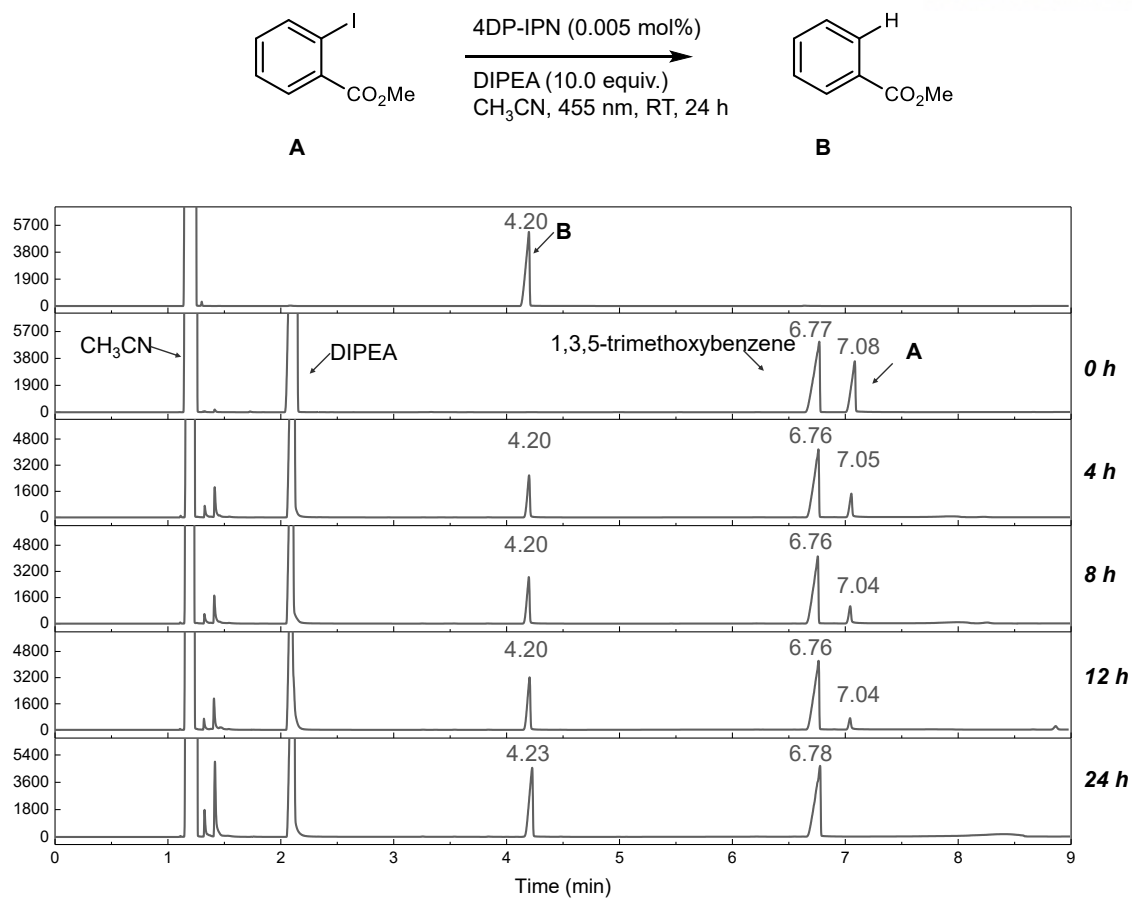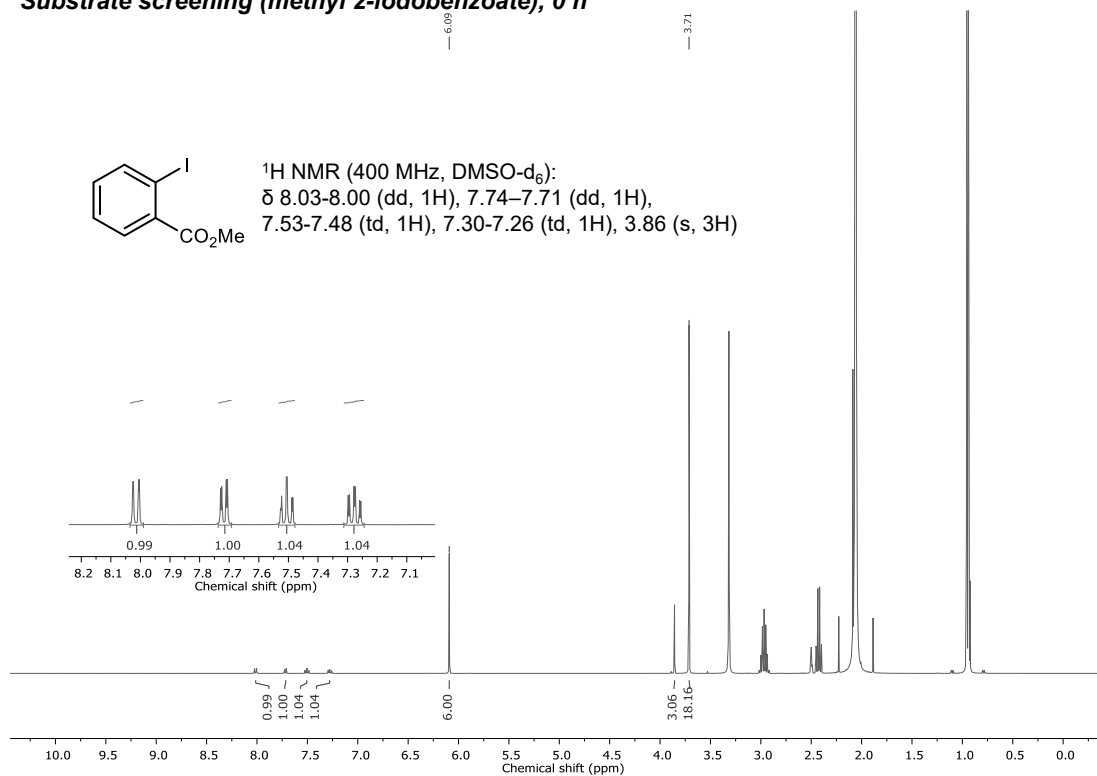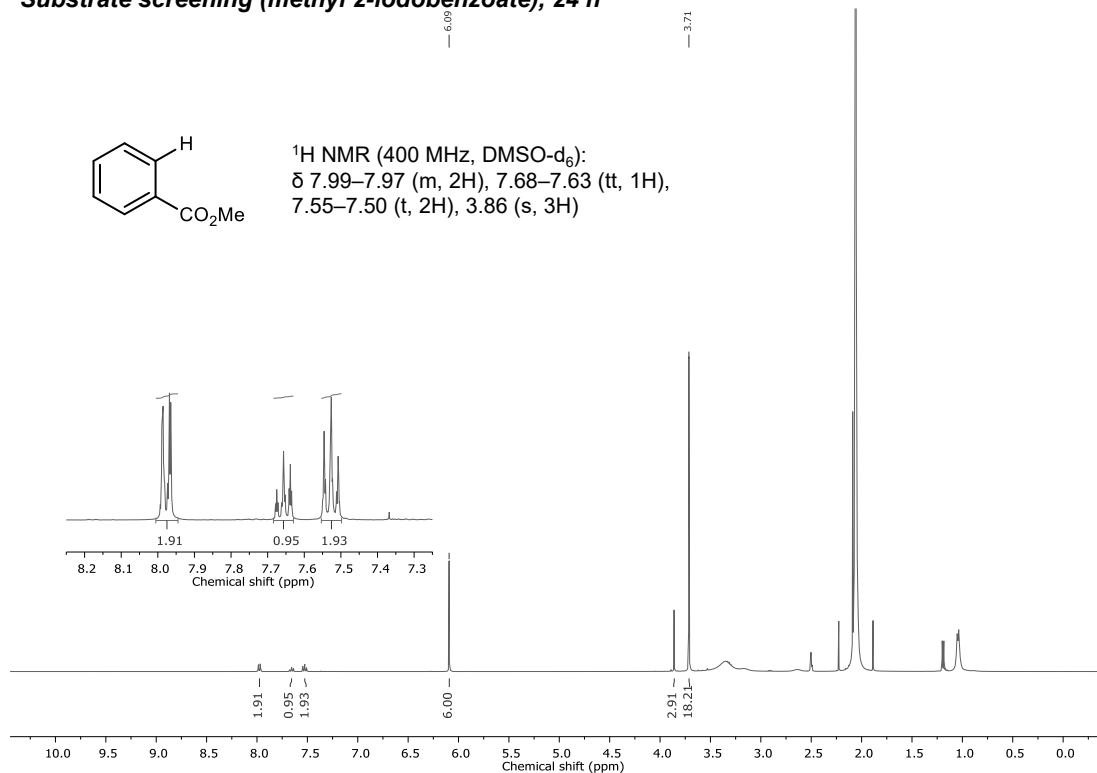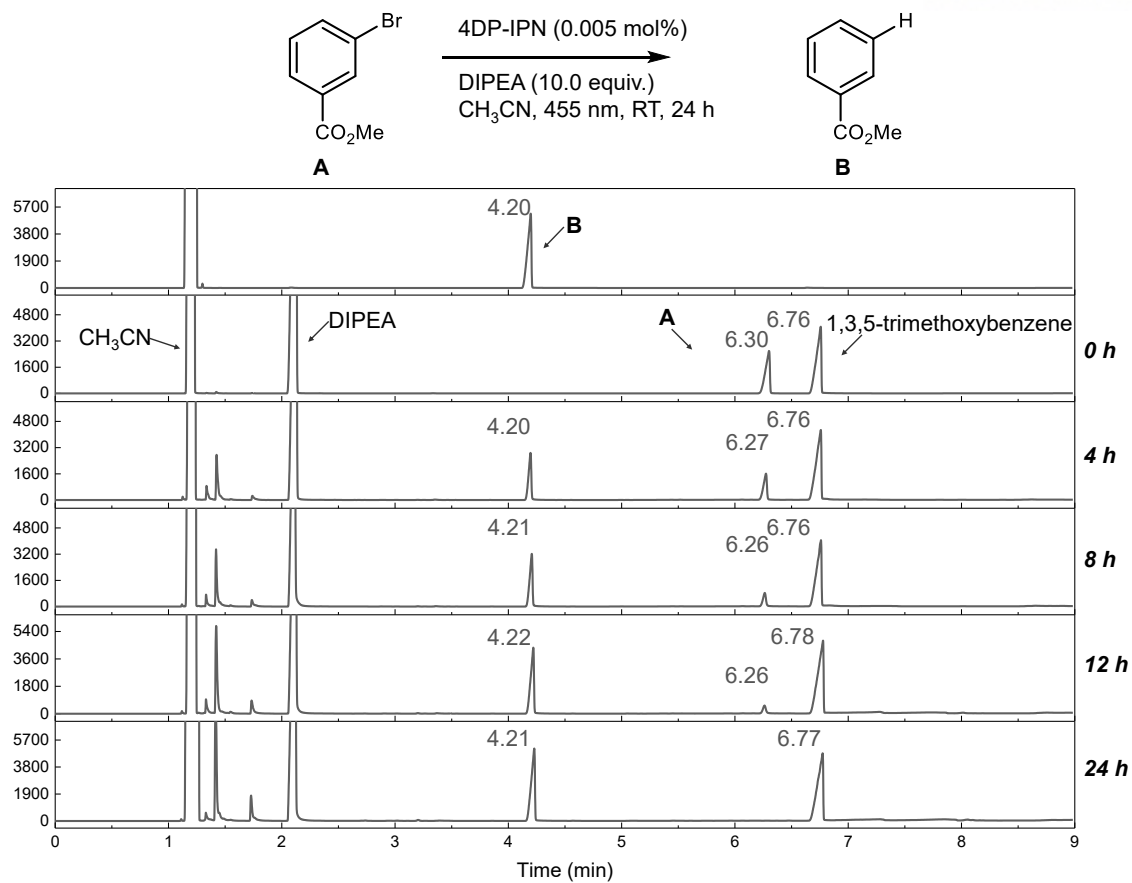
Figure A5.25 GC-FID spectra of photoredox reductive dehalogenation for methyl 3-bromobenzoate. Yield was measured by GC-FID using TMB as an internal standard.

Substrate screening (methyl 3-bromobenzoate), 0 h

^{1}H NMR (400 MHz, DMSO-d$_6$):
δ 8.07 (t, 1H), 7.98-7.96 (dt, 1H),
7.88-7.85 (dt, 1H), 7.5 (t, 1H),
3.7 (s, 3H)

Substrate screening (methyl 3-bromobenzoate), 24 h
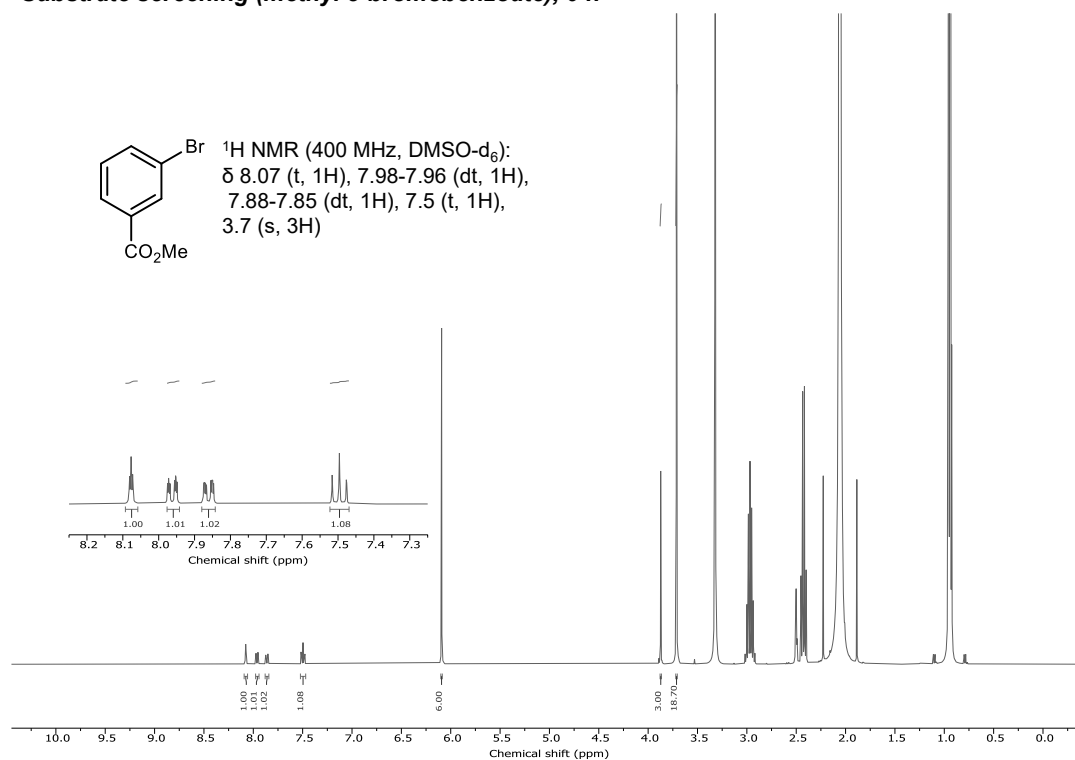
^{1}H NMR (400 MHz, DMSO-d$_6$):
δ 7.99–7.97 (m, 2H), 7.68–7.63 (tt,
1H), 7.55–7.50 (t, 2H), 3.86 (s, 3H)
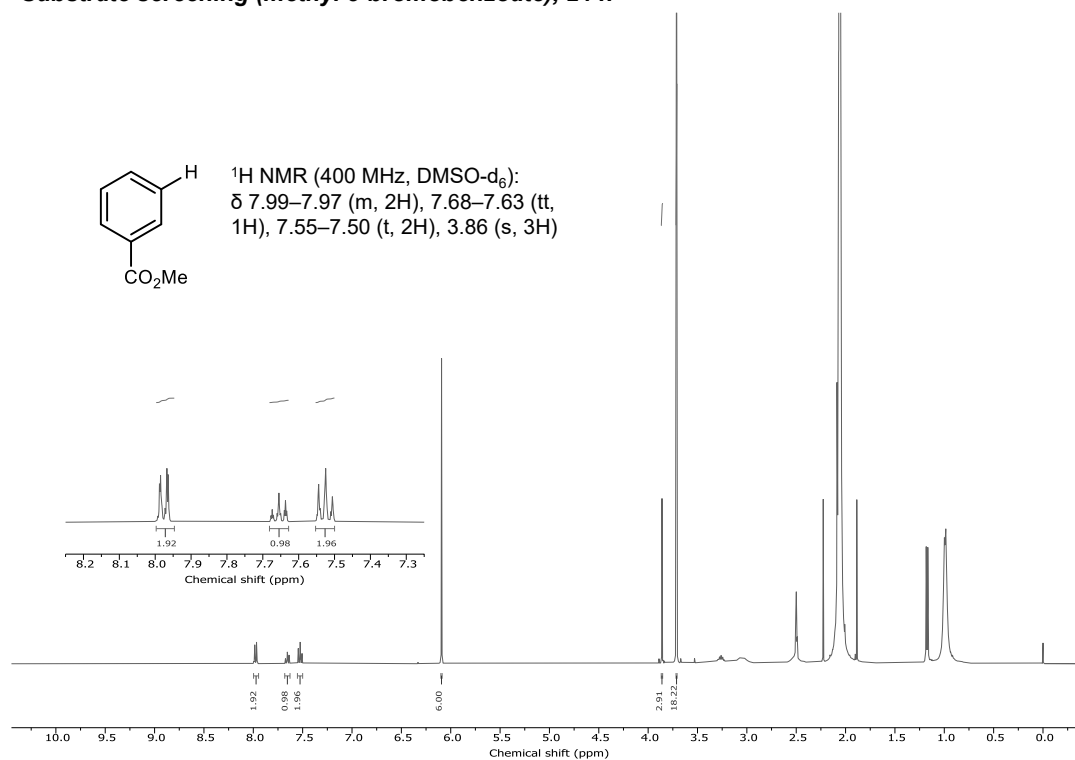
Figure A5.26 ^{1}H NMR data of photoredox reductive dehalogenation for methyl 3-bromobenzoate (400 MHz, DMSO-d$_6$); TMB: δ 6.09 (s, 3H), 3.71 (s, 9H).
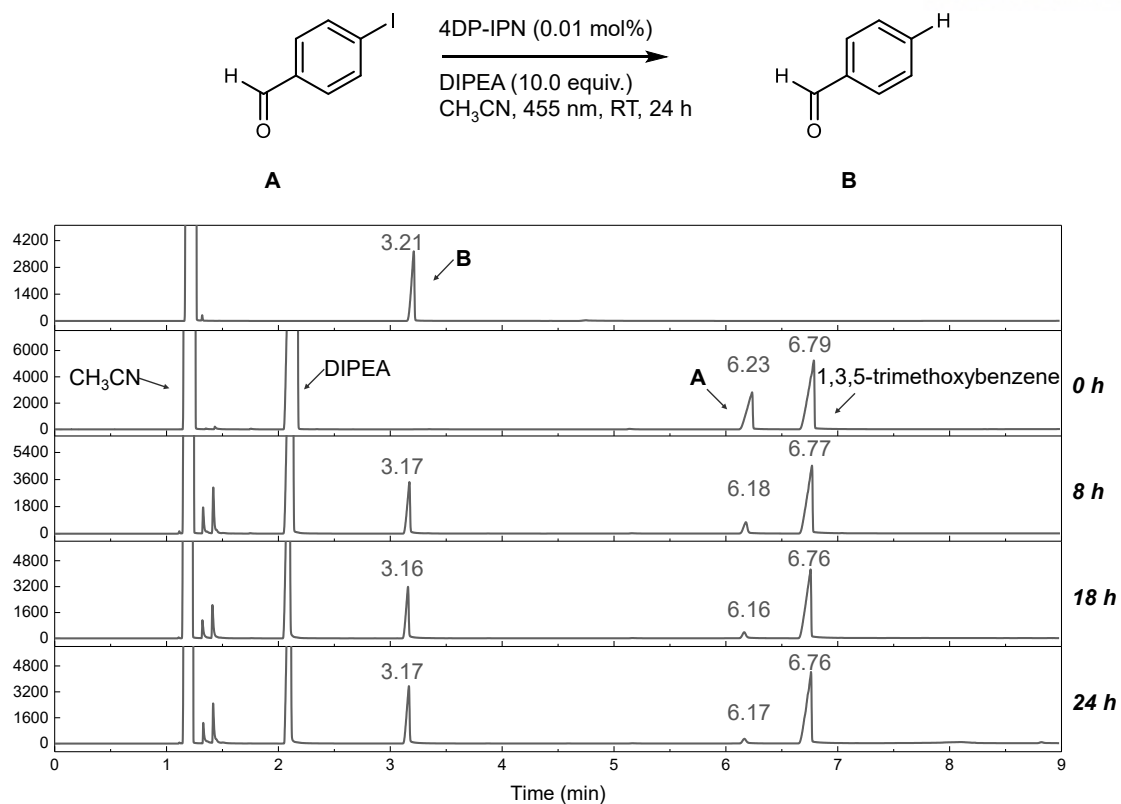
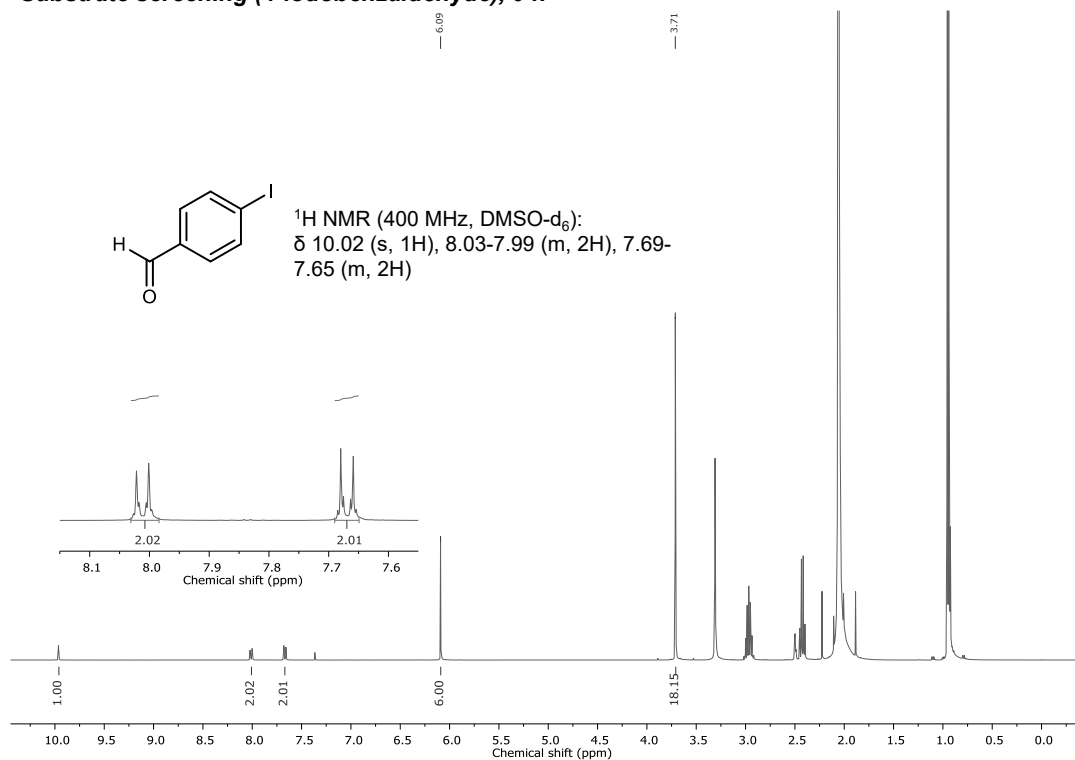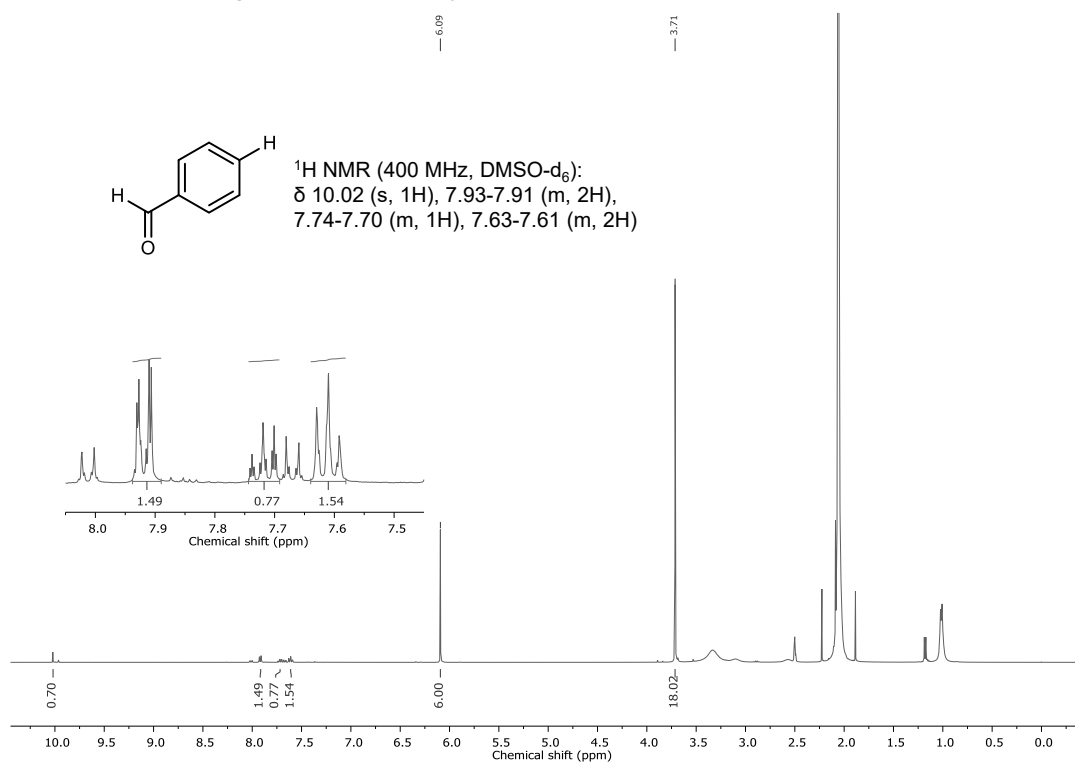**Figure A5.27** GC-FID spectra of photoredox reductive dehalogenation for methyl 2-bromobenzoate. Yield was measured by GC-FID using TMB as an internal standard.

Substrate screening (methyl 2-bromobenzoate), 0 h

^{1}H NMR (400 MHz, DMSO-d_6):
δ 7.78-7.75 (m, 2H), 7.53-7.47 (m, 2H), 7.88-7.85 (td, 1H), 7.5 (t, 1H), 3.7 (s, 3H)

Substrate screening (methyl 2-bromobenzoate), 12 h
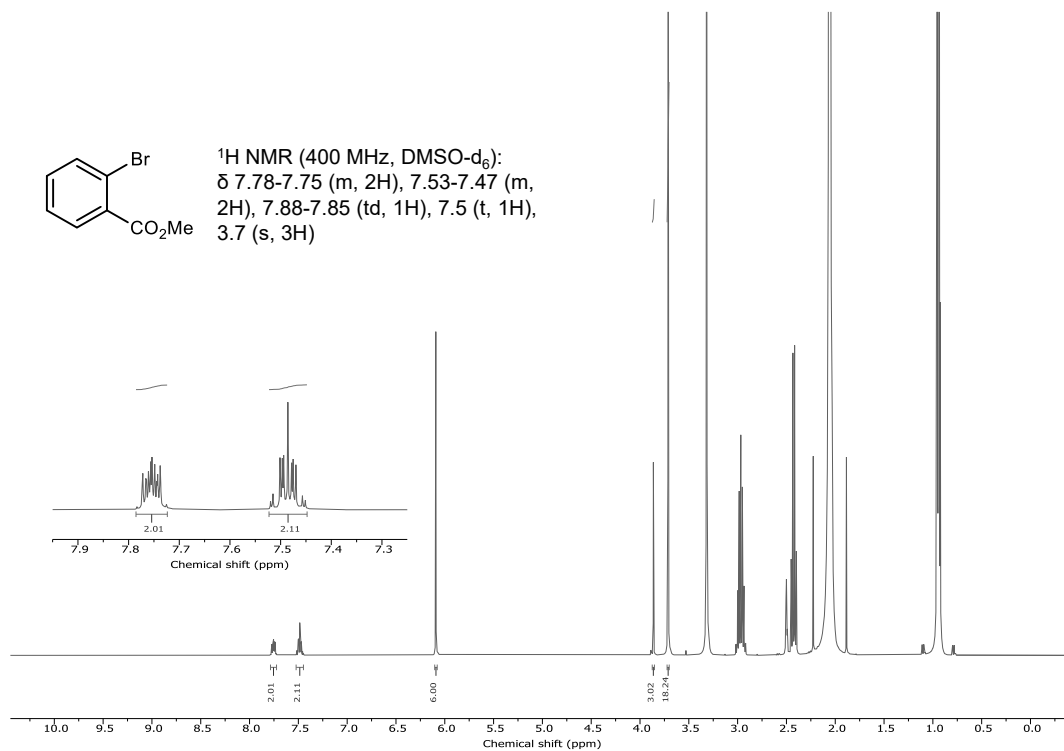
^{1}H NMR (400 MHz, DMSO-d_6):
δ 7.99–7.97 (m, 2H), 7.68–7.63 (tt, 1H), 7.55–7.50 (t, 2H), 3.86 (s, 3H)
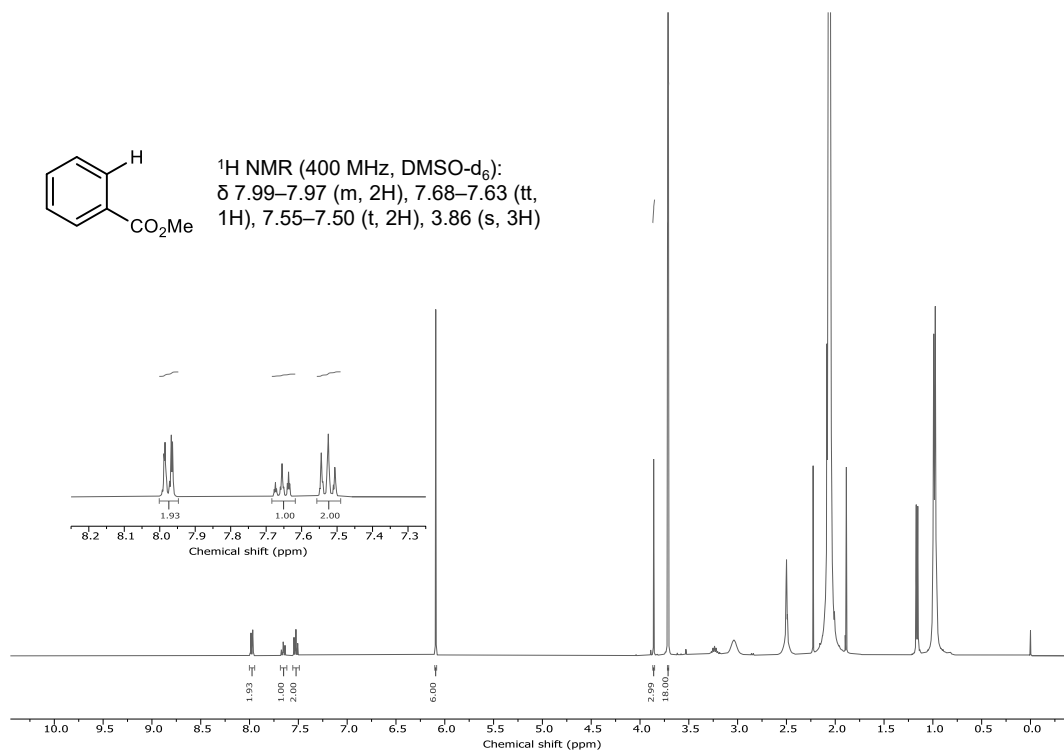
Figure A5.28 ^{1}H NMR data of photoredox reductive dehalogenation for methyl 2-bromobenzoate (400 MHz, DMSO-d_6); TMB: δ 6.09 (s, 3H), 3.71 (s, 9H).
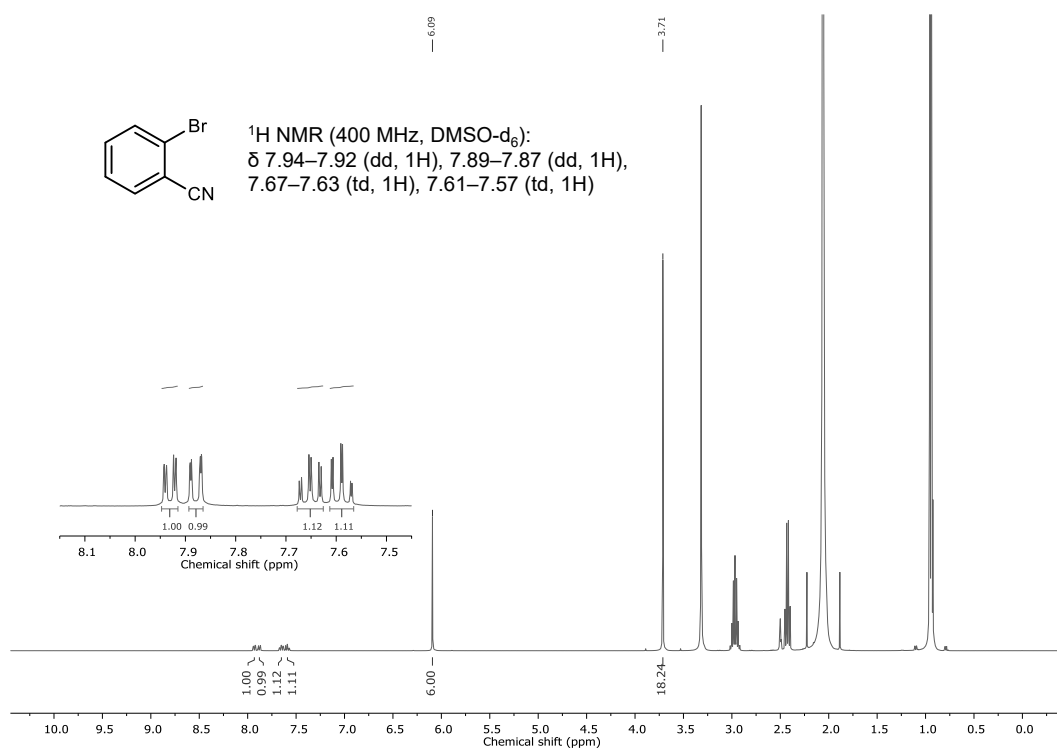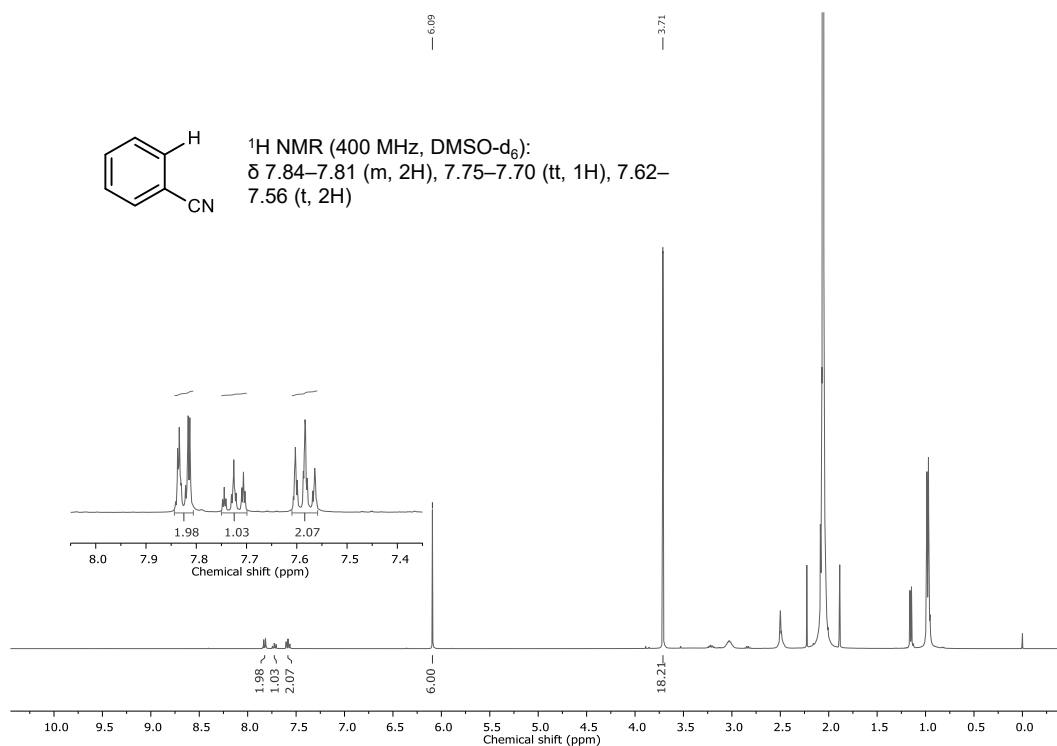
131
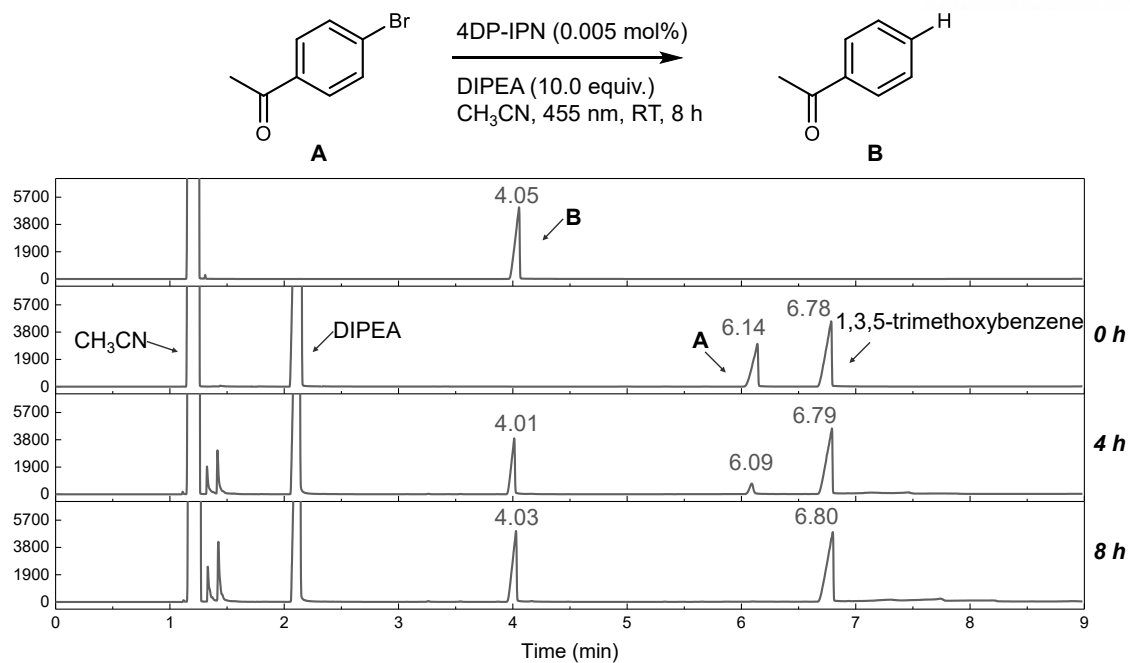
Figure A5.29 GC-FID spectra of photoredox reductive dehalogenation for 4-bromoacetophenone. Yield was measured by GC-FID using TMB as an internal standard.

Substrate screening (4-bromoacetophenone), 0 h

¹H NMR (400 MHz, DMSO-d₆):
δ 7.93-7.87 (dt, 2H), 7.75–7.73 (dt, 2H)

Substrate screening (4-bromoacetophenone), 8 h
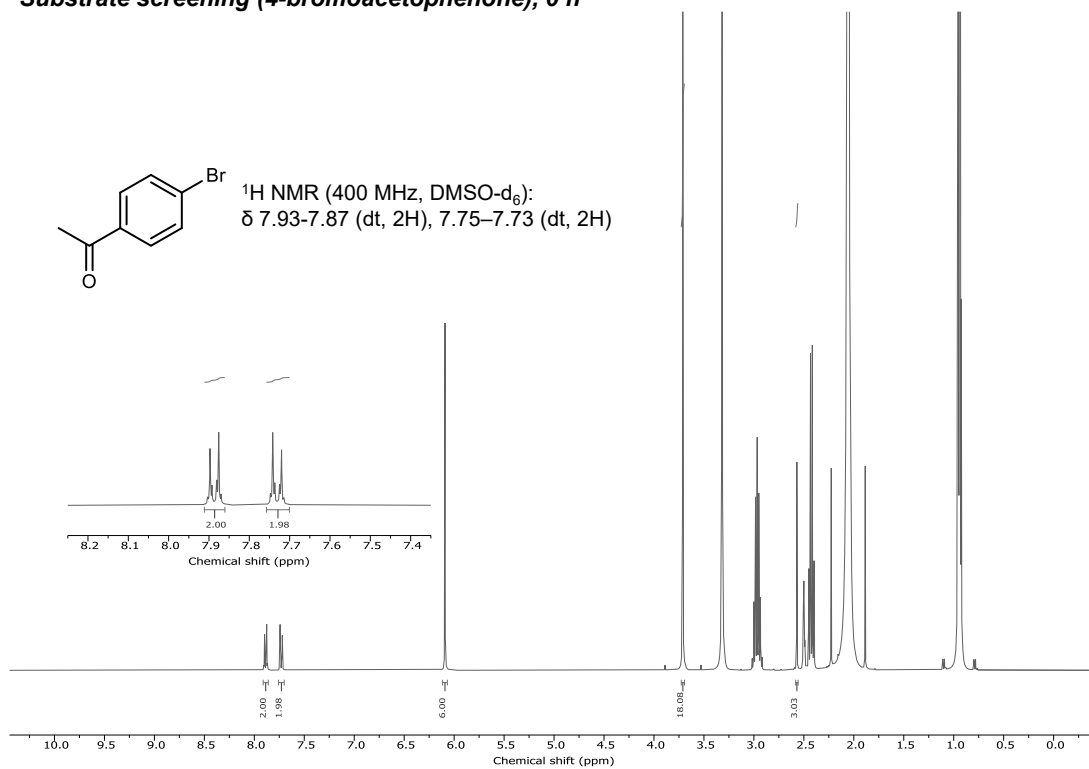
¹H NMR (400 MHz, DMSO-d₆):
δ 7.99–7.94 (dt, 2H), 7.68–7.63
(tt, 1H), 7.55–7.50 (t, 2H)
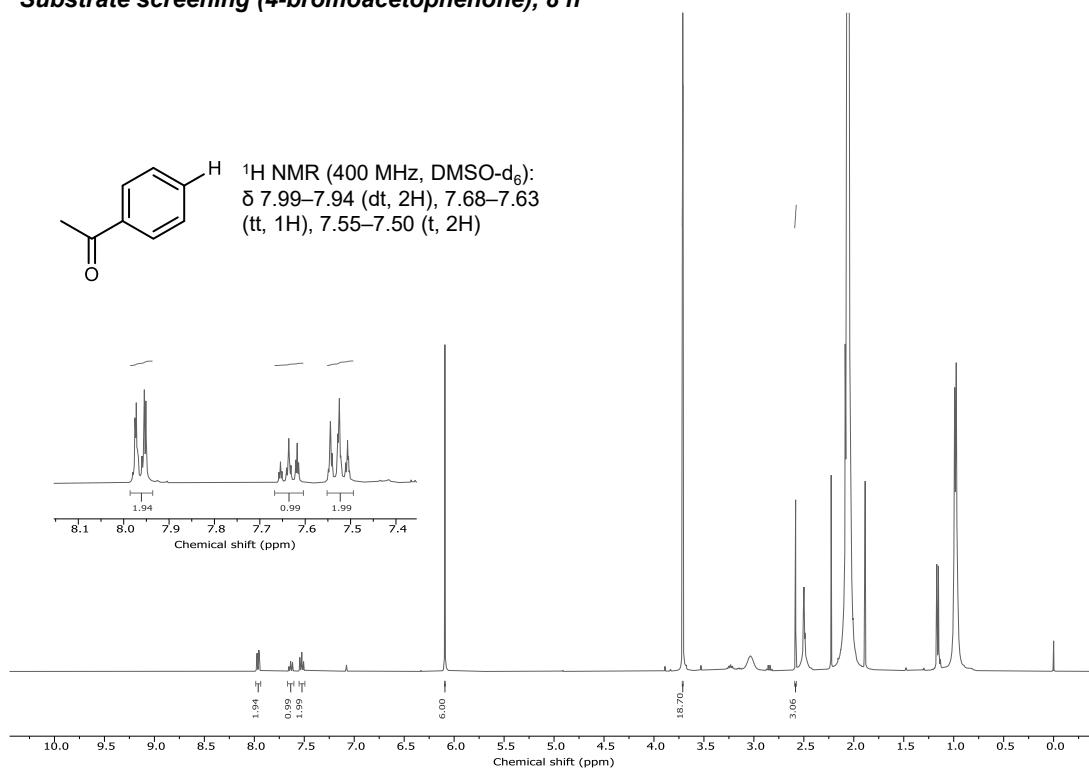
Figure A5.30 ¹H NMR data of photoredox reductive dehalogenation for 4-bromoacetophenone (400
MHz, DMSO-d₆); TMB: δ 6.09 (s, 3H), 3.71 (s, 9H).
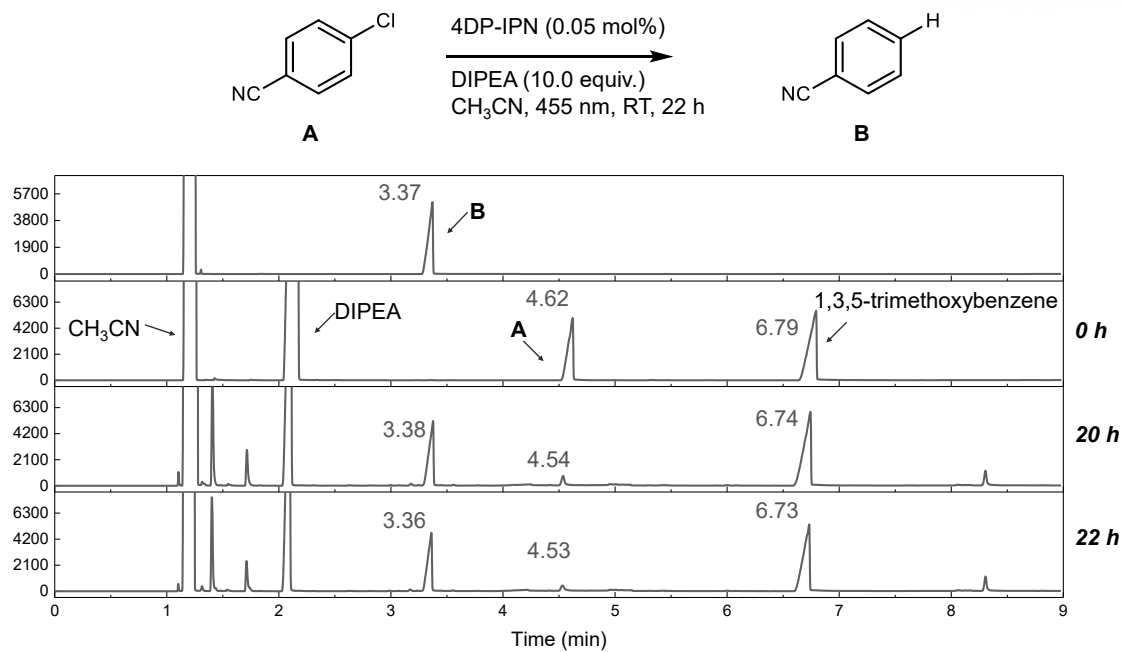
Figure A5.31 GC-FID spectra of photoredox reductive dehalogenation for 4-chlorobenzonitrile. Yield was measured by GC-FID using TMB as an internal standard.
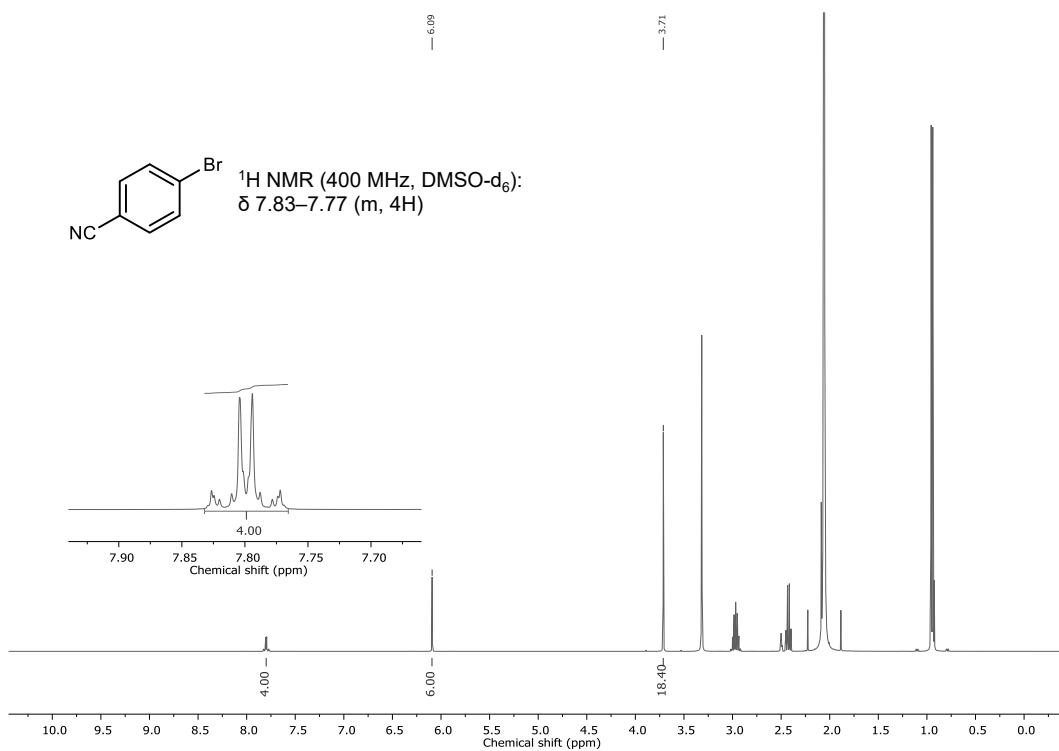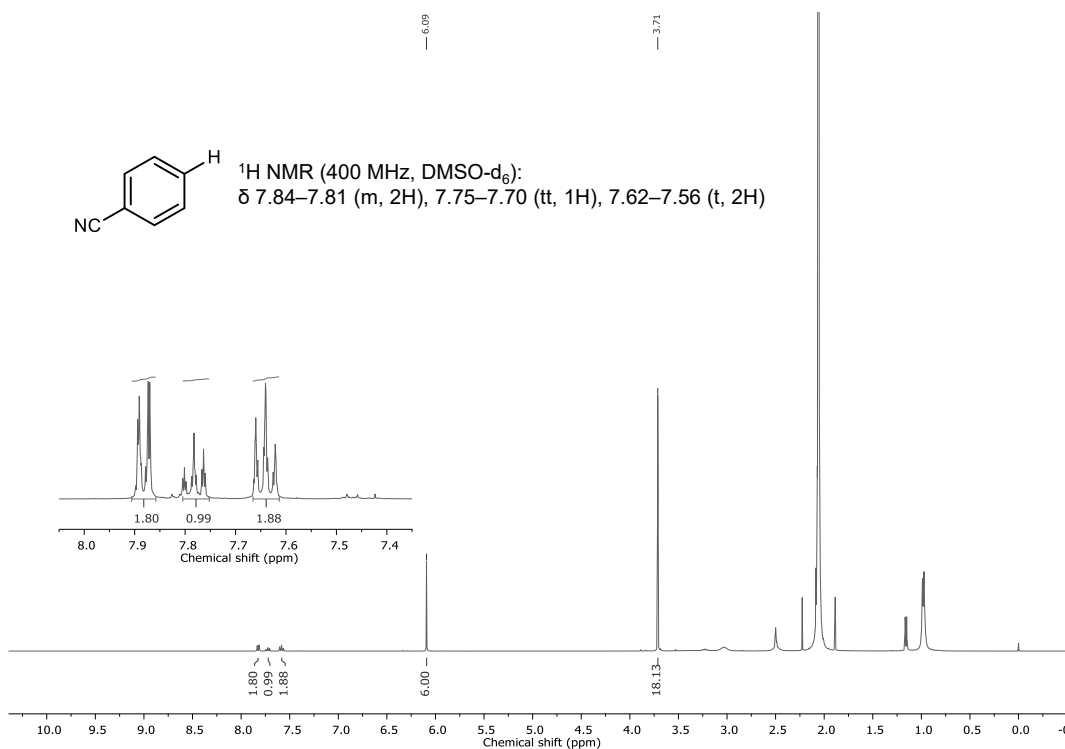
Substrate screening (4-chlorobenzonitrile), 0 h

^{1}H NMR (400 MHz, DMSO-d_6):
δ 7.87–7.85 (dt, 2H), 7.68–7.65 (dt, 2H)

Substrate screening (4-chlorobenzonitrile), 22 h
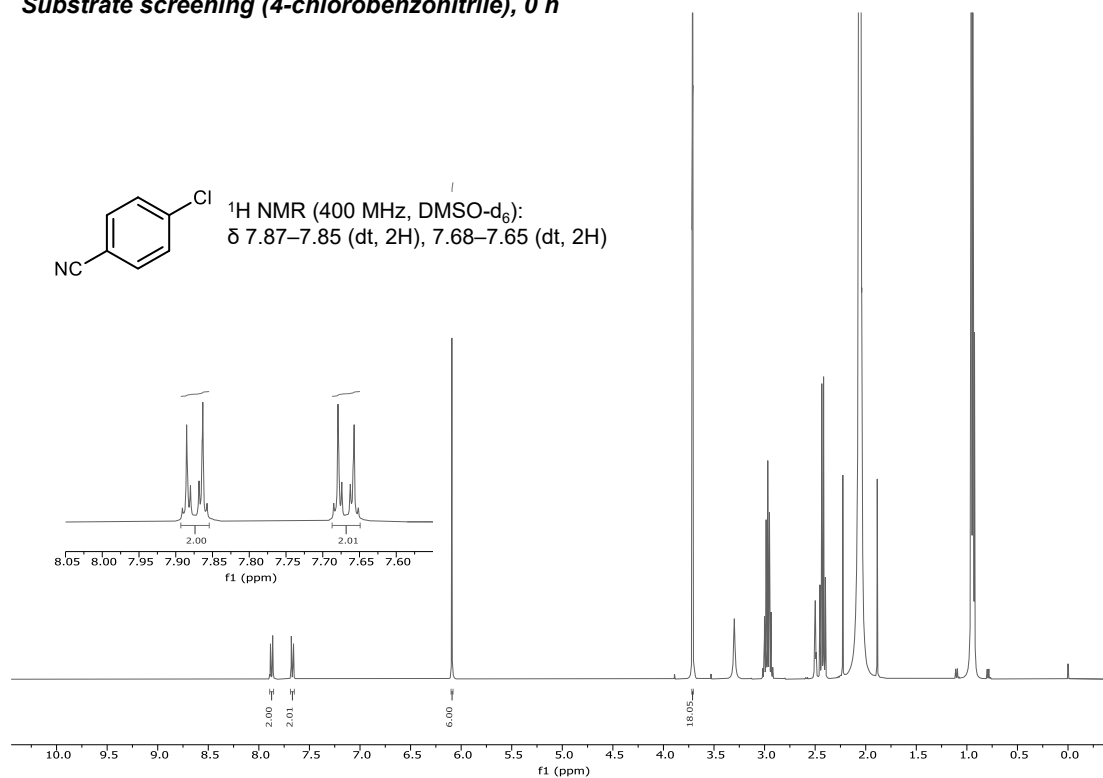
^{1}H NMR (400 MHz, DMSO-d_6):
δ 7.84–7.81 (m, 2H), 7.75–7.70
(tt, 1H), 7.62–7.56 (t, 2H)
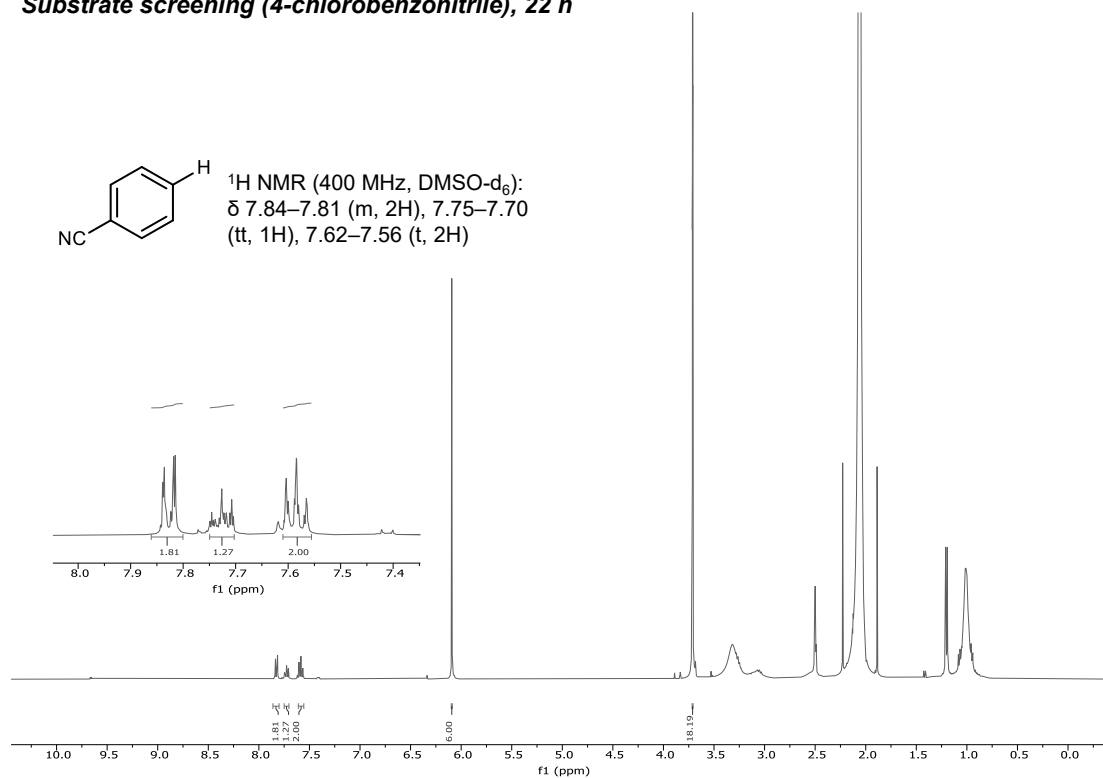
Figure A5.32 ^{1}H NMR data of photoredox reductive dehalogenation for 4-chlorobenzonitrile (400 MHz, DMSO-d_6); TMB: δ 6.09 (s, 3H), 3.71 (s, 9H).

135
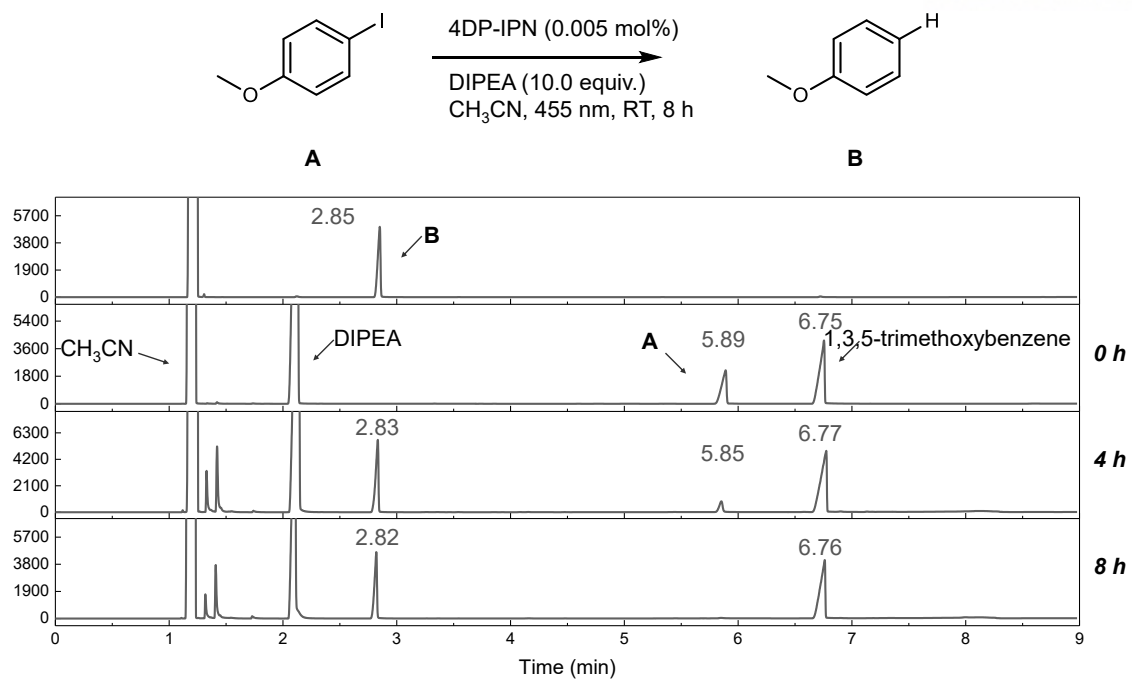
Figure A5.33 GC-FID spectra of photoredox reductive dehalogenation for 4-iodoanisole. Yield was measured by GC-FID using TMB as an internal standard.

Substrate screening (4-iodoanisole), 0 h

^{1}H NMR (400 MHz, DMSO-d_6):
δ 7.61-7.57 (m, 2H), 6.80-6.77 (m, 2H),
3.74 (s, 3H)

Substrate screening (4-iodoanisole), 8 h
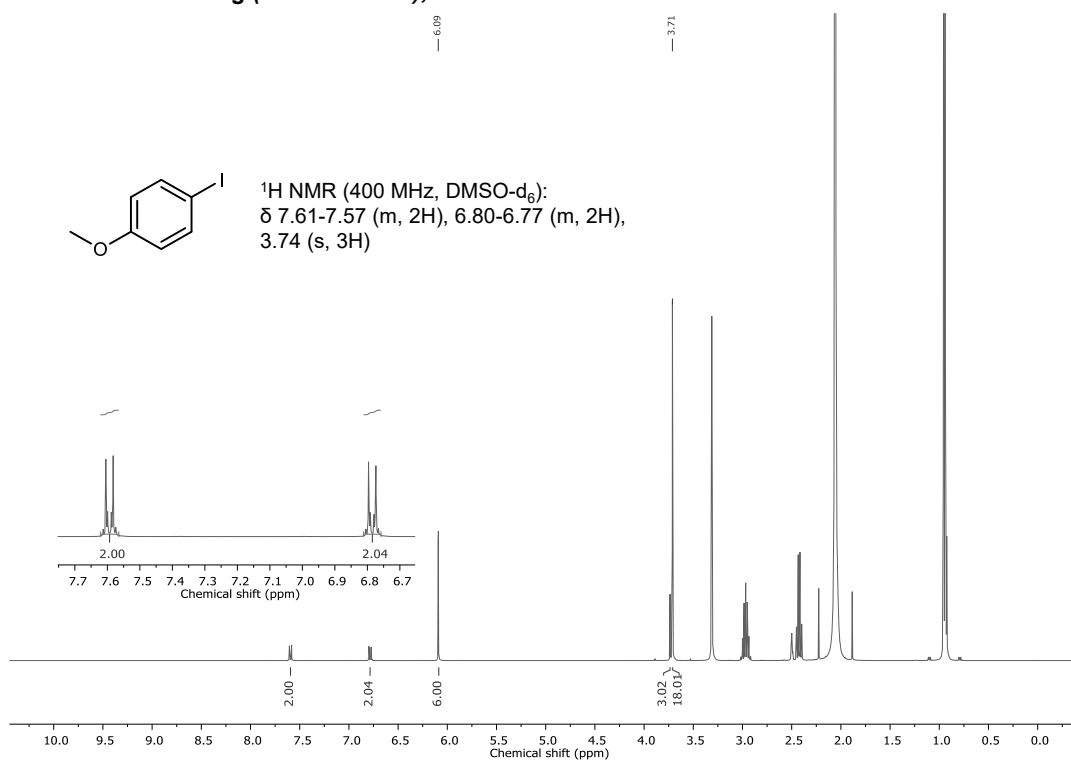
^{1}H NMR (400 MHz, DMSO-d_6):
δ 7.32-7.26 (m, 2H), 6.95-6.91
(m, 3H), 3.75 (s, 3H)

Figure A5.34 ^{1}H NMR data of photoredox reductive dehalogenation for 4-iodoanisole (400 MHz, DMSO-d_6); TMB: δ 6.09 (s, 3H), 3.71 (s, 9H).
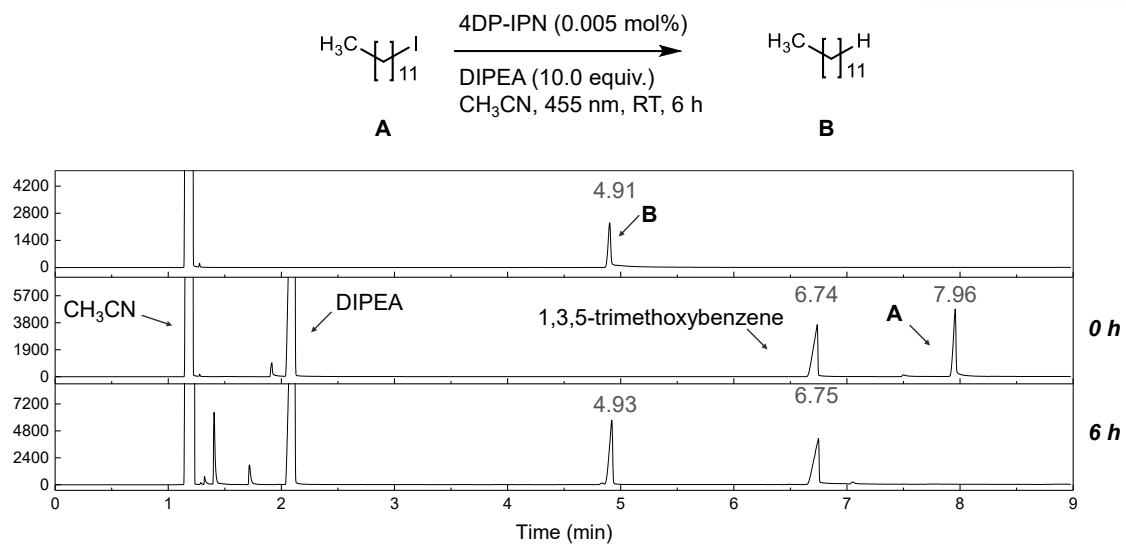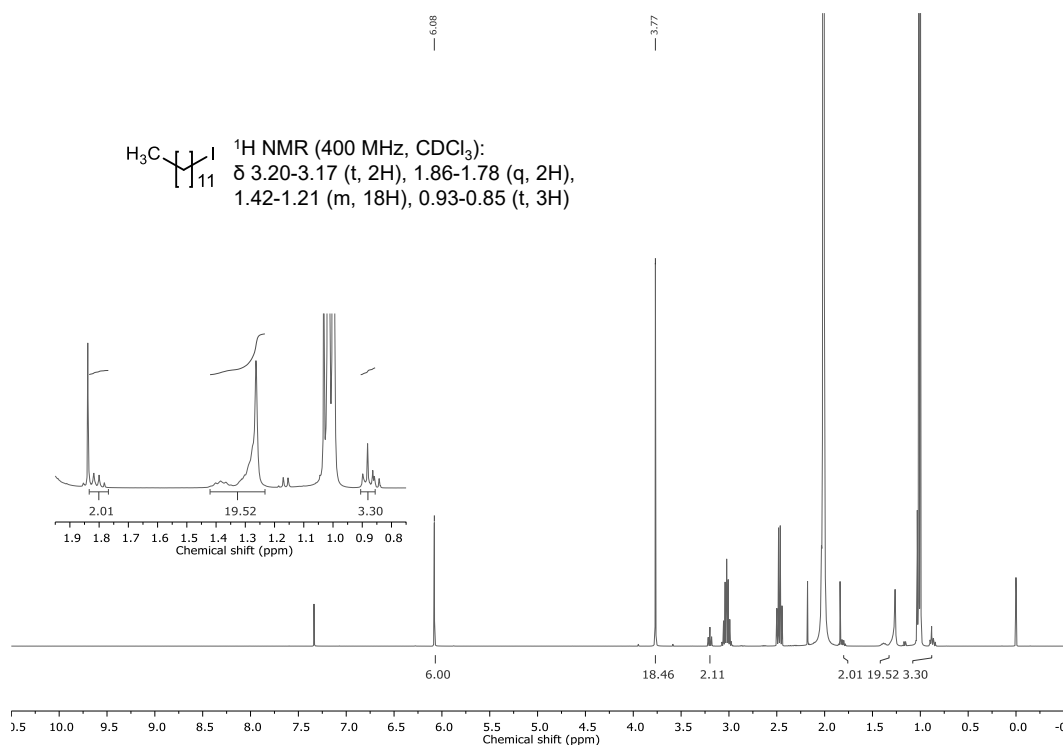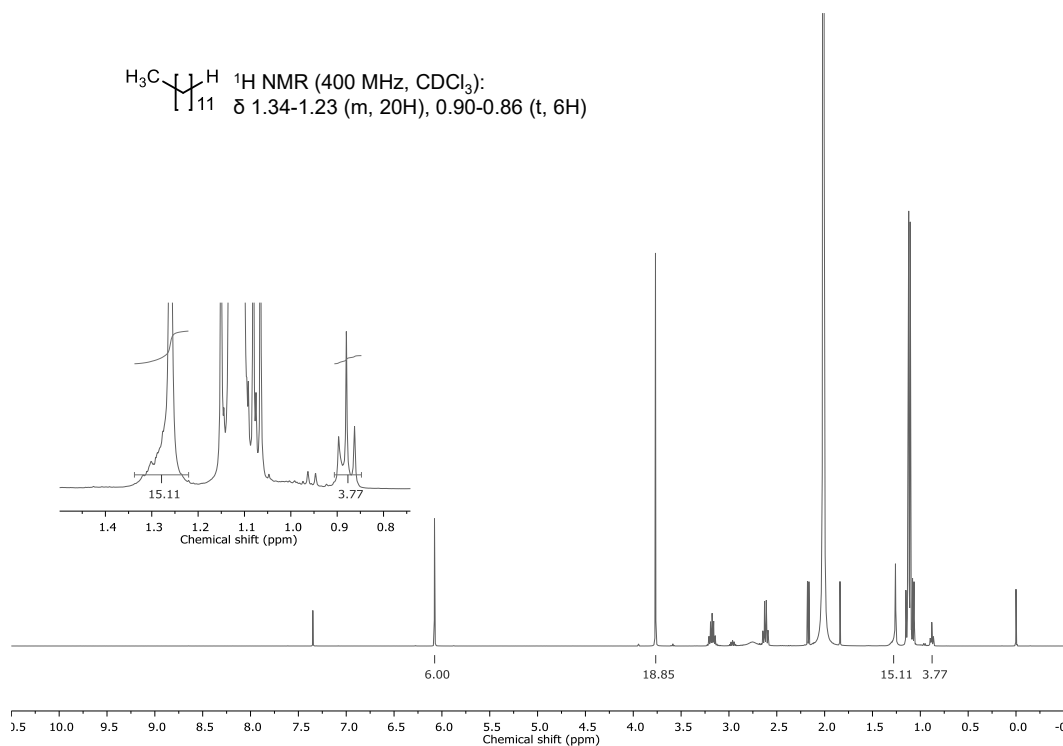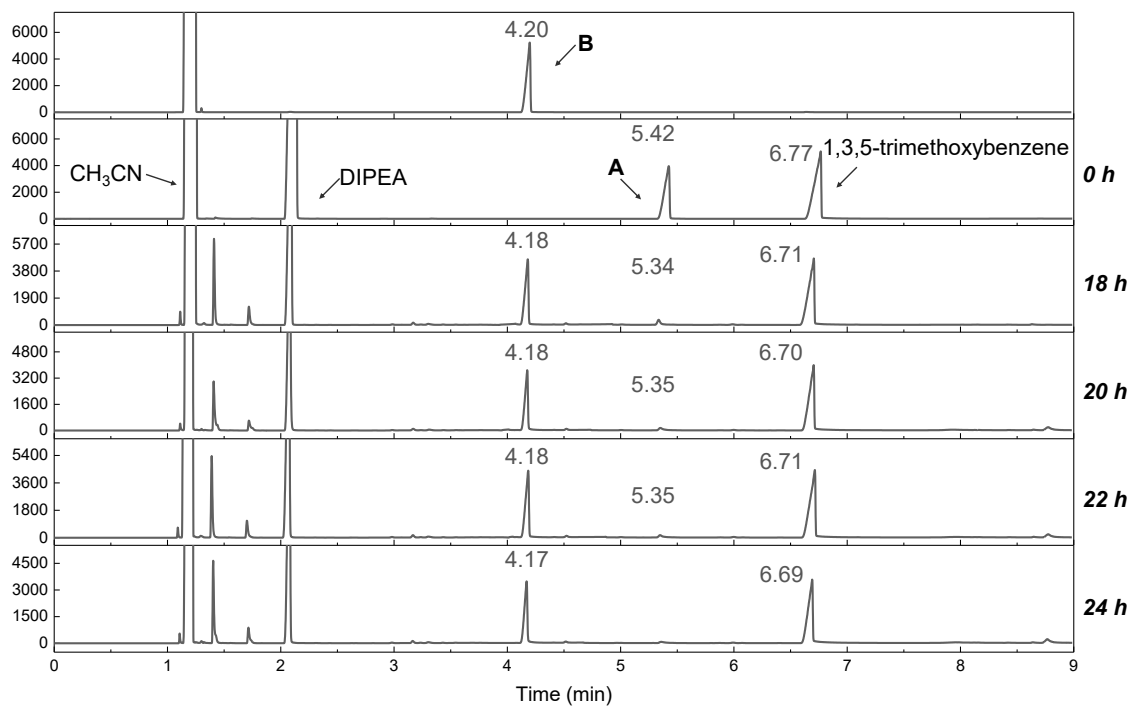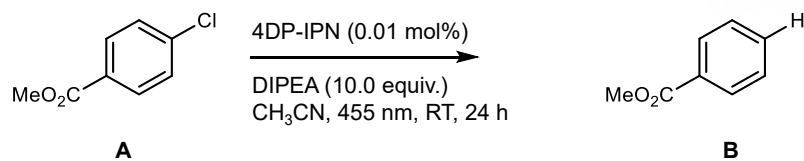
Figure A5.35 GC-FID spectra of photoredox reductive dehalogenation for methyl 4-chlorobenzoate. Yield was measured by GC-FID using TMB as an internal standard.

Substrate screening (methyl 4-chlorobenzoate), 0 h

^{1}H NMR (400 MHz, DMSO-d$_6$):
δ 8.00–7.95 (dd, 2H), 7.61–7.57 (dd, 2H), 3.8 (s, 3H)

Substrate screening (methyl 4-chlorobenzoate), 24 h
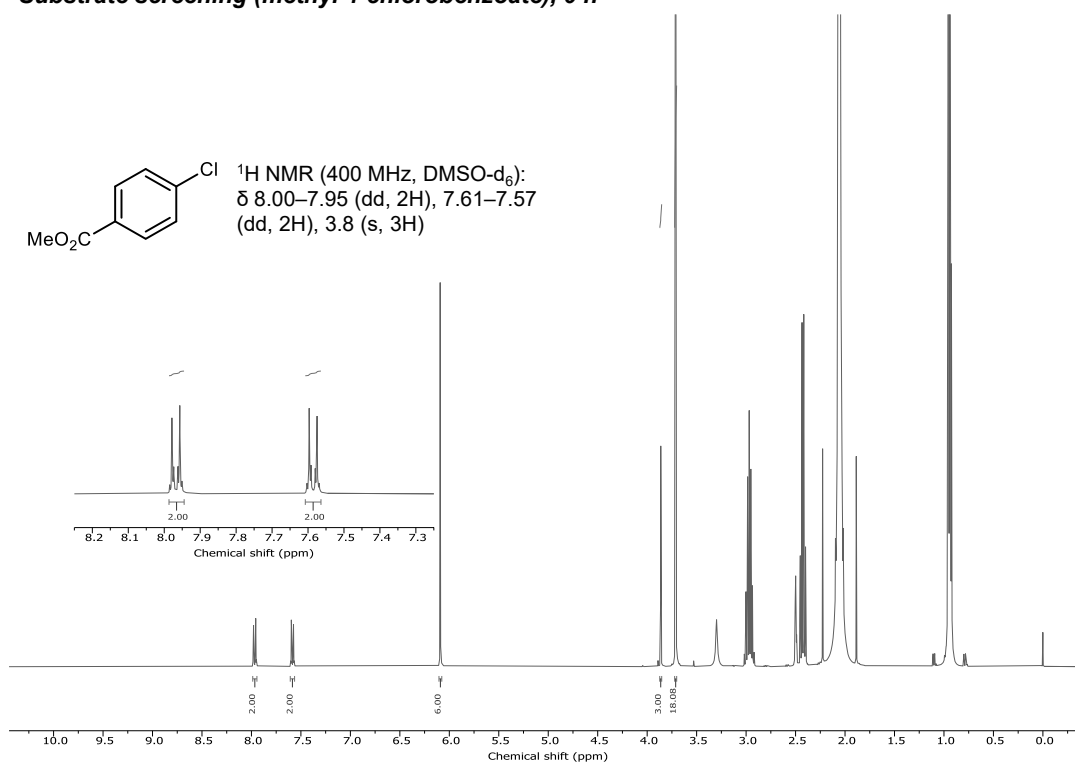
^{1}H NMR (400 MHz, DMSO-d$_6$):
δ 7.99–7.97 (m, 2H), 7.68–7.63 (tt, 1H), 7.55–7.50 (t, 2H), 3.86 (s, 3H)
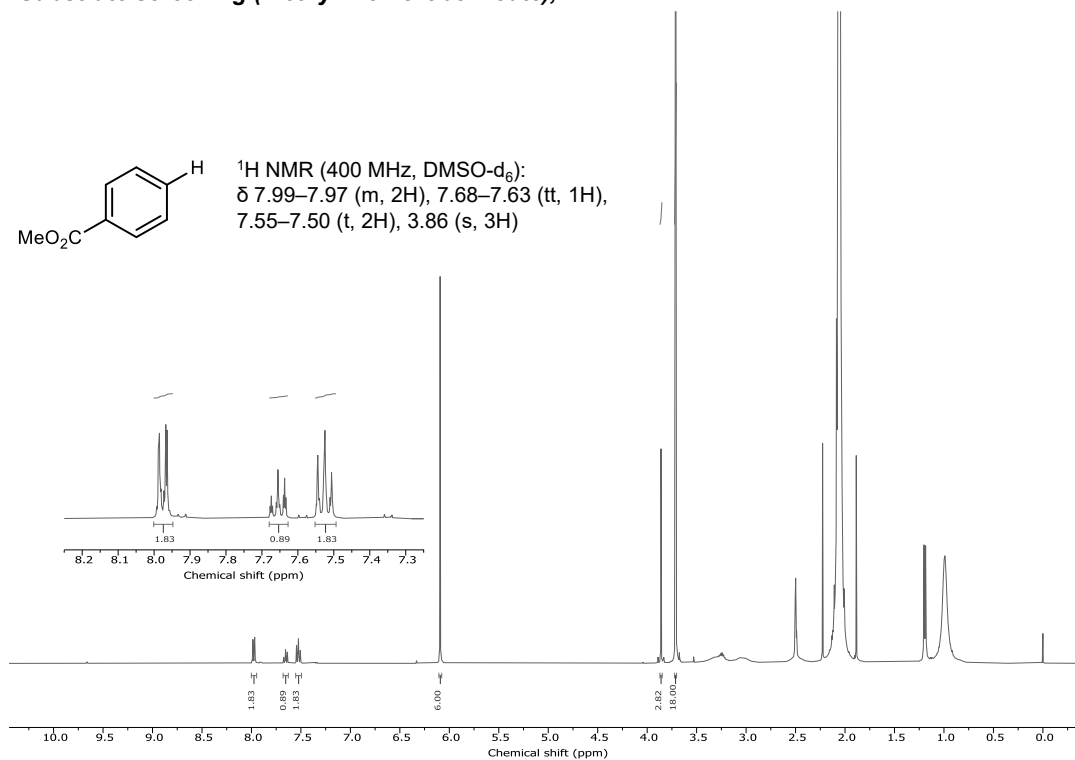
Figure A5.36 ^{1}H NMR data of photoredox reductive dehalogenation for methyl 4-chlorobenzoate (400 MHz, DMSO-d$_6$); TMB: δ 6.09 (s, 3H), 3.71 (s, 9H).
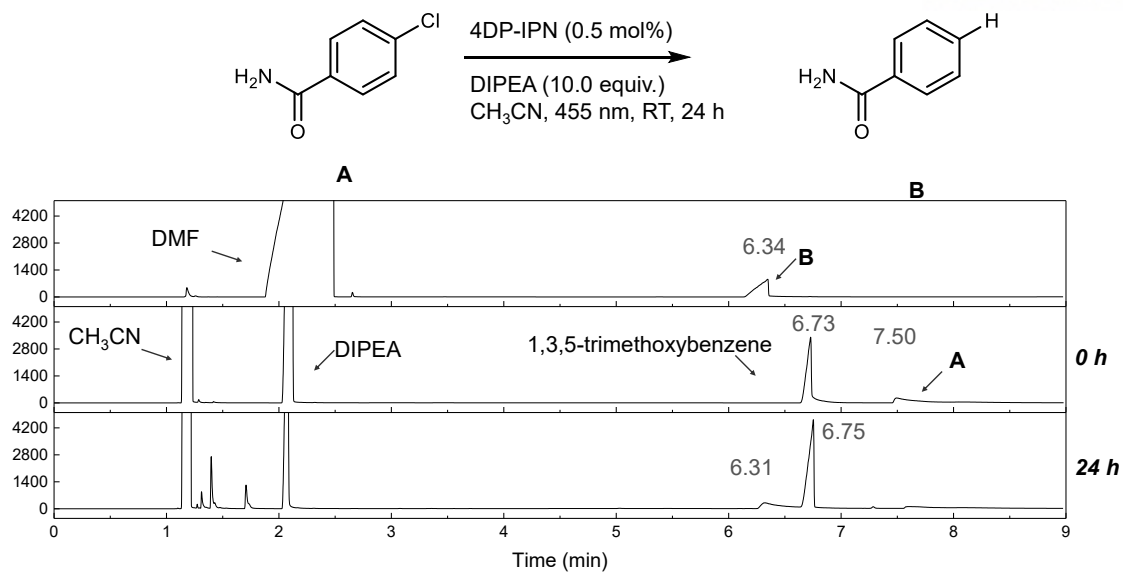
Figure A5.37 GC-FID spectra of photoredox reductive dehalogenation for 4-chlorobenzamide.

Substrate screening (4-chlorobenzamide), 0 h

^{1}H NMR (400 MHz, DMSO-d$_6$):
δ 8.08–7.95 (broad, 1H),
7.90–7.88 (dd, 2H), 7.55–7.48
(dd, 2H), 7.45–7.38 (broad, 1H)

Substrate screening (4-chlorobenzamide), 24 h
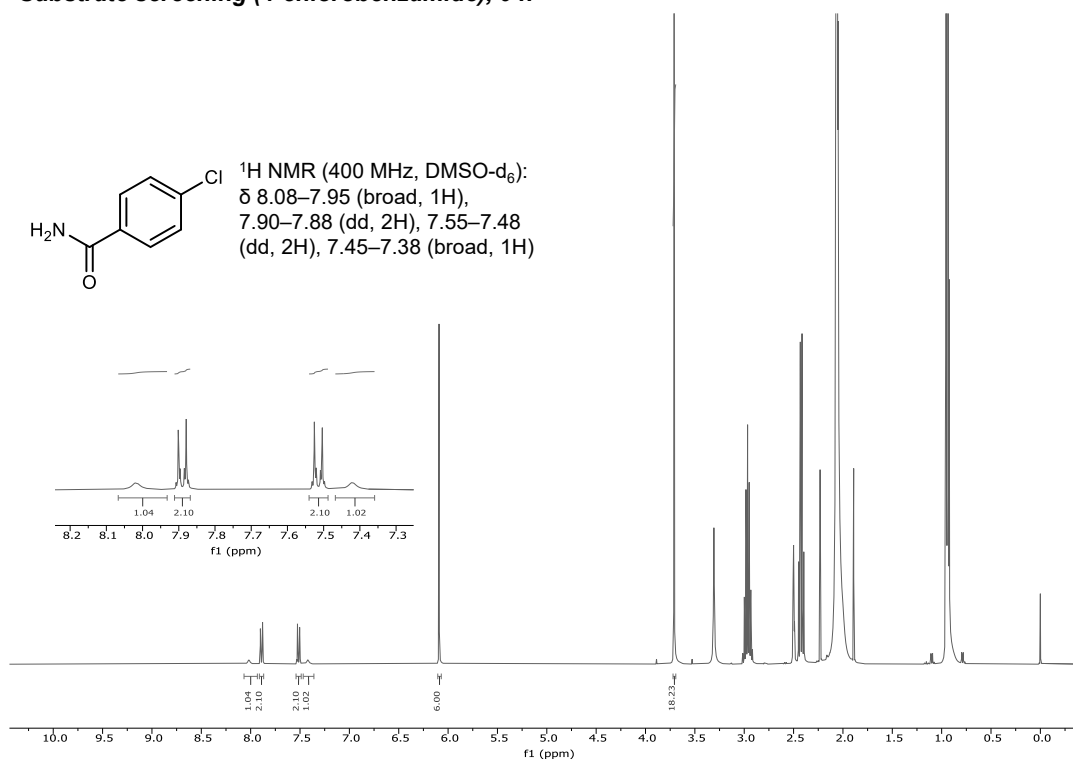
^{1}H NMR (400 MHz, DMSO-d$_6$):
δ 7.98–7.91 (broad, 1H), 7.90–7.85
(dd, 2H), 7.55–7.50 (dd, 1H), 7.45–
7.41 (t, 1H),
7.35–7.29 (broad, 1H)
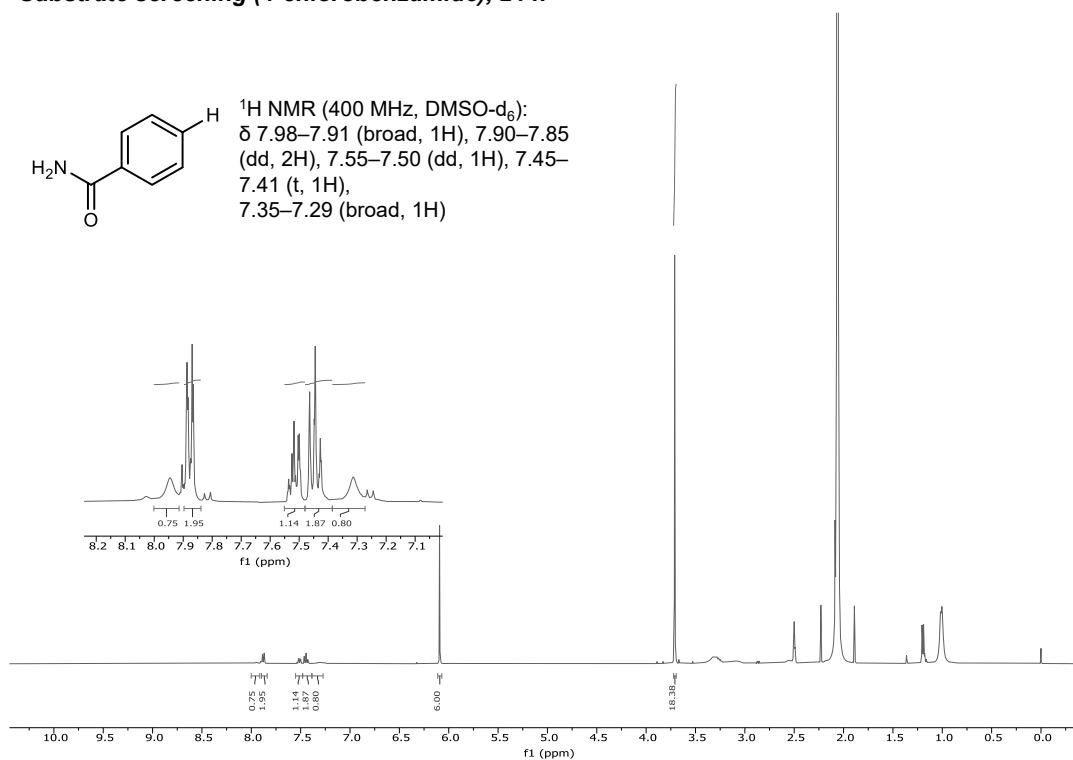
Figure A5.38 ^{1}H NMR data of photoredox reductive dehalogenation for 4-chlorobenzamide (400 MHz, DMSO-d$_6$): TMB: δ 6.09 (s, 3H), 3.71 (s, 9H). Yield was measured by ^{1}H NMR using TMB as an internal standard.
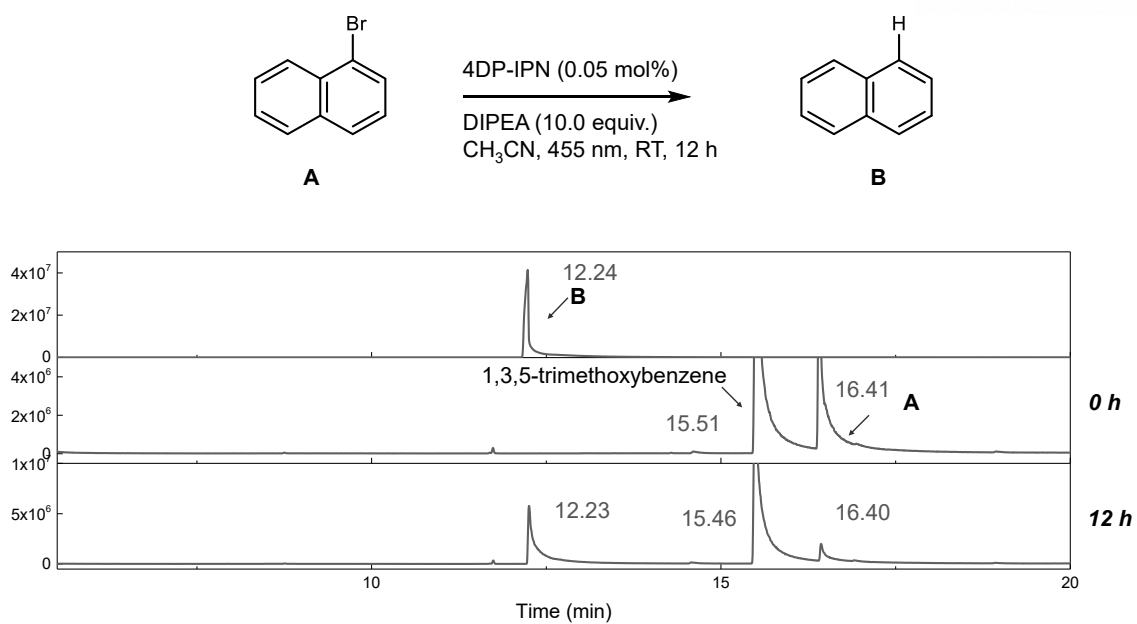
Figure A5.39 GC-FID spectra of photoredox reductive dehalogenation for 1-bromonaphthalene.

Substrate screening (1-bromonaphthalene), 0 h

^{1}H NMR (400 MHz, DMSO-d$_6$):
δ 8.17–8.12 (d, 1H) 8.01–7.96 (dd, 2H)
7.92–7.87 (d, 1H) 7.73–7.67 (dt, 1H)
7.66–7.60 (dt, 1H), 7.48–7.42 (t, 1H)

Substrate screening (1-bromonaphthalene), 12 h
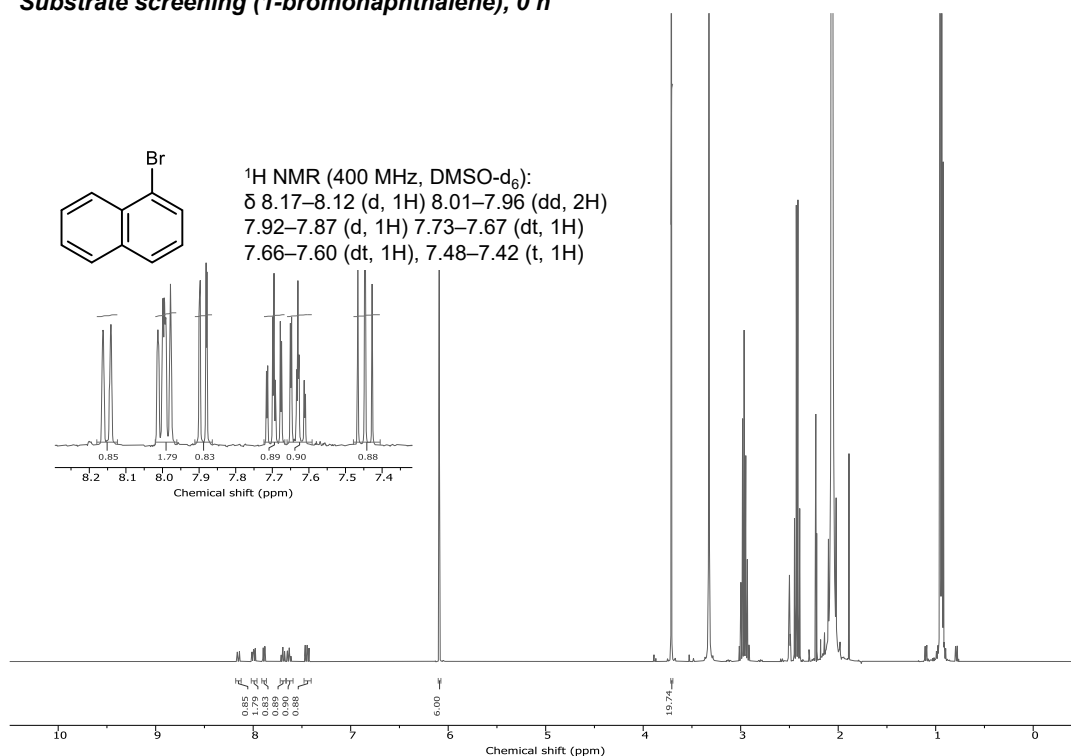
^{1}H NMR (400 MHz, DMSO-d$_6$):
δ 7.95–7.86 (dd, 4H), 7.54–7.46 (dd, 4H)

Figure A5.40 ^{1}H NMR data of photoredox reductive dehalogenation for 1-bromonaphthalene (400 MHz, DMSO-d$_6$); TMB: δ 6.09 (s, 3H), 3.71 (s, 9H). Yield was measured by ^{1}H NMR using TMB as an internal standard.
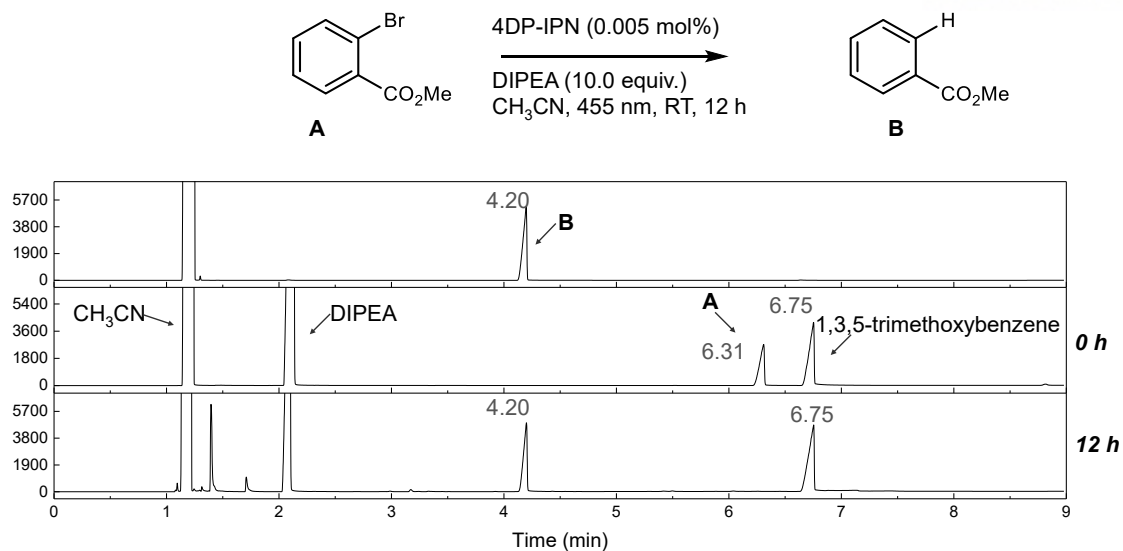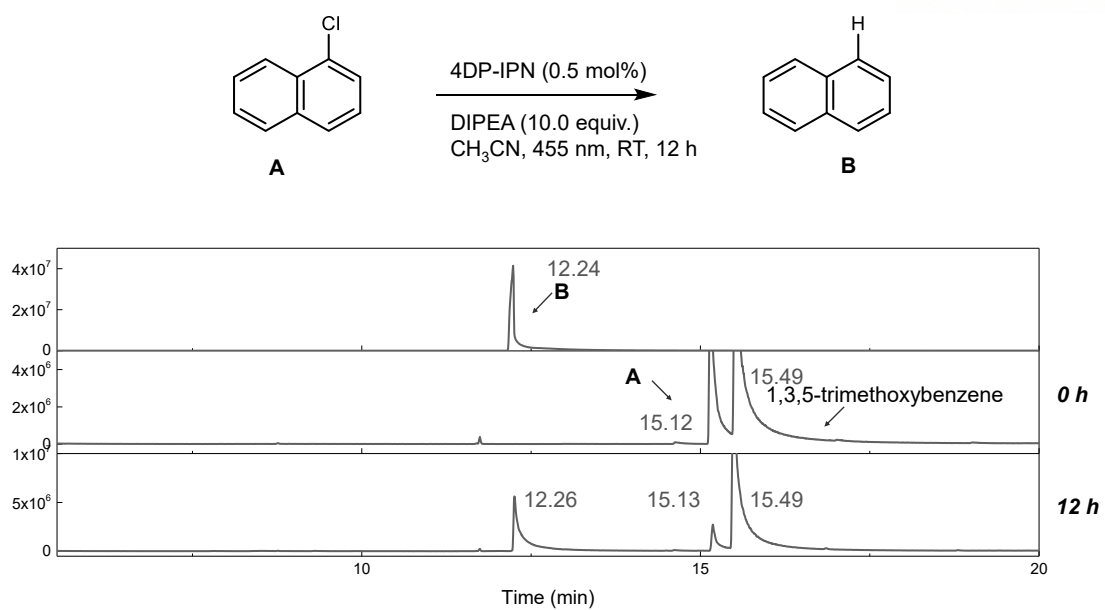
Figure A5.41 GC-FID spectra of photoredox reductive dehalogenation for 1-chloronaphthalene.

Substrate screening (1-chloronaphthalene), 0 h

^{1}H NMR (400 MHz, DMSO-d$_6$):
δ 8.23–8.15 (d, 1H) 8.05–8.00 (d, 1H)
7.98–7.90 (d, 1H) 7.73–7.61 (m, 3H),
7.54–7.49 (t, 1H)

Substrate screening (1-chloronaphthalene), 12 h

^{1}H NMR (400 MHz, DMSO-d$_6$):
δ 7.95–7.86 (dd, 4H), 7.54–7.46 (dd, 4H)

Figure A5.42 ^{1}H NMR data of photoredox reductive dehalogenation for 1-chloronaphthaelene (400 MHz, DMSO-d$_6$); TMB: δ 6.09 (s, 3H), 3.71 (s, 9H). Yield was measured by ^{1}H NMR using TMB as an internal standard.

145

Figure A5.43 GC-FID spectra of photoredox reductive dehalogenation for 2-bromopyridine.

Substrate screening (2-bromopyridine), 0 h

1H NMR (400 MHz, DMSO-d$_6$):
δ 8.4 (m, 1H), 7.78–7.75 (dt, 1H),
7.65–7.63 (d, 1H), 7.48–7.43 (m, 1H)

Substrate screening (2-bromopyridine), 24 h

1H NMR (400 MHz, DMSO-d$_6$):
δ 8.6 (m, 2H), 7.8-7.77 (tt, 1H), 7.40–
7.35 (m, 2H)

Figure A5.44 1H NMR data of photoredox reductive dehalogenation for 2-bromopyridine (400 MHz, DMSO-d$_6$); TMB: δ 6.09 (s, 3H), 3.71 (s, 9H). Yield was measured by 1H NMR using TMB as an internal standard.

147

Figure A5.45 GC-FID spectra of photoredox reductive dehalogenation for 2-chloropyridine.

Substrate screening (2-chloropyridine), 0 h

^{1}H NMR (400 MHz, DMSO-d$_6$):
δ 8.4 (m, 1H), 7.88–7.82 (td, 1H),
7.5 (d, 1H), 7.42–7.38 (dd, 1H)

Substrate screening (2-chloropyridine), 24 h
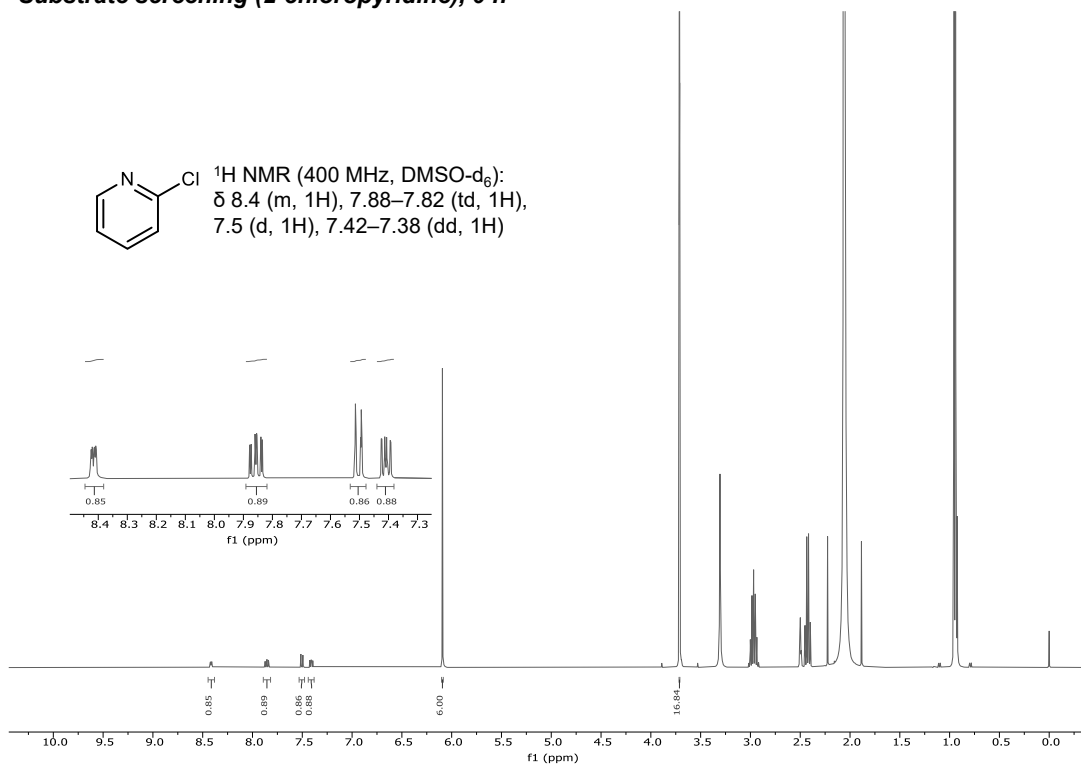
^{1}H NMR (400 MHz, DMSO-d$_6$):
δ 8.6 (m, 2H), 7.8-7.77 (tt, 1H),
7.40–7.35 (m, 2H)

Figure A5.46 ^{1}H NMR data of photoredox reductive dehalogenation for 2-chloropyridine (400 MHz, DMSO-d$_6$); TMB: δ 6.09 (s, 3H), 3.71 (s, 9H). Yield was measured by ^{1}H NMR using TMB as an internal standard.
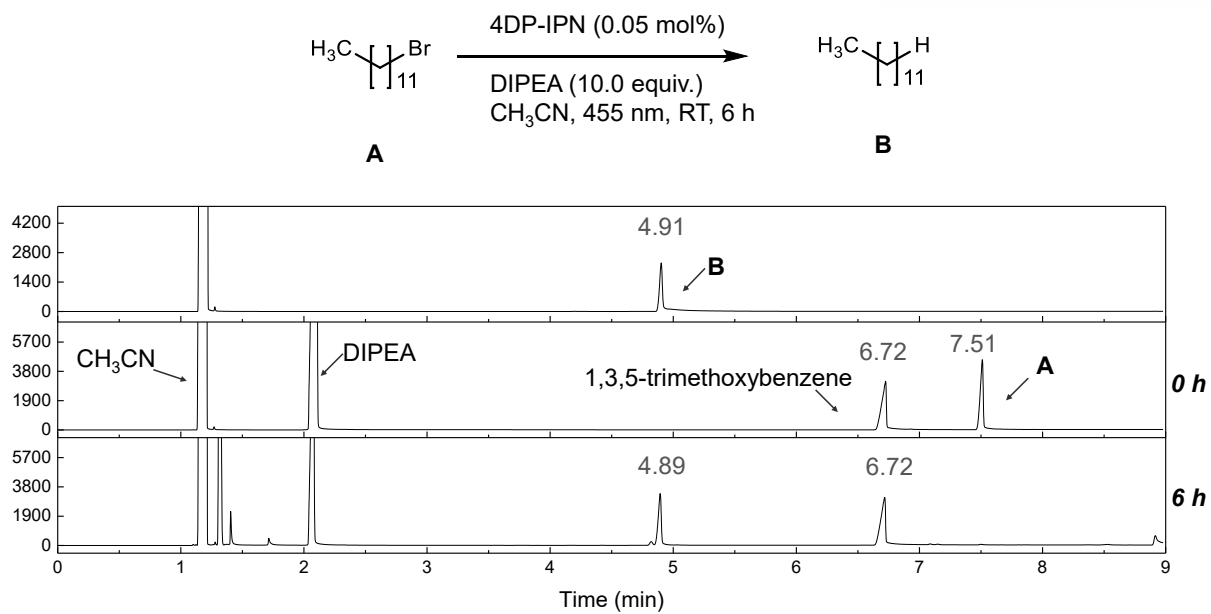
Figure A5.47 GC-FID spectra of photoredox reductive dehalogenation for 1-bromododecane.

Substrate screening (1-bromododecane), 0 h

H_3C — [— Br]$_{11}$

^{1}H NMR (400 MHz, CDCl$_3$):
δ 3.60-3.40 (t, 2H), 1.19 (q, 2H), 1.50-1.40 (m, 2H), 1.40-1.20 (br, 16H), 0.90-0.80 (t, 3H)

Substrate screening (1-bromododecane), 6 h

H_3C — [— H]$_{11}$

^{1}H NMR (400 MHz, CDCl$_3$):
δ 1.34-1.23 (m, 20H), 0.90-0.86 (t, 6H)

Figure A5.48 ^{1}H NMR data of photoredox reductive dehalogenation for 1-bromododecane (400 MHz, CDCl$_3$); TMB: δ 6.09 (s, 3H), 3.71 (s, 9H). Yield was measured by ^{1}H NMR using TMB as an internal standard.
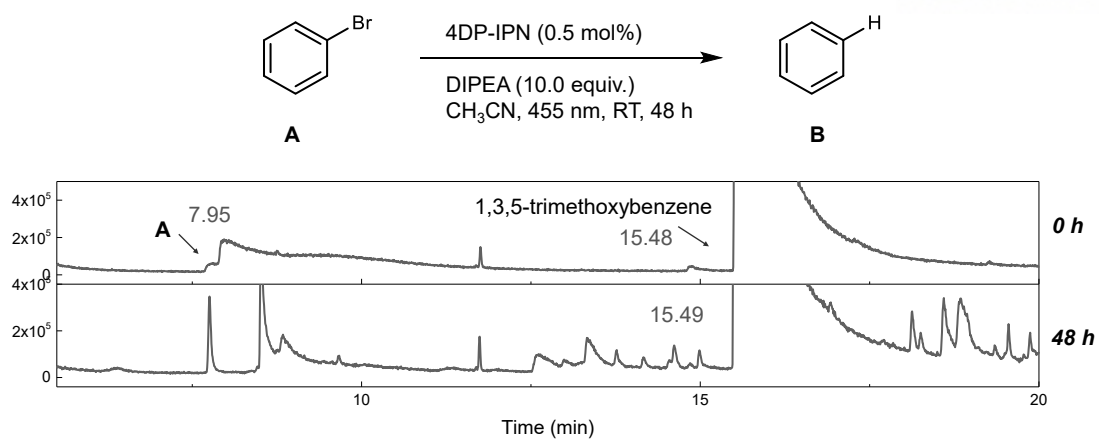
Figure A5.49 GC-FID spectra of photoredox reductive dehalogenation for bromobenzene. Due to high injection-temperature of GC-FID, benzene product was not observed in our GC-FID system. Therefore, we evaluated the conversion and yield from ^{1}H NMR using TMB as an internal standard.

Substrate screening (bromobenzene), 0 h

^{1}H NMR (400 MHz, DMSO-d$_6$):
δ 7.60–7.53 (m, 2H), δ 7.42–7.31 (m, 3H)

Substrate screening (bromobenzene), 48 h
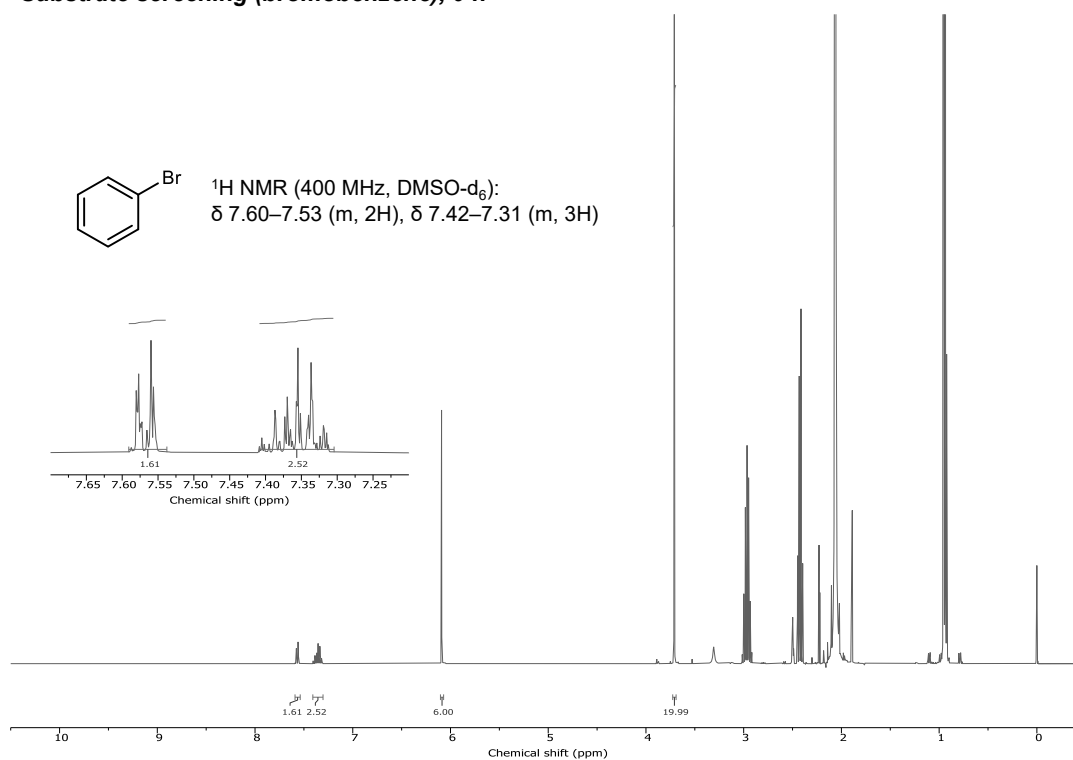
^{1}H NMR (400 MHz, DMSO-d$_6$):
δ 7.37 (s, 6H)

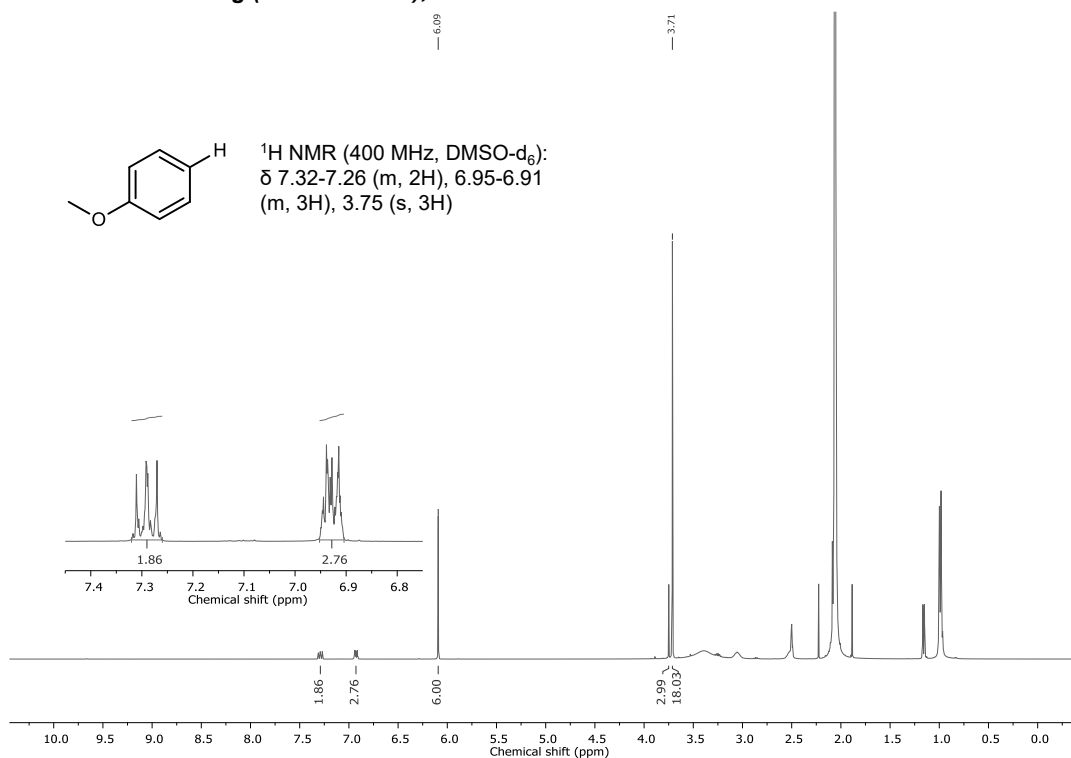**Figure A5.50** ^{1}H NMR data for photoredox reductive dehalogenation for bromobenzene (400 MHz, DMSO-d$_6$); TMB: δ 6.09 (s, 3H), 3.71 (s, 9H). Yield was measured by ^{1}H NMR using TMB as an internal standard.

153
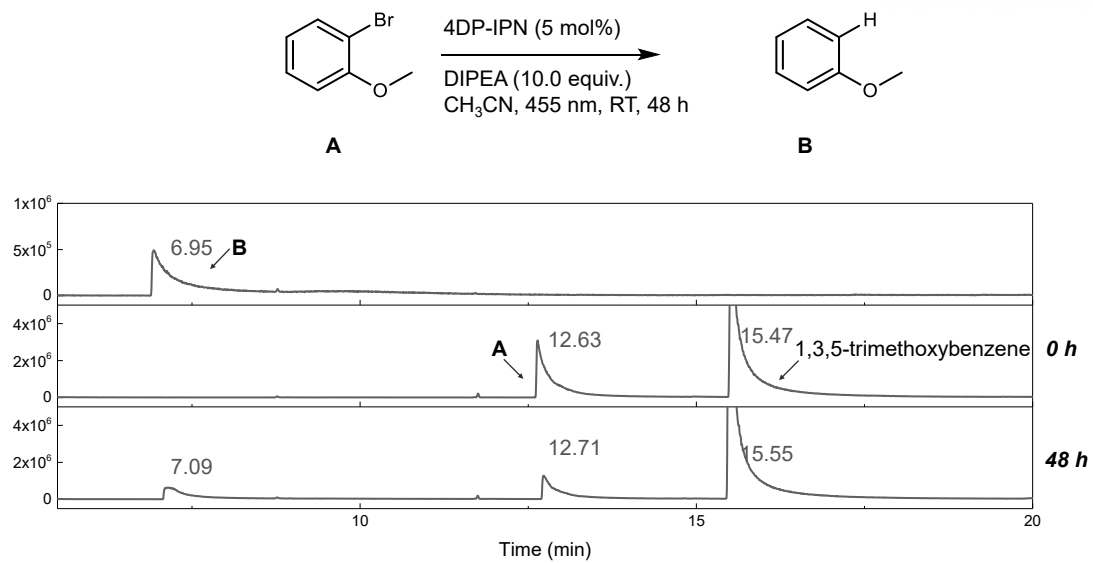
Figure A5.51 GC-FID spectra for photoredox reductive dehalogenation for 2-bromoanisole.

Substrate screening (2-bromoanisole), 0 h

¹H NMR (400 MHz, DMSO-d₆):
δ 7.58–7.55 (dd, 1H), 7.38–7.34 (dt, 1H),
7.15–6.95 (dd, 1H), 6.93–6.87 (dt, 1H),
3.85 (s, 3H)

Substrate screening (2-bromoanisole), 48 h
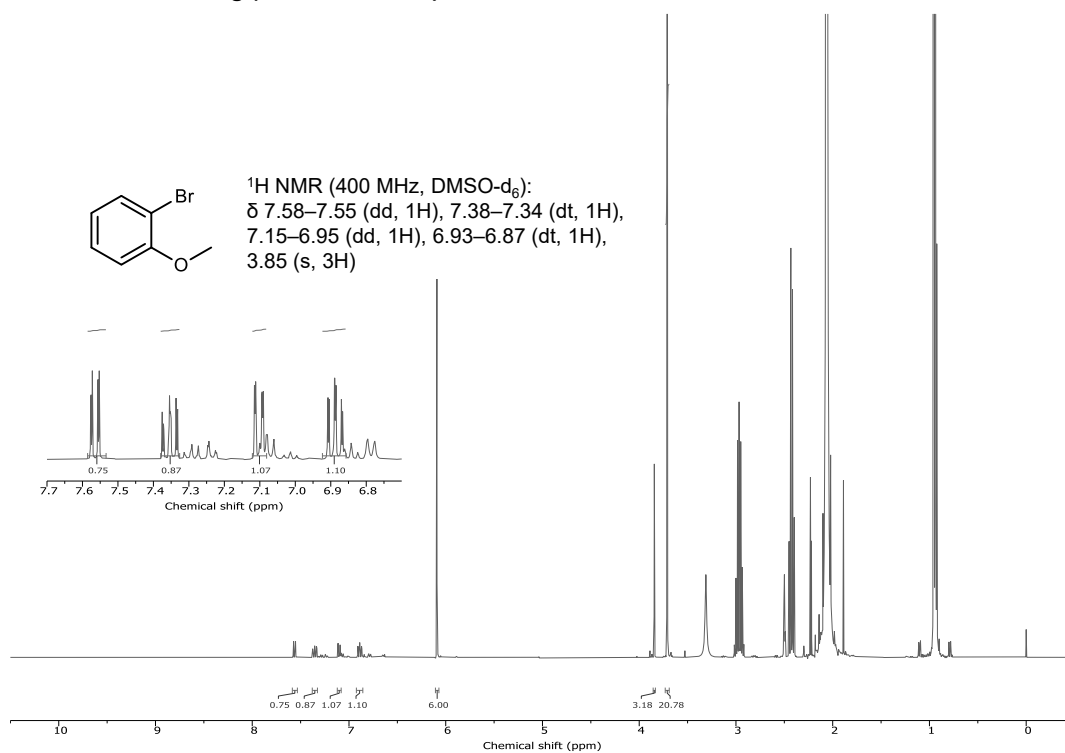
¹H NMR (400 MHz, DMSO-d₆):
δ 7.35–7.25 (dt, 2H), 6.95–6.91
(m, 3H), 3.75 (s, 3H)
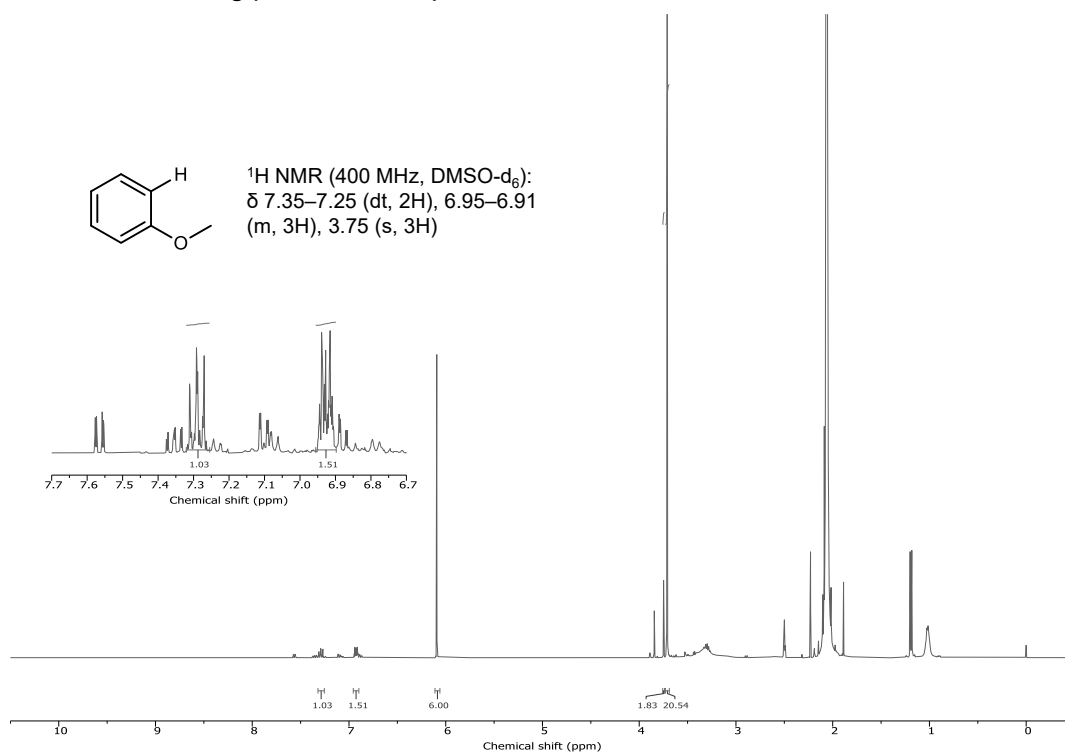
Figure A5.52 ¹H NMR data for photoredox reductive dehalogenation for 2-bromoanisole (400 MHz, DMSO-d₆); TMB: δ 6.09 (s, 3H), 3.71 (s, 9H). Yield was measured by ¹H NMR using TMB as an internal standard.
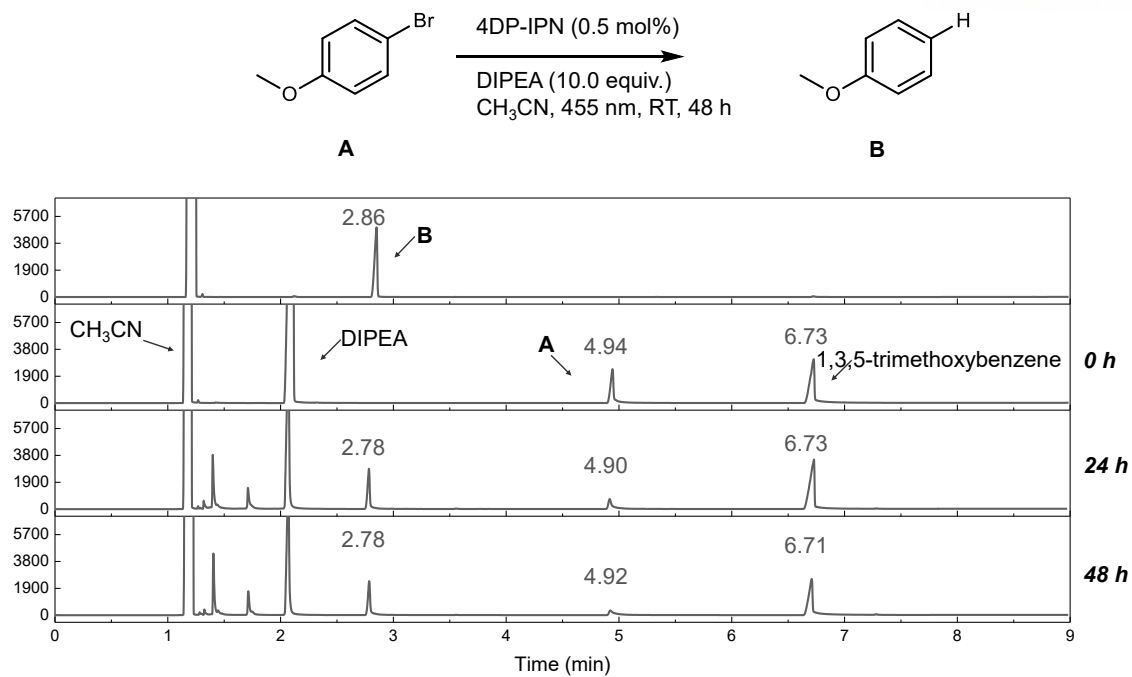
Figure A5.53 GC-FID spectra for photoredox reductive dehalogenation for 4-bromoanisole.

Substrate screening (4-bromoanisole), 0 h

¹H NMR (400 MHz, DMSO-d₆):
δ 7.5–7.4 (dt, 2H), 6.95–6.87 (dt, 2H), 3.7 (s, 3H)

Substrate screening (4-bromoanisole), 48 h
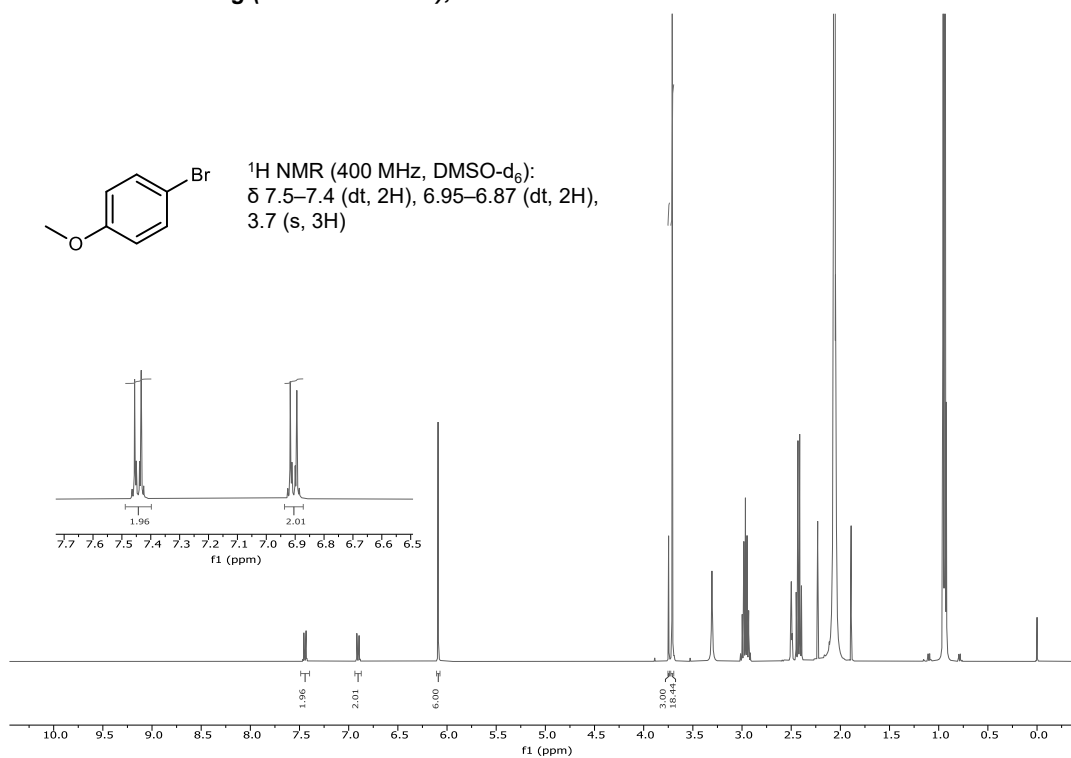
^{1}H NMR (400 MHz, DMSO-d$_6$):
δ 7.35–7.25 (dt, 2H), 6.95–6.91 (m, 3H), 3.75 (s, 3H)

Figure A5.54 ^{1}H NMR data for photoredox reductive dehalogenation for 4-bromoanisole (400 MHz, DMSO-d$_6$); TMB: δ 6.09 (s, 3H), 3.71 (s, 9H). Yield was measured by ^{1}H NMR using TMB as an internal standard.

157
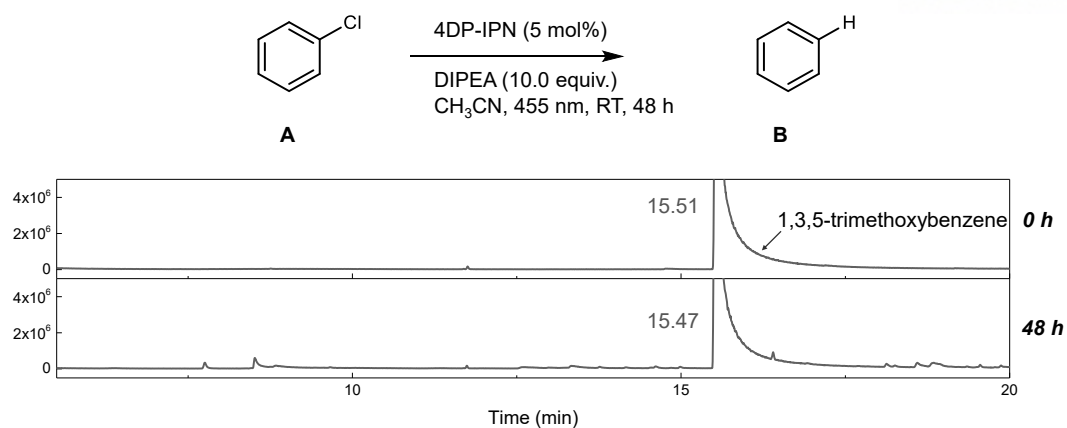
Figure A5.55 GC-FID spectra for photoredox reductive dehalogenation for chlorobenzene. Due to high injection-temperature of GC-FID, chlorobenzene and benzene product was not observed in our GC-FID system. Therefore, we evaluated the conversion and yield from ^{1}H NMR using TMB as an internal standard.

Substrate screening (chlorobenzene), 0 h

^{1}H NMR (400 MHz, DMSO-d$_6$):
δ 7.45–7.38 (m, 5H)

Substrate screening (chlorobenzene), 48 h
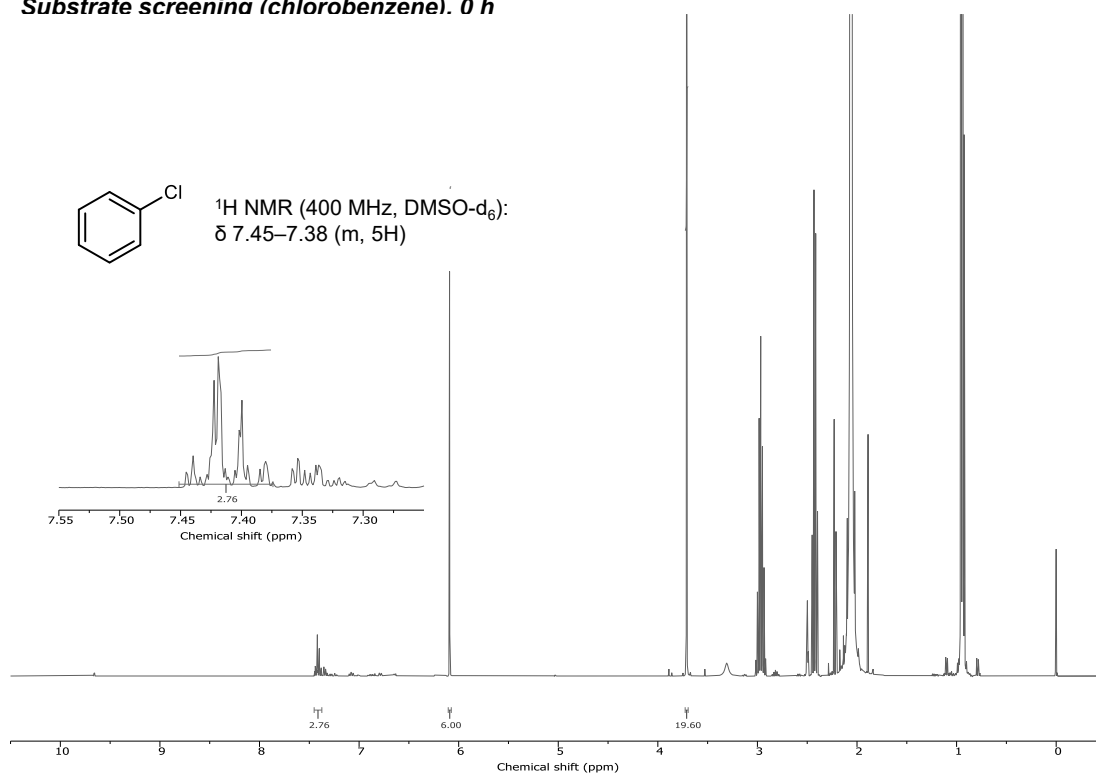
^{1}H NMR (400 MHz, DMSO-d$_6$):
δ 7.37 (s, 6H)
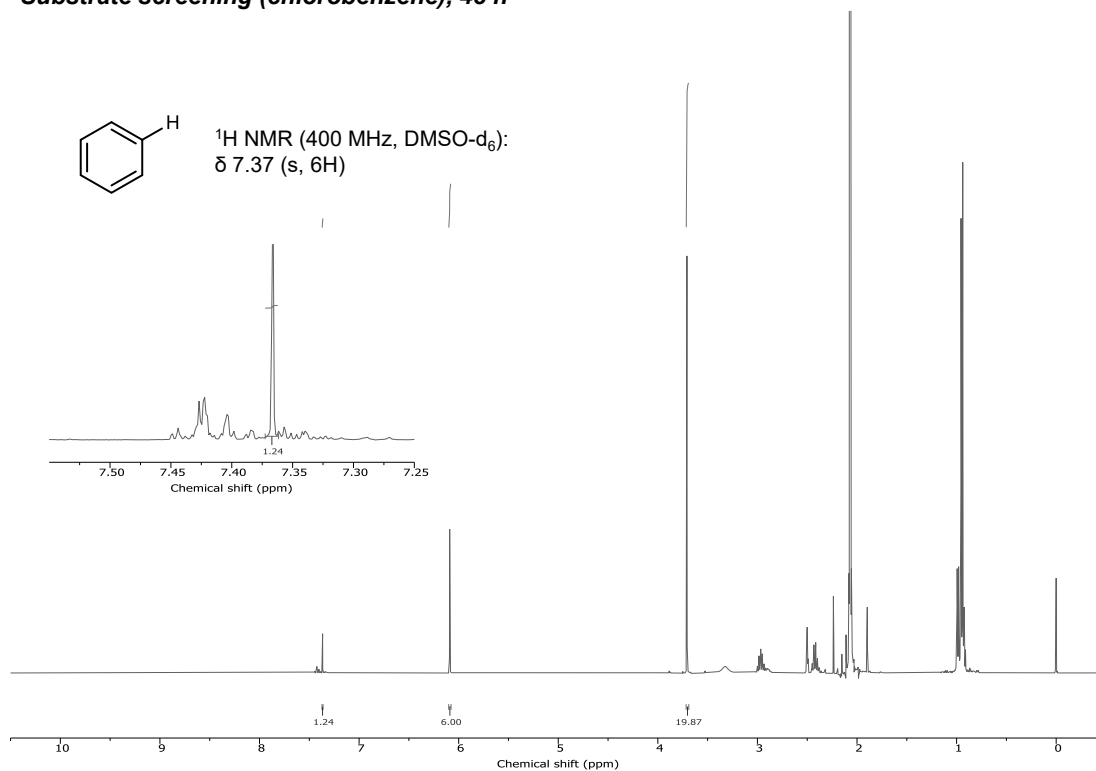
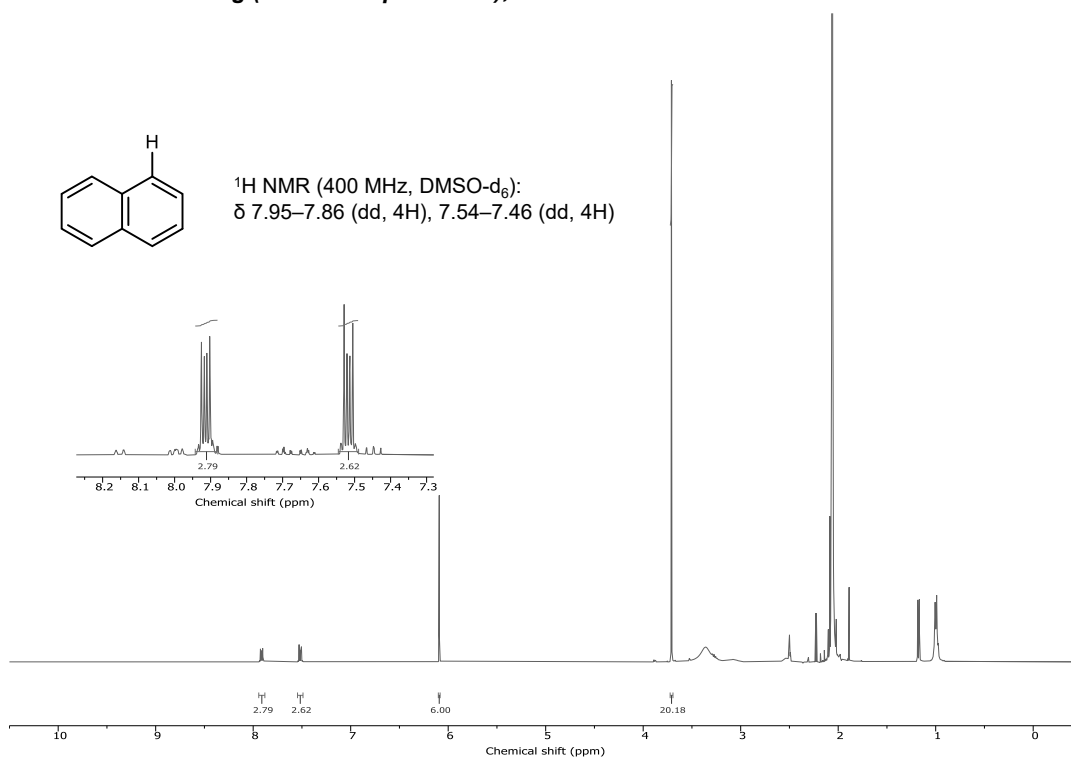**Figure A5.56** ^{1}H NMR data for photoredox reductive dehalogenation for chlorobenzene (400 MHz, DMSO-d$_6$); TMB: δ 6.09 (s, 3H), 3.71 (s, 9H). Yield was measured by ^{1}H NMR using TMB as an internal standard.
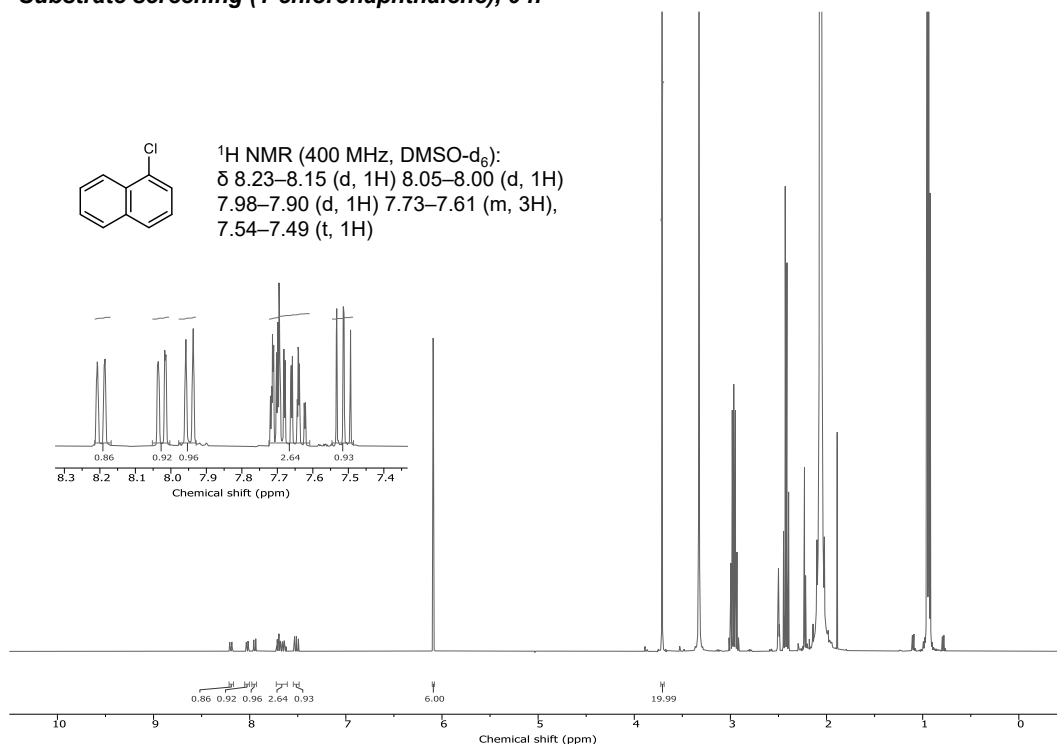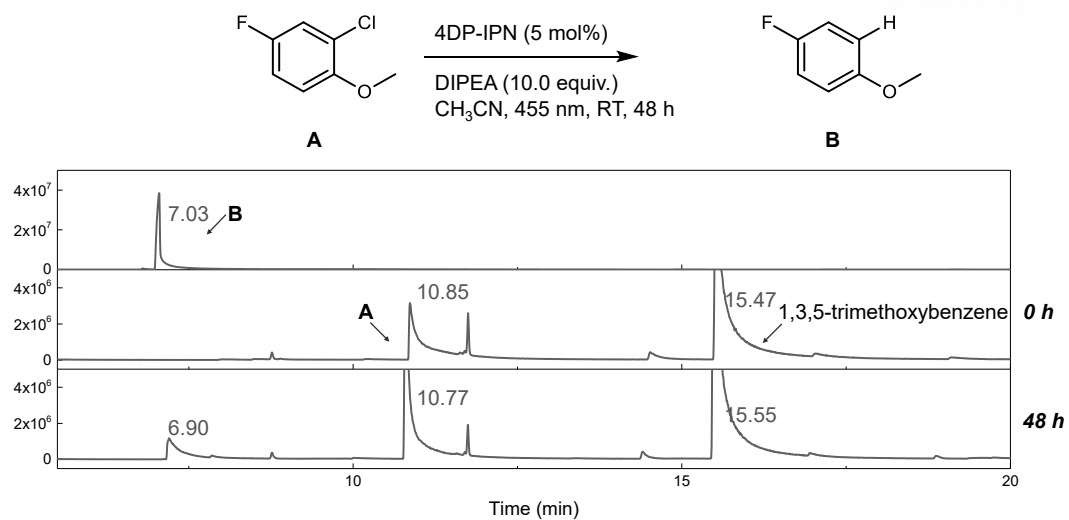
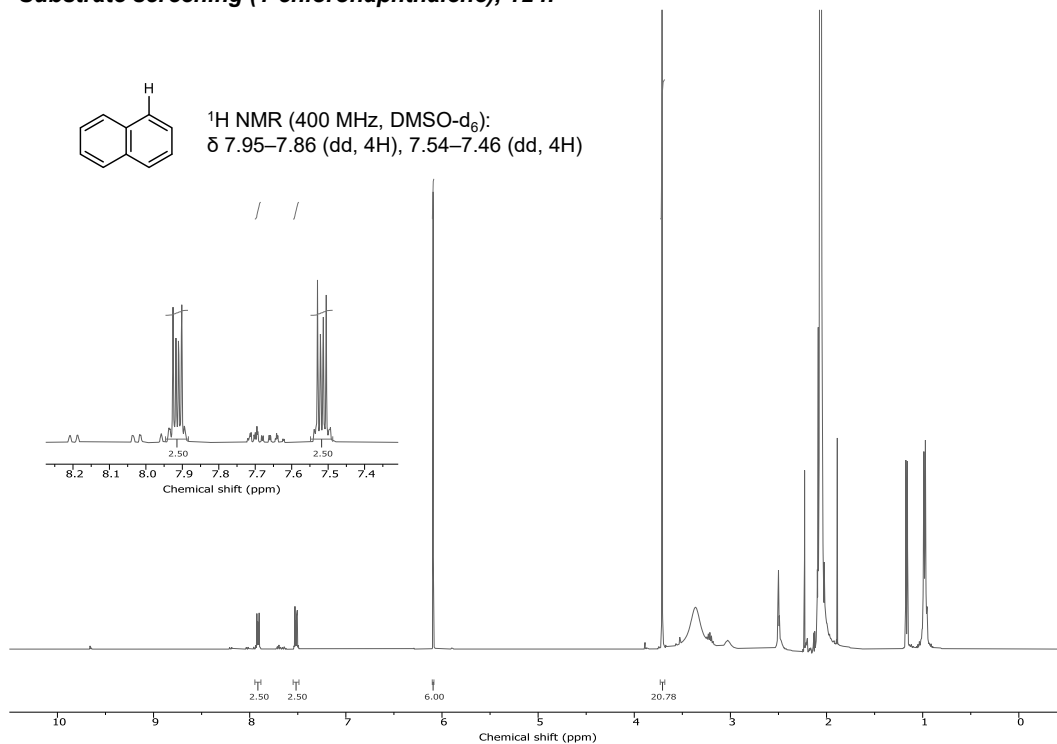**Figure A5.57** GC-FID spectra for photoredox reductive dehalogenation for 2-chloro-4-fluoroanisole.

Substrate screening (2-chloro-4-fluoroanisole), 0 h

^{1}H NMR (400 MHz, DMSO-d$_6$):
δ 7.42–7.38 (dd, 1H), 7.20–7.14 (m, 2H),
3.84 (s, 3H)

Substrate screening (2-chloro-4-fluoroanisole), 48 h
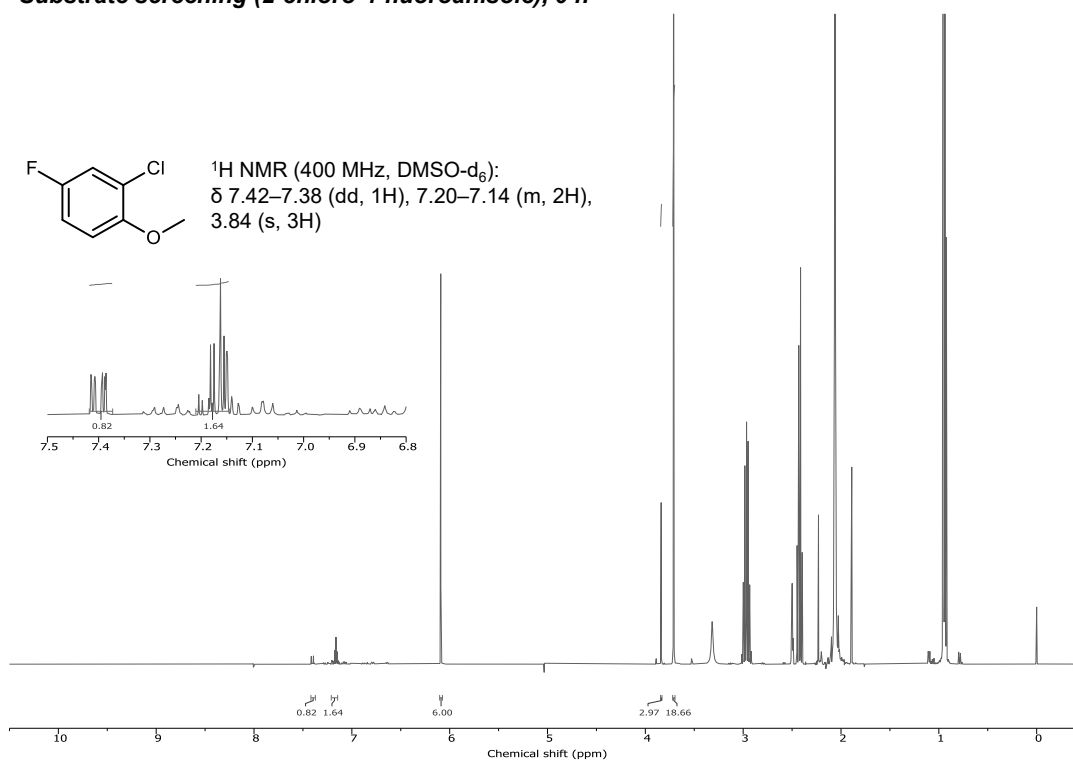
^{1}H NMR (400 MHz, DMSO-d$_6$):
δ 7.12–7.07 (d, 2H), 6.95–6.91
(m, 2H), 3.74 (s, 3H)
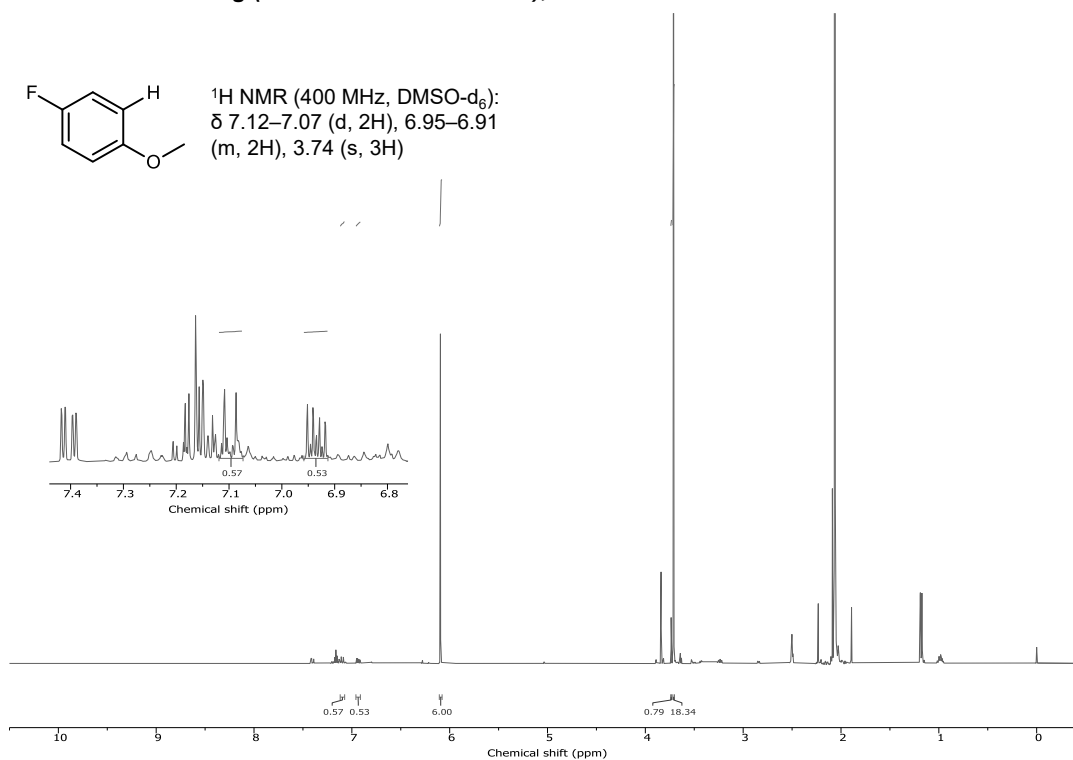
Figure A5.58 ^{1}H NMR data for photoredox reductive dehalogenation for 2-chloro-4-fluoroanisole (400 MHz, DMSO-d$_6$); TMB: δ 6.09 (s, 3H), 3.71 (s, 9H). Yield was measured by ^{1}H NMR using TMB as an internal standard.
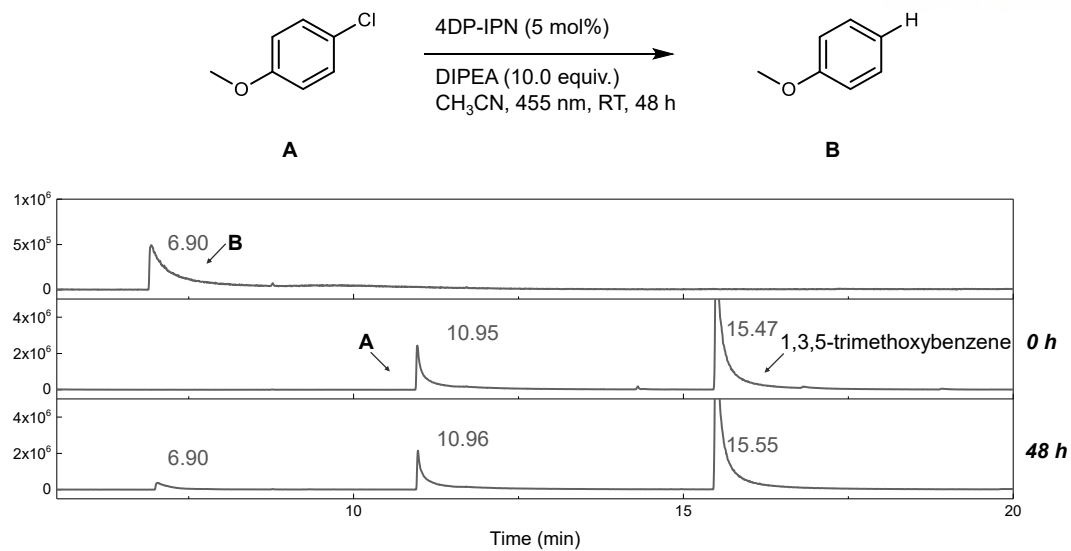
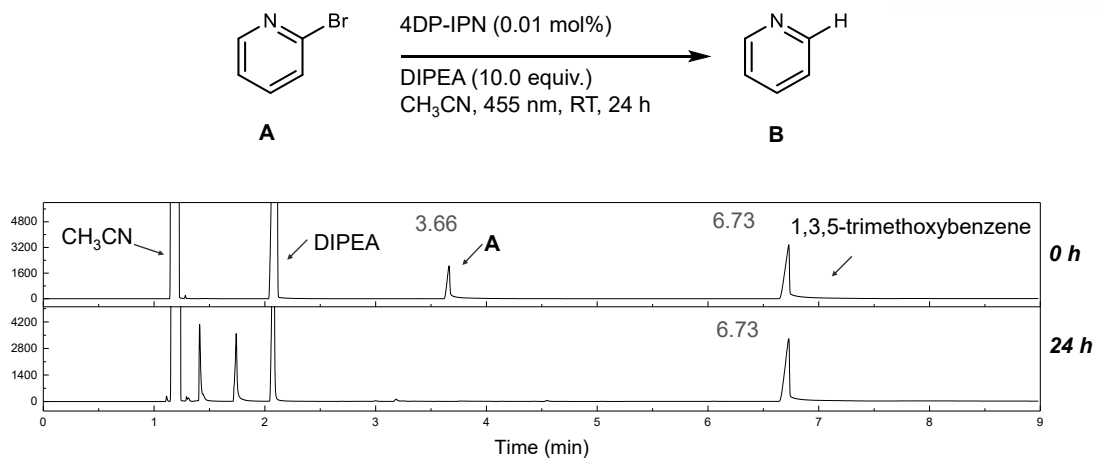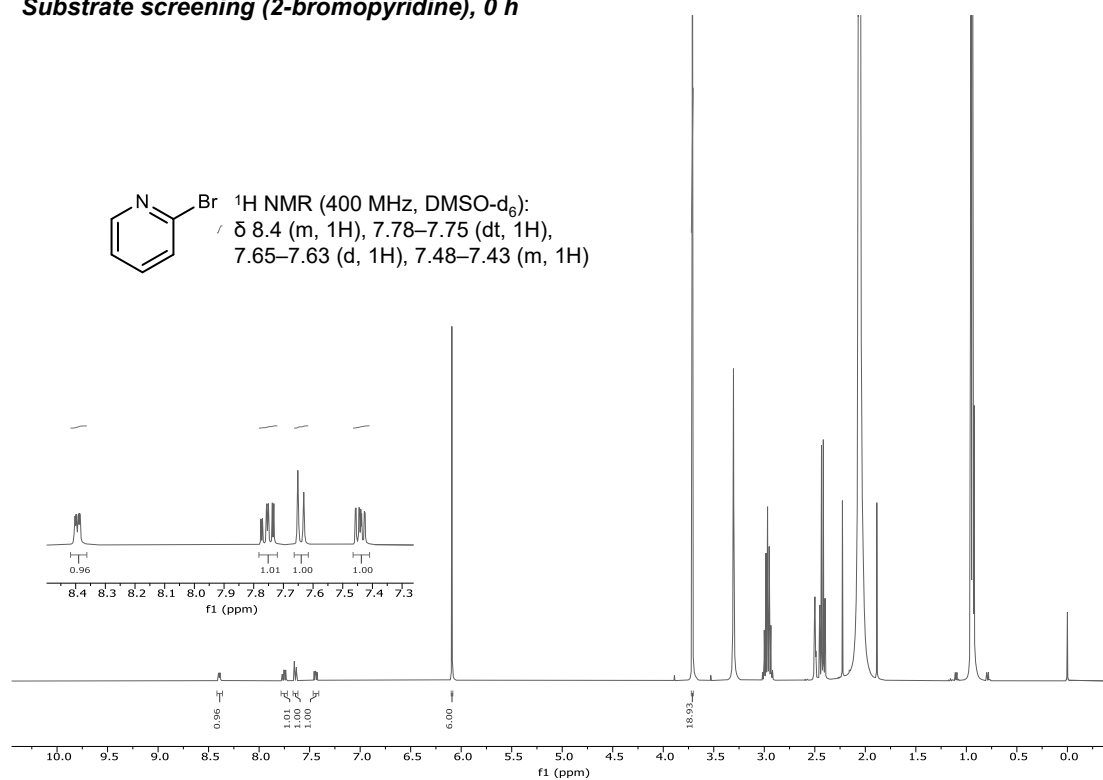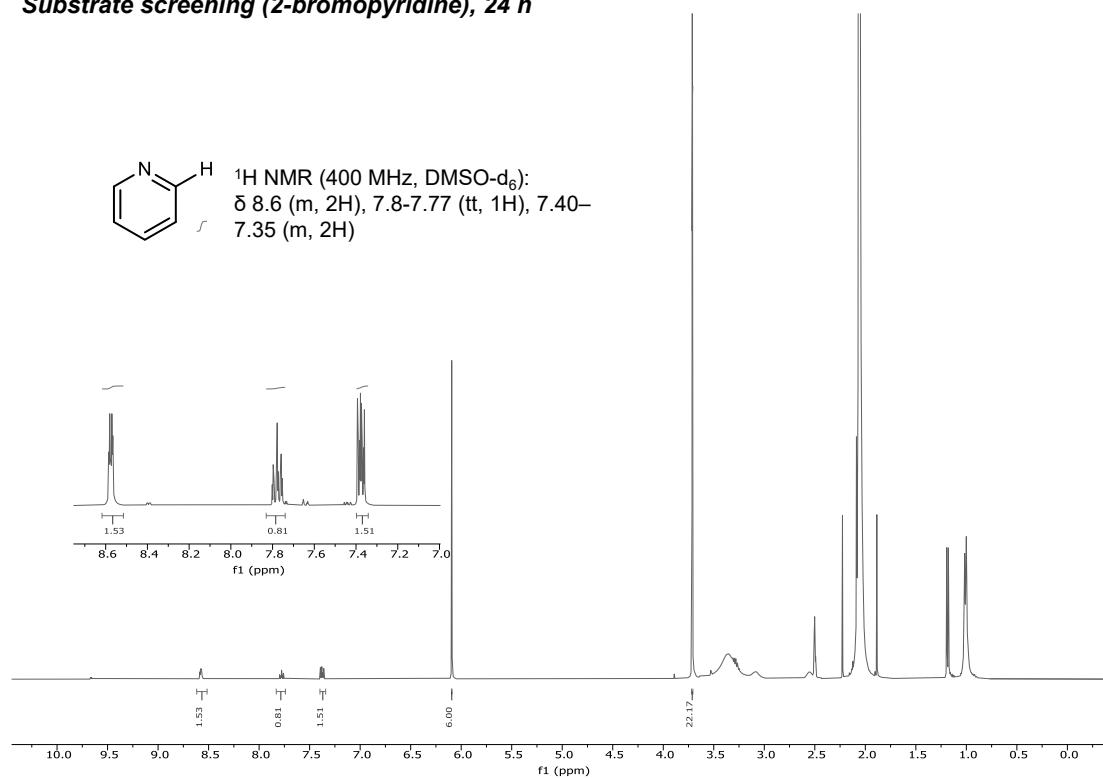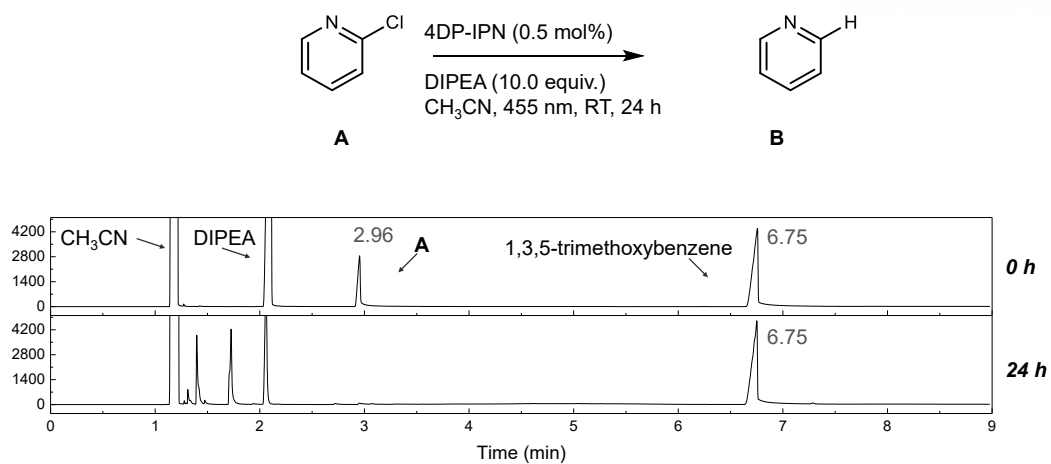**Figure A5.59** GC-FID spectra for photoredox reductive dehalogenation for 4-chloroanisole. Yield was measured by ^{1}H NMR using TMB as an internal standard.

Substrate screening (4-chloroanisole), 0 h

¹H NMR (400 MHz, DMSO-d₆):
δ 7.35–7.30 (dt, 2H), 6.97–6.93 (dt, 2H),
3.75 (s, 3H)

Substrate screening (4-chloroanisole), 48 h
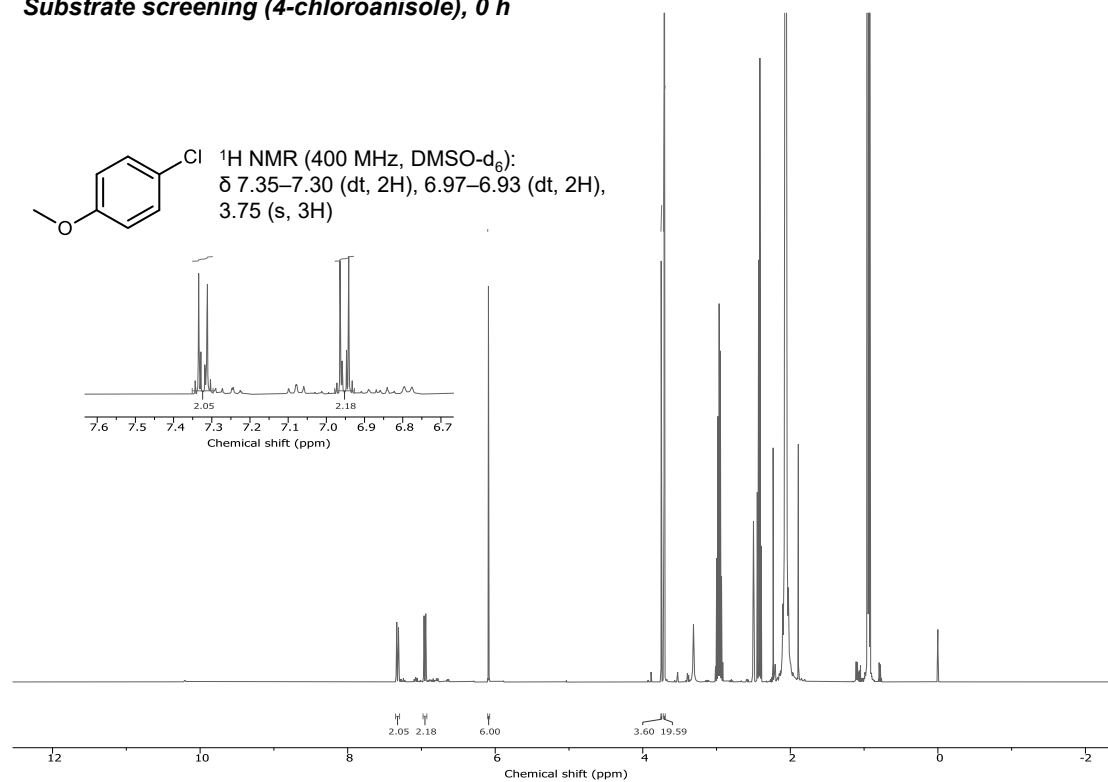
¹H NMR (400 MHz, DMSO-d₆):
δ 7.35–7.25 (dt, 2H), 6.95–6.91
(m, 3H), 3.75 (s, 3H)
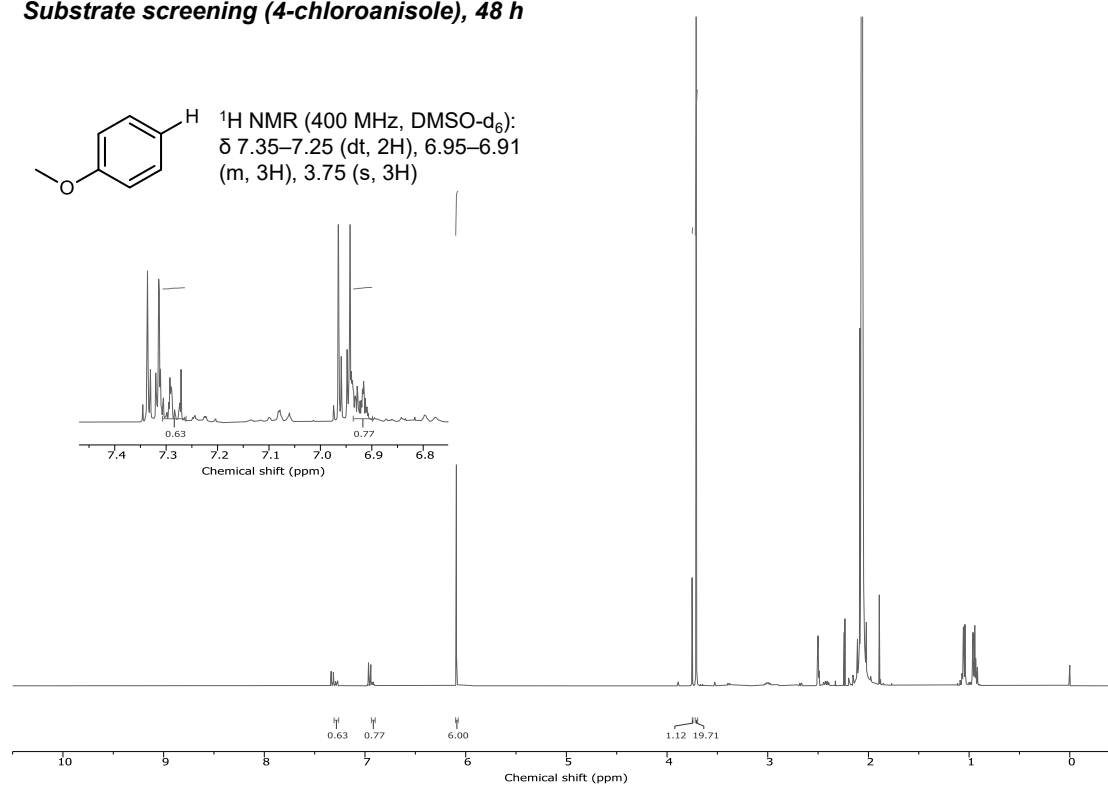
Figure A5.60 ¹H NMR data for photoredox reductive dehalogenation for 4-chloroanisole (400 MHz, DMSO-d₆); TMB: δ 6.09 (s, 3H), 3.71 (s, 9H).
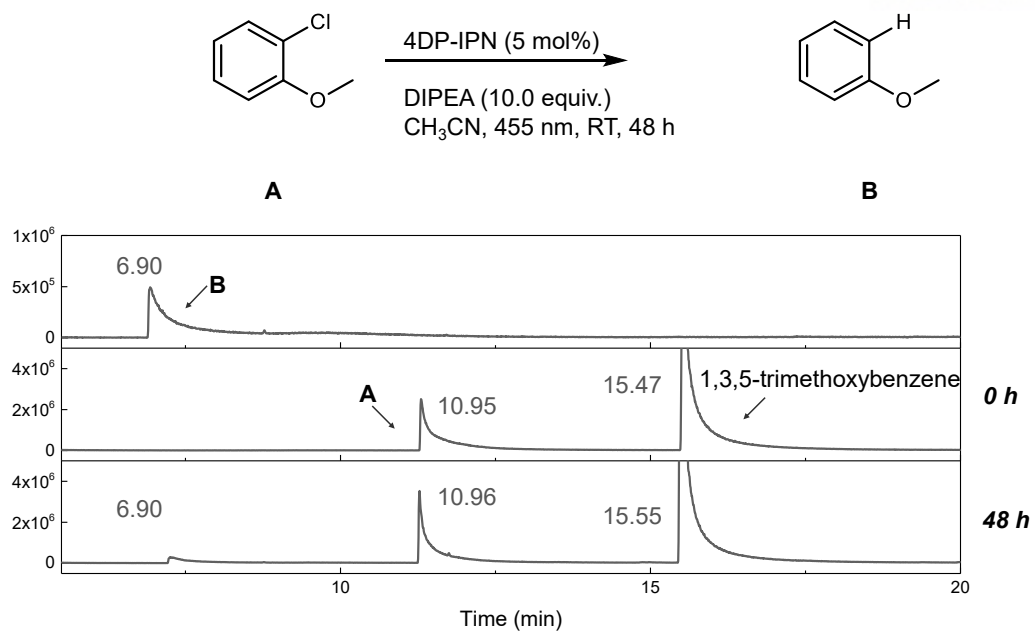
Figure A5.61 GC-FID spectra for photoredox reductive dehalogenation for 2-chloroanisole.

Substrate screening (2-chloroanisole), 0 h

^{1}H NMR (400 MHz, DMSO-d$_6$):
δ 7.35–7.30 (dt, 2H), 6.97–6.93 (dt, 2H),
3.85 (s, 3H)

Substrate screening (2-chloroanisole), 48 h
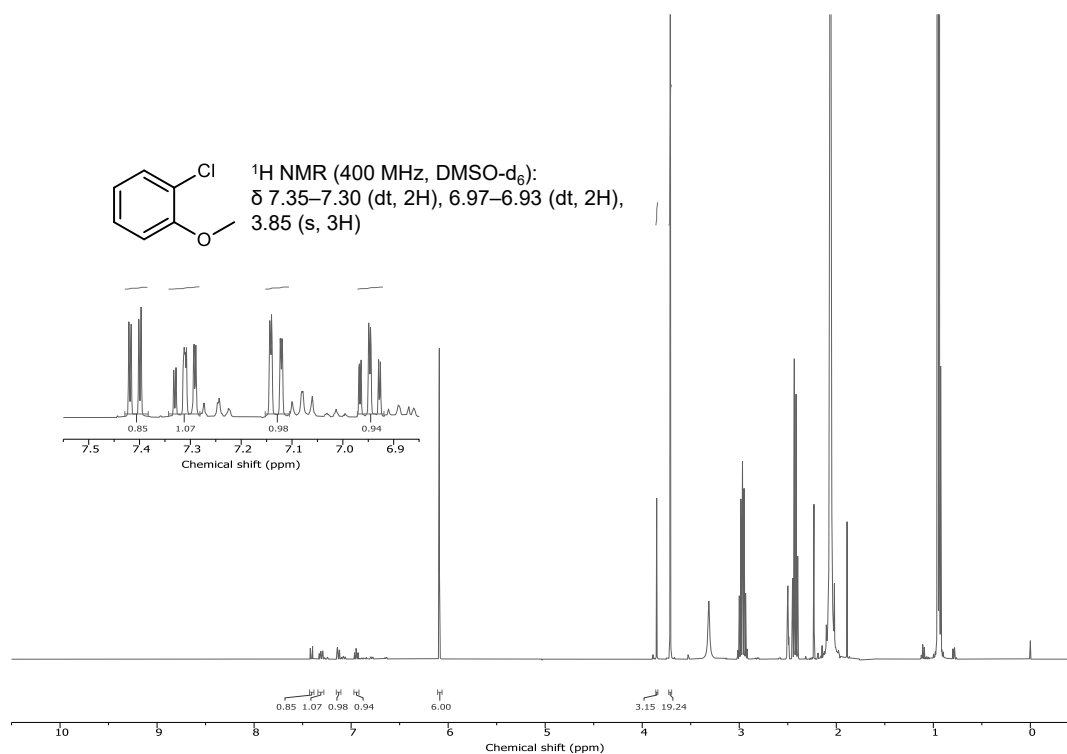
^{1}H NMR (400 MHz, DMSO-d$_6$):
δ 7.35–7.25 (dt, 2H), 6.95–6.91
(m, 3H), 3.75 (s, 3H)
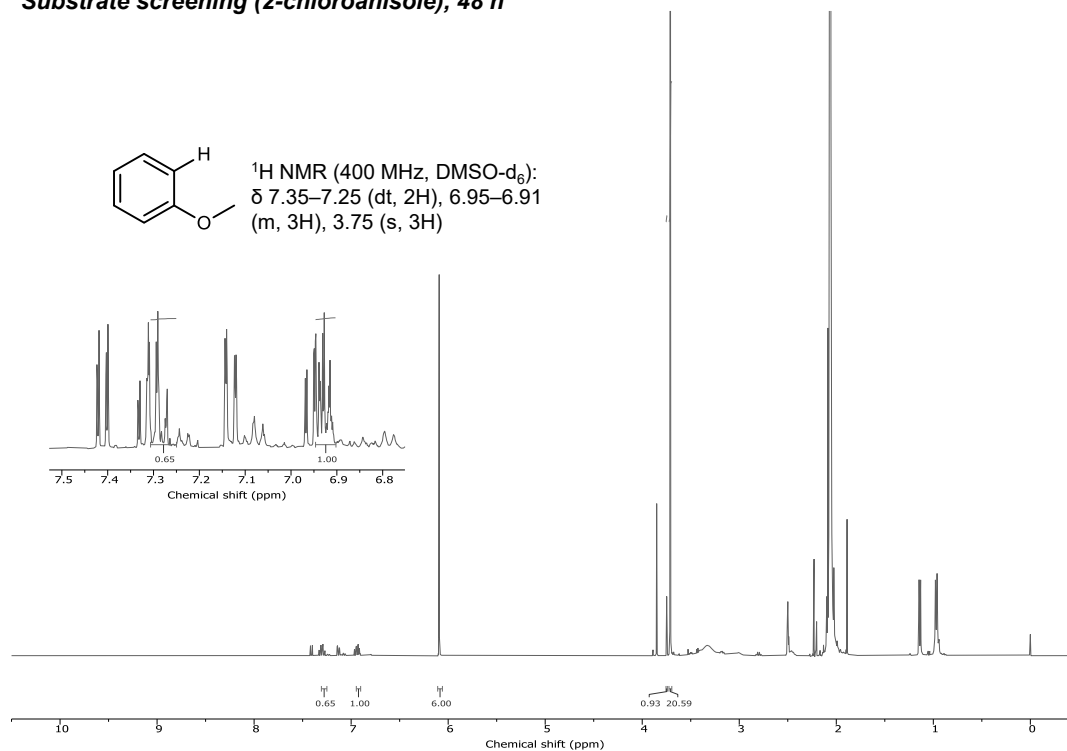
Figure A5.62 ^{1}H NMR data for photoredox reductive dehalogenation for 2-chloroanisole (400 MHz, DMSO-d$_6$); TMB: δ 6.09 (s, 3H), 3.71 (s, 9H). Yield was measured by ^{1}H NMR using TMB as an internal standard.
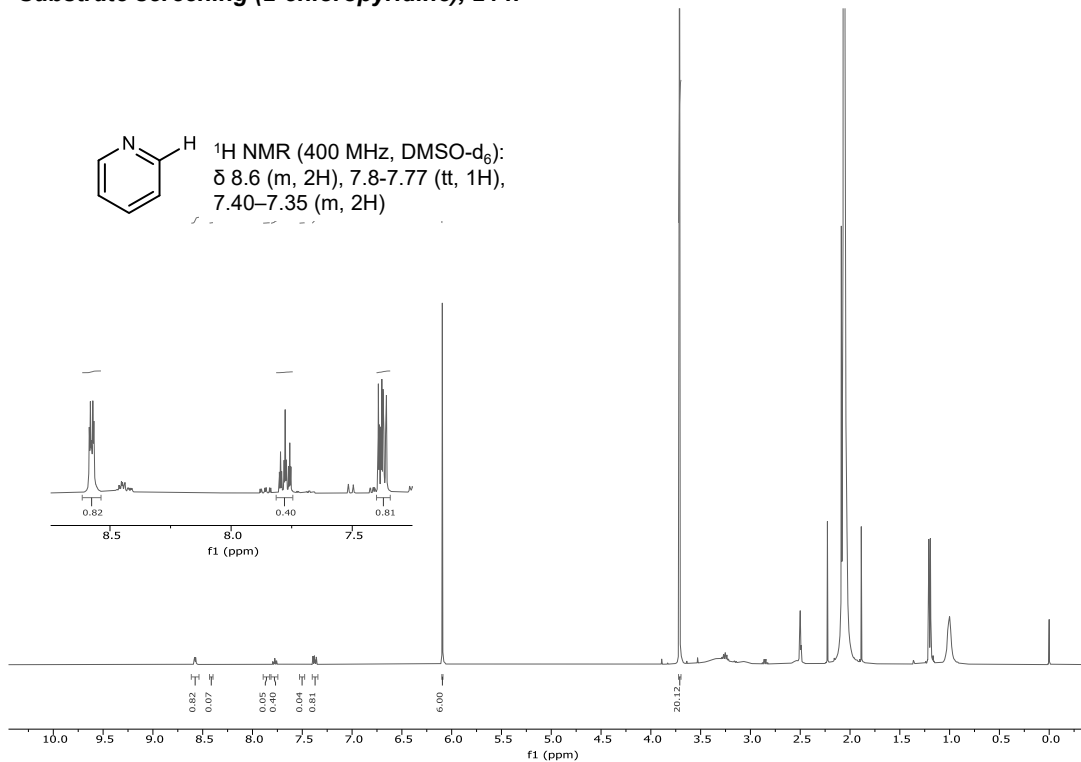
References

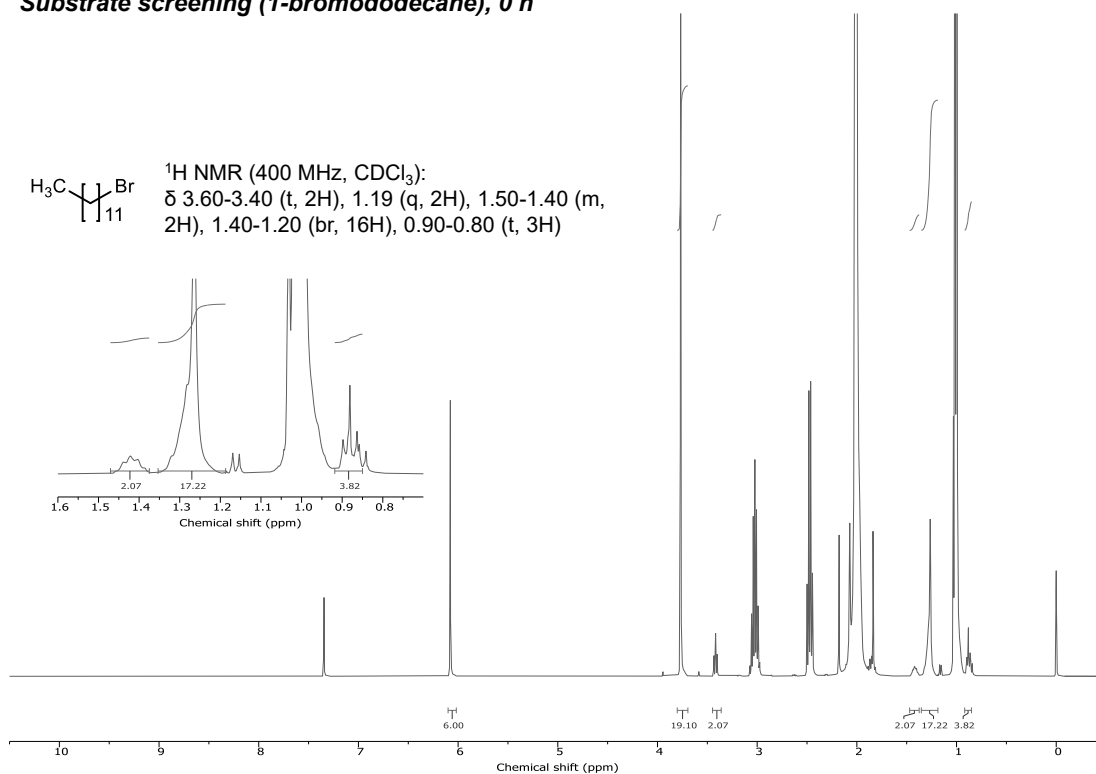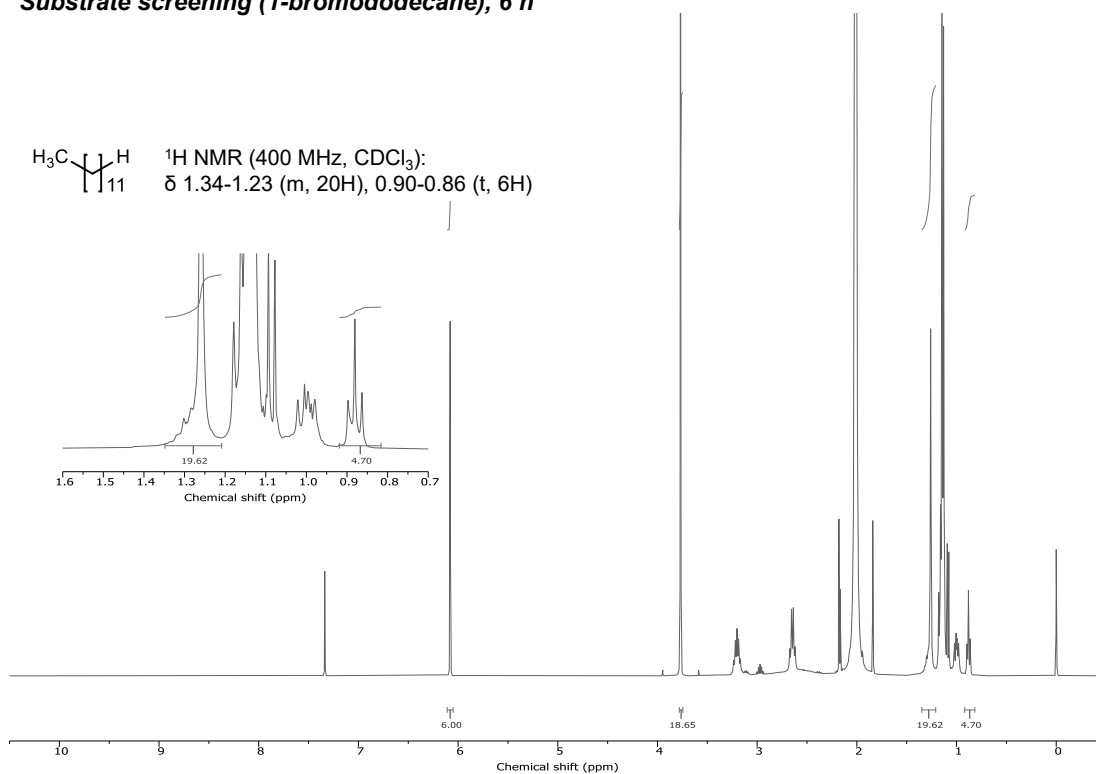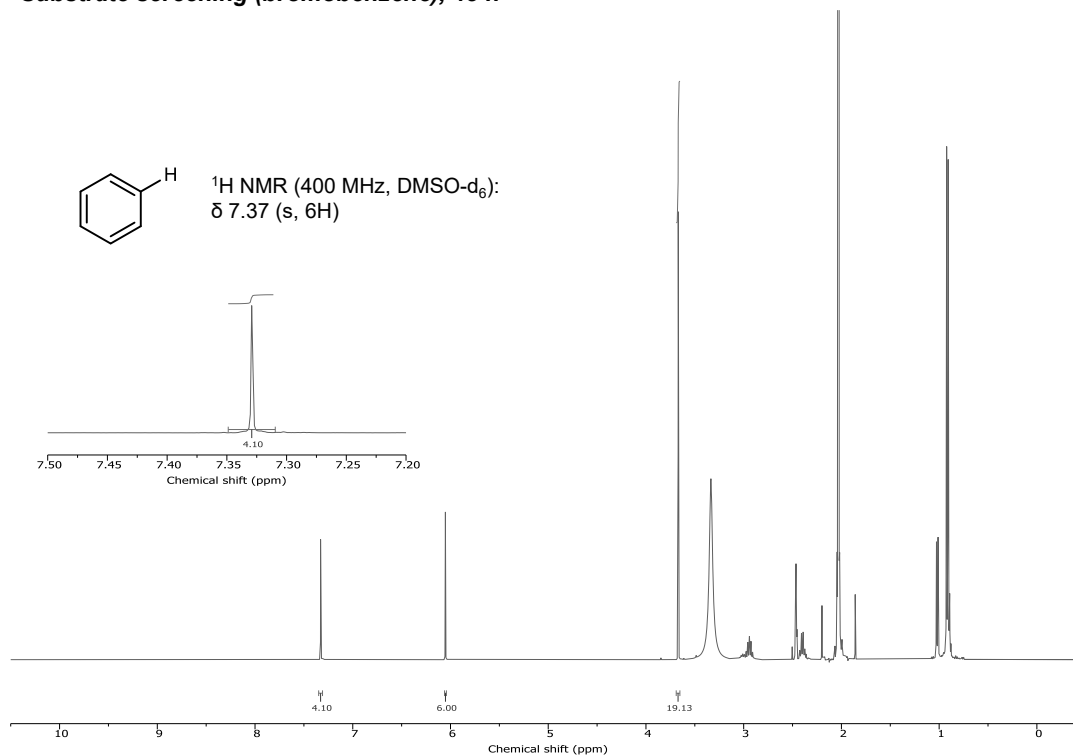(1)   Roth, H. D. The Beginnings of Organic Photochemistry. *Angew. Chem. Int. Ed.* **1989**, *28* (9), 1193–1207.

(2)   Prier, C. K.; Rankic, D. A.; MacMillan, D. W. C. Visible Light Photoredox Catalysis with Transition Metal Complexes: Applications in Organic Synthesis. *Chem. Rev.* **2013**, *113* (7), 5322–5363.

(3)   Yoon, T. P.; Ischay, M. A.; Du, J. Visible Light Photocatalysis as a Greener Approach to Photochemical Synthesis. *Nat. Chem.* **2010**, *2* (7), 527–532.

(4)   Narayanam, J. M. R.; Stephenson, C. R. J. Visible Light Photoredox Catalysis: Applications in Organic Synthesis. *Chem. Soc. Rev.* **2011**, *40* (1), 102–113.

(5)   Romero, N. A.; Nicewicz, D. A. Organic Photoredox Catalysis. *Chem Rev*. American Chemical Society September 14, 2016, pp 10075–10166.

(6)   Buzzetti, L.; Crisenza, G. E. M.; Melchiorre, P. Mechanistic Studies in Photocatalysis. *Angew. Chem. Int. Ed.* **2019**, *58* (12), 3730–3747.

(7)   MacKenzie, I. A.; Wang, L.; Onuska, N. P. R.; Williams, O. F.; Begam, K.; Moran, A. M.; Dunietz, B. D.; Nicewicz, D. A. Discovery and Characterization of an Acridine Radical Photoreductant. *Nature* **2020**, *580* (7801), 76–80.

(8)   Barham, J. P.; König, B. Synthetic Photoelectrochemistry. *Angew. Chem. Int. Ed..* **2020**, *59* (29), 11732–11747.

(9)   Cybularczyk-Cecotka, M.; Szczepanik, J.; Giedyk, M. Photocatalytic Strategies for the Activation of Organic Chlorides. *Nat. Catal.* **2020**, *3* (11), 872–886.

(10)   Lee, Y.; Kwon, M. S. Emerging Organic Photoredox Catalysts for Organic Transformations. *Eur. J. Org. Chem.* **2020**, 6028–6043.

(11)   Singh, V. K. et al., Highly Efficient Organic Photocatalysts Discovered via a Computer-Aided-Design Strategy for Visible-Light-Driven Atom Transfer Radical Polymerization. *Nat. Catal.* **2018**, *1* (10), 794–804.
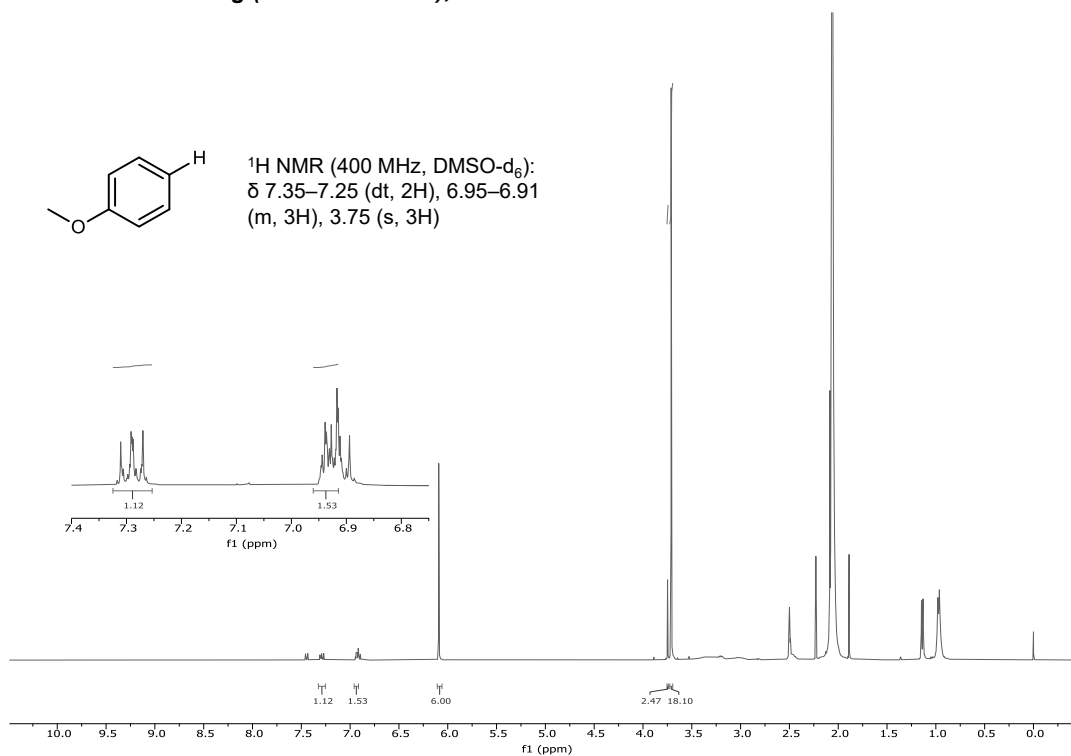
(12)   Lee, Y et al. A Water-Soluble Organic Photocatalyst Discovered for Highly Efficient Additive-Free Visible-Light-Driven Grafting of Polymers from Proteins at Ambient and Aqueous Environments. *Adv. Mater.* **2022**, *2108446*, 2108446.

(13)   Wu, C.; Liu, W.; Lim, C. H.; Miyake, G.; Lim, C. H. Rational Design of Photocatalysts for Controlled Polymerization: Effect of Structures on Photocatalytic Activities. *Chem. Rev.* **2021**. *122, (6)*, 5476-5518.

(14)   Fors, B. P.; Hawker, C. J. Control of a Living Radical Polymerization of Methacrylates by Light. *Angew. Chem. Int. Ed.* **2012**, *51* (35), 8850–8853.

(15)   Theriot, J. C.; Lim, C. H.; Yang, H.; Ryan, M. D.; Musgrave, C. B.; Miyake, G. M. Organocatalyzed Atom Transfer Radical Polymerization Driven by Visible Light. *Science.* **2016**, *352* (6289), 1082–1086.

(16)   Xu, J.; Jung, K.; Atme, A.; Shanmugam, S.; Boyer, C. A Robust and Versatile Photoinduced Living Polymerization of Conjugated and Unconjugated Monomers and Its Oxygen Tolerance. *J. Am. Chem. Soc.* **2014**, *136* (14), 5508–5519.

(17) Silverstein, T. P. Marcus Theory: Thermodynamics CAN Control the Kinetics of Electron Transfer Reactions. *J. Chem. Educ.* **2012**, *89* (9), 1159–1167.

(18) Pan, X.; Fang, C.; Fantin, M.; Malhotra, N.; So, W. Y.; Peteanu, L. A.; Isse, A. A.; Gennaro, A.; Liu, P.; Matyjaszewski, K. Mechanism of Photoinduced Metal-Free Atom Transfer Radical Polymerization: Experimental and Computational Studies. *J. Am. Chem. Soc.* **2016**, *138* (7), 2411–2425.

(19) Costentin, C.; Robert, M.; Savéant, J. M. Electron Transfer and Bond Breaking: Recent Advances. *Chem. Phys.* **2006**, *324* (1), 40–56.

(20) Nguyen, J. D.; D'Amato, E. M.; Narayanam, J. M. R.; Stephenson, C. R. J. Engaging Unactivated Alkyl, Alkenyl and Aryl Iodides in Visible-Light-Mediated Free Radical Reactions. *Nat. Chem.* **2012**, *4* (10), 854–859.

(21) Giedyk, M.; Narobe, R.; Weiß, S.; Touraud, D.; Kunz, W.; König, B. Photocatalytic Activation of Alkyl Chlorides by Assembly-Promoted Single Electron Transfer in Microheterogeneous Solutions. *Nat. Catal.* **2020**, *3* (1), 40–47.

(22) Kim, H.; Lee, C. Visible-Light-Induced Photocatalytic Reductive Transformations of Organohalides. *Angew. Chem. Int. Ed.* **2012**, *124* (49), 12469–12472.

(23) Nicewicz, D. A.; MacMillan, D. W. C. Merging Photoredox Catalysis with Organocatalysis: The Direct Asymmetric Alkylation of Aldehydes. *Science.* **2008**, *322* (3), 77–80.

(24) Ischay, M. A.; Anzovino, M. E.; Du, J.; Yoon, T. P. Efficient Visible Light Photocatalysis of [2+2] Enone Cycloadditions. *J. Am. Chem. Soc.* **2008**, *130* (39), 12886–12887.

(25) Narayanam, J. M. R.; Tucker, J. W.; Stephenson, C. R. J. Electron-Transfer Photoredox Catalysis: Development of a Tin-Free Reductive Dehalogenation Reaction. *J. Am. Chem. Soc.* **2009**, *131* (25), 8756–8757.

(26) Tucker, J. W.; Narayanam, J. M. R.; Krabbe, S. W.; Stephenson, C. R. J. Electron Transfer Photoredox Catalysis: Intramolecular Radical Addition to Indoles and Pyrroles. *Org. Lett.* **2010**, *12* (2), 368–371.

(27) Nguyen, J. D.; Tucker, J. W.; Konieczynska, M. D.; Stephenson, C. R. J. Intermolecular Atom Transfer Radical Addition to Olefins Mediated by Oxidative Quenching of Photoredox Catalysts. *J. Am. Chem. Soc.* **2011**, *133* (12), 4160–4163.

(28) Tlili, A.; Lakhdar, S. Acridinium Salts and Cyanoarenes as Powerful Photocatalysts: Opportunities in Organic Synthesis. *Angew. Chem. Int. Ed.* **2021**, *133* (36), 19678–19701.

(29) Ravelli, D.; Fagnoni, M.; Albini, A. Photoorganocatalysis. What For? *Chem. Soc. Rev.* **2013**, *42* (1), 97–113.

(30) Slanina, T.; Oberschmid, T. Rhodamine 6G Radical: A Spectro (Fluoro) Electrochemical and Transient Spectroscopic Study. *ChemCatChem* **2018**, *10* (18), 4182–4190.

(31) Marzo, L.; Ghosh, I.; Esteban, F.; König, B. Metal-Free Photocatalyzed Cross Coupling of Bromoheteroarenes with Pyrroles. *ACS Catal.* **2016**, *6* (10), 6780–6784.

(32) Srivastava, V.; Singh, P. P. Eosin y Catalysed Photoredox Synthesis: A Review. *RSC Adv.* **2017**, *7* (50), 31377–31392.

(33) Pan, Y.; Wang, S.; Kee, C. W.; Dubuisson, E.; Yang, Y.; Loh, K. P.; Tan, C. H. Graphene Oxide and Rose Bengal: Oxidative C–H Functionalisation of Tertiary Amines Using Visible Light. *Green Chem.* **2011**, *13* (12), 3341–3344.

(34)   Yu, Z. Y.; Zhao, J. N.; Yang, F.; Tang, X. F.; Wu, Y. F.; Ma, C. F.; Song, B.; Yun, L.; Meng, Q. W. Rose Bengal as Photocatalyst: Visible Light-Mediated Friedel-Crafts Alkylation of Indoles with Nitroalkenes in Water. *RSC Adv.* **2020**, *10* (8), 4825–4831.

(35)   Sartor, S. M.; Chrisman, C. H.; Pearson, R. M.; Miyake, G. M.; Damrauer, N. H. Designing High-Triplet-Yield Phenothiazine Donor-Acceptor Complexes for Photoredox Catalysis. *J. Phys. Chem. A* **2020**, *124* (5), 817–823.

(36)   Discekici, E. H.; Treat, N. J.; Poelma, S. O.; Mattson, K. M.; Hudson, Z. M.; Luo, Y.; Hawker, C. J.; De Alaniz, J. R. A Highly Reducing Metal-Free Photoredox Catalyst: Design and Application in Radical Dehalogenations. *Chem. Commun.* **2015**, *51* (58), 11705–11708.

(37)   Nicewicz, D. A.; Nguyen, T. M. Recent Applications of Organic Dyes as Photoredox Catalysts in Organic Synthesis. *ACS Catal.* **2014**, *4* (1), 355–360.

(38)   Ghosh, I.; Ghosh, T.; Bardagi, J. I.; König, B. Reduction of Aryl Halides by Consecutive Visible Light-Induced Electron Transfer Processes. *Science* **2014**, *346* (6210), 725–728.

(39)   Brandl, F. et al., Consecutive Photoinduced Electron Transfer (ConPET)_The Mechanism of the Photocatalyst Rhodamine 6G. *Chem. Eur. j.* **2020**, *26*, 7946–7954.

(40)   Xu, J. et al., Unveiling Extreme Photoreduction Potentials of Donor-Acceptor Cyanoarenes to Access Aryl Radicals from Aryl Chlorides. *J. Am. Chem. Soc.* **2021**, *143* (33), 13266–13273.

(41)   Chernowsky, C. P.; Chmiel, A. F.; Wickens, Z. K. Electrochemical Activation of Diverse Conventional Photoredox Catalysts Induces Potent Photoreductant Activity. *Angew. Chem. Int. Ed.* **2021**, *60* (39), 21418–21425.

(42)   Chmiel, A. F.; Williams, O. P.; Chernowsky, C. P.; Yeung, C. S.; Wickens, Z. K. Non-Innocent Radical Ion Intermediates in Photoredox Catalysis: Parallel Reduction Modes Enable Coupling of Diverse Aryl Chlorides. *J. Am. Chem. Soc.* **2021**, *143* (29), 10882–10889.

(43)   Cowper, N. G. W.; Chernowsky, C. P.; Williams, O. P.; Wickens, Z. K. Potent Reductants via Electron-Primed Photoredox Catalysis: Unlocking Aryl Chlorides for Radical Coupling. *J. Am. Chem. Soc.* **2020**, *142* (5), 2093–2099.

(44)   Targos, K.; Williams, O. P.; Wickens, Z. K. Unveiling Potent Photooxidation Behavior of Catalytic Photoreductants. *J. Am. Chem. Soc.* **2021**, *143* (11), 4125–4132.

(45)   Cole, J. P.; Chen, D. F.; Kudisch, M.; Pearson, R. M.; Lim, C. H.; Miyake, G. M. Organocatalyzed Birch Reduction Driven by Visible Light. *J. Am. Chem. Soc.* **2020**, *142* (31), 13573–13581.

(46)   Zeman, C. J.; Kim, S.; Zhang, F.; Schanze, K. S. Direct Observation of the Reduction of Aryl Halides by a Photoexcited Perylene Diimide Radical Anion. *J. Am. Chem. Soc.* **2020**, *142* (5), 2204–2207.

(47)   Rieth, A. J.; Gonzalez, M. I.; Kudisch, B.; Nava, M.; Nocera, D. G. How Radical Are "Radical" Photocatalysts? A Closed-Shell Meisenheimer Complex Is Identified as a Super-Reducing Photoreagent. *J. Am. Chem. Soc.* **2021**, *143* (35), 14352–14359.

(48)   Uoyama, H.; Goushi, K.; Shizu, K.; Nomura, H.; Adachi, C. Highly Efficient Organic Light-Emitting Diodes from Delayed Fluorescence. *Nature* **2012**, *492* (7428), 234–238.

(49)   Bryden, M. A.; Zysman-Colman, E. Organic Thermally Activated Delayed Fluorescence (TADF) Compounds Used in Photocatalysis. *Chem. Soc. Rev.* **2021**, *50* (13), 7587–7680.

(50)   Luo, J.; Zhang, J. Donor-Acceptor Fluorophores for Visible-Light-Promoted Organic Synthesis: Photoredox/Ni Dual Catalytic C(Sp3)-C(Sp2) Cross-Coupling. *ACS Catal.* **2016**, *6* (2), 873–877.

(51)   Speckmeier, E.; Fischer, T. G.; Zeitler, K. A Toolbox Approach to Construct Broadly Applicable Metal-Free Catalysts for Photoredox Chemistry: Deliberate Tuning of Redox Potentials and Importance of Halogens in Donor-Acceptor Cyanoarenes. *J. Am. Chem. Soc.* **2018**, *140* (45), 15353–15365.

(52)   Lewis-Borrell, L.; Sneha, M.; Bhattacherjee, A.; Clark, I. P.; Orr-Ewing, A. J. Mapping the Multi-Step Mechanism of a Photoredox Catalyzed Atom-Transfer Radical Polymerization Reaction by Direct Observation of the Reactive Intermediates. *Chem. Sci.* **2020**, *11* (17), 4475–4481.

(53)   Sartor, S. M.; McCarthy, B. G.; Pearson, R. M.; Miyake, G. M.; Damrauer, N. H. Exploiting Charge-Transfer States for Maximizing Intersystem Crossing Yields in Organic Photoredox Catalysts. *J. Am. Chem. Soc.* **2018**, *140* (14), 4778–4781.

(54)   McCarthy, B. G.; Pearson, R. M.; Lim, C. H.; Sartor, S. M.; Damrauer, N. H.; Miyake, G. M. Structure-Property Relationships for Tailoring Phenoxazines as Reducing Photoredox Catalysts. *J. Am. Chem. Soc.* **2018**, *140* (15), 5088–5101.

(55)   Buss, B. L.; Lim, C. H.; Miyake, G. M. Dimethyl Dihydroacridines as Photocatalysts in Organocatalyzed Atom Transfer Radical Polymerization of Acrylate Monomers. *Angew. Chem. Int. Ed.* **2020**, *59* (8), 3209–3217.

(56)   Glaser, F.; Kerzig, C.; Wenger, O. S. Multi-Photon Excitation in Photoredox Catalysis: Concepts, Applications, Methods. *Angew. Chem. Int. Ed.* **2020**, *59* (26), 10266–10284.

(57)   Constantin, T.; Zanini, M.; Regni, A.; Sheikh, N. S.; Juliá, F.; Leonori, D. Aminoalkyl Radicals as Halogen-Atom Transfer Agents for Activation of Alkyl and Aryl Halides. *Science* **2020**, *367* (6481), 1021–1026.

(58)   Shang, T. Y.; Lu, L. H.; Cao, Z.; Liu, Y.; He, W. M.; Yu, B. Recent Advances of 1,2,3,5-Tetrakis(Carbazol-9-Yl)-4,6-Dicyanobenzene (4CzIPN) in Photocatalytic Transformations. *Chem. Commun.* **2019**, *55* (38), 5408–5419.

(59)   Liu, Y.; Chen, X. L.; Li, X. Y.; Zhu, S. S.; Li, S. J.; Song, Y.; Qu, L. B.; Yu, B. 4CzIPN-TBu-Catalyzed Proton-Coupled Electron Transfer for Photosynthesis of Phosphorylated N-Heteroaromatics. *J. Am. Chem. Soc.* **2021**, *143* (2), 964–972.

(60)   Singh, P. P.; Srivastava, V. Recent Advances in Using 4DPAIPN in Photocatalytic Transformations. *Org. Biomol. Chem.* **2021**, *19* (2), 313–321.

(61)   Song, Y. et al., Organic Photocatalyst for Ppm-Level Visible-Light-Driven Reversible Addition-Fragmentation Chain-Transfer (Raft) Polymerization with Excellent Oxygen Tolerance. *Macromolecules* **2019**, *52* (15), 5538–5545.

(62)   Back, J.; Kwon, Y.; Cho, H.; Lee, H.; Ahn, D.; Kim, H.; Yu, Y.; Kim, Y.; Lee, W.; Kwon, M. S. Visible Light Curable Acrylic Resins Toward UV-light Blocking Adhesives for Foldable Displays. *Adv. Mater.* **2022**, 2204776.

(63)   Back, J. H. et al., Synthesis of Solvent-Free Acrylic Pressure-Sensitive Adhesives: Via Visible-Light-Driven Photocatalytic Radical Polymerization without Additives. *Green Chem.* **2020**, *22* (23), 8289–8297.

(64)   Back, J.; Kwon, Y.; Kim, H.; Yu, Y.; Lee, W.; Kwon, M. S. Adhesives via Photoredox-Mediated Radical Polymerization. *Molecules* **2021**, *26*, 385–396.

(65)   Al Mousawi, A. et al., Carbazole Derivatives with Thermally Activated Delayed Fluorescence Property as Photoinitiators/Photoredox Catalysts for LED 3D Printing Technology. *Macromolecules* **2017**, *50* (13), 4913–4926.

(66) Gould, I. R.; Ege, D.; Moser, J. E.; Farid, S. Efficiencies of Photoinduced Electron-Transfer Reactions: Role of the Marcus Inverted Region in Return Electron Transfer within Geminate Radical-Ion Pairs. *J. Am. Chem. Soc.* **1990**, *112* (11), 4290–4301.

(67) IanR.Gould, DenizEge, SusanL.Mattes, and S. Return Electron Transfer within Geminate Radical Ion Pairs. Observation of the Marcus Inverted Region. **1987**, *109*, 3796–3797.

(68) Kohtani, S.; Mori, M.; Yoshioka, E.; Miyabe, H. Photohydrogenation of Acetophenone Using Coumarin Dye-Sensitized Titanium Dioxide under Visible Light Irradiation. *Catalysts* **2015**, *5* (3), 1417–1424.

(69) Adenier, A.; Chehimi, M. M.; Gallardo, I.; Pinson, J.; Vilà, N. Electrochemical Oxidation of Aliphatic Amines and Their Attachment to Carbon and Metal Surfaces. *Langmuir* **2004**, *20* (19), 8243–8253.

(70) Tucker, J. W.; Nguyen, J. D.; Narayanam, J. M. R.; Krabbe, S. W.; Stephenson, C. R. J. Tin-Free Radical Cyclization Reactions Initiated by Visible Light Photoredox Catalysis. *Chem. Commun.* **2010**, *46* (27), 4985–4987.

(71) Koike, T.; Akita, M. Visible-Light Radical Reaction Designed by Ru- and Ir-Based Photoredox Catalysis. *Inorg. Chem. Front.* **2014**, *1* (8), 562–576.

(72) Yan, Q.; Yue, K.; Yu, C.; Zhao, D. Oligo- and Polyfluorene-Tethered Fac-Ir(Ppy)3: Substitution Effects. *Macromolecules* **2010**, *43* (20), 8479–8487.

(73) Hedley, G. J.; Ruseckas, A.; Samuel, I. D. W. Ultrafast Luminescence in Ir(Ppy)3. *Chem. Phys. Lett.* **2008**, *450* (4–6), 292–296.

(74) Deronzier, A. Photophysical Properties of Soluble Polypyrrole - Polypyridyl - Ruthenium (II) Complexes. **2001**, *2* (II), 4801–4809.

(75) Lewis, F. D. Proton-Transfer Reactions of Photogenerated Radical Ion Pairs. *Acc. Chem. Res.* **1986**, *19* (12), 401–405.

(76) Zhao, H.; Leonori, D. Minimization of Back-Electron Transfer Enables the Elusive Sp3 C−H Functionalization of Secondary Anilines. *Angew. Chem. Int. Ed.* **2021**, *60* (14), 7669–7674.

(77) Etherington, M. K.; Gibson, J.; Higginbotham, H. F.; Penfold, T. J.; Monkman, A. P. Revealing the Spin-Vibronic Coupling Mechanism of Thermally Activated Delayed Fluorescence. *Nat. Commun.* **2016**, *7*, 1–7.

(78) Gierschner, J.; Shi, J.; Milián-Medina, B.; Roca-Sanjuán, D.; Varghese, S.; Park, S. Y. Luminescence in Crystalline Organic Materials: From Molecules to Molecular Solids. *Adv. Opt. Mater.* **2021**, *9* (13), 1–46.

(79) Shi, J. et al., Solid State Luminescence Enhancement in π-Conjugated Materials: Unraveling the Mechanism beyond the Framework of AIE/AIEE. *J. Phys. Chem. C* **2017**, *121* (41), 23166–23183.

(80) Gierschner, J.; Cornil, J.; Egelhaaf, H. J. Optical Bandgaps of π-Conjugated Organic Materials at the Polymer Limit: Experiment and Theory. *Adv. Mater.* **2007**, *19* (2), 173–191.

(81) Grotjahn, S.; König, B. Photosubstitution in Dicyanobenzene-Based Photocatalysts. *Org. Lett.* **2021**, *23* (8), 3146–3150.

(82) Wayner, D. D. M.; Dannenberg, J. J.; Griller, D. Oxidation Potentials of α-Aminoalkyl Radicals: Bond Dissociation Energies for Related Radical Cations. *Chem. Phys. Lett.* **1986**, *131* (3), 189–191.

(83)   Beatty, J. W.; Stephenson, C. R. J. Amine Functionalization via Oxidative Photoredox Catalysis: Methodology Development and Complex Molecule Synthesis. *Acc. Chem. Res.* **2015**, *48* (5), 1474–1484.

(84)   Wang, J.; Zheng, N. The Cleavage of a C-C Bond in Cyclobutylanilines by Visible-Light Photoredox Catalysis: Development of a [4+2] Annulation Method. *Angew. Chem. Int. Ed.* **2015**, *54* (39), 11424–11427.

(85)   Wang, Q.; Zheng, N. A Photocatalyzed Synthesis of Naphthalenes by Using Aniline as a Traceless Directing Group in [4 + 2] Annulation of Amino-Benzocyclobutenes with Alkynes. *ACS Catal.* **2017**, *7* (6), 4197–4201.

(86)   Roth, H. G.; Romero, N. A.; Nicewicz, D. A. Experimental and Calculated Electrochemical Potentials of Common Organic Molecules for Applications to Single-Electron Redox Chemistry. *Synlett* **2016**, *27* (5), 714–723.

(87)   Houser, K. J.; Bartak, D. E.; Hawley, M. D. Electrochemical Studies of the Formation and Decomposition of the Fluorobenzonitrile Radical Anions. *J. Am. Chem. Soc.* **1973**, *95* (18), 6033–6040.

(88)   Rondinini, S.; Mussini, P. R.; Muttini, P.; Sello, G. Silver as a Powerful Electrocatalyst for Organic Halide Reduction: The Critical Role of Molecular Structure. *Electrochim. Acta* **2001**, *46* (20), 3245–3258.

(89)   Baciocchi, E.; Del Giacco, T.; Lapi, A. Quenching of Singlet Oxygen by Tertiary Aliphatic Amines. Structural Effects on Rates and Products. *Helv. Chim. Acta* **2006**, *89* (10), 2273–2280.

(90)   Enemærke, R. J.; Christensen, T. B.; Jensen, H.; Daasbjerg, K. Application of a New Kinetic Method in the Investigation of Cleavage Reactions of Haloaromatic Radical Anions. *J. Chem. Soc. Perkin Trans. 2* **2001**, *1* (9), 1620–1630.

(91)   Isse, A. A.; Durante, C.; Gennaro, A. One-Pot Synthesis of Benzoic Acid by Electrocatalytic Reduction of Bromobenzene in the Presence of CO2. *Electrochem. commun.* **2011**, *13* (8), 810–813.

(92)   Gavioli, G. B.; Borsari, M.; Fontanesi, C. Theoretical Study of the Electroreduction of Halogenated Aromatic Compounds. Part 2. - Bromine and Chlorine Derivatives in Different Organic Solvents. *Journal of the Chemical Society, Faraday Transactions*. **1993**, *89,* (21), 3931–3939.

(93)   Poizot, P.; Laffont-Dantras, L.; Simonet, J. The One-Electron Cleavage and Reductive Homo-Coupling of Alkyl Bromides at Silver-Palladium Cathodes. *J. Electroanal. Chem.* **2008**, *624* (1), 52–58.

(94)   Feldstein, M. M.; Dormidontova, E. E.; Khokhlov, A. R. Pressure Sensitive Adhesives Based on Interpolymer Complexes. *Prog. Polym. Sci.* **2015**, *42*, 79–153.

(95)   T. Abrahamson, J.; Z. Beagi, H.; Salmon, F.; J. Campbell, C. Optically Clear Adhesives for OLED. *Lumin. - OLED Technol. Appl.* **2020**. 63.

(96)   Han, Z.; Fina, A. Thermal Conductivity of Carbon Nanotubes and Their Polymer Nanocomposites: A Review. *Prog. Polym. Sci.* **2011**, *36* (7), 914–944.

(97)   Taboada, G. M.; Yang, K.; Pereira, M. J. N.; Liu, S. S.; Hu, Y.; Karp, J. M.; Artzi, N.; Lee, Y. Overcoming the Translational Barriers of Tissue Adhesives. *Nat. Rev. Mater.* **2020**, *5* (4), 310–329.

(98)   Kwak, M. K.; Jeong, H. E.; Suh, K. Y. Rational Design and Enhanced Biocompatibility of a Dry Adhesive Medical Skin Patch. *Adv. Mater.* **2011**, *23* (34), 3949–3953.

(99) Hillmyer, M. A.; Tolman, W. B. Aliphatic Polyester Block Polymers: Renewable, Degradable, and Sustainable. *Acc. Chem. Res.* **2014**, *47* (8), 2390–2396.

(100) Heinrich, L. A. Future Opportunities for Bio-Based Adhesives-Advantages beyond Renewability. *Green Chem.* **2019**, *21* (8), 1866–1888.

(101) Lee, H. E.; Lee, D.; Lee, T. I.; Shin, J. H.; Choi, G. M.; Kim, C.; Lee, S. H.; Lee, J. H.; Kim, Y. H.; Kang, S. M.; Park, S. H.; Kang, I. S.; Kim, T. S.; Bae, B. S.; Lee, K. J. Wireless Powered Wearable Micro Light-Emitting Diodes. *Nano Energy* **2019**, *55* (November 2018), 454–462.

(102) Campbell, C. J. Optically ClearAdhesives Enabling Foldableand FlexibleOLED Displays. *SID Symp. Dig. Tech. Pap.* **2017**, *48*, 2009–2011.

(103) Kim, S.; Kwon, H. J.; Lee, S.; Shim, H.; Chun, Y.; Choi, W.; Kwack, J.; Han, D.; Song, M.; Kim, S.; Mohammadi, S.; Kee, I.; Lee, S. Y. Low-Power Flexible Organic Light-Emitting Diode Display Device. *Adv. Mater.* **2011**, *23* (31), 3511–3516.

(104) Ligon, S. C.; Husár, B.; Wutzel, H.; Holman, R.; Liska, R. Strategies to Reduce Oxygen Inhibition in Photoinduced Polymerization. *Chem. Rev.* **2014**, *114* (1), 577–589.

(105) Ollivier, C.; Renaud, P. Organoboranes as a Source of Radicals. *Chem. Rev.* **2001**, *101* (11), 3415–3434.

(106) Zhang, Z. C.; Chung, T. C. M. Reaction Mechanism of Borane/Oxygen Radical Initiators during the Polymerization of Fluoromonomers. *Macromolecules* **2006**, *39* (16), 5187–5189.

(107) Ahn, D.; Stevens, L. M.; Zhou, K.; Page, Z. A. Additives for Ambient 3D Printing with Visible Light. *Adv. Mater.* **2021**, *33* (44), 1–8.

(108) Hoyle, C. E.; Bowman, C. N. Thiol-Ene Click Chemistry. *Angew. Chem. Int. Ed.* **2010**, *49* (9), 1540–1573.

(109) Zhang, L.; Wu, C.; Jung, K.; Ng, Y. H.; Boyer, C. An Oxygen Paradox: Catalytic Use of Oxygen in Radical Photopolymerization. *Angew. Chem. Int. Ed.* **2019**, No. Ii, 16811–16814.

(110) Wu, C.; Jung, K.; Ma, Y.; Liu, W.; Boyer, C. Unravelling an Oxygen-Mediated Reductive Quenching Pathway for Photopolymerisation under Long Wavelengths. *Nat. Commun.* **2021**, *12* (1), 1–9.

(111) Lim, D.; Baek, M. J.; Kim, H. S.; Baig, C.; Lee, D. W. Carboxyethyl Acrylate Incorporated Optically Clear Adhesives with Outstanding Adhesion Strength and Immediate Strain Recoverability for Stretchable Electronics. *Chem. Eng. J.* **2022**, *437* (P2), 135390.

(112) Corrigan, N.; Rosli, D.; Jones, J. W. J.; Xu, J.; Boyer, C. Oxygen Tolerance in Living Radical Polymerization: Investigation of Mechanism and Implementation in Continuous Flow Polymerization. *Macromolecules* **2016**, *49* (18), 6779–6789.

(113) Hayyan, M.; Hashim, M. A.; Alnashef, I. M. Superoxide Ion: Generation and Chemical Implications. *Chem. Rev.* **2016**, *116* (5), 3029–3085.

(114) Islam, M. M.; Ohsaka, T. Roles of Ion Pairing on Electroreduction of Dioxygen in Imidazolium-Cation-Based Room-Temperature Ionic Liquid. *J. Phys. Chem. C* **2008**, *112* (4), 1269–1275.

(115) Rueping, M.; Vila, C.; Koenigs, R. M.; Poscharny, K.; Fabry, D. C. Dual Catalysis: Combining Photoredox and Lewis Base Catalysis for Direct Mannich Reactions. *Chem. Commun.* **2011**, *47* (8), 2360–2362.

(116) Hari, D. P. Photoredox Catalyzed C-P Bond Forming Reactions - Visible Light Mediated Oxidative Phosphonylations of Amines. *Org. Lett.* **2011**, *13* (15), 3852–3855.

(117) Baldo, M. A.; Y. You, D. F. O.; Shoustikov, A.; Sibley, S.; Thompson, M. E.; Forrest, S. R. Highly Efficient Phosphorescent Emission from Organic Electroluminescent Devices. *Nature* **1998**, *395* (6698), 151-154.

(118) Würth, C.; Grabolle, M.; Pauli, J.; Spieles, M.; Resch-Genger, U. Comparison of Methods and Achievable Uncertainties for the Relative and Absolute Measurement of Photoluminescence Quantum Yields. *Anal. Chem.* **2011**, *83* (9), 3431–3439.

(119) Singh, P. S.; Evans, D. H. Study of the Electrochemical Reduction of Dioxygen in Acetonitrile in the Presence of Weak Acids. *J. Phys. Chem. B* **2006**, *110* (1), 637–644.

(120) Pospíšil, J.; Nešpurek, S. Photostabilization of Coatings. Mechanisms and Performance. *Prog. Polym. Sci.* **2000**, *25* (9), 1261–1335.

(121) Zarwell, S.; Rück-Braun, K. Synthesis of an Azobenzene-Linker-Conjugate with Tetrahedrical Shape. *Tetrahedron Lett.* **2008**, *49* (25), 4020–4025.

(122) Roscales, S.; Csákÿ A. G. Synthesis of Di(Hetero)Arylamines from Nitrosoarenes and Boronic Acids: A General, Mild, and Transition-Metal-Free Coupling. *Org. Lett.* **2018**, *20* (6), 1667–1671.

(123) Kataoka, N.; Shelby, Q.; Stambuli, J. P.; Hartwig, J. F. Air Stable, Sterically Hindered Ferrocenyl Dialkylphosphines for Palladium-Catalyzed C-C, C-N, and C-O Bond-Forming Cross-Couplings. *J. Org. Chem.* **2002**, *67* (16), 5553–5566.

(124) Maiti, D.; Fors, B. P.; Henderson, J. L.; Nakamura, Y.; Buchwald, S. L. Palladium-Catalyzed Coupling of Functionalized Primary and Secondary Amines with Aryl and Heteroaryl Halides: Two Ligands Suffice in Most Cases. *Chem. Sci.* **2011**, *2* (1), 57–68.

(125) Murase, T.; Fujita, M. Highly Blue Luminescent Triazine-Amine Conjugated Oligomers. *J. Org. Chem.* **2005**, *70* (23), 9269–9278.

(126) Kretzschmar, A.; Patze, C.; Schwaebel, S. T.; Bunz, U. H. F. Development of Thermally Activated Delayed Fluorescence Materials with Shortened Emissive Lifetimes. *J. Org. Chem.* **2015**, *80* (18), 9126–9131.

(127) Etherington, M. K.; Kukhta, N. A.; Higginbotham, H. F.; Danos, A.; Bismillah, A. N.; Graves, D. R.; McGonigal, P. R.; Haase, N.; Morherr, A.; Batsanov, A. S.; Pflumm, C.; Bhalla, V.; Bryce, M. R.; Monkman, A. P. Persistent Dimer Emission in Thermally Activated Delayed Fluorescence Materials. *J. Phys. Chem. C* **2019**, *123* (17), 11109–11117.

(128) Speckmeier, E.; Fischer, T. G.; Zeitler, K. A Toolbox Approach to Construct Broadly Applicable Metal-Free Catalysts for Photoredox Chemistry: Deliberate Tuning of Redox Potentials and Importance of Halogens in Donor-Acceptor Cyanoarenes. *J. Am. Chem. Soc.* **2018**, *140* (45), 15353–15365.

(129) Korth, H. G.; Mulder, P. Phenolic Hydrogen Transfer by Molecular Oxygen and Hydroperoxyl Radicals. Insights into the Mechanism of the Anthraquinone Process. *J. Org. Chem.* **2020**, *85* (4), 2560–2574.

(130) Furukawa, T.; Nakanotani, H.; Inoue, M.; Adachi, C. Dual Enhancement of Electroluminescence Efficiency and Operational Stability by Rapid Upconversion of Triplet Excitons in OLEDs. *Sci. Rep.* **2015**, *5*, 8429.

(131) Baleizão, C.; Berberan-Santos, M. N. Thermally Activated Delayed Fluorescence as a Cycling Process between Excited Singlet and Triplet States: Application to the Fullerenes. *J. Chem. Phys.* **2007**, *126* (20). 204510.

Acknowledgement